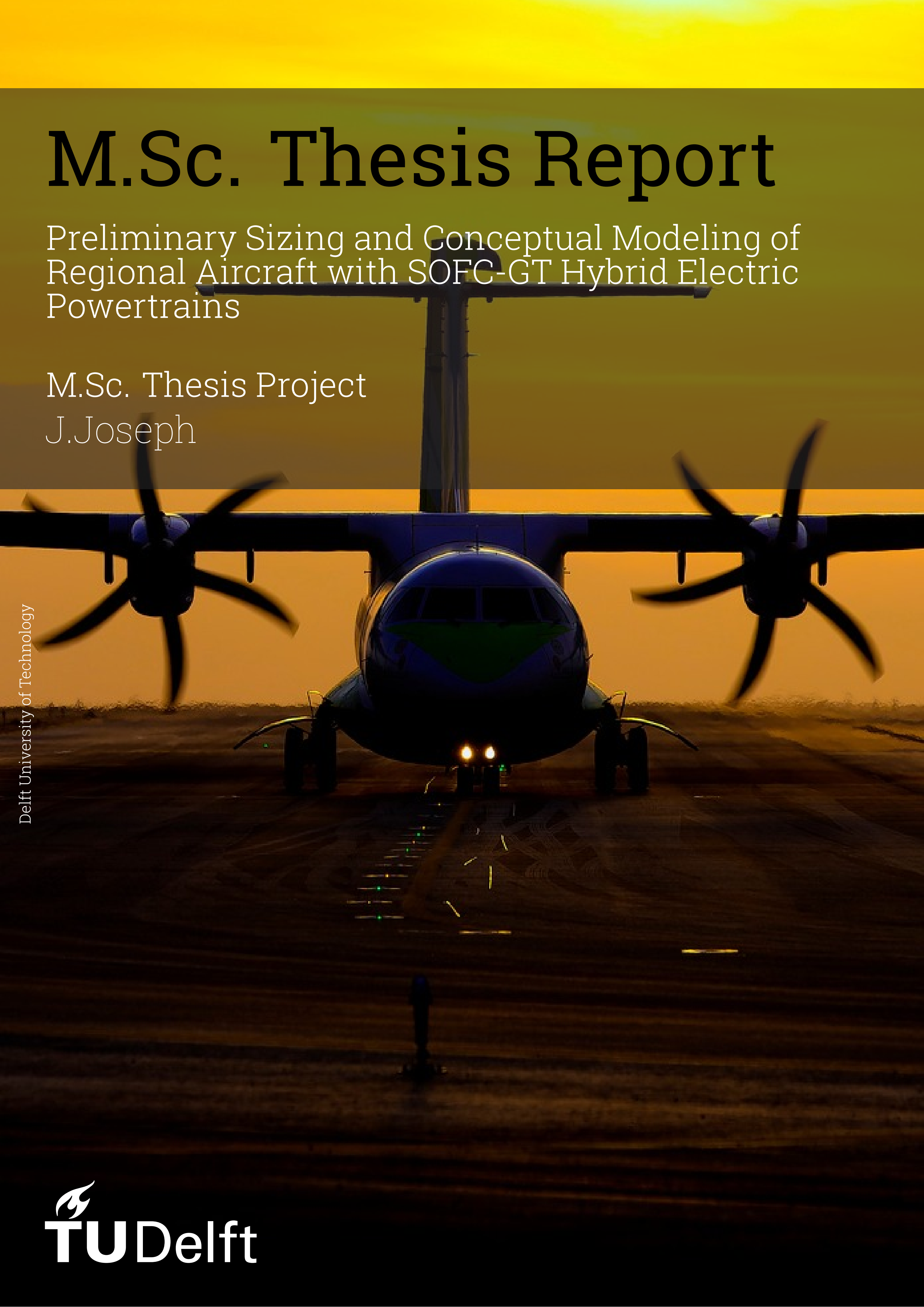

M.Sc. Thesis Report

Preliminary Sizing and Conceptual Modeling of Regional Aircraft with SOFC-GT Hybrid Electric Powertrains

M.Sc. Thesis Project

J.Joseph

Delft University of Technology

M.Sc. Thesis Report

Preliminary Sizing and Conceptual Modeling of Regional Aircraft with SOFC-GT Hybrid Electric Powertrains

by

J.Joseph

to obtain the degree of Master of Science at the Delft University of Technology,
and to be defended publicly on Tuesday, the 16th of September, 2025 at 9:00 AM CEST.

Student Number:	5945232	
Project Duration:	December 2024 - September 2025	
Thesis Committee:	Dr.ir. M.F.M. (Maurice) Hoogreef	TU Delft, Thesis Supervisor
	Prof. Dr. Arvind Gangoli Rao	TU Delft, Committee Chair
	Ir. O. Stroosma	TU Delft, External Examiner
Faculty:	Faculty of Aerospace Engineering, Delft	

Cover: A Canarias Airlines ATR 72-600 taxiing on the runway, photo by Manuel Estevez Rodriguez
Style: TU Delft Report Style, with modifications by Daan Zwaneveld

TU Delft

πλὴν μὴ τὸ θέλημά μου ἀλλὰ τὸ σὸν γινέσθω

“Let not mine, but Thy will be done.”

The Gospel of St. Luke, as originally written in Koine Greek
Chapter 22, Verse 42

Acknowledgment

This work is dedicated to my parents, without whose support I wouldn't have dared to dream again. My mom, who always saw her kid beneath the hardened soldier, and my dad, who constantly remained my strongest pillar of support. To just say that I will be indebted to you would be an understatement; I hope I can make you proud today through this small effort of mine.

The past two years of my Master's, and especially the last nine months during which almost all of this work materialized, would not have been possible without the continuous support of my close group of very dear friends, or 'Ricenberg', as we fondly call ourselves. We traveled, celebrated, endured, cried, and laughed together, making two years feel like a time-lapse you wouldn't mind re-living if you ever had the chance to. Thank you for being my home away from home.

Lots of love to you, Bhaiya and Caro chechi, for being there throughout, despite us being almost at opposite ends of the planet. Now that the Masters is coming to an end, I promise to dedicate my efforts full-time to preparing to be the best uncle!

Most importantly, I am incredibly grateful to my supervisor, Dr. Maurice Hoogreef, for providing me with this topic and for your wonderful guidance and support throughout this entire period. Thank you for providing me with the right direction and always carefully ensuring that I remained within the scope of my research objectives. I will always cherish the opportunity to not just work with you, but also being able to learn a great deal from the meetings we've had.

Last but not least, my sincere gratitude also extends to Alessandro Borgia, Ardya Inderavan, and Debdutta Chatterjee for dealing with the smallest of my doubts, directing me toward essential fundamentals, and helping me get started with the project. I'm also genuinely grateful to Prof. Gianfranco La Rocca and Dr. Fabrizio Oliviero for providing me with the opportunity to assist with the MDO course during the duration of my Master's Thesis project.

To study at TU Delft Aerospace Engineering, one of the finest schools for aerospace engineering in the world, has been an honor and will always remain a dream come true for me. To every professor I could learn from, every researcher I had the opportunity to interact with, and every student who was part of my journey here, I am truly indebted from the bottom of my heart.

Would I do TU Delft all over again if I ever had the chance to?

Anytime, in the skip of a heartbeat.

J.Joseph
Delft, September 2025

Abstract

This work presents the methodology for the conceptual modeling and preliminary sizing of Solid Oxide Fuel Cell–Gas Turbine (SOFC–GT) hybrid powertrains within a conceptual aircraft design framework. SOFC–GT hybrid systems, long investigated in commercial power generation, offer higher combined power output, improved overall thermal efficiency, and greater fuel flexibility compared to similar FC–GT architectures. As high-temperature solid oxide fuel cells (HT–SOFCs) are not electrochemically bound by a theoretical efficiency limit like the Carnot cycle for gas turbines, their integration with conventional engines has the potential to significantly improve system efficiencies while retaining high power densities.

The primary objective of this work is to evaluate their integration into regional turboprop aircraft and compare them against conventional aircraft with kerosene/SAF and LH_2-based gas turbine powertrains for similar Top Level Aircraft Requirements (TLAR). The sizing methodologies for SOFC-GT aircraft are incorporated within the Class 1 sizing loop of the Aircraft Design Initiator (ADI), an in-house conceptual aircraft design tool developed by the Faculty of Aerospace Engineering at Delft University of Technology for rapid design evaluation. For this, the powertrain model previously developed by De Vries (for hybrid-electric powertrains) and Borgia (for hydrogen-based hybrid-electric powertrains) was extended for the sizing of SOFC-GT aircraft.

The modeling approach starts at the fuel cell level, using validated electrochemical and thermodynamic models for the SOFC. A baseline tubular SOFC geometry is selected and modified to improve stack-level gravimetric power density through reductions in component thicknesses, dominant ohmic losses, and an increase in the effective cell area. The cell-level model is then integrated into a system-level representation of the SOFC-GT powertrain, which is then incorporated into the ADI's Class 1 sizing loop to meet the propulsion and power requirements of the baseline ATR 72-600 aircraft.

At the system level, the Class 1 sizing results of the SOFC-GT aircraft (at a design current density of 400 mA/cm², cruise H_2 split of 50%, and 75% fuel utilization) show an overall thermal efficiency of 44.17% in cruise, representing a 48% improvement over the baseline ATR 72-600 and 44% over the LH_2-based aircraft. These gains are accompanied by increases in MTOM (19.2% and 14.7%) and OEM (+45.2% and +23%) compared to kerosene and LH_2 aircraft, respectively. Nevertheless, the higher efficiency reduces the required energy mass for the full-range design mission by 65% and 13.5%, while the larger wingspan (29.44 m) remains within ICAO Class C limits. Consequently, the lower H_2 demand also decreases H_2O and NOX emissions by 15.3% and 50.26% relative to conventional LH_2 aircraft.

Results from parametric analyses indicate that the hydrogen power split between the gas turbine and the SOFC stacks in cruise is the most influential design parameter for maximizing performance, with higher values improving overall thermal efficiency but also significantly increasing the aircraft operating empty mass (OEM) and energy requirements for the design mission. The trade-off between fuel cell and gas turbine contributions is sensitive to fuel utilisation, where low utilisation reduces efficiency by shifting power production toward the less efficient gas turbine. On the other hand, increasing anode fuel utilisation above 75% improves overall thermal efficiency but can reduce gravimetric power density at the stack level due to mass transport losses, the effect of which can be partially mitigated by increasing the excess air supply at the cathode.

Additionally, the SOFC system pressure and operating temperature were also observed to be important design parameters that could improve the performance of the SOFC-GT powertrain. However, the cruise thermal efficiency exhibits an asymptotic trend at higher pressures and temperatures, beyond which the benefits diminish. At elevated temperatures, further gains are offset by an increase in system mass, while at higher pressures, the additional Balance of Plant (BoP) power requirements lead to reductions in both gas turbine and SOFC efficiencies.

Contents

List of Figures

List of Tables

Nomenclature

Abbreviations

Abbreviation	Definition
AEO	All Engine Operative
APS	Atmospheric Plasma Spray
APU	Auxiliary Power Unit
AR	Wing Aspect Ratio
ASR	Area Specific Resistance
ADI	Aircraft Design Initiator
BFFM2	Boeing Fuel Flow Method 2
BoP	Balance of Plant
DMFC	Direct Methanol Fuel Cell
DOH	Degree of Hybridization
EASA	European Union Aviation Safety Agency
EM	Energy Mass
EM1	Primary Electrical Machine (EM1)
EVD	Electrochemical Vapor Deposition
FF	Fuel Fraction
FCS	Fuel Cell System
FTF	Fuel Type Fraction
GB	Gearbox
GI	Gravimetric Index
GT	Gas Turbine
GWP	Global Warming Potential
HEP	Hybrid Electric Propulsion
HPC	High-Pressure Compressor
HPC	High-Pressure Turbine
HX	Heat Exchanger
ISA	International Standard Atmosphere
KCAS	Knots Calibrated Airspeed
KIAS	Knots Indicated Airspeed
KTAS	Knots True Airspeed
LHV	Lower Heating Value
LPC	Low Pressure Compressor
LSM	Lanthanum Strontium Manganite
LTO	Landing and Take-Off (ICAO cycle)
MCFC	Molten Carbonate Fuel Cell
MLW	Maximum Landing Weight
MPLM	Maximum Payload Mass
MTOM	Maximum Takeoff Mass
MTOW	Maximum Takeoff Weight
MZFW	Maximum Zero Fuel Weight
NPSS	Numerical Propulsion System Simulations
NTU	Number of Transfer Units
OEM	Operating Empty Mass
OEI	One Engine Inoperative
OPR	Overall Pressure Ratio
PAFC	Phosphoric Acid Fuel Cell

Abbreviation	**Definition**
PEMFC	Proton Exchange Membrane Fuel Cell
PMAD	Power Management and Distribution
PNNL	Pacific Northwest National Laboratory
PST	Porous Support Tube
PT	Power Turbine
ScZ	Scandium Doped Zirconia
SAF	Sustainable Aviation Fuel
SHP	Shaft Horsepower
SOFC	Solid Oxide Fuel Cell
SPPH	Serial-Parallel Partial Hybrid
TLAR	Top-Level Aircraft Requirements
TPB	Triple Phase Boundary
TMS	Thermal Management System
TOM	Takeoff Mass
YSZ	Yittria Stabilized Zirconia
ZFM	Zero Fuel Mass

Symbol	**Definition**	**Unit**
$\mathrm{A_{cell}}$	Area of a SOFC	$\mathrm{cm^2}$
$\mathrm{AR_{wing}}$	Wing aspect ratio	–
α	Charge transfer coefficient	–
b	Wingspan	m
β_{air}	Molar fraction of O_2 in air	–
β_{HPC}	HPC pressure ratio	–
β_{LPC}	LPC pressure ratio	–
$\mathrm{c_p}$	Specific heat at constant pressure	$\mathrm{kJ\,kg^{-1}\,K^{-1}}$
$\mathrm{C_{L,max}}$	Maximum lift coefficient	–
$\mathrm{C_{D,0}}$	Skin friction drag coefficient	–
$\mathrm{D_{eff}}$	Effective diffusivity	$\mathrm{m^2\,s^{-1}}$
$\mathrm{D_h}$	Hydraulic diameter	m
δ	Reference pressure ratio P/P_{SL}	–
$\delta_{\mathrm{H_2}}$	Anode fuel composition	–
e	Oswald efficiency factor	–
E	Exponential term in cell resistance equation	K
$\mathrm{E_{bat}}$	Energy of batteries	J
$\mathrm{E_{fuel}}$	Energy of fuel	J
EI	Emission index	$\mathrm{g\,kg^{-1}}$
ϵ	Heat exchanger effectiveness	–
F	Faraday's constant	$\mathrm{C\,mol^{-1}}$
g	Gravitational acceleration	$\mathrm{m\,s^{-2}}$
γ	Adiabatic exponent	–
$\mathrm{GI_{HX}}$	Heat exchanger gravimetric index	$\mathrm{kg\,m^{-2}}$
$\mathrm{GI_{FC}}$	Fuel cell gravimetric power density	$\mathrm{kW\,kg^{-1}}$
H	Humidity correction factor (BFFM2)	–
η_{FC}	Fuel cell thermal efficiency	–
η_{GT}	Gas turbine thermal efficiency	–
η_{overall}	Overall thermal efficiency	–
h	Convective heat transfer coefficient	$\mathrm{W\,m^{-2}\,K^{-1}}$
i	Cell operating current density	$\mathrm{mA\,cm^{-2}}$
$\mathrm{i_0}$	Exchange current density	$\mathrm{mA\,cm^{-2}}$
$\mathrm{i_L}$	Limiting current density	$\mathrm{mA\,cm^{-2}}$
K	Correction factor for Class 1 wing mass estimation	–

Symbol	**Definition**	**Unit**
$\mathrm{i_n}$	Internal current density	$\mathrm{mA\,cm^{-2}}$
k	Thermal conductivity	$\mathrm{W\,m^{-1}\,K^{-1}}$
$\mathrm{l_{cell}}$	Length of SOFC	m
$\mathrm{l_{fuselage}}$	Length of fuselage extension	m
Λ	Wing sweep angle	deg
λ_{air}	Cathode air stoichiometry	–
M	Mach number	–
$\mathrm{M_{component}}$	Component mass	kg
$\dot{\mathrm{m}}$	Mass flow rate	$\mathrm{kg\,s^{-1}}$
μ	Dynamic viscosity	$\mathrm{kg\,m^{-1}\,s^{-1}}$
$\dot{\mathrm{n}}$	Molar flow rate	$\mathrm{mol\,s^{-1}}$
$\mathrm{n_{ult}}$	Ultimate load factor	–
$\mathrm{n_{stacks}}$	Number of stacks	–
$\mathrm{N_{cell}}$	Number of cells in a stack	–
$\mathrm{N_{eng}}$	Number of engines	–
Nu	Nusselt number	–
p_i	Partial pressure of species i	Pa
P	Power	kW
$\mathrm{p_{amb}}$	Ambient static pressure	Pa
$\mathrm{p_t}$	Total pressure	Pa
Pr	Prandtl number	–
ϕ	Supplied power ratio	–
ψ	Shaft power ratio	–
q	Dynamic pressure	Pa
$\dot{q}_{\mathrm{th,cell}}$	Heat generation rate of a single SOFC (per area)	$\mathrm{W\,cm^{-2}}$
$\dot{\mathrm{Q}}$	Rate of heat energy	W
r	Bulk internal area-specific resistance	$\mathrm{k\Omega\,cm^{-2}}$
$\mathrm{r_{cell}}$	Radius of cell component layer	m
R	Universal gas constant	$\mathrm{J\,mol^{-1}\,K^{-1}}$
Re	Reynolds number	–
ρ	Density	$\mathrm{kg\,m^{-3}}$
$\mathrm{s_{TO}}$	Takeoff distance	m
S_w	Wing planform area	$\mathrm{m^2}$
σ	Exhaust gas splitting ratio	–
$\mathrm{t_{cell}}$	Thickness of cell component layer	m
$\mathrm{t_{fin}}$	Fin thickness	m
$\mathrm{T_{amb}}$	Ambient static temperature	K
$\mathrm{T_{cruise}}$	Cruise thrust	N
$\mathrm{T_t}$	Total temperature	K
$\mathrm{T_{SOFC}}$	SOFC operating temperature	K
τ	Tortuosity	–
θ	Reference temperature ratio T/T_{SL}	–
U	Overall heat transfer coefficient	$\mathrm{W\,m^{-2}\,K^{-1}}$
$\mathrm{U_{fuel}}$	Fuel utilization factor (SOFC)	–
V	Voltage	V
$\mathrm{V_s}$	Stall speed	$\mathrm{m\,s^{-1}}$
$\mathrm{V_{venting}}$	Venting volume for $\mathrm{LH_2}$ tank	$\mathrm{m^3}$
$\mathrm{W/S}$	Wing loading	$\mathrm{N\,m^{-2}}$
$\mathrm{W/P}$	Power loading	$\mathrm{N\,W^{-1}}$
Y_i	Mass fraction of species i	–
$y_{\mathrm{O_2}}$	Mole fraction of $\mathrm{O_2}$ in air	–
z	Number of participating electrons	–
φ	Relative humidity	–
ω	Humidity ratio	–

(This page has intentionally been left blank.)

1

Introduction

The aviation industry is currently going through a phase of radical changes that aim to reduce the impact of climate change on aircraft, with several EU-funded research projects spearheading the goal of lowering emission levels by 45% in 2030 and net zero emissions by 2050. These goals are deemed achievable through technological advancements, operational optimization, infrastructure enhancement, use of novel propulsion technologies, and implementation of offsets and carbon mitigation strategies. It is worth noting in this context that there has been a significant reduction over the years, with CO_2 emissions per passenger per kilometer being reduced by almost 54% in the last 30 years.

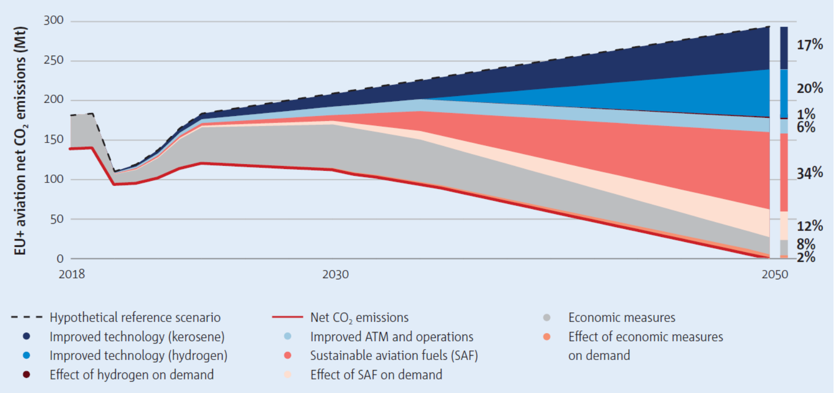

Figure 1.1: Projection of CO_2 emissions from aviation. y axes represents metric tonnes in CO_2 emissions [85]

One of the principal approaches to solving this fundamental problem in the aviation sector has been to explore the electrification of aircraft, which may be classified as fully-electric or hybrid-electric based on the degree of electrification [78]. Although fully-electric aircraft for medium to long range missions remain the ultimate solution to solving this conundrum, this solution remains quite dependent on technological advancements in the development of batteries with sufficient gravimetric energy density and highly efficient electrical systems to become a reality. Therefore, R&D on fully-electrified aircraft is limited in their scope currently, and feasible for mostly short-range missions.

It is in this context that hybrid-electric propulsion configurations are being explored in detail currently, as they provide a scope of technology-bridging to achieve emission targets in the aviation sector as it marches towards the solution of full-electrification to achieve net-zero emission goals. A 'hybrid' propulsion system incorporates conventional gas turbine propulsion with electric systems (either battery-powered or fuel-cell powered) in an attempt to increase the overall efficiency of the propulsion system. Battery-based hybrid systems use the gas turbine engine for the primary propulsion and recharging the batteries, while the batteries supply a fixed portion of power during various phases of the flight mission profile. On the other hand, fuel-cell-based hybrid systems make use of a single energy source like a hydrocarbon-based fuel and air to produce electricity and water, with the power produced by the fuel cell system (FCS) supplementing the required power of the aircraft at various phases of the mission profile [66]. Compared to battery-based hybrid systems, FC-based hybrid systems thus provide an added advantage of power production that is fully independent/partially dependent on the gas turbine engine, and only dependent on a single-energy source. Added to the fact that progress in battery technology is slow, FC-based hybrid systems thus provide great promise of integration into aircraft that are tailored for short and medium-range missions.

FC-based hybrid propulsion systems have thus emerged as a key candidate for their potential to transform aircraft propulsion systems. Fuel cells are essentially electrochemical devices that convert chemical energy to electric energy through a controlled reaction between hydrogen and oxygen. Not limited by Carnot efficiency, they offer a promising alternative to combustion engines, providing a cleaner and more efficient source of power. FC-based hybrid propulsion systems not only provide an opportunity for reducing greenhouse emissions, but also help mitigate noise pollution due to their fewer moving parts and reduced fuel consumption for airline operators.

Out of the candidates for fuel cells that could be integrated into this hybrid architecture, Proton-Exchange Membrane (PEM) Fuel Cells and Solid Oxide Fuel Cells (SOFCs) show the most promise. While PEM fuel cells with their low temperature application and high specific power output make them a primary candidate for automotive applications, they can be very sensitive to fuel impurities, especially carbon monoxide, when integrated into propulsion systems that use hydrocarbon-based fuel sources. This contrasts with an SOFC, which, although has a lower specific power output and a slower starting capability, is compatible with a wide range of hydrocarbon-based fuels when coupled with a reformer. Additionally, being high-temperature application fuel cells, they provide an opportunity to utilize the fuel cell thermal output for gas turbine combustion, an architecture which could potentially increase thermal efficiency when compared to conventional gas turbine engines [25].

This project aims to explore how a SOFC-GT powertrain can be modeled and sized with better fidelity within a conceptual aircraft design tool. De Vries [19] developed methodologies to conceptually size hybrid-electric propulsion systems, which were later extended to the case of hydrogen-based FC-GT architectures by Alessandro Borgia [9]. Therefore, the primary objective of this research is to improve the fidelity of the hybrid Class 1 sizing methodologies within the Aircraft Design Initiator by incorporating thermodynamic, electrochemical, and sizing models specific to SOFC–GT powertrain architectures. The results of these models are then validated against data available in literature, following which a parametric study to study the effect of key powertrain design parameters on Class 1 sizing results is conducted.

2

Literature Review

2.1. The need for Hydrogen

To meet the goals of net-zero emissions in the aviation sector by 2050, several decarbonization strategies are being explored currently; the most notable solutions being that of hybrid and full electrification for regional flights (short-medium range), and the use of SAF/liquid hydrogen combustion for longer range missions. Although full electrification is seen as the ultimate solution to meet emission goals, this is quite an ambitious goal due to battery specific energy density demands; especially given the fact that the most optimistic projections forecast this to be 500 Wh/kg by 2030, while a specific energy density of at least 800 Wh/kg is required for single-aisle size aircraft viability [66]. Current technological readiness level for batteries (low gravimetric energy densities of 200 to 500 Wh/kg and limited life cycles) does not meet this criterion, particularly for fuel-intensive journeys in long-haul flights [60]. Therefore, it is expected that battery-powered aircraft will be practically viable up to the sub-regional scale by 2035 [82].

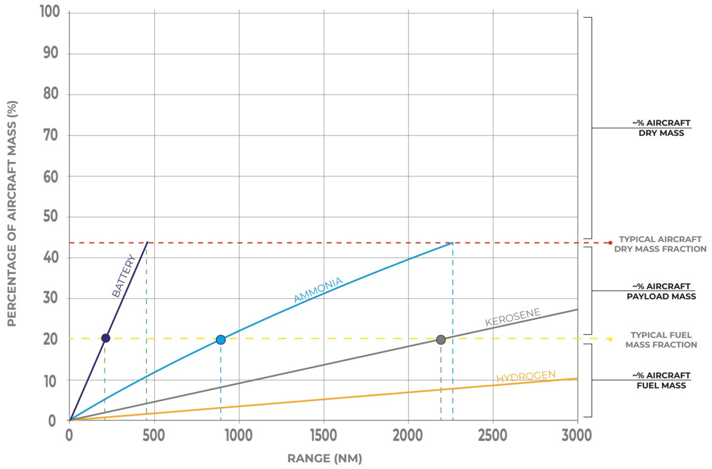

Figure 2.1: Mass of fuel and containment systems of different fuels relative to total aircraft mass (2030 technological level) against design range in nautical miles [89]

This explains why hydrogen and SAF-based engines, including hybrid-electric configurations, are being explored as interim solutions before we reach the necessary level of maturation in battery technology to achieve full-scale electrification goals. Hydrogen, especially in its cryogenic, liquid form, is particularly attractive due to its **high specific energy density** (around **2.8 times** that of kerosene-based fuels), resulting in a corresponding reduction of fuel utilized for missions [86]; albeit at a cost of additional components for fuel storage, conditioning, and distribution. Despite offering an advantage of higher specific energy density, the **volumetric energy density** of hydrogen, even when cryogenically cooled to its liquid form, is **four times less dense** than kerosene-based fuels, necessitating the need for heavier tanks with greater volume for fuel storage, and complex cryogenic systems for fuel distribution and conditioning. Although this adds to the operating empty weight (OEW) of the aircraft, increasing fuel burn, the possibilities of integrating this with the aircraft's thermal management system (TMS) would help increase overall engine efficiency and lead to fewer emissions [82].

Future engines operating on hydrogen could have two possible configurations, one that would produce thrust solely by direct liquid hydrogen combustion, and the other being hybrid-electric powertrains that would utilize hydrogen via fuel cells. From an emissions point of view, direct hydrogen combustion could lead to two primary by-products with considerable Global Warming Potential (GWP), namely nitrogen oxides (NO_x) and water vapor. In comparison to conventional gas turbine engines that operate on kerosene-based fuels, direct hydrogen combustion leads to 50-70% lesser NO_x emissions, while the use of fuel cells leads to zero NO_x [77]. However, water emission in hydrogen-based engines is 2.6 times more than that of conventional engines operating on kerosene-based fuels, but with the key absence of soot formation. This unique property of hydrogen combustion also affects contrail formation, with preliminary contrail models suggesting that direct H_2 combustion forms heavier ice crystals that precipitate faster and are optically thinner; meaning the contrails have a lesser radiative forcing effect (around 30-50% lesser GWP of contrails when compared to kerosene, [77]). However, the complete environmental impact of hydrogen-based engines is still not fully certain and is still under active investigation ([54],[43]). Additionally, it is also worth noting that fuel-cell-based hybrid-electric powertrains could potentially offer an added advantage of exhaust water vapor conditioning based on the atmospheric state to avoid contrails [82].

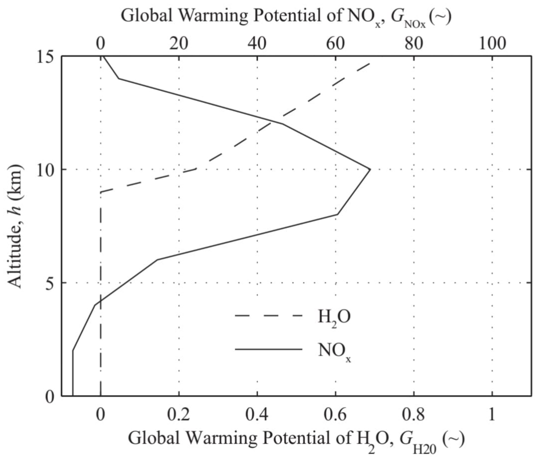

Figure 2.2: Change in Global Warming Potential (GWP), of H_2O and NO_x with altitude, relative to that of CO_2 [80]

2.2. Hybrid Electric Propulsion Systems (HEPS)

Due to the hurdles in achieving full-electrification for medium-long range narrow/wide-body aircraft for reaching net-zero emission goals, various interim solutions like *hybrid-electric powertrains* (stand-alone, or in combination with hydrogen fuel cells) are being explored actively. In these *hybrid-electric propulsion* (HEP) configurations, a portion of the power obtained from the energy source(s) is transferred to the propulsors as electrical power. Such configurations are seen as highly desirable because of their ability to improve powertrain efficiencies. Such hybrid-electric configurations can exploit the high conversion efficiency of electric machines to drive propulsors [34], and can be used to downsize and improve off-design performance [[56],[96]] and surge margins of conventional gas turbine engines [14]. Such a design strategy would require the use of batteries/hydrogen fuel cells, which could be integrated into the aircraft without significant modifications to the airframe. The use of an electric energy source can also benefit from taxiing, engine starting capabilities, help replace hydraulic/bleed air systems for environmental control and control surface actuation [75], and most importantly, help improve the aero-propulsive efficiency of the aircraft; by providing possibilities to integrate distributed propulsion systems

[19].

Based on the classification of hybrid-electric powertrain configurations by the National Academy of Engineering [66], De Vries described and elaborated upon a methodology to size these powertrain architectures, except for integrated hydrogen fuel cells. These configurations, referred generally to as the **Series-Parallel Partial Hybrid (SPPH)**, are shown in Figure 2.3. A total of nine possible combinations are shown in Figure 2.3, with the SPPH configuration (Figure 2.3.6) being the most generic one. These simplified representations of powertrain architectures include energy sources, nodes, power conversion components, and power paths to connect the various elements of the powertrain [19].

The various components in Figure 2.3 are divided into elements that either constitute the *primary powertrain* (components that are directly/indirectly mechanically coupled to the gas turbine engine) or the *secondary powertrain* (components that are directly/indirectly coupled to the electrical system). Although this method of modeling is quite useful for preliminary sizing of the powertrain, it does take into account several assumptions for the sake of simplicity. The nozzle thrust of the gas turbine engine is not explicitly accounted for, as the core thrust is assumed to be small with respect to the total engine thrust. Power converters/transformers are not explicitly modeled as they do not change the type of power (electrical) being transmitted through the powertrain, while the weight and efficiencies of smaller electrical elements are grouped as the Power Management and Distribution element (PMAD) [19]. All components are represented in terms of their efficiencies, which play a huge role in determining component weights through powertrain sizing.

The SPPH architecture is defined using component efficiencies and two hybridization parameters (supplied power ratio, ϕ (originally defined by Isikveren et.al [48]) and shaft power ratio, ψ - shown in Equations 2.1 and 2.2) that model the power splits in the hybrid-electric powertrain. Additionally, the conventional gas turbine settling can be modeled using a parameter for engine throttle, as shown in Equation 2.3.

$$\phi = \frac{P_{bat}}{P_{bat} + P_{fuel}} \tag{2.1}$$

$$\psi = \frac{P_{s2}}{P_{s1} + P_{s2}} \tag{2.2}$$

$$\xi = \frac{P_{GT}}{P_{GT,max}} \tag{2.3}$$

Configuration	Φ	φ
1. Conventional	0	0
2. Turboelectric	0	1
3. Serial	·	1
4. Parallel	·	0
5. Partial TE	0	·
6. S/P partial hybrid	·	·
7. Full-electric 1	1	0
8. Full-electric 2	1	1
9. Dual-electric	1	·

Table 2.1: Supplied power ratio and shaft power ratio values associated with each of the hybrid architectures shown in Figure 2.3 [19].

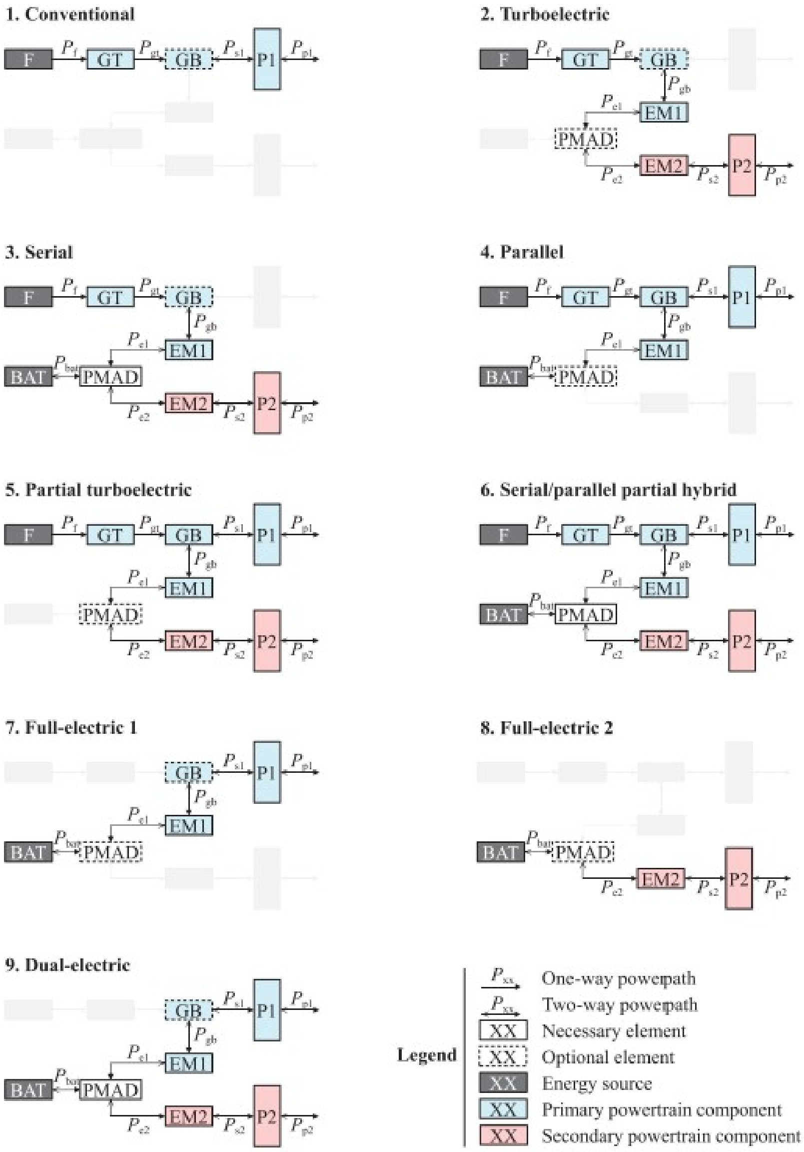

Figure 2.3: Simplified models of the nine possible hybrid-electric powertrain architectures (not including fuel cells) suggested by Vries [19]

Using the values of component efficiencies, the supplied power ratio (ϕ), the shaft power ratio (ψ), and the total propulsive power requirement (obtained from flight-performance equations for a given flight condition), the powers of various components (unknown) in the SPPH powertrain configuration can be solved using a system of 10 equations (as the SPPH configuration has 10 components), which represent the power flow through the powertrain. This general system of equations that represent the SPPH configuration is shown in matrix notation in Equation 2.5 - where **A** is the coefficient matrix that contains various component efficiencies and the hybridization parameters, **P** is the column vector containing the unknown component powers and the right-hand-side column vector **b** depends on the constraints imposed on the system of powertrain equations. Therefore, the matrix notion shown below in 2.5 can be represented generally as-

$$\mathbf{A.p} = \mathbf{b} \tag{2.4}$$

$$\begin{bmatrix} -\eta_{\mathrm{GT}} & 1 & 0 & 0 & 0 & 0 & 0 & 0 & 0 & 0 \\ 0 & -\eta_{\mathrm{GB}} & 1 & 1 & 0 & 0 & 0 & 0 & 0 & 0 \\ 0 & 0 & 0 & -\eta_{\mathrm{P1}} & 0 & 0 & 0 & 0 & 1 & 0 \\ 0 & 0 & -\eta_{\mathrm{EM1}} & 0 & 1 & 0 & 0 & 0 & 0 & 0 \\ 0 & 0 & 0 & 0 & -\eta_{\mathrm{PMAD}} & -\eta_{\mathrm{PMAD}} & 1 & 0 & 0 & 0 \\ 0 & 0 & 0 & 0 & 0 & 0 & -\eta_{\mathrm{EM2}} & 1 & 0 & 0 \\ 0 & 0 & 0 & 0 & 0 & 0 & 0 & -\eta_{\mathrm{P2}} & 0 & 1 \\ \Phi & 0 & 0 & 0 & 0 & (\Phi-1) & 0 & 0 & 0 & 0 \\ 0 & 0 & 0 & \varphi & 0 & 0 & 0 & (\varphi-1) & 0 & 0 \\ 0 & 0 & 0 & 0 & 0 & 0 & 0 & 0 & 1 & 1 \end{bmatrix} \cdot \begin{bmatrix} P_f \\ P_{\mathrm{gt}} \\ P_{\mathrm{gb}} \\ P_{\mathrm{s1}} \\ P_{\mathrm{el}} \\ P_{\mathrm{bat}} \\ P_{\mathrm{e2}} \\ P_{\mathrm{s2}} \\ P_{\mathrm{p1}} \\ P_{\mathrm{p2}} \end{bmatrix} = \begin{bmatrix} 0 \\ 0 \\ 0 \\ 0 \\ 0 \\ 0 \\ 0 \\ 0 \\ 0 \\ 0 \end{bmatrix} \tag{2.5}$$

System of equations for the generic SPPH powertrain 2.3.6 [19]

Once the powertrain size is determined, it may be useful to specify the throttle setting while treating propulsive power as a dependent variable. This is common during the climb phase of mission analysis, where engines operate at maximum continuous power, with excess power used for acceleration or altitude gain. In such cases, the equations can be solved as:

$$\begin{bmatrix} -\eta_{\mathrm{GT}} & 1 & 0 & 0 & 0 & 0 & 0 & 0 & 0 & 0 \\ 0 & -\eta_{\mathrm{GB}} & 1 & 1 & 0 & 0 & 0 & 0 & 0 & 0 \\ 0 & 0 & 0 & -\eta_{\mathrm{P1}} & 0 & 0 & 0 & 0 & 1 & 0 \\ 0 & 0 & -\eta_{\mathrm{EM1}} & 0 & 1 & 0 & 0 & 0 & 0 & 0 \\ 0 & 0 & 0 & 0 & -\eta_{\mathrm{PMAD}} & -\eta_{\mathrm{PMAD}} & 1 & 0 & 0 & 0 \\ 0 & 0 & 0 & 0 & 0 & 0 & -\eta_{\mathrm{EM2}} & 1 & 0 & 0 \\ 0 & 0 & 0 & 0 & 0 & 0 & 0 & -\eta_{\mathrm{P2}} & 0 & 1 \\ \Phi & 0 & 0 & 0 & 0 & (\Phi-1) & 0 & 0 & 0 & 0 \\ 0 & 0 & 0 & \varphi & 0 & 0 & 0 & (\varphi-1) & 0 & 0 \\ 0 & \xi_{\mathrm{GT}} & 0 & 0 & 0 & 0 & 0 & 0 & 0 & 0 \end{bmatrix} \cdot \begin{bmatrix} P_f \\ P_{\mathrm{gt}} \\ P_{\mathrm{gb}} \\ P_{\mathrm{s1}} \\ P_{\mathrm{el}} \\ P_{\mathrm{bat}} \\ P_{\mathrm{e2}} \\ P_{\mathrm{s2}} \\ P_{\mathrm{p1}} \\ P_{\mathrm{p2}} \end{bmatrix} = \begin{bmatrix} 0 \\ 0 \\ 0 \\ 0 \\ 0 \\ 0 \\ 0 \\ 0 \\ 0 \\ P_{\mathrm{GT,max}} \end{bmatrix} \tag{2.6}$$

2.3. Aircraft FC Systems

Fuel cell-gas turbine hybrids (FC-GT) have recently garnered significant attention due to their ability to efficiently convert chemical energy into electrical energy. While standalone fuel cells share challenges with battery-electric propulsion systems, particularly regarding gravimetric energy density for heavier, medium-to-long-range aircraft, FC-GT hybrids present a promising alternative to traditional gas turbine engines. These systems provide a cleaner and more efficient power source, aligning well with the aviation industry's goals to reduce carbon emissions, improve fuel efficiency, and minimize environmental impact in the coming decades. Further exploration and development of FC-GT hybrids could unlock their full potential as an innovative solution for sustainable aviation in the near future.

Table 2.2: Various fuel cells, their working temperatures, and applications [70].

Types of Fuel Cell (FC)	Working Temperature	Applications
Proton Exchange Membrane FC (PEMFC)	10–100 °C	Space, public buses, military, aircraft
Alkaline FC (AFC)	20–120 °C	Space, military
Solid Oxide FC (SOFC)	600–1000 °C	Utility, vehicles, aircraft
Direct Methanol FC (DMFC)	50–120 °C	Transportation, portable devices
Phosphoric Acid FC (PAFC)	~200 °C	Distributed generation
Molten Carbonate FC (MCFC)	600–700 °C	Utility, distributed generation

Table 2.2 summarizes various fuel cell types, along with their operating conditions and applications. Out of these, **Solid Oxide Fuel Cells** (SOFCs) and **Proton Exchange Membrane Fuel Cells** (PEM-

FCs) are of specific interest, having emerged as promising choices for aircraft propulsion- and this is discussed in the following section.

As shown in Figure 2.4, fuel cells, when compared to electrochemical batteries, demonstrate lower power density but significantly higher gravimetric energy density. Therefore, a promising solution to enhance the response performance of fuel cell-based propulsion systems would be the integration of batteries or super-capacitors (SCs) into a hybrid system, ensuring an efficient and reliable power supply for aircraft operations [[72],[24]].

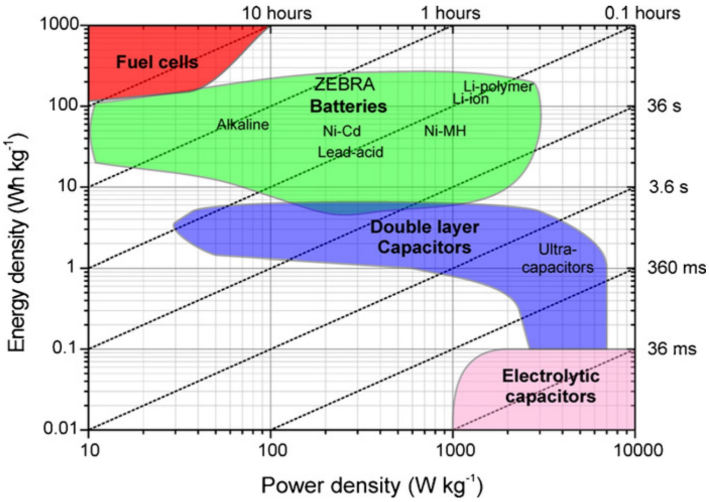

Figure 2.4: A Ragone Plot showing the comparison of fuel cells and other electrical power sources, with respect to energy and power densities [12]

2.3.1. PEMFCs and SOFCs

Out of their many advantages, PEMFCs have gained popularity within the aviation industry and remain a leading candidate in aerospace applications, mainly due to their swift warm-up and starting capabilities along with their ability to function optimally at lower temperatures in comparison to other fuel cell types (typically ranging from 80 to 100°C). Furthermore, PEMFCs exhibit a shorter response time, which enables their quick adaptation to power requirements during flight [78].

On the other hand, SOFCs operate at highly elevated temperatures (600 to 1000°C), which is quite challenging from an aircraft integration point of view. However, SOFCs do offer superior overall efficiencies and the potential to work with a broader range of fuels, especially kerosene-based jet fuel. The higher temperature ceramic-based SOFC tolerates fuel impurities and allows the utilization of carbon monoxide as a fuel (which can be converted to hydrogen through a water-gas shift reaction). In stark contrast to PEMFCs, liquid hydrocarbon fuels are much easier to use in an SOFC due to the relaxed constraints on the fuel anode inlet gas [25]. This makes them an interesting candidate for FC-GT hybrid powertrains, with the high exothermic nature of the fuel cell reaction kinetics offering a possibility of heat recuperation to boost thermal efficiencies. Additionally, solid-state design imparts durability and vibration resistance: qualities that can prove to be advantageous in varying operating conditions [78].

Regarding power range, PEMFCs are better suited for small aircraft, drones, UAVs, and Auxiliary Power Units (APUs) due to their power output being in the range of a few hundred kilowatts. Conversely, SOFCs possess the capacity to deliver power on the scale of megawatts, and are thus suited towards application for larger aircraft and longer ranges [78].

2.3.2. FC-based Hybrid Powertrains

This section builds upon the generic hybrid-electric configurations (based on the SPPH powertrain configuration discussed in Section 2.2), with the key distinction being the introduction of hydrogen-based fuel cells into the architecture. This could be done in two ways: one, by fully replacing the conventional gas turbine with a fuel-cell-based propulsion system (FCPS) in full-electric/dual-electric configurations, or by introducing the FCPS along with battery-electric and conventional gas turbine-based propulsion systems (kerosene-based fuel or hydrogen fuel combustion), with its integration into either the primary or secondary powertrains. With the integration of fuel cells into the SPPH architecture, the total number of possible powertrain configurations now becomes 28 (with 10 practically possible operating modes), in contrast to the 9 possible configurations explored by De Vries [19] shown in Figure 2.3. The study involving all possible 28 FC-based hybrid powertrain architectures was studied by Alessandro Borgia [9] in his Thesis, and these configurations can be found in the Appendix A of this Report.

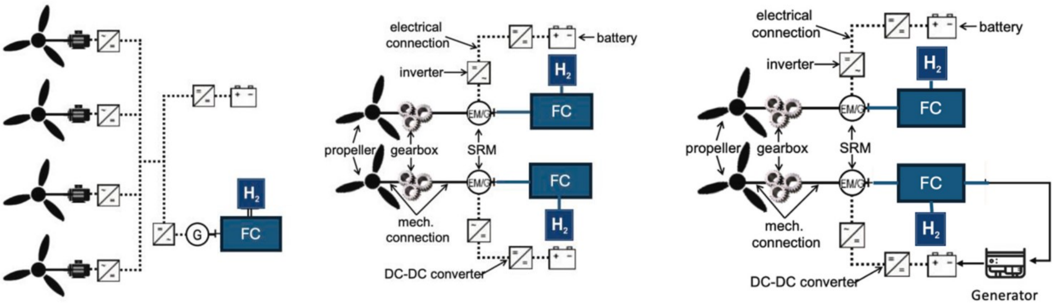

Figure 2.5: Dual Electric FC-based Hybrid Powertrains in series, parallel, and series-parallel configurations [38]

Soleymani et.al [78] reviewed fully electric and dual-electric FC-based hybrid powertrain architectures and broadly classified them into passive and active, depending on the use of a power converter to connect the fuel cells and batteries to the load. The passive configuration does not use any converter to connect the two power sources to the load, and can have three different versions, depending on the use of switching diodes for individual power paths (from the energy sources) and a battery charger between the two (second configuration). These three variations of the passive type are summarized in Figure 2.6.

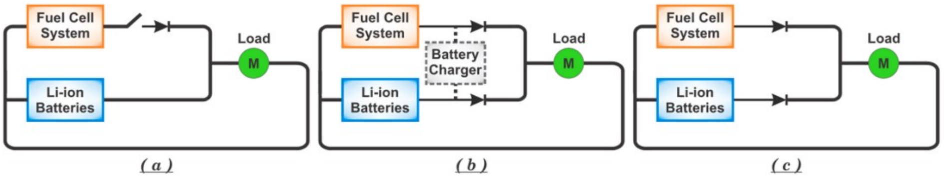

Figure 2.6: Passive FC-based hybrid electric configurations [93], [32]

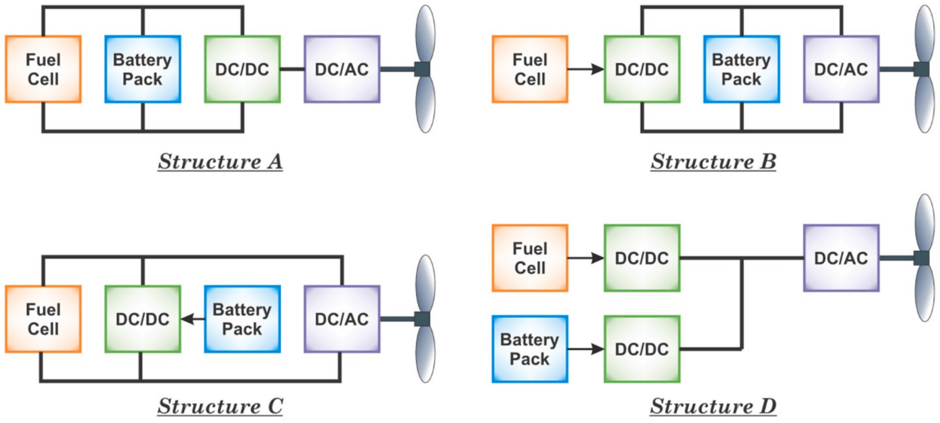

Figure 2.7: Active FC-based hybrid electric configurations [93], [51]

Conversely, active dual-electric hybrid powertrain configurations have a power converter (DC-DC/DC-

AC) in the power paths, and variations of these can be seen in Figure 2.8. In Structure A, the battery directly connects to the FC, acting as an energy buffer and handling transients, but requires a robust DC-DC converter design to manage power sharing. Structure B connects the FC to the battery via a DC-DC converter, providing quick load responses but facing challenges with uncontrolled battery charging/discharging and battery aging. Structure C positions the DC-DC converter at the battery's end, ensuring controlled charging/discharging and reducing FC current ripple, but compromises system dynamics and increases costs under high-voltage conditions. Structure D integrates both the FC and battery through DC-DC converters, enabling precise power sharing and optimal battery operation, though at the expense of slightly degraded dynamic performance.

2.4. Solid Oxide Fuel Cell- Gas Turbine (SOFC-GT) Architectures

2.4.1. Operation of High-Temperature Solid Oxide Fuel Cells (HT-SOFCs)

The solid oxide fuel cell (SOFC) is a fully solid-state electrochemical device that utilizes an oxide-ion-conducting ceramic electrolyte. Unlike low-temperature fuel cells, the SOFC operates at elevated temperatures (typically 800–$1100\ ^\circ$C), which eliminates the need for precious metal catalysts and enables direct use of hydrocarbon-derived fuels via internal reforming. The electrolyte is commonly yttria-stabilized zirconia (YSZ), which exhibits sufficient oxide-ion conductivity above approximately $700\ ^\circ$C.

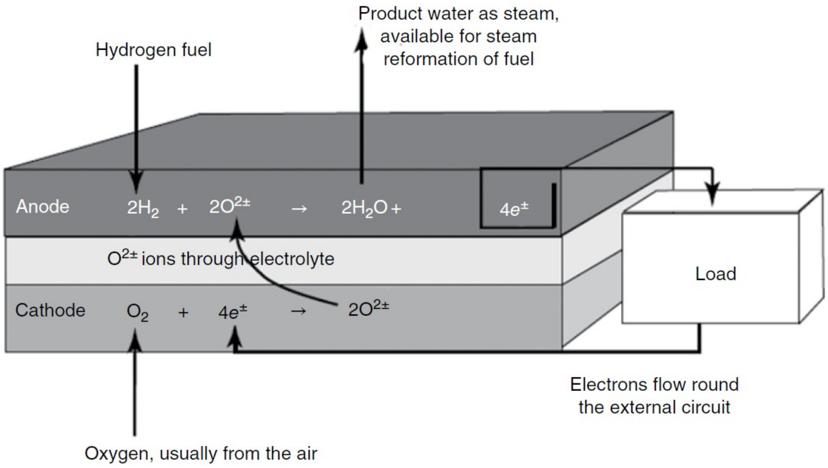

Figure 2.8: Anode and Cathode Reactions for the SOFC, when utilizing pure H_2 fuel [20]

In an SOFC, negatively charged oxygen ions are transported from the cathode through the electrolyte to the anode, where the fuel undergoes electrochemical oxidation. The half-cell reactions and overall cell reaction are expressed as follows:

$$\text{Cathode:} \quad \mathrm{O_2 + 4\,e^- \longrightarrow 2\,O^{2-}} \tag{2.7}$$

$$\text{Anode:} \quad \mathrm{2\,H_2 + 2\,O^{2-} \longrightarrow 2\,H_2O + 4\,e^-} \tag{2.8}$$

$$\text{Overall:} \quad \mathrm{2\,H_2 + O_2 \longrightarrow 2\,H_2O} \tag{2.9}$$

The anode typically consists of a nickel/YSZ cermet, which provides both electronic conductivity (Ni increases electrical conductivity and is chemically stable under reducing conditions) and catalytic activity for reforming reactions. The cathode is generally fabricated from mixed ionic-electronic conducting ceramics, such as strontium-doped lanthanum manganite (LSM, $La_{1-x}Sr_xMnO_3$). Water is produced at the anode side, leaving product steam available for potential reforming of hydrocarbon fuels.

A key advantage of the SOFC is its high electrical efficiency ($> 50\%$ LHV), which can be further increased in combined-cycle or hybrid gas turbine configurations. Although the open-circuit voltage (OCV) at $1000\ ^\circ$C is reduced compared to molten carbonate fuel cells due to thermodynamic limitations, the lower internal resistance and the ability to employ thinner electrolytes enable operation at high current densities. The tubular SOFC design, pioneered by Westinghouse, further enhances thermal stress tolerance at such elevated operating conditions.

2.4.2. SOFC-GT Architectures

As discussed in Section 2.3.1, the solid oxide electrolyte material in SOFCs enables them to operate within a wide range of high temperatures, typically between 600 and 1000 ° C, which results in high energy conversion efficiencies without the need for expensive catalysts in PEMFCs. As SOFCs can utilize a variety of hydrocarbon-based fuels such as methane, propane, biofuels, and gasoline in addition to hydrogen, they make a versatile candidate for SOFC-GT hybrid electric powertrains.

The high operating temperature of SOFCs enables their integration with turbine-less jet engines [8][1] [91]. In such systems, the SOFC discharge can be used to preheat compressed air and premixed hydrocarbon fuels. Additionally, the discharge can be combusted within the jet engine, significantly improving fuel efficiency [91]. This hybrid SOFC-jet engine propulsion system can achieve a specific energy density of up to 800 Wh/kg [91]. Moreover, SOFC systems eliminate the need for a water management system, unlike low-temperature fuel cells such as PEMFCs, because the water produced in the form of steam exits the system. However, the energy density of SOFCs is inferior to that of PEMFCs (resulting in increased propulsion system weight), and the long warm-up and start-up times can be a disadvantage [78] [63].

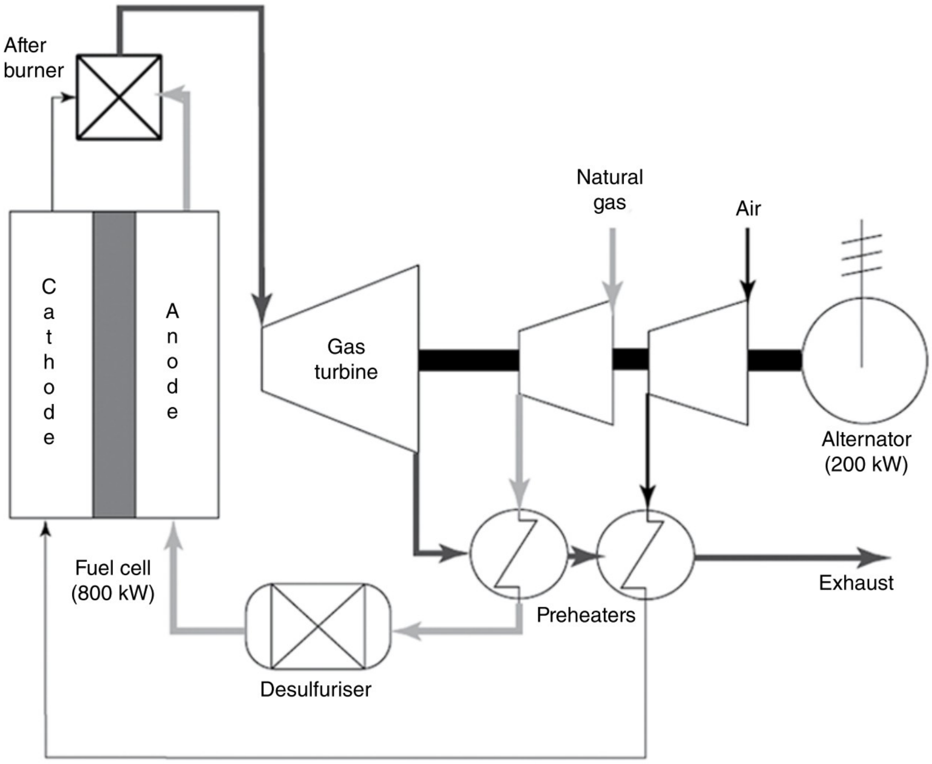

Figure 2.9: SOFC-GT Combined Cycle Architecture for Industrial Applications [20].

It is for these reasons that combining SOFCs with conventional gas turbine engines to increase overall efficiency is quite interesting and a subject of active scientific research. The SOFC provides highly efficient electrochemical conversion, while the hot exhaust gases from the stack can be expanded through a turbine to generate additional power, thereby improving system efficiency and fuel utilization. The general schematic diagram of such an SOFC–GT configuration is shown in Figures 2.9 and 2.10. While Figure 2.9 shows a combined-cycle architecture for industrial power generation applications, Figure 2.10 represents a parallel SOFC-GT hybrid-electric architecture for aerospace applications. Both architectures are based on hydrocarbon fuels, which require reformers to produce hydrogen through a water-gas shift reaction.

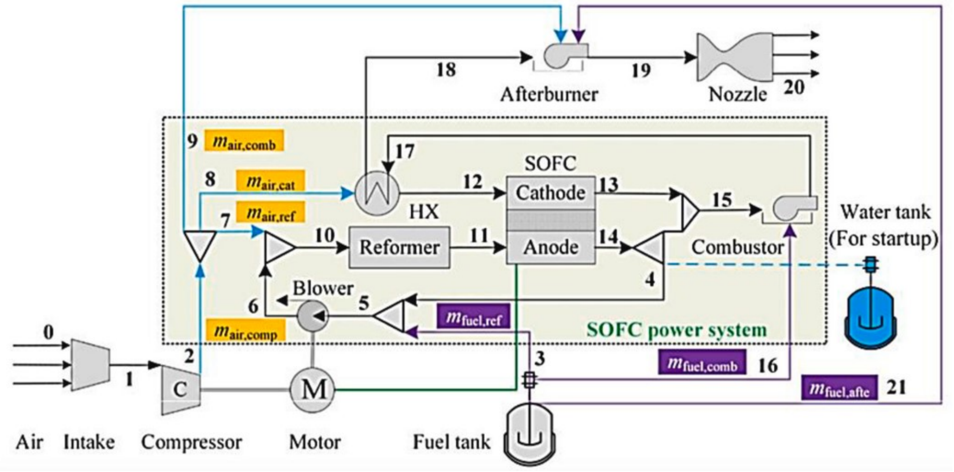

Figure 2.10: Schematic Diagram of an SOFC-GT hybrid electric propulsion system [49].

Ji et al. [49] evaluated the performance of a SOFC hybrid jet engine across four operating modes to achieve 50%–100% thrust variation. Mode 1 adjusts fuel flow in the reformer with constant SOFC air flow, while Mode 2 regulates fuel flow in the afterburner with no fresh air intake. Mode 3 modifies both fuel and air flow in the SOFC, and Mode 4 adjusts fuel flow in the afterburner with constant air flow. Mode 4, found to be the most effective, allows a wide performance range by increasing afterburner temperature from 832 K to 2261 K. Figure 2.11 shows such an SOFC-GT hybrid configuration applied to a jet engine, and used for this study.

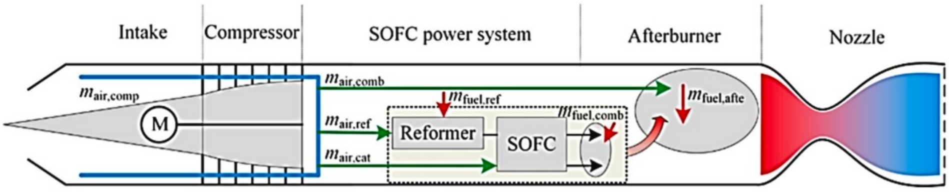

Figure 2.11: Schematic diagram for the SOFC power system in a hybrid jet engine [49].

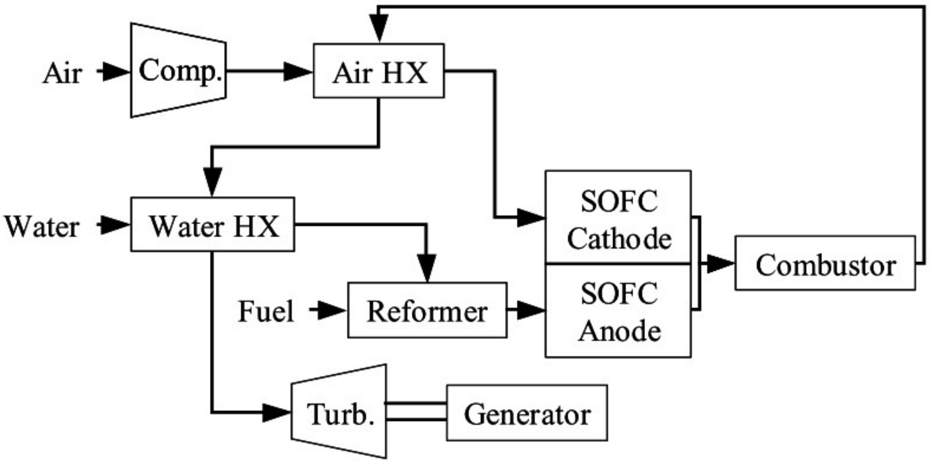

Figure 2.12: Hydrocarbon fuel-based SOFC-GT Hybrid Configuration suggested by Freeh et. al [25]

Freeh et al. developed steady-state models for solid oxide fuel cells (SOFC) and reformers within the Numerical Propulsion Systems Simulations (NPSS) modeling platform. The SOFC model was validated against experimental data across variations in pressure, temperature, and anode inlet composition, demonstrating its accuracy in predicting SOFC performance based on design specifications and operating conditions. Additionally, a 200 kW hybrid SOFC/gas turbine system was simulated using this model, the layout of which is shown in Figure 2.12.

Alsamri et. al proposed a H_2 – basedSOFC-GT architecture as shown in Figure 2.14 for use in medium-long range aircraft. The performance of a Cessna S550 Citation S/I retrofitted with this SOFC-GT architecture was studied using static and dynamic powertrain modeling. In this model, an oxidizer is used to raise the exit temperature for use in a recuperator that raises the temperature of the compressed air, before expanding through a turbine to generate electric power through a generator [2].

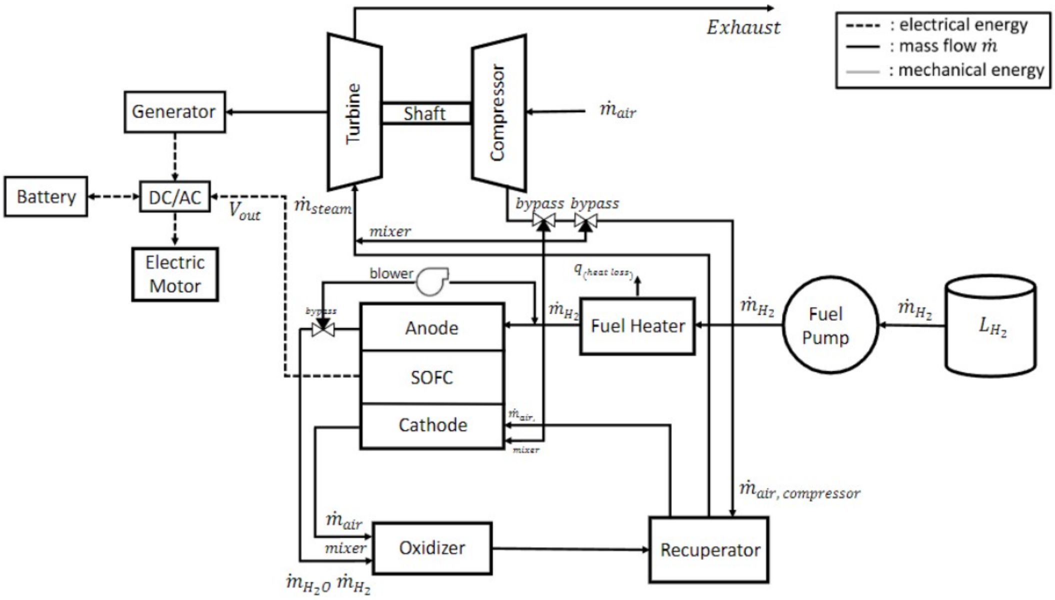

Figure 2.13: SOFC-based Fuel Cell System (FCS) suggested by Alsamri et.al. for use in medium-long range Aircraft [2].

2.4.3. SOFC Modeling at Cell and Stack Level, including Balance of Plant

Electrochemical Model - Cell Level

Nernst Equation is used to calculate the reversible voltage of the SOFC system as given below [20]:

$$V_{\mathrm{rev}} = -\frac{\Delta_f G^\circ}{nF} + \frac{RT}{nF}\ln\frac{pp\mathrm{H}_2 \cdot (pp\mathrm{O}_2)^{1/2}}{pp\mathrm{H}_2\mathrm{O}} \tag{2.10}$$

where, ΔG° is the Gibbs free energy under standard conditions, n is the number of electrons transferred during the electrochemical reaction, F is Faraday's constant (96485 C/mol e^-), R is the universal gas constant, T is the cell operating temperature, and pp represents the partial pressure of the reacting gases.

Irreversible voltage losses in fuel cells arise from various chemical, physical, and electrochemical processes. In the current approach, these losses are categorized into three primary types of polarization: (1) activation, (2) ohmic, and (3) concentration. These losses are determined by Equations 2.11 to 2.13 as outlined in [52]:

$$V_{\mathrm{Activation}} = \frac{RT}{n\alpha F}\ln\left[\frac{i+i_n}{i_o}\right] \tag{2.11}$$

$$V_{\text{Ohmic}} = r \cdot (i + i_n) \tag{2.12}$$

$$V_{\text{Concentration}} = \frac{RT}{nF} \ln \left[\frac{i - i_n}{i_L} \right] \tag{2.13}$$

In equations 2.11 to 2.13, i represents the stack current, i_{n} denotes the internal current density, i_o is the exchange current density, and i_L is the limiting current density. Detailed definitions and explanations of these current density terms can be found in [52].

The current density of a solid oxide fuel cell (SOFC) stack is defined as in [91]:

$$i = 4F \cdot \dot{n}_{\text{O}_2} \tag{2.14}$$

where $\dot{n}_{\text{O}_2}$ represents the molar consumption rate of oxygen at the SOFC cathode.

The bulk internal resistance, r, can either be treated as a constant or modeled as temperature-dependent for each stack component (anode, cathode, electrolyte, and interconnect), following a relationship described in [27]:

$$r = \sum r_{\text{Component}} = \sum A e^{E/T} \tag{2.15}$$

Finally, the operating cell voltage is given by:

$$V_{\text{Oper}} = V_{\text{rev}} - V_{\text{Activation}} - V_{\text{Concentration}} - V_{\text{Ohmic}} \tag{2.16}$$

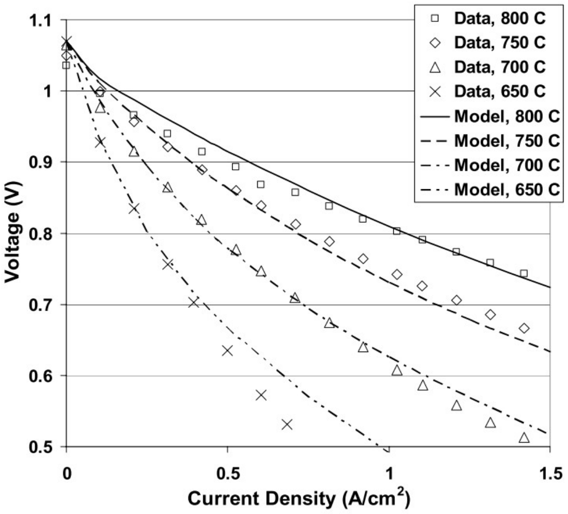

Figure 2.14: Variation of operating cell voltage with current density, NPSS numerical model compared to experimental data for a parametric sweep of SOFC operating temperatures [25]

Mass Balance

Faraday's Law can be modified to calculate the specific hydrogen and air flow rates ($\dot{m}_{\text{H}_2}$ and $\dot{m}_{air}$) in $gs^{-1}cm^{-2}$, as a function of the cell's current density i by taking into account the molecular massed of hydrogen and air as well as the excesses of both hydrogen and oxygen in the electrodes (denoted by λ_{H_2} and λ_{air} respectively); while y_{O_2} represents the concentration of oxygen in air in Equation 2.18.

$$\dot{m}_{\text{H}_2}(i) = \lambda_{\text{H}_2} \frac{i}{2F} \text{M}_{\text{H}_2} \tag{2.17}$$

$$\dot{m}_{air}(i) = \frac{\lambda_{air}}{y_{\mathrm{O_2}}} \frac{i}{4F} \mathrm{M}_{air} \tag{2.18}$$

At the stack level, the mass flow rates can be written as follows:

$$\dot{m}_{\mathrm{H_2,stack}} = \frac{\dot{m}_{\mathrm{H_2}} \cdot A_{\mathrm{cell}} \cdot N_{\mathrm{cells}}}{U_{\mathrm{fuel}}} \tag{2.19}$$

$$\dot{m}_{\mathrm{air,stack}} = \dot{m}_{\mathrm{air}} \cdot A_{\mathrm{cell}} \cdot N_{\mathrm{cells}} \tag{2.20}$$

Powers and Efficiencies (at Cell and Stack Levels)

The power output at the cell level is given by the product of the operating voltage, V_{Oper} from Equation 2.16 and the cell operating current density i from Equation 2.14:

$$P_{\mathrm{cell}} = V_{\mathrm{Oper}} \cdot i \tag{2.21}$$

At the stack level, the cell power is multiplied by the number of cells in the stack, N_{cell}, and the total active stack area to get the output stack power. Note that Equation 2.22 gives the SOFC stack power output in kW.

$$P_{\mathrm{Stack}} = \frac{P_{\mathrm{cell}} \cdot N_{\mathrm{cell}} \cdot A_{\mathrm{cell}}}{1000} \tag{2.22}$$

The heat generated by the operation of an SOFC stack can be calculated by Equation 2.23, where $\Delta\dot{H}$ represents the difference in the enthalpies of the inlet and outlet flows:

$$\dot{Q}_{\mathrm{Gen,stack}} = \Delta\dot{H} - P_{\mathrm{Stack}} \tag{2.23}$$

At the cell and stack levels, two efficiencies can be calculated, namely the overall stack efficiency (defined in Equation 2.25) and the cell electrochemical efficiency (defined in Equation 2.26), where U is the overall stack fuel utilization (defined in Equation 2.24, assuming methane as a fuel in the FCS, and the associated internal reforming reactions) [25]:

$$U = \frac{\Delta_{(\mathrm{IN-OUT})}\left(\dot{n}_{\mathrm{H_2}} + \dot{n}_{\mathrm{CO}} + 4\dot{n}_{\mathrm{CH_4}}\right)}{\left(\dot{n}_{\mathrm{H_2}} + \dot{n}_{\mathrm{CO}} + 4\dot{n}_{\mathrm{CH_4}}\right)_{\mathrm{IN}}} \tag{2.24}$$

$$\eta_{\mathrm{Overall}} = U \cdot \frac{P_{\mathrm{Stack}}}{\Delta\dot{H}} \tag{2.25}$$

$$\eta_{\mathrm{electrochemical,stack}} = U_{fuel} \cdot \frac{V_{\mathrm{Oper}}}{V_{\mathrm{rev}}} \tag{2.26}$$

The internal reforming reactions associated with using methane as fuel for the SOFC-based FCS are shown below. This is similar to the internal reforming reactions for other long-chain hydrocarbon fuels as well (including jet and diesel fuels), with methane being chosen here as an example for simplicity. It is also worth noting here that the consideration of the water gas-shift reaction allows us to safely ignore the electrochemical oxidation of CO in the determination of electrical power/heat outputs, as the fraction of CO being directly electrochemically oxidized by the fuel cell is reasonably small when compared to the amount consumed by the water gas-shift reaction as long as the primary fuel is not CO [25] [90].

The methane-steam reforming reaction:

$$\mathrm{CH_4} + \mathrm{H_2O} \longrightarrow \mathrm{CO} + 3\,\mathrm{H_2} \tag{2.27}$$

The water-gas shift reaction:

$$CO + H_2O \longrightarrow CO_2 + H_2 \tag{2.28}$$

Balance of Plant (BoP)

The term Balance of Plant (BoP) refers to all the required equipment to control and condition fuel and air inputs, along with the temperature, water content, and electrical output of a fuel cell system (FCS). Balance of Plant design depends on aircraft operating conditions, weights, and space limitations [78]. Since components supporting the functioning of a fuel cell within the FCS are directly powered by it, it is necessary to appropriately size these in order to determine the gross power output from the stack, and the stack size [60].

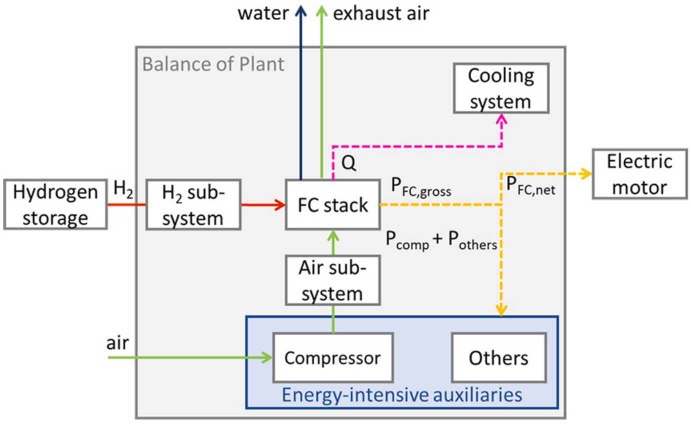

Figure 2.15: General layout of the propulsion system of a hydrogen fuel-cell powered aircraft, showing hydrogen storage systems, fuel cell system (FCS), and electric motor [61]

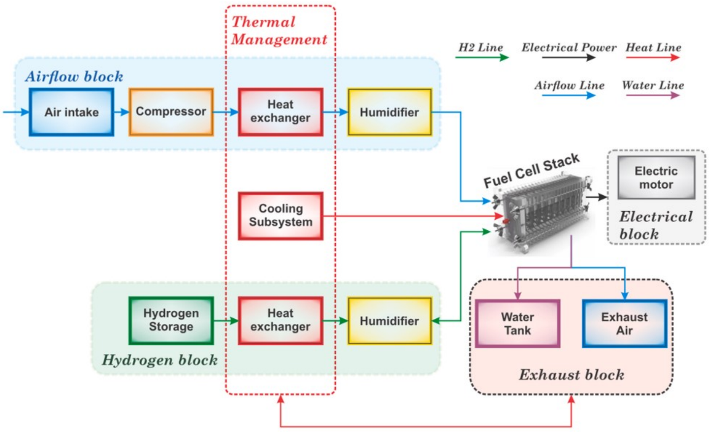

Figure 2.16: General Fuel Cell System architecture [61]

The power consumption of the air compressor used in the FCS, which is a function of the cell current density i and the altitude h; and assuming adiabatic conditions and fixed efficiencies, is given by Equation 2.29. The flow rate of the air at stack level $\dot{m}_{\text{air,stack}}$ here is derived in a similar manner to that at the cell level, given by Equation 2.18-

$$P_{\text{compr}}(i,h) = \dot{m}_{\text{air,stack}}(i) c_{p,\text{air}} T_{\text{in,air}} \left(\beta_{\text{compr}}^{\frac{\gamma_{\text{air}}-1}{\gamma_{\text{air}}}} - 1 \right) \frac{1}{\eta_{\text{is}} \eta_{\text{em}}} \tag{2.29}$$

The parameters for intake conditions needed to calculated required compressor power (Equation 2.29), such as the inlet temperature, $T_{\text{in,air}}$ and pressure, $P_{\text{in,air}}$ are both dependent on altitude, and are mentioned in Equations 2.30 and 2.31. It should be noted that while the compressor specific work increases significantly due to the pressure drop with altitude, the decreasing temperatures have the opposite effect. As the first factor is more critical than the latter, this leads to an overall increase in the required compressor specific power with altitude. Therefore, the maximum power needed for compressor operation can be defined as a critical design criterion, based on the maximum operating cruise altitude of the aircraft [60].

$$T_{\text{in,air}} = 288.19 - 0.00649h \tag{2.30}$$

$$p_{\text{in,air}} = 1.0129 \left(\frac{T_{\text{in,air}}}{288.08} \right)^{5.256} \tag{2.31}$$

Other parameters used in Equation 2.29 such as the adiabatic exponent, γ_{air} and the specific hear capacity of air, $c_{\text{p,air}}$ in $kJkg^{-1}K^{-1}$ are calculated as a function of compressor inlet temperature, $T_{\text{in,air}}$ by curve-fitting of thermophysical data; while the compression ratio, $\beta_{\text{compressor}}$, can be calculated as the ratio between the air pressure at the compressor inlet and the cathode pressure as given in Equation 2.32:

$$\beta_{\text{compressor}} = \frac{p_{\text{cathode}}}{p_{\text{in,air}}} \tag{2.32}$$

The power consumption from smaller, auxiliary units such as pumps, valves, control units, etc., that are in constant operation can be modeled as a fixed percentage of the maximum stack power point (stack design point, from Equation 2.22). This can be reasonably assumed to be around 1% of the maximum stack power [61], which is y_{others} in Equation 2.33.

$$P_{\text{others}} = y_{\text{others}} \cdot P_{\text{stack,max}} \tag{2.33}$$

The cooling system can be modeled and sized depending on the thermal power generated by the stack, $\dot{Q}_{\text{Gen,stack}}$, which is a function of the cell exchange current i, and given by Equation 2.23. Alternatively, the heat generated at the stack level can also be defined from the heat of a single cell (in kW), as follows:

$$\dot{Q_{\text{stack}}}(i) = \frac{\dot{q}_{\text{th,cell}}((i) \cdot N_{\text{cell}} \cdot A_{\text{cell}}}{1000} \tag{2.34}$$

where $p_{\text{thermal,fc}}$ is the specific heat released per cell during FC operation (in Wm^{-2}), and can be defined as in Equation 4.22. The value of the cell operating voltage, V_{Oper}, is obtained from Equation 2.16 and the value of the molar enthalpy of reaction, $\Delta\hat{h}_{\text{react}}$, can be assumed constant with fuel cell operating temperature at -286,000 $Jmol^{-1}$ [60].

$$\dot{q}_{\text{th,cell}}(i) = i \left(-\frac{\Delta\hat{h}_{\text{react}}}{2F} - V_{\text{Oper}}(i) \right) \tag{2.35}$$

The heat generated at the stack level (given by Equations 2.23 and 2.34) is an important parameter for determining the size of the cooling system in the subsequent step of aircraft-scale dimensioning of the FCS.

Net Power and System Efficiency

The net electrical power at stack level $P_{\text{stack,net}}$, which is a function of the altitude h and the cell operating current density i, is crucial for the sizing of the FCS at aircraft level, and is given by Equation 2.37

$$P_{\text{stack,net}}(i,h) = P_{\text{stack}}(i) - P_{\text{comp}}(i,h) - P_{\text{others}} \tag{2.36}$$

$$P_{\text{stack,net}}(i) = P_{\text{stack}}(i) - P_{\text{others}} \tag{2.37}$$

From the net stack power defined in Equation 2.37, the specific hydrogen flow rate at stack level $\dot{m}_{H_2,stack}$, and the Lower Heating Value (LHV) of liquid hydrogen, the net efficiency curve of the fuel cell system at stack level can be defined as a function of cell operating current density i and altitude h by:

$$\eta_{\text{stack,net}}(i,h) = \frac{P_{\text{stack,net}}(i,h)}{\dot{m}_{\text{H}_2,\,\text{stack}}(i)\text{LHV}_{\text{H}_2} \cdot 10^3} \tag{2.38}$$

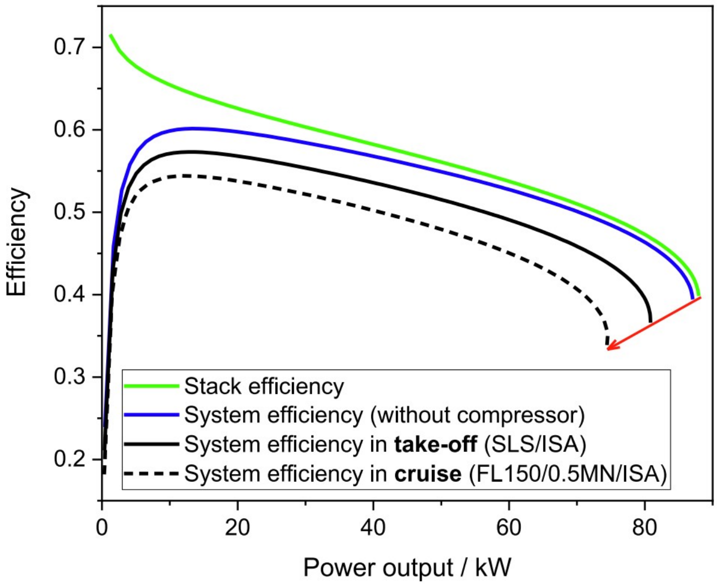

Figure 2.17: FCS Efficiencies as a function of Power Outputs [61]

Figure 2.17 illustrates the efficiency of the fuel cell group for the conversion of the ATR 72-600 aircraft, calculated based on the hydrogen's lower heating value:

- **Stack Efficiency (green curve)**: Represents the efficiency relative to hydrogen's theoretical chemical potential, decreasing with increasing current.
- **System Efficiency (blue curve)**: Includes the fixed contribution of general auxiliaries (excluding the air compressor), peaking at a certain point.
- **Overall Efficiency (black curve)**: Incorporates the air compressor, resulting in a further reduction in efficiency.

While the gross and net power align at the stack level, net power decreases at the system level due to the balance of plant's power demands. The air compressor's power requirement, influenced by altitude-dependent inlet air pressure and temperature, creates parametric efficiency curves varying with altitude.

FCS Sizing Criteria

The number of fuel cell stacks needed for the FCS system can be determined based on the total propulsive power needed for the mission (P_{tot}, defined in the next Section), the net power generated by individual stacks ($P_{\text{stack,net}}$)), and the electro-mechanical efficiency of the electric motor. The number of stacks needed for the FCS system is also a function of operating cell current density and altitude, and is given by:

$$n_{\text{stack}}(i,h) = \frac{P_{\text{tot}}(h)}{\eta_{\text{em}} P_{\text{stack,net}}(i,h)} \tag{2.39}$$

The amount of hydrogen needed for the mission (for a fully FCS-based propulsion system) can be calculated (in kg) as shown below in Equation 2.40, where the Lower Heating Value (LHV) of hydrogen is in MJ/kg:

$$M_{\text{H}_2} = \frac{1}{10^3 \text{LHV}_{\text{H}_2}} \int_0^{t_{\text{end}}} \frac{P_{\text{mission}}(t)}{\eta_{\text{EM}} \eta_{\text{net}}(i,h)} \, dt \tag{2.40}$$

2.4.4. SOFC-GT Powertrain Modeling

Based on the work of De Vries [19] on hybrid-electric powertrain architectures and the research gap of extending the generic SPPH model for hybrid-electric architectures to hydrogen fuel-cell-based architectures and hydrogen combustion, Alessandro Borgia [9] studied a novel powertrain model for conceptual design and sizing of hydrogen-based hybrid-electric architectures. This extended the generic SPPH architecture to 28 different configurations with 10 possible operating modes, which is shown in Appendix A of this report and described in detail in [9]. Similar to the De Vries model, the system is assumed to be in steady state, and fixed values of power conversion/transmission efficiencies are assumed for each component. Moreover, the model assumes a fixed efficiency for the fuel cell system (including the balance of plant components) with varying flight conditions, similar to the efficiencies of other components in the powertrain model. This model, called the ***double-hybrid powertrain model***, is based on the following elements:

- **Energy sources**: Kerosene, Hydrogen, and Batteries
- **1st propulsive line**: Gas turbine, Fuel cell, Electric motor, Gearbox, and Propeller(s)/Fan(s)
- **2nd propulsive line**: Electric motor, Gearbox, and Propeller(s)/Fan(s)
- **Power management and distribution**
- **Hydrogen supply chain and Power divider**

Double-Hybrid Powertrain - Control Parameters

The different configurations of the Double-Hybrid Powertrain (refer to Appendix A) necessitate the need to define power control parameters just like the generic SPPH powertrain to define energy sources and the power splits between them quantitatively [9].

The first two parameters, ϕ_1 and ϕ_2 denote the contributions of batteries and hydrogen to the total power utilized. This extends the power ratio concept introduced by Isikveren [48], which originally focused on batteries and kerosene, to include a combination of kerosene, hydrogen, and batteries as power sources.

$$\phi_1 = \frac{P_{bat}}{P_{\text{bat}} + P_{\text{H}_2} + P_{\text{k}}} \tag{2.41}$$

$$\phi_2 = \frac{P_{\text{H}_2}}{P_{\text{bat}} + P_{\text{H}_2} + P_{\text{k}}} \tag{2.42}$$

The sum of these two parameters is limited to a maximum value of 1, representing the energy source ratio. A value of 1 indicates that no kerosene is being used, and the engines are not harvesting additional power:

$$\Phi_1 + \Phi_2 \leq 1 \tag{2.43}$$

The hydrogen supply ratio, $\mathrm{H}_{2,\mathrm{split}}$, is defined as the ratio of the quantity of hydrogen supplied to the fuel-cell, in comparison to the total quantity of hydrogen used for the mission:

$$\mathrm{H}_{2,\mathrm{split}} = \frac{P_{\mathrm{H}_2,fc}}{P_{\mathrm{H}_2,fc} + P_{\mathrm{H}_2,gt}} \tag{2.44}$$

In addition to these parameters, the shaft power ratio, ψ, defined in Equation 2.2 and originally proposed by De Vries [19], can be used to define the power partition between the two powertrains in the double-hybrid architecture.

It is to be noted that when the power flow operates in a manner opposite to the conventional parameters of Operating Mode 1 (refer to Appendix A for the various operating modes), it is considered negative. As for the power control parameters, only $\mathrm{H}_{2,\mathrm{split}}$ stays within the range of [0,1] independent of the operating mode, while ϕ_1, ϕ_2, and ψ only stay within this range for nominal operating modes (OM1 and OM4) [9].

Powertrain Equations

This section details the powertrain of the double-hybrid model, emphasizing the identification of the system's 14 unknown variables, each representing a power flow in the SPPH configuration. To resolve the system, 14 equations are derived.

The first nine equations describe the power flow into and out of individual components, including those related to the PMAD and GB nodes, with η representing the component efficiencies. Equations 10 through 13 incorporate the double-hybrid system control parameters that were introduced in the previous section. While the first nine equations represent the power flows through each component, the last five equations represent the power control parameters and the total propulsive power P_{tot} needed to solve the system of equations.

$$\begin{bmatrix}
1 & 0 & 0 & 0 & 0 & -\eta_{\mathrm{gt,h2}} & 0 & 0 & -\eta_{\mathrm{gt,k}} & 0 & 0 & 0 & 0 & 0 \\
0 & 1 & 0 & 0 & 0 & 0 & 0 & 0 & 0 & 0 & 0 & 0 & -\eta_{\mathrm{p1}} & 0 \\
0 & 0 & 1 & 0 & 0 & 0 & 0 & 0 & 0 & 0 & 0 & 0 & 0 & -\eta_{\mathrm{p2}} \\
0 & 0 & 0 & 1 & 0 & 0 & 0 & 0 & 0 & -\eta_{\mathrm{em1}} & 0 & 0 & 0 & 0 \\
0 & 0 & 0 & 0 & -\eta_{\mathrm{H2,sc}} & 1 & 1 & 0 & 0 & 0 & 0 & 0 & 0 & 0 \\
0 & 0 & 0 & 0 & 0 & 0 & 0 & -\eta_{\mathrm{pmad}} & 0 & 1 & 1 & -\eta_{\mathrm{pmad}} & 0 & 0 \\
0 & 0 & 0 & 0 & 0 & 0 & -\eta_{\mathrm{fc}} & 0 & 0 & 0 & 0 & 1 & 0 & 0 \\
-\eta_{\mathrm{gb}} & 0 & 0 & -\eta_{\mathrm{gb}} & 0 & 0 & 0 & 0 & 0 & 0 & 0 & 0 & 1 & 0 \\
0 & 0 & 0 & 0 & 0 & 0 & 0 & 0 & 0 & 0 & -\eta_{\mathrm{em2}} & 0 & 0 & 1 \\
0 & 0 & 0 & 0 & 0 & 0 & 0 & 0 & 0 & 0 & 0 & 0 & -\psi & 1-\psi \\
0 & 0 & 0 & 0 & -\phi_1 & 0 & 0 & 1-\phi_1 & -\phi_1 & 0 & 0 & 0 & 0 & 0 \\
0 & 0 & 0 & 0 & 1-\phi_2 & 0 & 0 & -\phi_2 & -\phi_2 & 0 & 0 & 0 & 0 & 0 \\
0 & 0 & 0 & 0 & 0 & -\mathrm{H}_{2,\mathrm{split}} & 1-\mathrm{H}_{2,\mathrm{split}} & 0 & 0 & 0 & 0 & 0 & 0 & 0 \\
0 & 1 & 1 & 0 & 0 & 0 & 0 & 0 & 0 & 0 & 0 & 0 & 0 & 0
\end{bmatrix}
\cdot
\begin{bmatrix}
P_{\mathrm{gt}} \\ P_{\mathrm{p1}} \\ P_{\mathrm{p2}} \\ P_{\mathrm{em1}} \\ P_{\mathrm{H2}} \\ P_{\mathrm{H2,gt}} \\ P_{\mathrm{H2,fc}} \\ P_{\mathrm{bat}} \\ P_{\mathrm{k}} \\ P_{\mathrm{el1}} \\ P_{\mathrm{el2}} \\ P_{\mathrm{fc}} \\ P_{\mathrm{s1}} \\ P_{\mathrm{s2}}
\end{bmatrix}
=
\begin{bmatrix}
0 \\ 0 \\ 0 \\ 0 \\ 0 \\ 0 \\ 0 \\ 0 \\ 0 \\ 0 \\ 0 \\ 0 \\ 0 \\ P_{\mathrm{tot}}
\end{bmatrix} \tag{2.45}$$

System of equations for the extended powertrain system using H_2, as shown in Appendix A [9]

It is to be noted that the set of equations in 2.45 only represents the generic operating mode (OM1) of the double-hybrid powertrain model in nominal conditions. For operating conditions different from nominal, the first nine equations need to be modified to account for negative power flow into nodes, which would result in the subsequent modification of the coefficient matrix **A** in 2.45. Changes to the system of equations depending on the operating mode of the double-hybrid powertrain are discussed in detail by Alessandro Borgia [9].

3

Research Questions

As discussed in the previous chapter, hybrid powertrain architectures show considerable promise, and extensive research has been conducted to explore the feasibility of conceptual FC-GT powertrains. However, these studies have produced varying conclusions regarding the feasibility and practicality of fuel-cell propulsion systems, highlighting the need for further investigation. This need is further emphasized by the fact that existing analyses often have a limited scope, considering only a restricted set of mission parameters and showing insufficient sensitivity to various technical factors. Moreover, many studies rely on multiple design tools to derive performance metrics. Ideally, a single design framework should be used for aircraft sizing to reduce biases associated with using different tools. Consequently, the **primary research objective** of this work is:

'To evaluate and study the performance and viability of SOFC-GT powertrains for integration into regional turboprop aircraft, and their comparison to LH2 and kerosene/SAF-based architectures for similar TLARs'

To guide the research and achieve the required research objective, the following additional research questions are identified:

RQ-1: ***How can the SOFC-GT architecture be modeled into the existing methodology of sizing for FC-GT hybrid-electric powertrains?***

- **RQ- 1.1**: What are the relevant modeling parameters at the cell, stack, and aircraft level, which could be incorporated into existing preliminary sizing methodologies for hydrogen-based FC-GT powertrains?
- **RQ- 1.2**: How could this sizing methodology be adapted to SOFC-GT powertrains, which recuperate the heat produced by high-temperature SOFCs to improve the thermal efficiency of the Gas Turbine Engine?
- **RQ- 1.3**: Keeping in mind the Balance of Plant (BoP) and the Thermal Management System required for SOFC-GT propulsion systems, what powertrain architecture could be chosen for this study?

RQ-2:***How do the Class 1 sizing results of an aircraft with an SOFC-GT hybrid-electric propulsion system compare to those with liquid hydrogen/kerosene-based propulsion systems for similar TLARs?***

- **RQ- 2.1**: How do the maximum takeoff mass (MTOM), operating empty mass (OEM), and energy requirements of an SOFC-GT aircraft compare to those of an aircraft with liquid hydrogen/kerosene-based propulsion systems for similar TLARs?

- **RQ- 2.2**: How does the overall thermal efficiency of the SOFC-GT propulsion system compare to that of full liquid hydrogen/kerosene-based propulsion systems?
- **RQ- 2.3**: How do the emissions of aircraft with SOFC-GT powertrains compare to those of conventional LH_2/kerosene-based aircraft that are sized for similar TLARs?

RQ-3:***What design parameters are the SOFC-GT aircraft most sensitive to?***

- **RQ- 3.1**: What effect would the hydrogen split between the Gas Turbine and SOFC stacks have on the overall thermal efficiency of the SOFC-GT aircraft in cruise conditions?
- **RQ- 3.2**: What effect do improvements in SOFC technological scenarios have on the overall thermal efficiencies of the SOFC-GT powertrains?
- **RQ- 3.3**: What effect do SOFC-GT powertrain design parameters such as current densities, cell operating temperatures, system pressures, cathode air stoichiometry, and stack-level fuel utilization have on preliminary sizing at the aircraft level?

4

Methodology

4.1. Overview

The primary objective of this Master Thesis Project is to develop a methodology for modeling Solid Oxide Fuel Cell–Gas Turbine (SOFC-GT) powertrains within a conceptual aircraft design framework. This methodology will then be applied to evaluate the impact of SOFC-GT propulsion systems on aircraft-level sizing at the system level.

Prior work by De Vries [19] established a methodology for conceptual sizing of hybrid-electric propulsion systems, which was later extended to hydrogen-based architectures by Alessandro Borgia [9]. Building upon this work, this research integrates an SOFC-GT propulsion architecture into the Class 1 sizing loop of the Aircraft Design Initiator [22]. The modeling begins at the fuel cell level, using electrochemical and thermodynamic models of the SOFC and the Gas Turbine, which is later scaled up to the system level where the integrated SOFC-GT powertrain is sized to meet the aircraft's power demands.

The results of the sizing loop is then validated against available data of SOFC-GT models (including experimental data for SOFC performance at various operating conditions) from literature, and compared against similar aircraft with kerosene-based/full-LH_2 propulsion systems for various performance metrics, including overall thermal efficiency, mass breakdown at aircraft level, and environmental impact.

As mentioned earlier, this work is done in the Aircraft Design Initiato,r which is an in-house conceptual aircraft design tool developed by the Faculty of Aerospace Engineering at Delft University of Technology for rapid design evaluation. The Hybrid Class 1 sizing loop of the Aircraft Design Initiator is modified in this project to incorporate the SOFC-GT powertrain and study its effects on preliminary aircraft sizing.

Finally, a parametric sweep is performed for the SOFC-GT model within the Hybrid Class 1 sizing loop, for various operating parameters such as SOFC temperature, pressure ratios, fuel utilization, and air stoichiometry to observe their sensitivity to Class 1 aircraft sizing results. In addition to SOFC operating parameters, different technological scenarios for HT-SOFCs, powertrain architecture parameters (such as the hydrogen supply ratio), and top-level aircraft requirements (such as the wing aspect ratio) are also studied for sensitivities to Class 1 aircraft sizing results. Based on these, several recommendations are proposed in Chapter 7 which are expected to provide guidelines for architecture optimization of SOFC-GT powertrains for applications in regional turboprop aircraft.

4.2. Cell-Level Electrochemistry

4.2.1. 0-D Cell Level SOFC Performance Model

In order to get started with integrating the SOFC-GT powertrain for preliminary aircraft sizing within the Hybrid Class 1 sizing loop of the Aircraft Design Initiator, it was deemed necessary to first incorporate a cell-level model of high temperature Solid Oxide Fuel Cells with sufficient fidelity in order to properly quantify the power output and mass flow rates of species at the cell and stack levels respectively. For this, a 0-D cell-level model is chosen, as it provides the right balance between a physics-based approach for estimation of actual cell voltage based on operating current densities and fuel cell properties, while also allowing for rapid evaluations of cell performance at stack and aircraft levels. The 0-D model uses lumped electrochemical modeling parameters for the High Temperature Solid Oxide Fuel Cell (HT-SOFC) and a thermodynamic approach for estimating losses during fuel cell operation, providing sufficient fidelity for integration within the Hybrid Class 1 Sizing Loop of the Aircraft Design Initiator.

The theoretical value of the 'no-loss'/ideal open-circuit voltage of a hydrogen fuel cell is expressed below:

$$V_r = \frac{-\Delta \bar{g}_f}{2F} \tag{4.1}$$

where $-\Delta g_f$ is the change in Gibb's Free Energy of formation of the reactants and the products in the cell reaction. While Equation 4.1 gives the theoretical value of cell voltage that can be achieved through the chemical reaction of H_2 and O_2 in the fuel cell, the actual cell voltage that can be harnessed through the fuel cell is lesser due to losses during operation, more about which is discussed in detail in the upcoming sections. For a high temperature Solid Oxide Fuel Cell operating at $900°$C, this theoretical value of open-circuit voltage is around 0.948 V.

A typical voltage-current density curve for a high-temperature SOFC operating at around $800°$C is shown below in Figure 4.1. It is important to note here that, unlike low-temperature PEMFCs, the open-circuit voltage in HT-SOFCs shows only a minimal difference to the 'no-loss' theoretical open circuit voltage given by Equation 4.1. The fairly 'linear' portion of the curve, where the operating voltage steadily decreases until suddenly deteriorating at a higher current density, is quite characteristic of HT-SOFCs, where, although the reversible OCV is lower than that of LT-PEMFCs, the actual operating voltages turn out to be higher due to lesser losses in general.

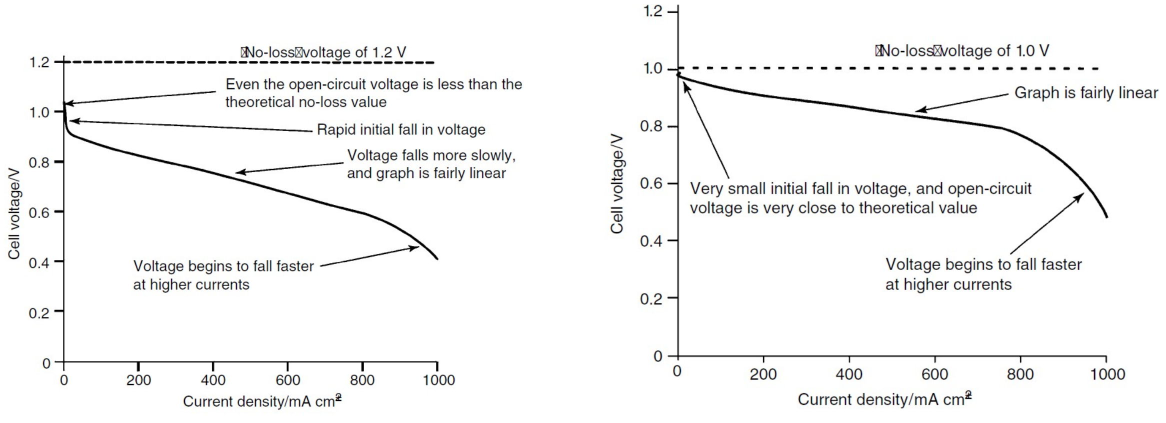

(a) Voltage versus current density curve for LT-FCs

(b) Voltage versus current density curve for HT-SOFCs

Figure 4.1: Comparison of voltage versus current density curves for (a) low-temperature fuel cells and (b) high-temperature SOFCs [20]

The Nernst Equation is used to calculate the reversible open circuit voltage (OCV) of the cell and is shown below in Equation 4.2 [20]:

$$V_{\text{rev}} = -\frac{\Delta_f G^\circ}{nF} + \frac{RT}{nF}\ln\frac{pp\text{H}_2 \cdot (pp\text{O}_2)^{1/2}}{pp\text{H}_2\text{O}} \tag{4.2}$$

where, ΔG° is the Gibbs free energy for the fuel cell reaction under standard conditions, n is the number of electrons transferred during the electrochemical reaction, F is Faraday's constant (96485 C/mol e^-), R is the universal gas constant, T is the cell operating temperature, and pp represents the partial pressure of the reacting gases.

Equation 4.2 can be modified further to represent the partial pressure of both reactants and products as a function of the system pressure. For fuel cell reactions involving pure hydrogen and oxygen, the partial pressures of H_2, O_2, and H_2O can be written as functions of the system pressure, as indicated by Larmine and Dicks [20], where $\alpha = 1$, $\beta = 0.2095$ and $\delta = 1$:

$$P_{\text{H}_2} = \alpha P; \quad P_{\text{O}_2} = \beta P; \quad P_{\text{H}_2\text{O}} = \delta P$$

This modifies the Nernst Equation into:

$$V_{\text{rev}} = -\frac{\Delta_f G^\circ}{nF} + \frac{RT}{2F}\ln\left(\frac{\alpha \cdot \sqrt{\beta_{\text{air}}}}{\delta}\right) + \frac{RT}{4F}\ln(P) \tag{4.3}$$

In addition to the fuel cell operating temperature and pressure, parameters such as the fuel utilization factor (U_{fuel}) and air stochiometric ratio (λ_{air} play a vital role in determining the open circuit voltage. Increasing fuel utilization is observed to decrease hydrogen activity at the anode, leading to a reduction in the available open circuit voltage, a phenomenon that scales with the operating temperature of the fuel cell. This makes the impact of fuel utilization particularly relevant for high-temperature SOFCs, where the local partial pressure of the reacting species is enhanced linearly by the operating temperature (refer to Equation 4.2). The air stoichiometric ratio, also known as the excess air used in the reaction, also has a significant effect on the OCV, and is an important process parameter for the design of the SOFC-GT system. The impact of both fuel utilization factor and the air stoichiometric ratio on the partial pressure of species and subsequently, in the Nernst Equation was characterized by Winkler [36] through the modified equilibrium constant K, which considers both the effects of fuel utilization and excess air. The form of the Nernst Equation that includes this equilibrium constant (Equation 4.5) is given in Equation 4.6.

$$\Delta E = -\frac{RT}{2F}\ln(K) \tag{4.4}$$

$$K = \frac{\text{U}_{\text{fuel}}\sqrt{\frac{\lambda}{\beta_{\text{air}}} - \text{U}_{\text{fuel}}}}{(1 - \text{U}_{\text{fuel}})\sqrt{P(\lambda - \text{U}_{\text{fuel}})}} \tag{4.5}$$

$$\text{V}_{\text{Nernst}} = -\frac{\Delta_f G^\circ}{nF} + \frac{RT}{2F}\ln\left(\frac{(1 - \text{U}_{\text{fuel}})\sqrt{P(\lambda - \text{U}_{\text{fuel}})}}{\text{U}_{\text{fuel}}\sqrt{\frac{\lambda}{\beta_{\text{air}}} - \text{U}_{\text{fuel}}}}\right) \tag{4.6}$$

Freeh et. al. [25] also studied the effects of anode fuel composition as a percentage of pure hydrogen available at the anode, which was found to have a significant effect on the OCV. Increasing the composition of fuel available for the reaction in the anode affects the local partial pressure of reacting species through the equilibrium constant, requiring a modification to the equilibrium constant in Equation 4.5 to study the effect of anode fuel composition. Equation 4.6 can be further modified to include the partial pressure effects due to varying anode fuel composition, and this is shown in Equation 4.7. Equation 4.7 is the final form of the Nernst Equation that will be used throughout this study to quantify the effects of system pressure, operating temperature, anode fuel composition, air stoichiometry, and fuel utilization on the open circuit voltage of the HT-SOFC.

$$\mathrm{V}_{\mathrm{Nernst}} = -\frac{\Delta_f G^\circ}{nF} + \frac{RT}{2F}\ln\left(\frac{\delta_{\mathrm{H_2}}(1-\mathrm{U}_{\mathrm{fuel}})\sqrt{P(\lambda-\mathrm{U}_{\mathrm{fuel}})}}{\mathrm{U}_{\mathrm{fuel}}\sqrt{\frac{\lambda}{\beta}-\mathrm{U}_{\mathrm{fuel}}}}\right) \tag{4.7}$$

When connected to an external load, fuel cells exhibit irreversible losses from the OCV, which can be modeled as a function of the current density of the fuel cell. Four main irreversible losses are of significance in the operation of a fuel cell, namely, the activation losses, fuel crossover losses, ohmic losses, and concentration or mass-transport losses. Out of these, the voltage losses due to fuel crossover currents are negligible as the crossover currents between the anode and the cathode through the electrolyte are quite small for high-temperature fuel cells. As their net effect is small with respect to the scale of the current densities of HT-SOFCs, fuel crossover losses can be safely assumed to be negligible in this study. However, a small internal current is used to model both activation and mass transport losses, which are discussed in detail in the next sections.

The net operating voltage of a high-temperature solid oxide fuel cell can therefore be determined by subtracting the activation, ohmic, and mass transport voltage losses from the reversible Nernst voltage given by Equation 4.7:

$$V_{\mathrm{operating}} = E - V_{\mathrm{activation}} - V_{\mathrm{concentration}} - V_{\mathrm{ohmic}} \tag{4.8}$$

4.2.2. Activation Losses

Activation Losses are representative of the rate of reaction taking place on the surface of the electrodes, and can be defined as the voltage loss that occurs in driving the chemical reaction that transfers the electrons to or from the electrode [20]. In other words, it can be defined as the overpotential that is required to overcome the activation energy required to start the chemical reaction in the fuel cell. Activation Losses are primarily characterized by the exchange current density i_0, which is the current density that needs to be achieved in order to overcome the activation energy that is required to start the flow of electrons from the anode to the cathode through the electrolyte. Higher exchange current densities imply lower activation losses in the fuel cell, and this is characteristic of high temperature fuel cells, where exchange current densities are on the scale of the operating current densities making activation losses, although significant, not as prominent as other losses.

The Butler-Volmer Equation can be used to determine the activation voltage losses for the forward and reverse reactions occurring in the fuel cell. This is quite useful for characterizing fuel cell kinetics where the forward and reverse reactions have different activation energies, characterized by different values of the charge transfer coefficient α, which is a reaction parameter that indicates the proportion of applied electrical energy that is harnessed in changing the rate of an electrochemical reaction. An α value of 0.5 suggests that both the forward and reverse reactions in the fuel cell are symmetric in nature. The Butler-Volmer Equation describes the net current density as a function of the activation energy of the forward and reverse reactions, and is shown below:

$$i = i_0\left(e^{\frac{n\alpha F V_{\mathrm{act}}}{RT}} - e^{\frac{-n(1-\alpha)F V_{\mathrm{act}}}{RT}}\right) \tag{4.9}$$

The Butler-Volmer Equation can be simplified using the Tafel approximation, where the voltage loss required for the activation energy needed in the forward reaction is only considered. This simplifies Equation 4.9 to the form shown below, and provides a reasonable estimate for the activation voltage loss in the fuel cell.

$$i = i_0\left(e^{\frac{n\alpha F V_{\mathrm{act}}}{RT}}\right) \tag{4.10}$$

which gives,

$$V_{\mathrm{activation}} = \frac{RT}{n\alpha F}\ln\left(\frac{i}{i_0}\right) \tag{4.11}$$

where $\frac{RT}{n\alpha F}$ is the Tafel Slope for the forward reaction. The Tafel Slope signifies the rate at which the reaction takes place, and is a primary characteristic of the fuel cell reaction kinetics. The effect of the Tafel Slope on reaction kinetics is shown in Figure 4.2.

As the Tafel approximation only theoretically holds when the exchange current density is much smaller than the cell operating current densities ($i_0 << i$), a modified form of Equation 4.11 is required to properly estimate the activation voltage losses in HT-SOFCs- where the magnitude of the exchange current density is on the scale of cell operating current densities. Equation 4.11 was further modified by Freeh et. al. [25] to include the effects of an internal/fuel-crossover current i_n during SOFC operation and provide a reasonable estimate of activation voltage losses in SOFCs, as shown below:

$$V_{\text{activation}} = \frac{RT}{n\alpha F} \ln\left[\frac{i + i_n}{i_o}\right] \tag{4.12}$$

Here n represents the number of electrons involved in the fuel cell forward reaction and has a value of 2 for the electrolysis of water. i_0 represents the exchange current density, R is the Universal Gas Constant (8.314 J/mol K), T is the SOFC Operating Temperature in K, α represents the charge transfer coefficient, and F is the Faraday's Constant (96500 C/mol).

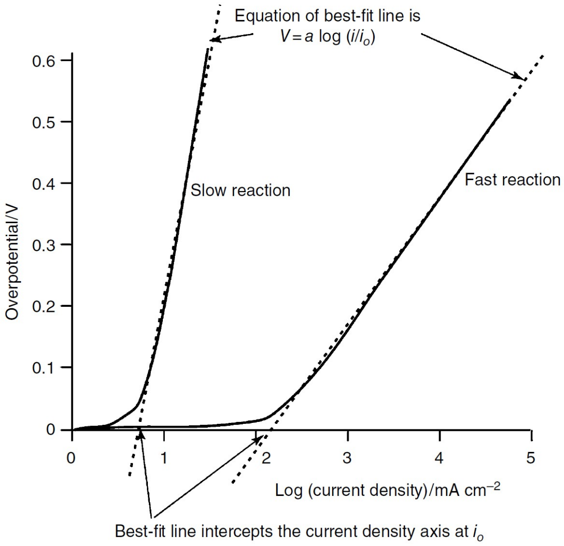

Figure 4.2: Tafel Plots for Slow and Fast electrochemical reactions, showing how the Tafel Slope is a characteristic of reaction kinetics [20].

4.2.3. Ohmic Losses

Ohmic losses in a fuel cell are representative of the resistance to the flow of electrons through the electrolyte and various interconnections, also including the resistance to the flow of ions through the electrolyte. These losses are modeled quite straightforwardly according to Ohm's Law, where the losses are proportional to the cell operating current density. The bulk internal resistance of the cell is a function of the electrode, electrolyte, and interconnect materials used in the fuel cell, as well as their relative thicknesses. In order to be consistent with the cell operating current density, the bulk cell resistance is often expressed per unit area, and is termed as the Area Specific Resistance (ASR) of the cell. The ASR of a cell plays a key role in determining its efficiency, as ohmic losses are quite prominent in high-temperature fuel cells.

Gemmen et. al. [27] modeled the ASR of high temperature fuel cells as a function of the fuel cell operating temperature as shown in Equation 4.13. The individual temperature-dependent internal resistances of each component (anode, cathode, electrolyte, and interconnect) are summed to get the total bulk area-specific resistance.

$$r = \sum r_{\mathrm{Component}} = \sum A e^{E/T} \tag{4.13}$$

Once the area-specific resistance for the fuel cell is calculated as a function of the cell operating temperature, it can be multiplied by the sum of the cell operating current density and the internal current density to get the ohmic losses per unit area of the fuel cell, as shown below:

$$V_{\mathrm{Ohmic}} = r \cdot (i + i_n) \tag{4.14}$$

Reducing the ohmic losses within a fuel cell presents one of the most challenging possibilities to fuel cell efficiency optimization, as the area-specific resistance is a function of the materials used and their relative thicknesses within the cell. For example, in an electrolyte-supported fuel cell, reducing the thickness of the electrolyte plays a pivotal role in reducing the bulk value of area-specific resistance. However, this is quite challenging due to the possibility of internal short-circuiting between the electrodes, structural integrity, or dielectric breakdown within the fuel cell. Choosing electrode materials that offer higher conductivity is also a key to reducing the bulk area-specific resistance of the fuel cell [20].

4.2.4. Mass Transport Losses

Mass Transport Losses, also known as Concentration Losses, occur due to the limitations of species transport within the fuel cell. Concentration losses are prominent at higher current densities, particularly after a limiting value of current density, beyond which the partial pressure of the reacting species drops to zero and the voltage deteriorates quite rapidly with increasing current density. This limiting current density (i_l) is a characteristic parameter of the fuel cell, and is the current density at which the supply mass flow rate of the reactants matches the consumption rate of the fuel cell, dropping the partial pressure of the reacting species to zero. Assuming a linear decrease in the partial pressure of the reacting species with the cell operating current density approaching its limiting current density, the voltage drop can be expressed by:

$$\Delta V = -\frac{RT}{nF} \ln \left[1 - \frac{i}{i_L} \right] \tag{4.15}$$

More specifically, the mechanism of concentration losses can be expressed by the difference in the local reactant concentration at the Triple-Phase-Boundary (TPB) between the electrolyte, cathode, and anode, where the electrochemical reaction occurs, and the bulk flow. Due to diffusion transport limitations within the electrodes, the local reactant concentration is usually lower at the TPB than the local product concentration, a phenomenon that scales up with the effect of cell operating current density. Concentration losses thus become a dominant voltage loss mechanism in fuel cells at higher cell operating current densities.

According to O'Hayre [67], concentration losses can be categorized into two primary mechanisms: the Nernstian mechanism and the activation mechanism. The effects of both of these phenomena can be modeled through the limiting current density, i_l, which represents the current density at which the reactant concentration at the triple phase boundary (TPB) drops to zero.

Physically, the limiting current density, i_{lim}, depends on several transport-related properties, including the effective diffusivity of the reactant species (D_{eff}), the porosity (ε) and tortuosity (τ) of the electrode, the bulk reactant concentration $(c_{R,0})$, and the thickness of the gas diffusion layer (δ). It is typically expressed as:

$$i_{\text{lim}} = \frac{2 F D_{\text{eff}} c_{R,0}}{\delta}$$

where F is Faraday's constant. Typical values of i_{l} range between $1\,\mathrm{A\,cm^{-2}}$ and $10\,\mathrm{A\,cm^{-2}}$.

To reasonably model the effects of mass transport on the voltage losses in IT/HT-SOFCs using the limiting current density, Equation 4.15 can be further modified to include the effects of fuel crossover through an internal current density, as given in Equation 4.16. The value of the limiting current density and the concentration voltage losses usually change with the type of fuel cell and operating parameters, the effect of which is discussed in later sections.

$$V_{concentration} = -\frac{RT}{nF}\ln\left[1-\frac{i+i_n}{i_L}\right] \tag{4.16}$$

4.3. SOFC Type Selection

The selection of the type of geometry for the baseline SOFC plays a crucial role in its practical application to aerospace systems. Over the years, both planar and tubular SOFCs have been at the forefront of practical usage in most commercial applications. While planar geometries offer the advantage of high power density (due to shorter current paths and associated ohmic losses) at the cell level, making them highly desirable choices for use in large-scale power generation, they face several key issues; such as complicated stack thermal management to ensure uniform temperature distribution and prevent the cracking and delamination of components at off-design temperature gradients and varied mechanical loading conditions [36]. Tubular geometry, on the other hand, does offer simplicity in design due to better thermal management and structural integrity under mechanical loading in off-design conditions, but operates at lower power densities and has higher manufacturing costs, which can be a bottleneck to their usage in large-scale commercial power systems. More about planar and tubular geometries is discussed in detail within the works of Singhal and Kendall [36], Larmine and Dicks [20], and O'Hayre [67].

To attain higher fuel cell performance at lower operating temperatures, recent developments in fuel cell design have focused on having a thin electrolyte film supported on conducting porous substrates or channeled dense metal sheets [62] [41] [36]. The substrate that is used for electrolyte support can be any electrode (either the cathode or anode), interconnect (metallic or ceramic,) or any other inactive insulator, shaped into tubular (cylindrical or flattened and ribbed) or planar geometry.

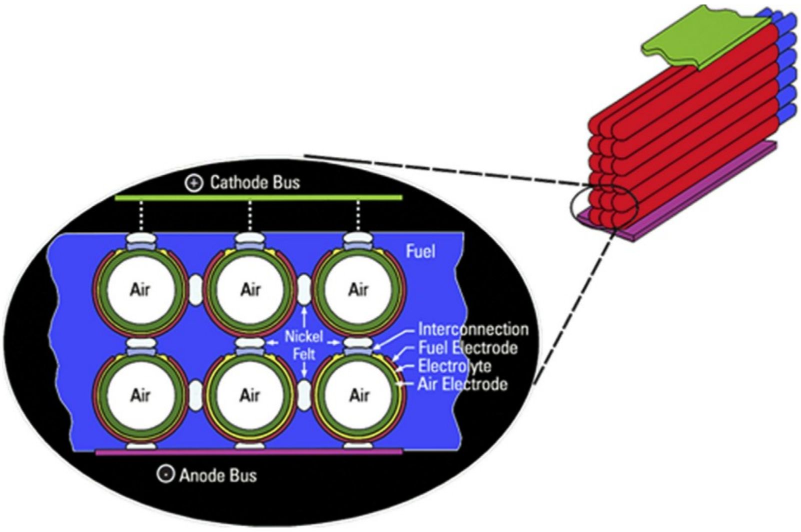

Figure 4.3: Cell-to-Cell Connections within s Siemens Westinghouse Cathode-Supported Tubular SOFC bundle [42]

When compared to planar SOFCs, tubular SOFCs have a closed end on one side, which offers the advantage of a seal-less design that allows for simplicity in integration. Planar SOFCs usually have high-temperature gas seals that help separate air from the fuel along the perimeters of the cathode-electrolyte-anode and the cathode-interconnect anode interfaces [28]. Also, when considering stack or bundle integration for tubular geometries, the compatibility between substrate type and cell geometry becomes critical. For instance, tubular geometries paired with cathode-supported designs offer notable benefits, such as allowing for cell-to-cell connections to be made in reducing environments, where cost-effective transition metals such as nickel can be employed [28] [29]. In contrast, connecting anode-supported tubular cells in oxidizing conditions requires the use of noble metals. While silver is commonly used for this purpose, there is a possibility that its high vapor pressure and mobility at elevated temperatures can compromise the long-term reliability of the stack [53] [40] [74]. This is also the reason why most tubular geometries for SOFCs feature cathode-supported designs. A schematic representation of the cell-to-cell connections in a Siemens Westinghouse cathode-supported tubular SOFC bundle is shown in Figure 4.4.

Although tubular SOFCs typically exhibit lower power densities compared to their planar counterparts [20], they are specifically chosen in this study due to their structural simplicity and suitability for integration into aerospace applications. Recent advancements in high-power-density micro-tubular SOFCs (MT-SOFCs) have significantly mitigated the drawbacks of conventional tubular designs, making them a promising candidate for use in SOFC-GT hybrid powertrains for aviation applications. In this context, a cathode-supported tubular SOFC is selected as the baseline configuration. The study begins by analyzing the most commonly used tubular design, the Siemens–Westinghouse tubular SOFC, and validating the zero-dimensional (0-D) SOFC electrochemical model against experimental data from the literature. Building on this, a modified tubular geometry is proposed to enhance the gravimetric power density at the stack level for its practical use in SOFC-GT hybrid powertrains for aerospace applications. Going ahead, technological improvements in this design are also studied and compared to the initial baseline SOFC geometry to quantify the effects of cell-level technological advancements on system-level performance.

4.3.1. Baseline SOFC Geometry

The original design of the Siemens-Westinghouse tubular SOFC geometry featured a Porous Support Tube (PST) made of Calcia-stabilized Zirconia (CSZ) (1-2 mm thickness, 20 mm internal diameter) onto which cylindrical anodes were deposited, followed by the electrolyte, interconnect, and the cathode, respectively [20] [42]. This design featuring the CSZ PST was later replaced by Siemens Westinghouse with a strontium-doped lanthanum manganite (LSM) cathode substrate to support the other layers, which resulted in moving the cathode to the inside and the anode on the outside; a design that went on to become a standard for cathode-supported tubular geometry in later years [30]. Such a design substantially improved fuel cell performance by reducing gas diffusion resistance and sheet resistance from the cathode substrate [30], but still suffered from high manufacturing costs and low-power density due to the longer current path within the cell and large voids in the stack between the tubes [20]. In order to cut down on manufacturing costs and further improve cell performance, more recent designs of the Siemens Westinghouse tubular SOFC featured porous Ca- and Ce-doped lanthanum manganite ($LaMnO_3$) instead of the LSM onto which the electrolyte and the anode were deposited by the cost-effective process of APS (Atmospheric Plasma Spray), replacing the original technique of EVD (Electrochemical Vapor Deposition) [42].

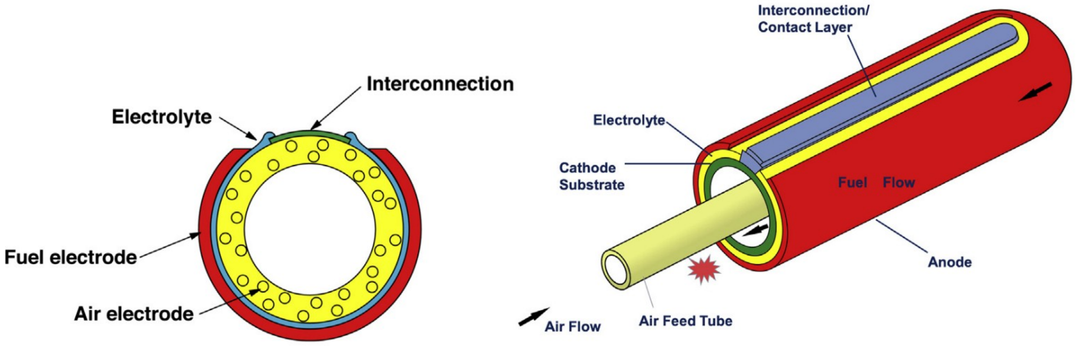

Figure 4.4: Cross-sectional and three-dimensional views of the Siemens Westinghouse Tubular Geometry [42]

The Siemens Westinghouse Tubular SOFC tubes are 150 cm in length and 2.2 cm in diameter, featuring concentric layers of the electrodes, electrolyte, and the interconnect; with the air electrode (cathode) being the innermost layer and the fuel electrode (anode) being the outermost. The materials used in each component layer and their respective thicknesses are summarized in Table 4.1.

Table 4.1: Cell materials employed in Siemens/Westinghouse cathode-supported tubular SOFCs [42]

Component	Material	Thickness
Cathode	Ca- and Ce-doped $LaMnO_3$	2.2 mm wall thickness
Electrolyte	Y_2O_3- or Sc_2O_3-doped ZrO_2	40–60 μm
Anode	Ni–electrolyte cermet	$100\,\mu m$
Interconnect	Ca- and Al-doped $LaCrO_3$	$100\,\mu m$

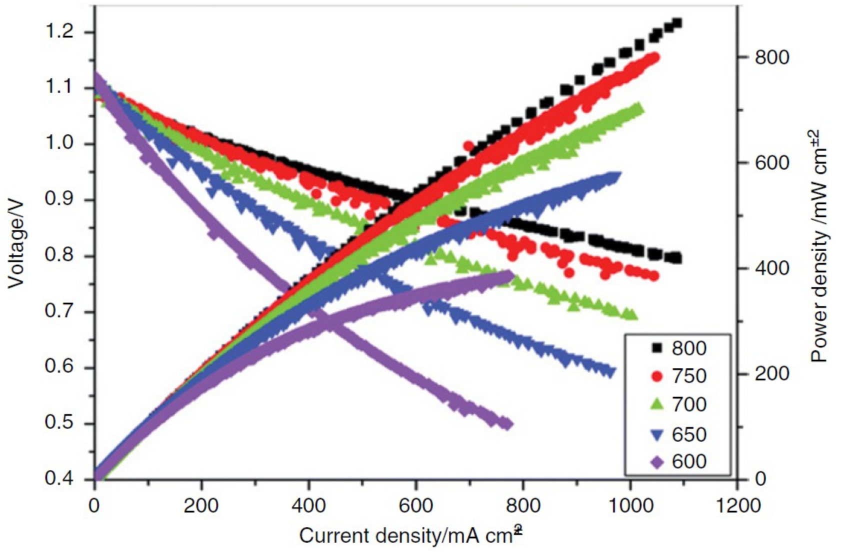

Figure 4.5: Voltage and power characteristics of single Siemens Westinghouse Tubular SOFC at $900\,°C$, $940\,°C$, and $1000\,°C$ [20]

The Siemens Westinghouse Tubular SOFC features a cell-level power density of around 0.2 W/cm^2 at 1000 °C , which is much lower than seen in most planar designs. To harness electrical power at a level for practical usage in commercial systems, individual cells are connected in an arrangement of 24 tubes (three rows of 8 serially-connected cells in parallel), termed by Siemens Westinghouse as an *SOFC bundle*. For the purpose of this study, four such bundles connected in parallel on top of each other, containing 96 such SOFC tubes in total, are considered as a single SOFC stack, featuring a stack gravimetric power density of around 350 W/kg at an operating temperature of 900°C. The V-i and power density characteristics of a single-tubular SOFC operating at $900\,°C$, $940\,°C$, and $1000\,°C$, respectively, fueled with a mixture of 89 vol.% H_2 and 11 vol.% H_2O, and operating at a fuel utilization of 85%, with air supplied as oxidant, is shown in Figure 4.5.

However, for practical application in aircraft, a stack-level gravimetric power density of atleast 700 W/kg is necessary when coupling a gas turbine with an SOFC stack [81], which makes the use of the original Siemens Westinghouse Tubular SOFC geometry quite infeasible for practical applications in a SOFC-GT hybrid system. Therefore for the purpose of this study, the original geometry of the Siemens Westinghouse tubular SOFC is modified by reducing the thickness of the porous cathode substrate to $570\,\mu m$ instead of the original 2.2 mm, while the electrolyte and anode thicknesses were adjusted to $11\,\mu m$ and $67\,\mu m$ respectively in order to reduce mass and ohmic losses at the cell level. Making this modification also increases the internal effective cell surface area to 965 cm^2 from the original 834 cm^2, boosting the power output at the stack level as well. This helps increase SOFC performance quite significantly at both cell and stack levels, increasing the stack level gravimetric density at 900°C and 400 mA/cm^2 to 812 W/kg. Although a cathode substrate thickness of around 8.5 times the anode thickness is maintained in this geometry, this modification to the baseline Siemens Westinghouse tubular geometry can, however, possibly come at a cost to the structural integrity and manufacturing complexity of the cathode-supported cell. However, an analysis of this was deemed beyond the scope of this work, and the modified SOFC geometry must only be seen as a simplified representative of high-power-density

SOFCs (HPD-SOFCs) with more complex geometries (flattened-ribbed/Delta type). A brief overview of other HPD SOFC designs in comparison to the original cylindrical Siemens Westinghouse tubular SOFC is presented in Table 4.3 and shown in Figure 4.6.

Table 4.2: Electrochemical Parameters for the baseline SOFC, at an operating temperature of 900°C, system pressure of 8.27 atm, stack fuel utilization of 75%, and a cathode air stoichiometric ratio of 4.

Parameter	Symbol	Value	Unit	Source
SOFC Operating Temperature	$\mathrm{T_{SOFC}}$	900	$^\circ\mathrm{C}$	—
System Pressure	$\mathrm{p_{system}}$	8.27	atm	—
Exchange Current Density	i_0	300	$\mathrm{mA/cm^2}$	[25]
Internal Current Density	i_n	2	$\mathrm{mA/cm^2}$	[25]
Limiting Current Density	i_L	1113	$\mathrm{mA/cm^2}$	Equation 5.1
Charge Transfer Coefficient	α	1.68	—	[25]
Area Specific Resistance	r	0.31	$\mathrm{k\,\Omega/cm^2}$	Equation 4.13, [27]
Air Stoichiometric Ratio	λ	4	—	—
Stack Fuel Utilization	$\mathrm{U_{fuel}}$	75	%	—

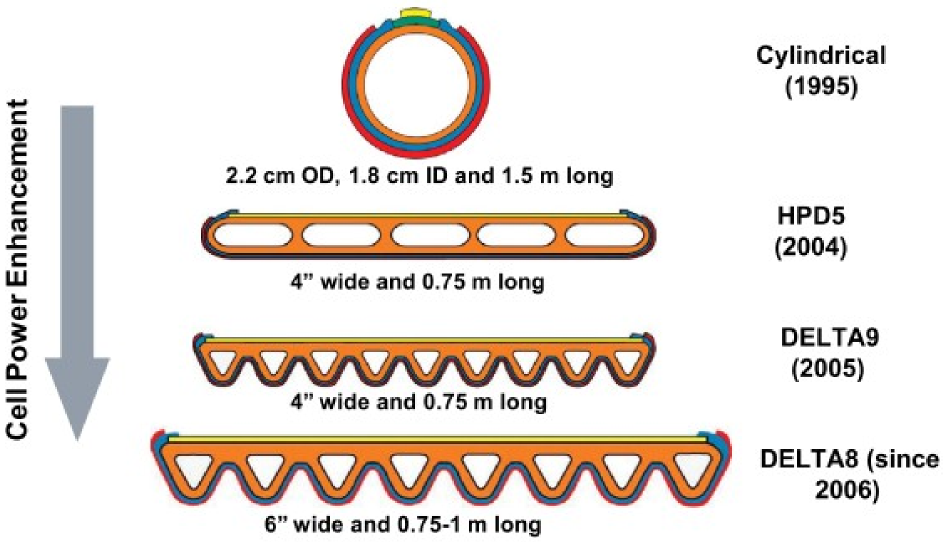

Figure 4.6: HPD-SOFC Geometries, in comparison to the Siemens Westinghouse Tubular geometry [42]

Table 4.3: Major geometrical parameters HPD-SOFCs in comparison to the Siemens Westinghouse Tubular geometry [42]

	Cylindrical	HPD5	HPD10	Delta9	Delta8
Length (cm)	150	75	75	75	75
Width (cm)	1.8–2.2	10	10	15	15
Effective surface area ($\mathrm{cm^2}$)	834	830	810	1250	2100

4.4. Power Outputs, Mass Flows, and Efficiencies - Cell and Stack Levels

4.4.1. Mass Flows of Reacting Species

The useful power, heat generated, and the mass flows of hydrogen and air needed at the cell and stack levels are essential parameters that need to be defined in order to quantify the performance and overall efficiency of the SOFC-GT powertrain at the system level. For a design current density, system parameters like fuel utilization ($\mathrm{U_{fuel}}$) and air stoichiometry ratio (excess air at the cathode, λ_{air}) affect the mass flow rate of both hydrogen and air needed at the anode and cathode, respectively. The required mass flows of both hydrogen and air at the cell level, taking into account both fuel utilization and excess air, are calculated through Faraday's Laws of Electrolysis.

The current produced by a single cell is proportional to the fuel that is utilized by it, can be calculated through Faraday's Law of Electrolysis as:

$$I = -zF\dot{n}_{fuel}\mathrm{U_{fuel}}\delta_{\mathrm{H_2}} \tag{4.17}$$

where $\dot{n}_{fuel}$ represents the number of moles of H_2 in the electrochemical reaction.

Rearranging Equation 4.17 for a design current density i in $\mathrm{mA/cm^2}$, the specific mass flow rate of hydrogen needed at the cell level, $\dot{m}_{\mathrm{H_2},cell}$, (in $\frac{\mathrm{kg}}{\mathrm{s\,cm^2}}$) for a given fuel utilization factor $\mathrm{U_{fuel}}$ can be written as:

$$\dot{m}_{\mathrm{H_2},cell} = \frac{iM_{\mathrm{H_2}}}{zF\mathrm{U_{fuel}}\delta_{\mathrm{H_2}}10^6} \tag{4.18}$$

where $M_{\mathrm{H_2}}$ is the molar mass of hydrogen gas in $\mathrm{g/mol}$, z is the number of electrons involved in the electrochemical reaction (which is 2 for the H_2-O_2 electrochemical reaction), and F is the Faraday's Constant, which has a value of 96,485 $\mathrm{C/mol}$.

The hydrogen gas mass flow rate at the stack level, $\dot{m}_{\mathrm{H_2},stack}$ in $\mathrm{kg/s}$ can now be calculated quite straightforwardly by accounting for the effective area of the cell (A_{cell}) and the total number of cells in the SOFC stack (N_{cells}) as follows:

$$\dot{m}_{\mathrm{H_2},stack} = \dot{m}_{\mathrm{H_2},cell} \times A_{cell} \times N_{cells} \tag{4.19}$$

Similarly, the mass flow rate of air required at the cathode, $\dot{m}_{air,cell}$ (in $\frac{\mathrm{kg}}{\mathrm{s\,cm^2}}$) can be calculated for s design current density i using the Faraday's Law of Electrolysis for Oxygen, while accounting for the excess air (λ_{air}) and the molar fraction of oxygen in the air (β) as:

$$\dot{m}_{air,cell} = \frac{\lambda_{air}iM_{air}}{\beta zF10^6} \tag{4.20}$$

where z takes the value of 4 for O_2, and β is 0.21. The stack level mass flow rate of air $\dot{m}_{air,stack}$ in $\mathrm{kg/s}$ is now calculated similarly as that of hydrogen gas in Equation 4.19:

$$\dot{m}_{air,stack} = \dot{m}_{air,cell} \times A_{cell} \times N_{cells} \tag{4.21}$$

4.4.2. Power Flows at Cell and Stack Level

The specific heat generated by a single fuel cell during operation, $\dot{q}_{\mathrm{th,cell}}$ in $\mathrm{W/cm^2}$ is computed through the difference between the molar enthalpy of reaction at the cell operating temperature and the useful power output for the fuel cell, and is given by:

$$\dot{q}_{\text{th,cell}}(i) = i\left(-\frac{\Delta\hat{h}_{\text{react}}}{2F} - V_{\text{operating}}(i)\right) \tag{4.22}$$

The total heat released by the fuel cell stack is calculated similarly as Equations 4.19 and 4.19, but accounting for the fuel utilization as well:

$$\dot{Q}_{\text{th,stack}}(i) = \dot{q}_{\text{th,cell}} \times A_{cell} \times N_{cells} \times \text{U}_{\text{fuel}} \tag{4.23}$$

The useful power density in W/cm^2 at the cell level can be given as:

$$\text{P}_{\text{cell}} = \text{V}_{\text{operating}} \times i \tag{4.24}$$

At the stack level, the power output in kW is simply given by the multiplication of the cell useful specific power P_{cell} with the number of cells in a single stack and the effective area of a single cell. The stack power at the stack level remains the same regardless of a series or parallel arrangement of the cells in a stack, as every cell is modeled as having the same ohmic resistance and the voltage drop/current through them (as per Ohm's Law) is therefore similar, adding up through the cells to produce the same output power.

$$\text{P}_{\text{stack}} = \frac{\text{P}_{\text{cell}} \times A_{cell} \times N_{cells}}{1000} \tag{4.25}$$

However, ohmic power losses through the current collectors in the SOFC stacks as well as the power drawn by electrical systems, pneumatic and hydraulic pumps in the Fuel Cell System (FCS) need to be treated as parasitic power losses at the stack level. As a result, the net stack power that contributes towards producing useful power for the aircraft's powertrain should be calculated by subtracting these from the stack-level power output given in Equation 4.25. For the purpose of this study, these losses are modeled as accounting to 1% of the total power at the stack level (represented by P_{aux}). Therefore, the net useful stack power which contributes to the SOFC-GT powertrain is now given by Equation 4.26 as:

$$\text{P}_{\text{stack,net}} = \text{P}_{\text{stack}} - \text{P}_{\text{aux}} \tag{4.26}$$

where P_{aux} represents the sum of the ohmic power losses at the stack level and the power drawn by auxiliary components in the Fuel Cell System (FCS).

4.4.3. Efficiencies at Cell and Stack Level

Following from Equations 4.19 and 4.26 where the hydrogen mass flow rate ($\dot{m}_{\text{H}_2,stack}$) and net power output at stack level ($\text{P}_{\text{stack,net}}$) are in kg/s and kW respectively, the stack thermal efficiency can now be defined by:

$$\eta_{\text{stack,net}} = \frac{\text{P}_{\text{stack,net}}}{\dot{m}_{\text{H}_2,stack} \times \text{LHV} \times 10^3} \tag{4.27}$$

Note that Equation 4.28 is different from the electrochemical efficiency of the fuel cell, which is the ratio of the operating voltage to the ideal Nernst voltage at cell level (given by Equation 4.7). The electrochemical efficiency is representative of the operating losses (ohmic, activation and mass-transport losses) at the cell level, which were discussed in detail in Section 4.2.

$$\eta_{\text{electrochemical}} = \frac{\text{V}_{\text{operating}}}{\text{V}_{\text{Nernst}}} \tag{4.28}$$

4.5. SOFC-GT Architecture

The choice of architecture for the SOFC-GT powertrain is crucial to understanding the system-level effect of combining the benefits of high temperature solid oxide fuel cells with gas turbines. As mentioned in Chapter 2, fuel cells do not produce useful power for the powertrain as stand-alone units; rather, they function along with high pressure compressors, heat exchangers, and pumps which need to be integrated along with the fuel cells while modeling the Fuel Cell System (FCS) as a whole. In comparison to smaller scale FCS units that are used for practical power generation applications, SOFC-GT powertrains that are sized for providing propulsion power in aircraft have the benefit of using pressured air from the stages of the gas turbine Low-Pressure/High-Pressure Compressors (LPCs/HPCs) rather than needing a seperate compressor to do so. Conversely, the gas turbine also benefits from functioning along with the HT-SOFC, as the underutilized preheated air and fuel from the fuel cell stacks along with SOFC waste heat ($\dot{Q}_{\mathrm{th,stack}}$) can be re-used for combustion within the gas turbine, requiring lesser fuel as a result to produce the same thermal power output (as the SOFC is thermally more efficient than the gas turbine), therefore enhancing the overall system thermal efficiency. As such, a complex flow of mass and energy is involved in the operation of a SOFC-GT powertrain, and an appropriate powertrain architecture needs to be chosen in order to model these effectively.

For the purpose of this study, a parallel configuration has been selected for the modeling of SOFC-GT powertrain, from the generic Serial-Parallel Partial Hybrid (SPPH) architecture for hydrogen-based double-hybrid powertrains by Alessandro Borgia [9], which was previously discussed in Chapter 2.4.4. The Parallel-3 Configuration (shown in Figure A.4 of Appendix A), a derivative of the generic SPPH architecture, was therefore chosen as the baseline configuration of the SOFC-GT architecture in this study. Although similar studies can be conducted in a serial configuration (refer to the Serial-3 configuration in Figure A.4) as well, the Parallel-3 configuration was specifically chosen to avoid the weight of an additional battery in the powertrain and to isolate sizing studies performed for SOFC-GT architectures exclusively. A schematic diagram of the SOFC-GT architecture chosen for this study is shown in Figure 4.8.

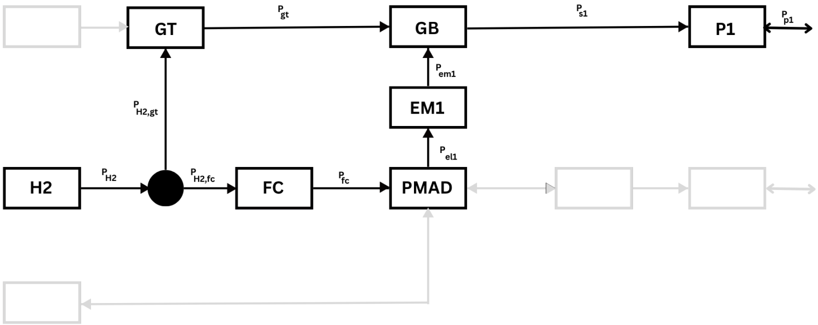

Figure 4.7: The Parallel-3 Configuration for the SOFC-GT Powertrain chosen for this study

It is also important to note that for FC-GT architectures with HT-SOFCs, the primary role of the heat exchangers is not the cooling of the fuel cell stacks, but the preheating of both air and fuel to SOFC operating conditions using hot exhaust gases from either the low pressure turbine (LPT), high pressure turbine (HPT), or from the combustion chamber. As heat is generated during SOFC operation, the high operating temperature of the SOFC stacks is maintained by the excess underutilized air that is supplied to the fuel cell cathode. This excess air has two functions: (1) removal of the waste heat from the fuel cells to maintain the SOFC operating temperature, and (2) reducing mass transport/concentration losses in the fuel cell cathode due to the increase in the limiting current density i_l (more on this is discussed in Section 4.2.4).

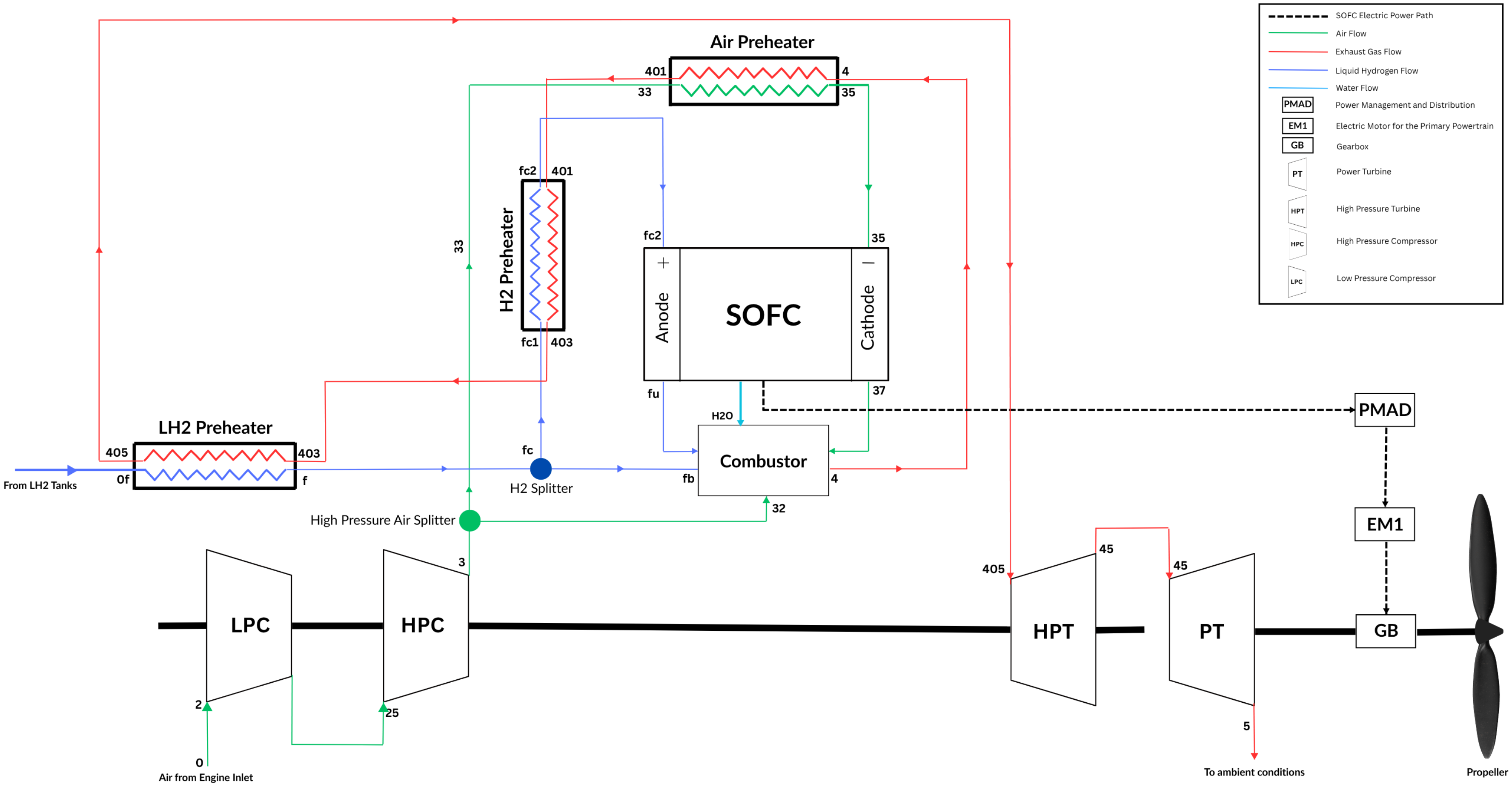

Figure 4.8: A schematic of the SOFC-GT Architecture chosen for this study

The placement of the heat exchangers in the proposed architecture is primarily influenced by the SOFC operating temperature, the design current density, and the cruise hydrogen split ratio. A higher SOFC operating temperature would require a higher maximum temperature difference, $\Delta T_{\mathrm{HX,max}}$ (between the cold inlet air and the hot exhaust gases), to always ensure that the heat exchanger effectiveness stays below 1. To always have a sufficient $\Delta T_{\mathrm{HX,max}}$ to pre-heat both the air and fuel being supplied to the SOFC stacks, the heat exchangers in this architecture are placed before the HPT, such that the hot exhaust gases are drawn directly from the combustion chamber before expansion through the turbines. This placement of the heat exchangers just after the combustion chamber has a slight effect on the total-total isentropic efficiencies of the turbines, and a 0.5% reduction (in comparison to the case where they are placed after the turbines) is assumed for similar corrected speeds.

Although the choice of placing the heat exchangers just after the combustion chamber reduces the gas turbine thermal efficiencies (due to higher total pressure losses) and necessitates the use of high-temperature metallic alloys or ceramics (which are generally heavier and have lower thermal conductivities in comparison to conventional metallic heat exchangers), such a placement ensures that the temperature of the hot exhaust gases can be utilized for sizing the heat exchangers across a wider range of SOFC operating temperatures, design current densities, and cruise hydrogen power split ratios. This is also explained in greater detail within Section B.3 of Appendix B, where an alternative placement of heat exchangers between the HPT and PT is also explored, with significant constraints on the SOFC operating temperature and cruise hydrogen split ratio limits.

4.6. Energy-Mass Balance of the SOFC-GT System

To fully understand the interdependence of powertrain components in the SOFC-GT architecture, a detailed study of the mass and power flows involved within the system is performed. The subsequent sections detail this energy-mass balance, accounting for the power paths that flow in and out of the whole system. Note that the numbering of stations is based on the ARP 755A [88], which is the internationally recognized standard for gas turbine nomenclature. A brief overview of the station numbering used in Figure 4.8 is presented in Table 4.4.

Table 4.4: Engine Station Numbering and Component Mapping, as per ARP 755A Nomenclature [88]

Station Number	Component
Station Numbering: Air and Exhaust Lines	
0, 1	Freestream Conditions, Air Inlet/Diffuser
2	LPC Inlet
25	HPC Inlet
3	HPC Outlet
32	HPC Air Split: Combustor
33	HPC Air Split: SOFC
33, 35	Inlet and Outlet: Air Preheater
35, 37	SOFC Cathode: Inlet/Outlet
4	Combustor Exit / Air Preheater Hot Side Inlet
401	Air Preheater Hot Side Exit / H_2 Preheater Hot Side Inlet
403	H_2 Preheater Hot Side Exit / LH_2 Preheater Hot Side Inlet
405	LH_2 Preheater Hot Side Exit / HPT Inlet
45	Power Turbine (PT) Inlet
5	Exhaust to Ambient
Station Numbering: Fuel Line	
0f	LH_2 Preheater Cold Side Inlet
fb	Combustor Fuel Inlet (LH_2 Tanks)
fc1	H_2 Preheater Cold Side Inlet
fc2	H_2 Preheater Cold Side Exit / SOFC Anode Inlet
fu	SOFC Underutilized Fuel: Combustor Inlet
fc	SOFC Fuel Line

4.6.1. Mass Balance Equations

The mass flow rate of the air stream through the low-pressure compressor (LPC) and high-pressure compressor (HPC) is considered to remain constant, as there is no mass addition/removal between these stations before the High-Pressure Air Splitter (refer to Figure 4.8). Therefore,

$$\dot{m}_2 = \dot{m}_{25} = \dot{m}_3 \tag{4.29}$$

The total mass flow of the air required by the SOFC system is bled from the outlet of the High Pressure Compressor (HPC) using a High Pressure Air Splitter and is given by Equation 4.30. Note that the total air mass flow requirement of the SOFC system operating at a given sizing current density i simply scales with the number of stacks.

$$\dot{m}_{33} = n_{\text{stacks}} \cdot \dot{m}_{\text{air,stack}} \tag{4.30}$$

The remainder of the air from the outlet of the HPC is sent directly to the combustor for combustion with LH_2 fuel from the tank, underutilized reactants from the SOFC, and the H_2O product from the stacks.

$$\dot{m}_{32} = \dot{m}_3 - \dot{m}_{33} \tag{4.31}$$

As mentioned previously, the air that is bled from the HPC outlet to the SOFC stacks contains an excess which is needed to maintain the SOFC operating temperature and minimal mass transport losses during SOFC operation. This is different from the actual stoichiometric requirement of air, which is required by the SOFC system to operate at a given sizing current density i. The stoichiometric air requirement by the SOFC system $\dot{m}_{\text{air,stoch}}$ given in Equation 4.32 is quite similar to the ones which were previously defined in Equations 4.20 and 4.21, but scaled with the number of stacks.

$$\dot{m}_{\text{air,stoich}} = \frac{\dot{m}_{33}}{\lambda_{\text{air}}} \tag{4.32}$$

The hydrogen mass flow rate into the engine, $\dot{m}_{\text{fb}}$, can be calculated as a function of the hydrogen split of the SOFC-GT system $\mathrm{H}_{2,\text{split}}$ in cruise:

$$\dot{m}_{\text{fb}} = \dot{m}_{\text{H}_2,\text{fc}} \cdot \left(\frac{1 - H2_{\text{split}}}{H2_{\text{split}}} \right) \tag{4.33}$$

Equations 4.35 and 4.34 define the distribution of the total hydrogen supplied to the SOFC stacks, specifying the fraction that is utilized within the stacks electrochemically and the remaining portion that is directed for combustion, respectively. An excess of hydrogen (specified by the reciprocal of the fuel utilization parameter) is supplied to the fuel cell anode for reducing the mass transport losses during fuel cell operation.

$$\dot{m}_{fu} = \dot{m}_{\text{H}_2,\text{fc}} \cdot (1 - U_{\text{fuel}}) \tag{4.34}$$

$$\dot{m}_{\text{H}_2,\text{stoich}} = \dot{m}_{\text{H}_2,\text{fc}} \cdot U_{\text{fuel}} \tag{4.35}$$

At chemical equilibrium, the number of moles of oxygen reacting within the fuel cell is half the number of moles of hydrogen stoichiometrically consumed. Likewise, the number of moles of water produced equals the number of moles of hydrogen that reacts stoichiometrically within the fuel cell. Accordingly, the mass flow rates of the reacting oxygen and the resulting water can be determined using the molecular masses of hydrogen (M_{H2}), oxygen (M_{O2}), and water ($\mathrm{M}_{\mathrm{H_2O}}$) in $\mathrm{g/mol}$, as given by Equations 4.36 and 4.37.

$$\dot{m}_{\text{O}_2,\text{stoich}} = \dot{m}_{\text{H}_2,\text{stoich}} \cdot \left(0.5 \cdot \frac{M_{\text{O}_2}}{M_{\text{H}_2}} \right) \tag{4.36}$$

$$\dot{m}_{\mathrm{H_2O}} = \dot{m}_{\mathrm{H_2,stoich}} \cdot \frac{M_{\mathrm{H_2O}}}{M_{\mathrm{H_2}}} \tag{4.37}$$

The mass flow rate of the air that leaves the fuel cell cathode after reacting with hydrogen is now devoid of the oxygen that has reacted within the fuel cell:

$$\dot{m}_{37} = \dot{m}_{35} - \dot{m}_{\mathrm{O_2,stoch}} \tag{4.38}$$

Finally, through mass balance, we can equate the mass of species that flows into the SOFC (the hydrogen fuel and air required by the SOFC stacks) and those that flow out of it (the sum of underutilized fuel and air, plus the water being produced through the electrochemical reaction between H_2 and O_2 in the fuel cell):

$$\dot{m}_{\mathrm{H_2,fc}} + \dot{m}_{35} = \dot{m}_{37} + \dot{m}_{fu} + \dot{m}_{\mathrm{H_2O}} \tag{4.39}$$

The products of combustion can also be equated through a similar mass balance equation, where the mass flow rate of the exhaust gas ($\dot{m}_4$) can be expressed as the sum of the mass flows of the reactants of combustion (i.e. underutilized air and fuel, hydrogen fuel from the fuel tank, and water produced in the electrochemical reaction):

$$\dot{m}_4 = \dot{m}_{37} + \dot{m}_{fuel} + \dot{m}_{32} + \dot{m}_{\mathrm{H_2O}} \tag{4.40}$$

where, the total fuel being utilized for combustion $\dot{m}_{\mathrm{fuel}}$ can be expressed as the sum of the hydrogen being supplied directly from the tank ($\dot{m}_{\mathrm{fb}}$) and the hydrogen that is not utilized by the fuel cell ($\dot{m}_{fu}$):

$$\dot{m}_{\mathrm{fuel}} = \dot{m}_{\mathrm{fb}} + \dot{m}_{fu} \tag{4.41}$$

Similar to Equation 4.42, the mass flow rate of the exhaust gas through the heat exchangers, the High Pressure Turbine (HPT) and the Power Turbine (PT) can be considered to be equal, as there is no further addition/removal of mass flows until the fully expanded exhaust gases exit to ambient static pressure conditions (Station 9):

$$\dot{m}_4 = \dot{m_{401}} = \dot{m_{403}} = \dot{m_{405}} = \dot{m_{45}} = \dot{m}_5 \tag{4.42}$$

4.6.2. Energy-Balance Equations

The energy balance equations, based on the Law of Conservation of Energy, can be written for any control volume by equating the total energy that flows into the system to the total energy that exits it. In terms of power that flows into and out of a thermodynamic system, this can be written as:

$$\Sigma \mathrm{P_{in}} = \Sigma \mathrm{P_{out}} \tag{4.43}$$

The Low-Pressure and High-Pressure Compressors (LPC and HPC) increase the total enthalpy of the working fluid by means of shaft work input, as adiabatic compression raises both the total pressure and total temperature of the airflow. Therefore, for the LPC we can write:

$$h_{25} = h_2 + \dot{\mathrm{W}}_{\mathrm{LPC}} \tag{4.44}$$

where,

$$\dot{\mathrm{W}}_{\mathrm{LPC}} = \dot{m}_2 c_{p,air}(T_{t,25} - T_{t,2}) \tag{4.45}$$

Similarly for the HPC,

$$h_3 = h_{25} + \dot{\mathrm{W}}_{\mathrm{HPC}} \tag{4.46}$$

where,

$$\dot{\mathrm{W}}_{\mathrm{HPC}} = \dot{m}_2 c_{p,air}(T_{t3} - T_{t,25}) \tag{4.47}$$

The pressurized air that exits the HPC is now divided into two streams by a High Pressure Air Splitter: one, which goes into the SOFC stacks through the Air Preheater (which raises the total temperature of the flow to SOFC operating temperature); and the other which goes directly into the combustion chamber. For the HP air stream that goes into the air preheater, we can write:

$$h_{35} - h_{33} = \dot{Q}_{air,HX} = \dot{m}_{33} c_{p.air}(T_{t,35} - T_{t,33}) \tag{4.48}$$

We can also express the energy balance for the heat exchangers that heat the liquid hydrogen coming from the fuel tank (LH_2 and H_2 preheaters) to the SOFC operating temperature in a similar manner as shown below in Equations 4.49 and 4.50:

$$h_f - h_{0f} = \dot{Q}_{\mathrm{LH_2},HX} = \dot{m}_{\mathrm{H_2}} c_{p,\mathrm{H_2}}(T_{tf} - T_{t,0f}) \tag{4.49}$$

As with the case of the high-pressure air stream, the pressurized H_2 gas that exits the LH_2 preheater is also split into two streams; one, which goes into the anodes of the SOFC stacks, and the other, which goes directly into the combustion chamber for combustion. For the pressurized H_2 gas stream that goes into the SOFC stacks via the H_2 preheater, the rise in the total enthalpy of the flow can be expressed as follows:

$$h_{fc2} - h_{fc1} = \dot{Q}_{\mathrm{H_2},HX} = \dot{m}_{\mathrm{H_2,\,fc}} c_{p,\mathrm{H_2}}(T_{t,fc2} - T_{t,fc1}) \tag{4.50}$$

The preheated air and LH_2 fuel that goes into the SOFC stacks now undergo an electrochemical reaction within the fuel cells that produces water as a by-product. As not all fuel and air is stoichiometrically utilized within the SOFCs, the by-products of this electrochemical reaction also include the underutilized air and fuel along with the H_2O product. The exothermic nature of the electrochemical reaction of H_2 and O_2 releases heat ($\dot{Q}_{\text{SOFC}}$), which leads to an increase in the total enthalpy of the products leaving the SOFC stacks:

$$\dot{m}_{35}h_{35} + \dot{m}_{fc2}h_{fc2} + (\dot{m}_{fc2} \times \mathrm{U}_{fuel} \times \mathrm{LHV}_{\mathrm{H_2}}) = \dot{m}_{37}h_{37} + \dot{m}_{\mathrm{H_2O}}h_{\mathrm{H_2O}} + \dot{m_{fu}}h_{fu} + \mathrm{P}_{\mathrm{FC}} \tag{4.51}$$

where the difference between the total energy of the utilized fuel and the useful electric work that can be extracted from it is the total waste heat that is released during SOFC operation:

$$(\dot{m}_{fc2} \times \mathrm{U}_{fuel} \times \mathrm{LHV}_{\mathrm{H_2}}) - \mathrm{P}_{\mathrm{FC}} = \dot{Q}_{\text{SOFC}} \tag{4.52}$$

Therefore, Equation 4.51 can now be re-written using Equation 4.52 as:

$$\dot{m}_{35}h_{35} + \dot{m}_{fc2}h_{fc2} + \dot{\mathrm{Q}}_{\text{SOFC}} = \dot{m}_{37}h_{37} + \dot{m}_{\mathrm{H_2O}}h_{\mathrm{H_2O}} + \dot{m_{fu}}h_{fu} \tag{4.53}$$

The underutilized fuel and air, along with the steam exiting the SOFC stacks is then considered to adiabatically mix with the high-pressure air from the HPC ($\dot{m}_{32}$) and the LH_2 fuel coming from the fuel tanks before undergoing combustion in the combustion chamber. The energy balance within the combustion chamber can be written as shown in Equation 4.54:

$$\dot{m}_{37}h_{37} + \dot{m}_{32}h_{32} + \dot{m}_{fu}h_{fu} + \dot{m}_{fb}h_{fb} + \dot{m}_{\mathrm{H_2O}}h_{\mathrm{H_2O}} + (\dot{m}_{fuel} \times \mathrm{LHV_{H_2}} \times \eta_{comb}) = \dot{m}_4 h_4 \tag{4.54}$$

where $\dot{m}_{fuel}$ and $\dot{m}_4$ is as defined previously by Equations 4.41 and 4.40.

The exhaust gases exiting the combustion chamber now go through the hot sides of the heat exchangers, which are responsible for pre-heating the pressurized air and LH_2 fuel to the operating temperature of the SOFC stacks. As a result of temperature drops across the heat exchangers, the total enthalpy of the exhaust gases also drops, as shown below in Equations 4.55, 4.56, and 4.57:

$$h_4 - \dot{\mathrm{Q}}_{\mathrm{air,HX}} = h_{401} \tag{4.55}$$

$$h_{401} - \dot{\mathrm{Q}}_{\mathrm{H_2,HX}} = h_{403} \tag{4.56}$$

$$h_{403} - \dot{\mathrm{Q}}_{\mathrm{LH_2,HX}} = h_{405} \tag{4.57}$$

After exiting the hot side of the preheaters, the exhaust gases now experience a drop in the total enthalpy following expansion through the High Pressure Turbine (HPT) and the Power Turbine (PT). The drop in the total enthalpy at Stations 45 and 5 corresponds to the work extracted by both turbines to provide the necessary shaft power required to run the LPC, HPC, and the propeller, respectively. Therefore, the energy balance for the turbines can be expressed as:

$$h_{405} - \mathrm{P_{HPT}} = h_{45} \tag{4.58}$$

$$h_{45} - \mathrm{P_{PT}} = h_5 \tag{4.59}$$

where $\mathrm{P_{HPT}}$ is defined as in Equation 4.99 in Section 4.6.3 and $\mathrm{P_{PT}}$ is defined by the power that can be extracted from the flow by adiabatic expansion of the exhaust gases to ambient static pressure (p_{amb}).

4.6.3. Cycle Calculations

The cycle calculations for the SOFC-GT powertrain by taking into account the energy and mass balances of the system are elaborated in the sections that follow. The assumed values of the parameters that are used in these calculations are presented in Table 4.5.

a. Air Inlet (Diffuser)

The primary function of the diffuser is to increase the pressure of the air by reducing the freestream velocity, to create favorable conditions at the inlet of the compressor at subsonic speeds. Point 0 represents external ambient conditions, and $\mathrm{T_0}$, $\mathrm{p_0}$, and $\mathrm{M_0}$ represent the freestream static temperature, pressure, and Mach number, respectively. As no work/heat is added to the flow within the diffuser, the total enthalpy within the diffuser is considered to be conserved.

By knowing the freestream conditions of the air at point 0, the total quantities of the air at the inlet of the Low Pressure Compressor (Point 2) can be calculated using isentropic relations, as shown below:

$$T_{t0} = T_0 \cdot \left(1 + \frac{\gamma_a - 1}{2} M_0^2\right) = T_{t2} \tag{4.60}$$

$$p_{t0} = p_0 \cdot \left(1 + \frac{\gamma_a - 1}{2} M_0^2\right)^{\frac{\gamma_a}{\gamma_a - 1}} \tag{4.61}$$

where γ_a represents the ratio of specific heat capacities of air at freestream conditions.

As the flow in the diffuser is not ideally isentropic, the total pressure is not conserved within the diffuser due to friction. The parameter ϵ_d is therefore introduced to account for the loss in total pressure along the length of the diffuser.

$$p_{t2} = p_{t0} \cdot \epsilon_d \tag{4.62}$$

where $\Delta p_{t,\text{inlet}}$ represents the percentage of total pressure loss within the diffuser.

$$\epsilon_d = (1 - \Delta p_{t,\text{inlet}}) \tag{4.63}$$

b. Low Pressure Compressor (LPC)

The inlet to the Low Pressure Compressor (LPC) is represented by Point 2, and is the first stage of the compression process. The LPC pressurizes the air even further and is driven by the High Pressure Turbine (HPT) on the same spool. Similar to the PW127 turboprop engine used in the baseline ATR 72-600 aircraft [47] [16], a single stage of compression is assumed for both the LPC and the HPC, and an overall pressure ratio (OPR) of 15 is assumed in this study.

The conditions at the inlet of the LPC are the same as those of the outlet of the diffuser, that is, Point 2. The pressure at the outlet of the LPC, that is, Point 25, can be easily calculated by accounting for the LPC pressure ratio (β_{LPC}):

$$p_{t,25} = \beta_{\text{LPC}} \cdot p_{t,2} \tag{4.64}$$

where,

$$\beta_{\text{LPC}} = \frac{p_{t,25}}{p_{t,2}} \tag{4.65}$$

Since compression through the LPC is not ideally isentropic, the real temperature at the outlet of the adiabatic LPC compression can be calculated by accounting for the isentropic efficiency of the LPC, as given in Equation 4.66:

$$T_{t,25} = T_{t2} \cdot \left(1 + \frac{\beta_{\text{LPC}}^{(\gamma_a - 1)/\gamma_a} - 1}{\eta_{\text{is,LPC}}}\right) \tag{4.66}$$

where the isentropic efficiency of the LPC can be written as:

$$\eta_{\text{is,LPC}} = \frac{T'_{t,25} - T_{t2}}{T_{t,25} - T_{t2}} \tag{4.67}$$

c. High Pressure Compressor (LPC)

The inlet and exit conditions at the High Pressure Compressor (HPC) are given by Points 25 and 3, respectively. Similar to the LPC, compression in the HPC is also considered as single-stage, and the outlet properties (total pressure and temperature) at the exit of the HPC are calculated similarly as shown previously for the LPC. β_{HPC} in Equation 4.68 represents the pressure ratio of the HPC, while $\eta_{\text{is,HPC}}$ is the isentropic efficiency of the HPC, and given by Equation 4.71.

$$p_{t3} = \beta_{\text{HPC}} \cdot p_{t,25} \tag{4.68}$$

where,

$$\beta_{\text{HPC}} = \frac{p_{t3}}{p_{t,25}} \tag{4.69}$$

$$T_{t3} = T_{t,25} \cdot \left(1 + \frac{\beta_{\text{HPC}}^{(\gamma_a - 1)/\gamma_a} - 1}{\eta_{\text{is,HPC}}}\right) \tag{4.70}$$

where,

$$\eta_{\text{is,HPC}} = \frac{T'_{t3} - T_{t,25}}{T_{t3} - T_{t,25}} \tag{4.71}$$

The high-pressure air at the exit of the HPC (Point 3) is now split into two streams using a high-pressure air splitter (see Figure 4.8): one stream flows directly into the combustor ($\dot{m}_{32}$), while the other is directed to the SOFC stacks via the air preheater ($\dot{m}_{33}$).

d. Air Preheater and SOFC

The air preheater is a counter-flow heat exchanger which pre-heats the pressurized air coming from the HPC to the operating temperature of the SOFC stacks, as shown in Equation 4.72. While the cold side of the air preheater uses air coming out of the HP air splitter, the hot side uses exhaust gases from the combustion chamber. The temperature difference between the hot side inlet (T_4) and the cold side inlet (T_{33}) preheats the pressurized air to the SOFC operating temperature. More about the sizing of the air-preheater based on this temperature difference is discussed in Section 4.7.

$$T_{t,35} = T_{\text{SOFC}} \tag{4.72}$$

As the pressurized air flows through the air preheater, it undergoes energy losses due to friction, resulting in a reduction in total pressure. This pressure drop accounts for the non-ideal nature of the flow, and is represented by the parameter $\epsilon_{air,HX}$.

$$p_{t,35} = p_{t,33} \cdot \epsilon_{air,HX} \tag{4.73}$$

where,

$$\epsilon_{air,HX} = (1 - \Delta p_{t,\text{HX}}) \tag{4.74}$$

The temperature of the underutilized air and hydrogen fuel, along with the water product at the outlet of the SOFC is given below. Equation 4.75, which gives the temperature of the species that exit the SOFC is derived from the energy balance of the SOFC control volume (refer to Section 4.6.2), and follows from the assumption that the waste heat produced from the SOFC stacks is distributed uniformly among the underutilized air and fuel, and the steam that exits the SOFC stacks.

$$T_{t,37} = \frac{\dot{Q}_{\text{SOFC}} + \dot{m}_{35} c_{p,\text{air}} T_{t,35} + \dot{m}_{\text{H}_2,\text{fc}} c_{p,\text{H}_2} T_{t,35}}{\dot{m}_{37} c_{p,\text{air}} + \dot{m}_{\text{H}_2\text{O}} c_{p,\text{H}_2\text{O}} + \dot{m}_{fu} c_{p,\text{H}_2,\mathrm{SOFC}}} \tag{4.75}$$

where,

$$\dot{Q}_{\text{SOFC}} = n_{stacks} \cdot \dot{Q}_{\mathrm{th,stack}} \tag{4.76}$$

The following assumptions are used in this mixing model:

- The underutilized air and hydrogen, along with the steam mix, are completely downstream of the SOFC in the combustion chamber.
- As the model is zero-dimensional (0-D), spatial variations in temperature, molar concentration, and mass flow rates of the species that exit the SOFC stacks are not modeled in this study.
- While the specific heat capacities at constant pressure (c_p) for the species entering the SOFC (i.e., hydrogen in the anode and air in the cathode) are evaluated at the operating temperature of the SOFC, the c_p values of the exiting species are calculated at $\mathrm{T}_{t,37}$.
- The uniform mixing of exiting species within the combustion chamber is considered to be adiabatic, with no additional losses of total enthalpy to the surroundings.

However, the total pressure of the flow decreases due to frictional losses within the SOFC stacks, as well as due to mixing and pressure equalization with the hydrogen and steam streams exiting the anode. These effects are collectively modeled using the total pressure loss parameter ϵ_{SOFC}, defined as:

$$p_{t,37} = p_{t,35} \cdot \epsilon_{\text{SOFC}} \tag{4.77}$$

where ϵ_{SOFC} accounts for irreversible losses within the SOFC and is defined as:

$$\epsilon_{\text{SOFC}} = 1 - \Delta p_{t,\text{SOFC}} \tag{4.78}$$

Here, $\Delta p_{t,\text{SOFC}}$ represents the fractional total pressure losses due to both internal friction within the SOFC stacks and the non-isentropic mixing of exiting species in the combustion chamber.

e. Combustion Chamber

The temperature of the exhaust gas after combustion is given below in Equation 4.79, and is derived from the energy balance in the combustion chamber (refer to Section 4.6.2). This energy balance assumes that all species entering the combustion chamber (including fuel from the fuel tanks, pressurized air from the HPC, underutilized air, and fuel from the SOFC stacks, and the steam product from SOFC operation) mix uniformly and adiabatically before combustion. The energy from combustion adds to the enthalpy of these species, so that the total enthalpy is conserved for the combustion chamber control volume. Here η_{comb} represents the combustion efficiency, while h_{mix} is the total enthalpy of the combined fuel stream following adiabatic mixing of the two fuel streams within the combustion chamber.

$$T_{t4} = \frac{\dot{m}_{\text{fuel}} \cdot \text{LHV}_{\text{H}_2} \cdot \eta_{\text{comb}} + \dot{m}_{\text{fuel}} c_{p,f} T_{tf} + \dot{m}_{37} c_{p,\text{air}} T_{t,37} + \dot{m}_{32}\ c_{p,\text{air}} T_{t,32} + \dot{m}_{\text{H}_2\text{O}} c_{p,\text{H}_{20}} T_{t,37}}{\dot{m}_4 c_{p,\text{gas}}} \tag{4.79}$$

The total temperature of the adiabatically mixed fuel stream in the combustion chamber, T_{tf}, in Equation 4.79 is given by:

$$T_{tf} = \frac{h_{\text{mix}}}{c_{p,f}} \tag{4.80}$$

where,

$$h_{\text{mix}} = \frac{\dot{m}_{\text{fb}} \cdot c_{p,\text{H}_2,\text{GT}} \cdot T_{\text{H}_2,\text{GT}} + \dot{m}_{fu} \cdot c_{p,\text{H}_2,\text{SOFC}} \cdot T_{t,37}}{\dot{m}_{\text{fuel}}} \tag{4.81}$$

As flow in the combustion chamber is not ideal and experiences irreversibilities due to friction, the total pressure losses in the combustion chamber can be modeled using the parameter ϵ_{comb}, as shown below:

$$p_{t4} = p_{t,37} \cdot \epsilon_{comb} \tag{4.82}$$

where,

$$\epsilon_{comb} = (1 - \Delta p_{t,\text{comb}}) \tag{4.83}$$

The assumptions involved in modeling the combustion of air, hydrogen, and the steam product within the combustion chamber in this model is summarized below:

- All incoming streams (pressurized air, underutilized air, and fuel from SOFC, steam, and additional fuel) mix adiabatically (without heat addition/removal to the surroundings) before combustion.

- The mixing of all species in the combustion chamber is assumed to be ideal and homogeneous.
- The hydrogen streams mix adiabatically to form a common fuel stream, but no combustion occurs during this mixing phase.
- The total enthalpy of the control volume (including chemical energy from the fuel and sensible enthalpy of all incoming species) is conserved during combustion.
- All species entering and exiting the combustion chamber remain in the gaseous phase.
- Irreversible losses due to friction and the non-ideal flow behavior in the combustion chamber is modeled using a pressure loss factor (ϵ_{comb}).

f. Air and H_2 Preheaters

The drop in total pressure and temperature of the exhaust gases flowing through the hot side of the air preheater can be estimated as shown below in Equations 4.84 to 4.87. As mentioned previously in Section 4.6.2, the exit total temperature at the cold side of the air preheater ($T_{t,35}$) is the operating temperature of the SOFC; hence, the total temperature rise in the cold side ($\Delta T_{c,\text{air HX}}$) can be used to calculate the heat transferred across the air preheater ($\dot{Q_{air,HX}}$), given that the heat capacity at constant pressure of the pressurized air ($C_{p,air}$) is known. By knowing the heat transferred, the inlet temperature at the hot side ($T_{t,4}$), and the heat capacity at constant pressure of the exhaust gases ($C_{p,gas}$), the exit temperature of the exhaust gases from the hot side of the air preheater ($T_{t,401}$) can now be estimated.

$$\Delta T_{c,\text{air HX}} = T_{t,35} - T_{t,33} \tag{4.84}$$

$$\Delta T_{h,\text{air HX}} = \frac{\Delta T_{c,\text{air HX}} \cdot \dot{m}_{33} \cdot c_{p,\text{air}}}{\dot{m}_4 \cdot c_{p,\text{gas}}} \tag{4.85}$$

$$T_{t,401} = T_{t4} - \Delta T_{h,\text{air HX}} \tag{4.86}$$

$$p_{t,401} = p_{t4} \cdot \epsilon_{air,HX} \tag{4.87}$$

where $\epsilon_{air,HX}$ can be written as,

$$\epsilon_{air,HX} = (1 - \Delta p_{t,\text{air HX}}) \tag{4.88}$$

Similarly, for the H_2 preheater we can write:

$$\Delta T_{c,\text{H2 HX}} = T_{t,fc2} - T_{t,fc1} \tag{4.89}$$

$$\Delta T_{h,\text{H2 HX}} = \frac{\Delta T_{c,\text{H2 HX}} \cdot \dot{m}_{fc1} \cdot c_{p,\mathrm{H_2}}}{\dot{m}_{401} \cdot c_{p,\text{gas}}} \tag{4.90}$$

$$T_{t,403} = T_{t,401} - \Delta T_{h,\text{H2 HX}} \tag{4.91}$$

$$p_{t,403} = p_{t,401} \cdot \epsilon_{\mathrm{H_2},HX} \tag{4.92}$$

where $\epsilon_{\mathrm{H_2},HX}$ can be written as,

$$\epsilon_{\mathrm{H_2},HX} = (1 - \Delta p_{t,\text{H2 HX}}) \tag{4.93}$$

and for the LH_2 preheater:

$$\Delta T_{c,\text{LH2 HX}} = T_{t,f} - T_{t,0f} \tag{4.94}$$

$$\Delta T_{h,\text{LH2 HX}} = \frac{\Delta T_{c,\text{LH2 HX}} \cdot \dot{m}_f \cdot c_{p,\mathrm{H_2}}}{\dot{m}_{403} \cdot c_{p,\text{gas}}} \tag{4.95}$$

$$T_{t,405} = T_{t,403} - \Delta T_{h,\text{LH2 HX}} \tag{4.96}$$

$$p_{t,405} = p_{t,403} \cdot \epsilon_{\mathrm{LH_2},HX} \tag{4.97}$$

where $\epsilon_{\mathrm{LH_2},HX}$ can be written as,

$$\epsilon_{\mathrm{LH_2},HX} = (1 - \Delta p_{t,\text{LH2 HX}}) \tag{4.98}$$

g. High Pressure Turbine (HPT)

The function of the High Pressure Turbine (HPT) is to provide sufficient power to drive both the Low and High Pressure compressors. As such the flow properties at the end of the HPT (Point 45) can be estimated by accounting for the total power needed by the LPC and the HPC:

$$P_{\text{HPT}} = \frac{P_{\text{HPC}} + P_{\text{LPC}}}{\eta_{\text{m,HPT}}} \tag{4.99}$$

where the power needed by the HPC and LPC are given by Equations 4.100 and 4.101:

$$P_{\mathrm{LPC}} = \frac{\dot{m}_2 c_{p,air}(T_{t,25} - T_{t,2})}{\eta_{m,LPC}} \tag{4.100}$$

$$P_{\mathrm{HPC}} = \frac{\dot{m}_2 c_{p,air}(T_{t,3} - T_{t,25})}{\eta_{m,HPC}} \tag{4.101}$$

where $\eta_{m,HPC}$, $\eta_{m,LPC}$, and $\eta_{m,HPT}$ represent the mechanical efficiencies of the HPC, LPC, and HPT respectively.

The temperature at the end of the HPT ($T_{t,45}$) is therefore given as follows:

$$T_{t,45} = \frac{\dot{m}_4 c_{p,gas} T_{t,405} - P_{\text{HPT}}}{\dot{m}_4 c_{p,gas}} \tag{4.102}$$

The pressure at the exit of the HPT can be estimated by accounting for the adiabatic nature of expansion through the HPT. The HPT isentropic efficiency ($\eta_{is,HPT}$) accounts for this, and is given by Equation 4.71:

$$p_{t,45} = p_{t,405} \left(1 - \frac{1 - \left(\frac{T_{t,45}}{T_{t,405}} \right)}{\eta_{\text{is,HPT}}} \right)^{\frac{\gamma_g}{\gamma_g - 1}} \tag{4.103}$$

where,

$$\eta_{\text{is,HPT}} = \frac{T_{t,405} - T_{t,45}}{T_{t,405} - T'_{t,45}} \tag{4.104}$$

h. Power Turbine

In a conventional turboprop engine, the function of the Power Turbine is to provide the total power required for the propeller. However, for the SOFC-GT hybrid powertrain in a parallel configuration, the total shaft power needed by the propeller is provided by the sum of the shaft powers of the power turbine and that of the electric motor powered by the SOFC stacks (refer to the SOFC-GT architecture in Figure 4.8). In this study, the total propulsive power needed by the aircraft in all phases of flight is considered to be from the propeller contribution alone, with the shaft power contribution of the gas turbine engine coming through the adiabatic expansion of the exhaust gases to the ambient static pressure in the power turbine.

The temperature at the exit of the power turbine, if the exhaust gases expand isentropically to ambient pressure, is given by Equation 4.105:

$$T_g = T_{t,45} \cdot \left(\frac{p_{\text{amb}}}{p_{t,45}} \right)^{(\gamma_g - 1)/\gamma_g} \tag{4.105}$$

Δh_{av} represents the enthalpy drop if the expansion of the exhaust gases in the power turbine is ideally isentropic:

$$\Delta h_{\text{av}} = \lambda \cdot c_p \cdot (T_{t,45} - T_g) \tag{4.106}$$

where λ represents the percentage of the isentropic enthalpy drop, Δh_{av}, that is allocated for expansion in the power turbine. Note that $\lambda = 1$ when the entire expansion to ambient static pressure is considered to be in the power turbine alone (that is, when the expansion only contributes to the gas turbine shaft power contribution, and not to any jet propulsive power by expansion through a nozzle.)

Equations 4.107 and 4.108 give the conditions at the exit of the power turbine when the expansion is considered to be ideally isentropic, while Equation 4.109 gives the actual temperature at the exit of the power turbine, accounting for the adiabatic nature of expansion. We can understand from Equations 4.107 and 4.108 that both T'_{t9} and p_{t9} are equal to T_g and p_{amb} when λ is considered to be 1.

$$T'_{t9} = T_{08} - \frac{\Delta h_{\text{av}}}{c_p} \tag{4.107}$$

$$p_{t9} = p_{t,45} \cdot \left(\frac{T'_{t9}}{T_{t,45}} \right)^{\gamma_g/(\gamma_g - 1)} \tag{4.108}$$

As mentioned earlier, the actual temperature of the exhaust gases at the exit of the power turbine can be given by accounting for the isentropic efficiency of the power turbine:

$$T_{t9} = T_{t,45} - \eta_{\text{is,PT}} \cdot (T_{t,45} - T'_{t9}) \tag{4.109}$$

where the isentropic efficiency of the power turbine, ($\eta_{\text{is,PT}}$) can be given by:

$$\eta_{\text{is,PT}} = \frac{T_{t,45} - T_{t,5}}{T_{t,45} - T'_{t,5}} \tag{4.110}$$

4.6.4. Gas Turbine Thermal Efficiency

In order to estimate the thermal efficiency of the gas turbine when used alongside the SOFC system in a hybrid SOFC-GT powertrain, the net power output of the system needs to be first calculated. This is done by first calculating the total power extracted from the turbines (HPT and PT), followed by subtracting the power used for the compression of air in the LPC and HPC. The total power extracted from the turbines is given by Equation 4.111, which accounts for the mechanical efficiencies of both turbines:

$$P_{\text{expansion}} = \dot{m}_4 \cdot c_{p,\text{gas}} \cdot (T_{t,405} - T_{t,45}) \cdot \eta_{\text{m,HPT}} + \dot{m}_4 \cdot c_{p,\text{gas}} \cdot (T_{t,45} - T_5) \cdot \eta_{\text{m,PT}} \tag{4.111}$$

The total power used for compression of air in the LPC and the HPC is given by Equation 4.112, where where the power needed by the HPC and LPC (P_{HPC} and P_{LPC}) were given previously by Equations 4.100 and 4.101:

$$P_{\text{compression}} = P_{\text{HPC}} + P_{\text{LPC}} \tag{4.112}$$

As mentioned earlier, the total heat input required to produce this useful work comes from both the combustion of fuel (combined fuel stream from the fuel tank and the SOFC stacks), along with the waste heat from the SOFC stacks. The heat from combustion of the fuel is given by Equation 4.113:

$$\dot{q}_{\text{combustion}} = \dot{m}_{\text{fuel}} \cdot \text{LHV}_{\text{H}_2} \cdot \eta_{\text{comb}} \tag{4.113}$$

Finally, the thermal efficiency of the gas turbine in the SOFC-GT system can be now estimated using Equations 4.111, 4.112, 4.113 and the total waste heat from the SOFC stacks ($\dot{Q}_{\text{SOFC}}$, given by Equation 4.76), as shown below:

$$\eta_{\text{thermal}} = \frac{P_{\text{expansion}} - P_{\text{compression}}}{\dot{Q}_{\text{SOFC}} + \dot{q}_{\text{combustion}}} \tag{4.114}$$

It is important to note here that the value of the gas turbine thermal efficiency given by Equation 4.114 cannot be directly used in the Double Hybrid Powertrain model, as the Parallel-3 configuration (refer to Figure 4.7) does not account for the additional mass flow and energy interactions between the gas turbine and the SOFC stacks. Therefore, a higher value of the gas turbine thermal efficiency must be used in the SOFC-GT sizing loop of the Double Hybrid Powertrain model in order to correct for the lower power input (in terms of the fuel mass flow being split between the GT and the FC) to the gas turbine engine, and the additional power input through the rejected heat energy and underutilized fuel mass flow from the SOFC stacks in the combustion chamber. This modified value of gas turbine thermal efficiency is defined as given below by Equation 4.115, and is used within the SOFC-GT sizing loop as shown by Figure 4.14.

$$\eta_{\text{thermal}} = \frac{P_{\text{expansion}} - P_{\text{compression}}}{\dot{m}_{\text{fb}} \cdot \mathrm{LHV}_{\mathrm{H}_2}} \tag{4.115}$$

Table 4.5: Parameters used for SOFC-GT Cycle Calculations

Parameter	Symbol	Value	Unit
Inlet Air Mass Flow	$\dot{m}_2$	8.49	kg/s
Inlet Total Pressure Loss	$\Delta p_{t,\text{inlet}}$	5	%
LPC Pressure Ratio	β_{LPC}	3.873	—
LPC Mechanical Efficiency	$\eta_{\mathrm{m,LPC}}$	98	%
LPC Isentropic Efficiency	$\eta_{\mathrm{is,LPC}}$	85	%
HPC Pressure Ratio	β_{HPC}	3.873	—
HPC Mechanical Efficiency	$\eta_{\mathrm{m,HPC}}$	98	%
LPC Isentropic Efficiency	$\eta_{\mathrm{is,HPC}}$	85	%
HX Total Pressure Loss	$\Delta p_{\mathrm{t,HX}}$	3	%
SOFC Total Pressure Loss	$\Delta p_{t,\text{SOFC}}$	3	%
Combustion Efficiency	η_{comb}	98	%
Combustion Total Pressure Loss	$\Delta p_{t,\text{SOFC}}$	5	%
HPT Mechanical Efficiency	$\eta_{\mathrm{m,HPT}}$	98	%
HPT Isentropic Efficiency	$\eta_{\mathrm{is,HPT}}$	88	%
PT Mechanical Efficiency	$\eta_{\mathrm{m,PT}}$	98	%
PT Isentropic Efficiency	$\eta_{\mathrm{is,PT}}$	92	%

4.7. Heat Exchanger Sizing

The sizing of all heat exchangers in this study is performed using the effectiveness–NTU method. This method is particularly appropriate when the outlet temperature of at least one stream is not known in advance. The process begins by defining the required heat transfer to achieve a target temperature rise on the cold side (typically the air stream), and proceeds through successive calculations of temperature changes, capacity rates, effectiveness, number of transfer units (NTU), and ultimately, the required surface area.

The desired temperature rise on the cold side (air into the fuel cell) is computed first:

$$\Delta \mathrm{T}_c = \mathrm{T}_{\text{c,out}} - \mathrm{T}_{\text{c,in}} \tag{4.116}$$

Next, the maximum possible temperature difference between the hot and cold streams is calculated,

$$\Delta \mathrm{T}_{\text{HX,max}} = \mathrm{T}_{h,\text{in}} - \mathrm{T}_{\text{c,in}} \tag{4.117}$$

The required heat transfer rate to achieve the cold side temperature rise is then given by:

$$\dot{Q}_{\text{required}} = \dot{m}_{\text{air,FC}} \cdot c_{p,\text{air}} \cdot \Delta T_c \tag{4.118}$$

Given this required heat input, the corresponding temperature drop on the hot side (exhaust stream) is:

$$\Delta \mathrm{T}_h = \frac{\dot{Q}_{\text{required}}}{\dot{m}_{\text{exhaust}} \cdot c_{p,\text{g}}} \tag{4.119}$$

Thus, the outlet temperature of the hot stream is:

$$\mathrm{T}_{h,\text{out}} = \mathrm{T}_{h,\text{in}} - \Delta \mathrm{T}_h \tag{4.120}$$

The heat capacity rates of both hot and cold streams are then calculated as:

$$\begin{aligned} \mathrm{C}_{\text{hot}} &= \dot{m}_{\text{exhaust}} \cdot c_{p,\text{g}} \\ \mathrm{C}_{\text{cold}} &= \dot{m}_{\text{air,FC}} \cdot c_{p,\text{air}} \end{aligned}$$

From these, the heat capacity ratio is defined as:

$$\mathrm{R} = \frac{C_{\min}}{C_{\max}} \tag{4.121}$$

The effectiveness of the heat exchanger is defined as the ratio of actual to maximum possible heat transfer. Depending on which stream has the minimum capacity rate, effectiveness is computed as:

$$\varepsilon = \begin{cases} \frac{\Delta T_h}{\Delta T_{\text{max}}}, & \text{if } C_{\text{hot}} < C_{\text{cold}} \\ \frac{\Delta T_c}{\Delta T_{\text{max}}}, & \text{otherwise} \end{cases}$$

Once the effectiveness is known, the number of transfer units (NTU) is determined using the relation for a counter-flow heat exchanger:

$$\mathsf{NTU} = -\frac{\ln\left(\frac{\varepsilon-1}{\varepsilon R-1}\right)}{1-R} \tag{4.122}$$

Finally, the required heat exchanger surface area is obtained from:

$$A_{\mathsf{HX}} = \frac{\mathsf{NTU}\cdot \mathrm{C}_{\min}}{\mathrm{U}} \tag{4.123}$$

where U is the overall heat transfer coefficient in $\mathrm{kW/m^2/K}$.

The overall heat transfer coefficient U is determined from the hot- and cold-side convective coefficients, each obtained using dimensionless analysis. For a channel of hydraulic diameter D_h, the Reynolds and Prandtl numbers for the cold side (air) and hot side (exhaust gas) are given by:

$$\mathrm{Re}_c = \frac{4\,\dot{m}_c}{\pi D_h\,\mu_c}, \qquad \mathrm{Pr}_c = \frac{c_{p,\mathrm{air}}\,\mu_c}{k_c} \tag{4.124}$$

$$\mathrm{Re}_h = \frac{4\,\dot{m}_h}{\pi D_h\,\mu_h}, \qquad \mathrm{Pr}_h = \frac{c_{p,\mathrm{g}}\,\mu_h}{k_h} \tag{4.125}$$

where $\dot{m}$ is the mass flow rate per channel, while μ and k are the dynamic viscosity and the thermal conductivity of the fluid, respectively. The Nusselt numbers for smooth, fully developed turbulent flow are calculated using the Dittus–Boelter correlations:

$$\mathrm{Nu}_c = 0.023\,\mathrm{Re}_c^{0.8}\,\mathrm{Pr}_c^{0.3} \tag{4.126}$$

$$\mathrm{Nu}_h = 0.023\,\mathrm{Re}_h^{0.8}\,\mathrm{Pr}_h^{0.4} \tag{4.127}$$

Fin efficiency corrections are applied assuming rectangular fins of height h_{fin}, thickness t_{fin}, and material thermal conductivity k_{fin}. The fin parameter m and corresponding efficiency η for each side are:

$$m_c = \sqrt{\frac{2\,(\mathrm{Nu}_c\,k_c/D_h)}{k_{\mathrm{fin}}\,t_{\mathrm{fin}}}}, \qquad \eta_c = \frac{\tanh(m_c\,h_{\mathrm{fin}})}{m_c\,h_{\mathrm{fin}}} \tag{4.128}$$

$$m_h = \sqrt{\frac{2\,(\mathrm{Nu}_h\,k_h/D_h)}{k_{\mathrm{fin}}\,t_{\mathrm{fin}}}}, \qquad \eta_h = \frac{\tanh(m_h\,h_{\mathrm{fin}})}{m_h\,h_{\mathrm{fin}}} \tag{4.129}$$

The convective heat transfer coefficients corrected for fin efficiency are now given by:

$$h_c = \eta_c\,\frac{\mathrm{Nu}_c\,k_c}{D_h} \tag{4.130}$$

$$h_h = \eta_h\,\frac{\mathrm{Nu}_h\,k_h}{D_h} \tag{4.131}$$

Finally, the overall heat transfer coefficient is obtained by combining the individual thermal resistances of the hot and cold sides:

$$U = \left(\frac{1}{h_c} + \frac{1}{h_h}\right)^{-1} \tag{4.132}$$

This value of the overall heat transfer coefficient U is then substituted in Equation 4.123 to estimate the total area required for heat transfer.

4.8. Baseline Aircraft: ATR 72-600

The ATR 72-600 is a twin-engine turboprop regional airliner manufactured by ATR (Avions de Transport Régional), a joint venture between Airbus and Leonardo. Designed for short-haul operations, the ATR 72-600 is widely regarded for its operational efficiency, low fuel consumption, and compatibility with regional airport infrastructure. Its relatively low cruise speed and fuel burn make it an ideal candidate for assessing novel propulsion technologies, such as hydrogen-based or hybrid-electric systems.

In this thesis, the ATR 72-600 is used as the baseline aircraft for evaluating the hybrid SOFC-GT propulsion architectures due to its mission profile being representative of most short-medium range aircraft and its level of technical maturity. Therefore, the choice of the ATR 72-600 is particularly relevant for trade studies focusing on 70–80 seat regional aircraft with a range of approximately $1500\,\mathrm{km}$.

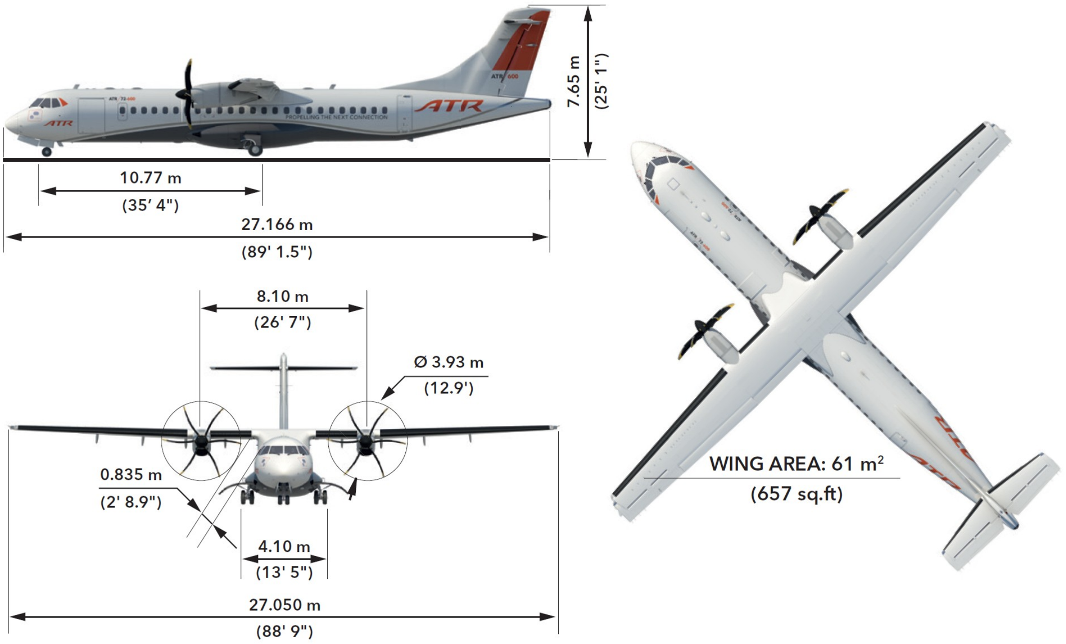

Figure 4.9: Dimension of the ATR 72-600, used for airport planning purposes [6]

4.8.1. Performance Metrics of the ATR 72-600

The key performance characteristics of the ATR 72-600 are summarized below, based on data from the manufacturer and supporting literature [6]:

- **Passenger capacity:** 72 seats (standard configuration)
- **Range (max pax):** 1404 km (758 NM)
- **Max cruise speed:** $510\,\mathrm{km/h}$ (275 KTAS at optimum FL)
- **Cruise altitude:** 5200 m
- **Takeoff distance (ISA SL, MTOW):** $1304\,\mathrm{m}$
- **Landing distance (basic MLW, SL):** $915\,\mathrm{m}$
- **Maximum takeoff weight (MTOW):** $23\,000\,\mathrm{kg}$
- **Maximum landing weight (MLW):** $22\,350\,\mathrm{kg}$
- **Operational empty weight (typical):** $13\,450\,\mathrm{kg}$
- **Maximum payload:** $7550\,\mathrm{kg}$
- **Maximum fuel load:** $5000\,\mathrm{kg}$
- **Engines:** 2 × Pratt & Whitney Canada PW127M/N

- **Engine power (takeoff):** 2475 SHP (each), up to 2750 SHP one-engine rating
- **Propeller:** 6-blade Hamilton Standard 568F, $3.93\,\mathrm{m}$ diameter

Table 4.6: ATR 72-600 Performance Data [6]

Engines	Pratt & Whitney Canada PW127M/N
Take-off Power	2,475 SHP
Take-off Power – One Engine	2,750 SHP
Max Continuous	2,500 SHP
Max Climb	2,192 SHP
Max Cruise	2,132 SHP
Propellers	Hamilton Standard 568F
Blades – Diameter	6 – 3.93 m – 12.9 ft
Max Take-off Weight (basic)	22,800 kg – 50,265 lb
Max Take-off Weight (option)	23,000 kg – 50,705 lb
Max Landing Weight (basic)	22,350 kg – 49,272 lb
Max Zero Fuel Weight (basic)	20,800 kg – 45,855 lb
Max Zero Fuel Weight (option 1)	21,000 kg – 46,296 lb
Operational Empty Weight (Tech. Spec.)	13,010 kg – 28,682 lb
Operational Empty Weight (Typical in-service)	13,450 kg – 29,652 lb
Max Payload (at typical in-service OEW)	7,550 kg – 16,645 lb
Max Fuel Load	5,000 kg – 11,023 lb
Take-off Distance (Basic – MTOW – ISA – SL)	1,279 m – 4,196 ft
Take-off Distance (Option 1 – MTOW – ISA – SL)	1,304 m – 4,278 ft
TOW for 300 NM – Max pax – SL – ISA	1,156 m – 3,793 ft
TOW for 300 NM – Max pax – 3,000 ft – ISA +10	1,383 m – 4,537 ft
Take-off Speed (V_2 min @ MTOW)	116 KCAS
Landing Field Length (Basic MLW – SL)	915 m – 3,002 ft
Landing Field Length (Max pax + reserves – SL)	870 m – 2,854 ft
Reference Speed at Landing	113 KIAS
Optimum Climb Speed	170 KCAS
Rate of Climb (ISA, SL, MTOW)	1,355 ft/min
Time to Climb to FL170	17.5 min
One Engine Net Ceiling (95% MTOW, ISA +10)	10,000 ft
Max Cruise Speed (95% MTOW – ISA – Optimum FL)	275 KTAS – 510 km/h
Fuel Flow at Cruise Speed	762 kg/h – 1,680 lb/h
Range with Max Pax	758 NM
200 NM Block Fuel	638 kg – 1,406 lb
200 NM Block Time	61 min
300 NM Block Fuel	879 kg – 1,937 lb
300 NM Block Time	84 min

4.9. Class 1 Sizing Methodology

4.9.1. Power Sizing and Design Point Selection

To identify a feasible design space and establish a design point that characterizes the optimal configuration defined in terms of maximum power, maximum take-off weight, and wing surface area, a set of matching requirements based on the wing loading $(\mathrm{W/S})$ and the power loading $(\mathrm{W/P})$ values is formulated. These requirements are generally expressed in the form shown below in Equation 4.133, with the thrust loading values being a function of wing loading values for each flight condition:

$$\frac{\mathrm{T_p}}{\mathrm{W_{ref}}} = f\left(\frac{\mathrm{W_{ref}}}{S}\right) \tag{4.133}$$

where:

- $\mathrm{T_p}$ is the thrust required for a specific flight condition,
- $\mathrm{W_{ref}}$ is the reference aircraft weight (equal to the take-off mass),
- S is the wing surface area.

These matching requirements reflect the force equilibrium and performance conditions across a range of flight phases. The primary constraints included in the analysis are:

- Cruise speed constraint,
- Stall speed constraint (based on landing approach),
- Take-off distance constraint.

In addition to these primary requirements, several critical certification constraints are evaluated, specifically those related to engine-out scenarios and climb performance. These include:

- One-engine-inoperative (OEI) balked landing constraint,
- OEI second-segment climb constraint,
- OEI take-off climb gradient with landing gear (LG) extended,
- OEI take-off climb gradient with LG retracted,
- OEI en-route climb gradient,
- OEI ceiling constraint,
- OEI discontinued approach climb constraint,
- OEI rate-of-climb constraint at sea level,
- All-engines-operating (AEO) balked landing constraint,
- AEO take-off climb gradient constraint,
- AEO cruise ceiling constraint,
- AEO rate-of-climb constraint at sea level,
- AEO residual rate-of-climb constraint at top of climb.

As an example, the thrust loading required in cruise conditions is expressed in the cruise speed constraint as:

$$\frac{\mathrm{T_{cruise}}}{\mathrm{W_{ref}}} = \frac{q \cdot \mathrm{C_{D_0}}}{\mathrm{W_{ref}}/S} + \frac{\mathrm{W_{ref}}/S}{q \cdot \pi \cdot \mathrm{AR} \cdot \mathrm{e}} \tag{4.134}$$

where:

- $q = \frac{1}{2}\rho {\mathrm{V_{cruise}}}^2$ is the dynamic pressure,
- $\mathrm{C_{D_0}}$ is the zero-lift drag coefficient,
- AR is the wing aspect ratio,

- e is the Oswald efficiency factor.

In hybrid-electric configurations, power loading diagrams are generally preferred over thrust loading diagrams, since the powertrain is dimensioned in terms of power rather than thrust. The relation between thrust loading and power loading is given by:

$$\frac{\mathrm{W_{ref}}}{\mathrm{P_p}} = \frac{1}{\mathrm{V}} \cdot \frac{\mathrm{W_{ref}}}{\mathrm{T}} \tag{4.135}$$

This implies that the propulsion system must deliver sufficient power to meet all mission and certification requirements. Each of the constraints mentioned previously defines a curve in the $\mathrm{W/S}$–$\mathrm{W/P}$ design space. The propulsion system must be capable of satisfying the lowest $\mathrm{W/P}$ value among all active constraints, with the wing requiring the maximum surface area to provide sufficient lift in all conditions (which corresponds to the lowest acceptable value of $\mathrm{W/S}$). This process results in identifying a feasible design space that satisfies all operational and regulatory constraints.

For a double hybrid powertrain configuration, component-specific constraint diagrams are derived using the total propulsive power requirement, the input variables of the double hybrid powertrain such as ϕ_1, ϕ_2, $\mathrm{H_{2,split}}$, and component efficiencies. A design point is first selected for the entire aircraft, following which, at the design value of wing loading, the limiting value of power loading is evaluated for each component of the double-hybrid powertrain.

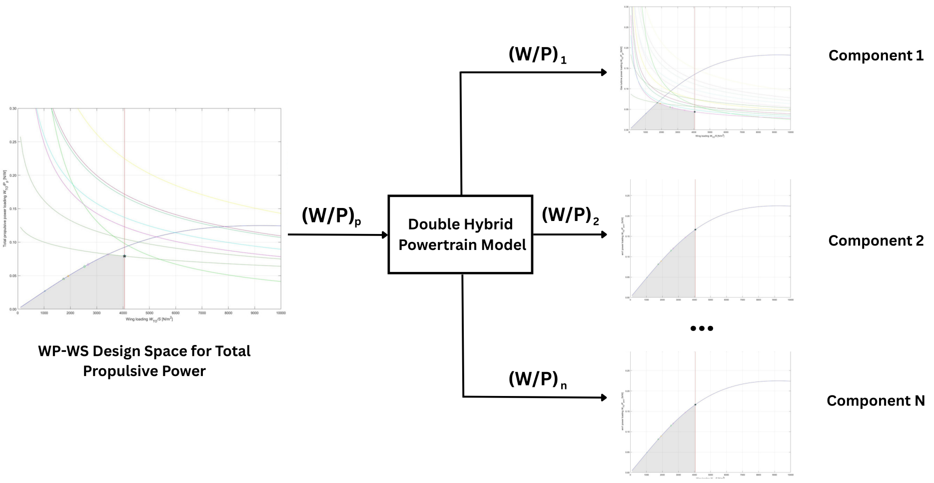

Figure 4.10: Power Sizing of Individual Powertrain Components using the Double Hybrid Powertrain Model [9]

The equations used to derive the power loading and wing loading values for different constraints in the $\mathrm{W/S}$-$\mathrm{W/P}$ design space is summarized below:

Table 4.7: Equations for $\mathrm{P/W}$ and $\mathrm{W/S}$ values for various performance constraints

Performance requirement	Expression
Stall speed	$\left(\frac{W}{S}\right)_{V_s} = 0.5\,\rho_{\mathrm{SL}} V_s^2 C_{L_{\max}}$
Takeoff distance	$\left(\frac{P_{\mathrm{shaft,SL}}}{W}\right)_{\mathrm{takeoff}} = \frac{V_{\mathrm{TO}} \cdot \left(\mu - \left(\mu + \frac{C_{D_g}}{C_{L_R}}\right) e^{\left(\frac{0.6\rho_{\mathrm{h,TOmax}} g C_{D_g} s_{\mathrm{TO}}}{\frac{\mathrm{W}}{\mathrm{S}}}\right)}\right)}{\xi_{70} \eta_{P,\mathrm{TO}} \left(1 - e^{\left(\frac{0.6\rho_{\mathrm{h,TOmax}} g C_{D_g} s_{\mathrm{TO}}}{\frac{\mathrm{W}}{\mathrm{S}}}\right)}\right)}$

Landing distance	$\left(\frac{W}{S}\right)_{\text{landing}} = \frac{C_{L_{\text{max}}}\rho\cdot\frac{s_{\text{landing}}}{0.5847}}{\frac{2W_{\text{landing}}}{W_{\text{TO}}}}$
Maximum rate of climb	$\left(\frac{P_{\text{shaft,SL}}}{W}\right)_{\text{ROC}_{\text{max}}} = \frac{1}{\xi_{70}}\left(\frac{\text{ROC}_{\text{max}}}{\eta_{P,\text{climb}}} + \frac{1.155}{\eta_{P,\text{climb}}\left(\frac{L}{D}\right)_{\text{max,SL}}}\sqrt{\frac{2}{\rho_{\text{SL}}\sqrt{\frac{3C_{D_0}}{k}}}\frac{W}{S}}\right)$
Absolute ceiling	$\left(\frac{P_{\text{shaft,SL}}}{W}\right)_{\text{ceiling}} = \frac{1.155}{\xi_{\text{cruise}}\eta_{P,\text{cruise}}\left(\frac{L}{D}\right)_{\text{max,ceiling}}\frac{\rho_{\text{ceiling}}}{\rho_{\text{SL}}}}\sqrt{\frac{2}{\rho_{\text{ceiling}}\sqrt{\frac{3C_{D_0}}{k}}}\frac{W}{S}}$
Maximum load factor	$\left(\frac{P_{\text{shaft,SL}}}{W}\right)_{\text{load factor}} = \frac{1}{\xi_{\text{cruise}}}\left(\frac{1}{2}\rho V^3 C_{D_0}\frac{1}{W/S} + \frac{2kn_{\text{max}}^2}{\rho V}\frac{W}{S}\right)$
Maximum cruise speed	$\left(\frac{P_{\text{shaft,SL}}}{W}\right)_{V_{\text{max}}} = \frac{1}{\xi_{\text{cruise}}}\left(\frac{\eta_{P,\text{cruise}}C_{D_0}\rho_{\text{SL}}V_{\text{max}}^3}{2}\frac{1}{W/S} + \frac{2\eta_{P,\text{cruise}}k\rho_{\text{SL}}}{\rho_{\text{cruise}}^2 V_{\text{max}}}\frac{W}{S}\right)$
EASA CS 25.111	$\left(\frac{\mathrm{P}_{\text{shaft,SL}}}{\mathrm{W}}\right)_{\text{CS25.111}} = \frac{N\left(c_{\text{gradient}}+\frac{C_{D_{TO}}}{C_{L_{TO}}}\right)\sqrt{\frac{2}{\rho_{\text{SL}}C_{L_{TO}}}\frac{W}{S}}}{\eta_{P_{\text{max power}}}(N-1)}$ If $N = 2$: $c_{\text{gradient}} = 0.012$ If $N = 3$: $c_{\text{gradient}} = 0.015$ If $N = 4$: $c_{\text{gradient}} = 0.017$
EASA CS 25.119	$\left(\frac{\mathrm{P}_{\text{shaft,SL}}}{\mathrm{W}}\right)_{\text{CS25.119}} = \frac{\left(c_{\text{gradient}}+\frac{C_{D_{landing}}}{C_{L_{landing}}}\right)\sqrt{\frac{2}{\rho_{\text{SL}}C_{L_{landing}}}\frac{W}{S}}}{\eta_{P_{\text{max power}}}}$ $c_{\text{gradient}} = 0.032$
EASA CS 25.121a	$\left(\frac{\mathrm{P}_{\text{shaft,SL}}}{\mathrm{W}}\right)_{\text{CS25.121a}} = \frac{N\left(c_{\text{gradient}}+\frac{C_{D_{TO}}}{C_{L_{TO}}}\right)\sqrt{\frac{2}{\rho_{\text{SL}}C_{L_{TO}}}\frac{W}{S}}}{\eta_{P_{\text{max power}}}(N-1)}$ If $N = 2$: $c_{\text{gradient}} = 0.000$ If $N = 3$: $c_{\text{gradient}} = 0.003$
EASA CS 25.121b	$\left(\frac{\mathrm{P}_{\text{shaft,SL}}}{\mathrm{W}}\right)_{\text{CS25.121b}} = \frac{N\left(c_{\text{gradient}}+\frac{C_{D_{TO}}}{C_{L_{TO}}}\right)\sqrt{\frac{2}{\rho_{\text{SL}}C_{L_{TO}}}\frac{W}{S}}}{\eta_{P_{\text{max power}}}(N-1)}$ If $N = 2$: $c_{\text{gradient}} = 0.024$ If $N = 3$: $c_{\text{gradient}} = 0.027$ If $N = 4$: $c_{\text{gradient}} = 0.030$
EASA CS 25.121c	$\left(\frac{\mathrm{P}_{\text{shaft,SL}}}{\mathrm{W}}\right)_{\text{CS25.121c}} = \frac{N\left(c_{\text{gradient}}+\frac{C_{D_{cruise}}}{C_{L_{cruise}}}\right)\sqrt{\frac{2}{\rho_{\text{1500ft}}C_{L_{cruise}}}\frac{W}{S}}}{\eta_{P_{\text{max power}}}(N-1)}$ If $N = 2$: $c_{\text{gradient}} = 0.012$ If $N = 3$: $c_{\text{gradient}} = 0.015$ If $N = 4$: $c_{\text{gradient}} = 0.017$
EASA CS 25.121d	$\left(\frac{\mathrm{P}_{\text{shaft,SL}}}{\mathrm{W}}\right)_{\text{CS25.121d}} = \frac{N\left(c_{\text{gradient}}+\frac{C_{D_{landing}}}{C_{L_{landing}}}\right)\sqrt{\frac{2}{\rho_{\text{SL}}C_{L_{landing}}}\frac{W}{S}}}{\eta_{P_{\text{max power}}}(N-1)}$ If $N = 2$: $c_{\text{gradient}} = 0.021$ If $N = 3$: $c_{\text{gradient}} = 0.024$ If $N = 4$: $c_{\text{gradient}} = 0.027$

4.9.2. Energy Sizing

In the double-hybrid powertrain model [9], the mission analysis is carried out using a numerical methodology, in which the energy required for the design mission is estimated by dividing it into distinct flight segments. For short-duration segments such as taxiing, take-off, and landing, fixed energy fractions for each segment $(\mathrm{E_{Segment}}/\mathrm{E_{Total}})$ are assigned, which replace the fuel fraction values typically estimated in conventional preliminary aircraft design methods and also accounts for battery energy consumption (if any) during these phases.

For the remaining segments, such as climb and cruise, a dedicated mission analysis is performed for each segment individually through a quasi-steady approach. Each segment is divided into discrete time-steps Δt, during which the aircraft weight, thrust, propulsive power input, and aerodynamic coefficients are assumed to be constant. For each time-step of the considered segment, the fuel consumption (kerosene/LH_2/both) and the battery energy consumption (if defined) are computed as shown in Equation 4.136, where P_s is the power consumption during each time-step of the segment:

$$e_s = \mathrm{P_s} \cdot \Delta t \tag{4.136}$$

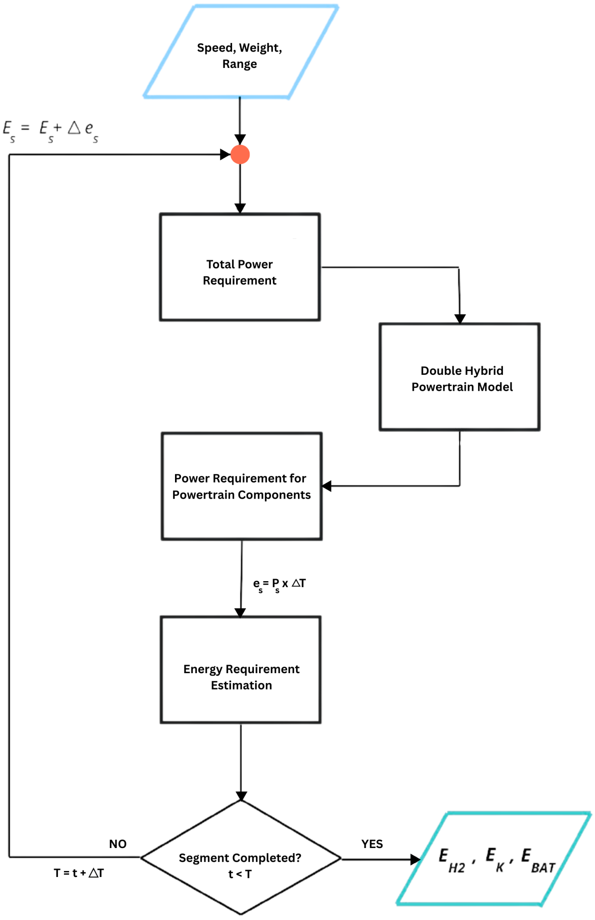

Figure 4.11: Segment Mission Analysis [9]

The mission analysis loop begins with initial estimates for the Take-off mass (TOM), Fuel type fraction (FTF), Fuel fraction (FF), and the Degree of hybridization (DOH) values (defined by Equations 4.137 and 4.138) for both the fuel and battery. It is important to note here that the value of the battery degree of hybridization $(\mathrm{DOH_{bat}})$ is zero in all cases, as the SOFC-GT and the conventional powertrain architectures (kerosene and LH_2-based) considered in this study do not use batteries as an additional source of energy.

$$\mathrm{DOH_{fuel}} = \frac{\mathrm{E_{H_2}}}{\mathrm{E_{H_2}} + \mathrm{E}_k} \tag{4.137}$$

$$\mathrm{DOH_{bat}} = \frac{\mathrm{E_{bat}}}{\mathrm{E_{bat}} + \mathrm{E_{H_2}} + \mathrm{E}_k} \tag{4.138}$$

The fuel-type fraction (FTF) is analogous to the fuel degree of hybridization $(\mathrm{DOH_{fuel}})$ in Equation 4.137 and the hydrogen power ratio (ϕ_2) of the double hybrid powertrain model (defined by Equation 2.42 in Section 2.4.4) in the absence of a battery, while the fuel fraction (FF) is defined as the ratio of the fuel mass $(\mathrm{M_{fuel}})$ to the take-off mass (TOM):

$$\mathrm{FTF} = \frac{\mathrm{M_{H_2}}}{\mathrm{M_{H_2}} + \mathrm{M}_k} \tag{4.139}$$

$$\mathrm{FF} = \frac{\mathrm{M_{H_2}} + \mathrm{M}_k}{\mathrm{TOM}} \tag{4.140}$$

The loop iterates until the error, defined as a function of the change in these variables between iterations, falls below a given convergence threshold. This error in the energy sizing loop is expressed as:

$$\mathrm{Err} = f\big([\mathrm{TOM_1} - \mathrm{TOM_0}] + [\mathrm{FTF_1} - \mathrm{FTF_0}] + [\mathrm{FF_1} - \mathrm{FF_0}] + [\mathrm{DOH_1} - \mathrm{DOH_0}]\big) \tag{4.141}$$

A schematic of this iterative process is presented below in Figure 4.13.

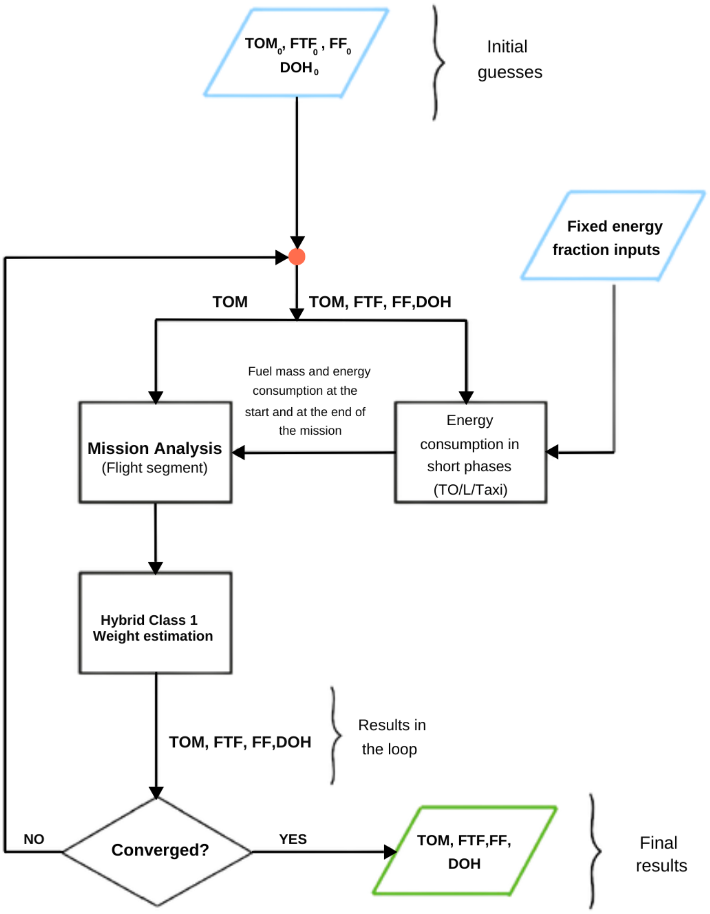

Figure 4.12: Mission Analysis Convergence Loop of the Double Hybrid Powertrain Model [9]

4.10. Class 1 Mass Estimation

This section presents the methodology for the Class-1 Weight estimation of hybrid-electric aircraft with SOFC-GT powertrains. Conventional methodologies of Operating Empty Weight (OEW) estimation for the preliminary design of aircraft are heavily reliant on statistical data, which is not available for hybrid-electric aircraft designs. This necessitates modifications to existing methodologies of Class 1 weight estimation for the preliminary sizing of aircraft that make unconventional powertrains like SOFC-GT hybrid configurations.

For conventional aircraft designs, the Operating Empty Mass (OEM) can be approximately estimated by Class 1 Sizing Methodologies using the following formulation presented by Torenbeek [83]:

$$\mathrm{OEM} = \mathrm{c_1 PL} + \mathrm{c_2 TOM} + \mathrm{c_3} \tag{4.142}$$

where,

- The first term $\mathrm{c_1}$,represents the body group weight, and consists of components directly influenced by cabin dimensions determined by the Maximum Payload (MPL). This includes structures such as the fuselage and vertical tail, as well as systems like air conditioning, pressurization, electrical and electronic systems, passenger accommodations, cabin furnishings, and operational items. The body group weight is primarily a function of the payload accommodation density (PAD), which is defined as the ratio of the MPL to the cabin floor area or volume.
- The second term $\mathrm{c_2}$ represents weight components that are directly related to the Maximum Take-off Mass (MTOM). These include components of the aircraft such as the wing, the horizontal tail, the landing gear, and the powerplant.
- Finally, the third term $\mathrm{c_3}$, accounts for the flight crew weight, inclusive of their accommodation. For a given aircraft category, this is normally considered to be independent of the payload and the take-off mass (TOM) [83].

A convenient method for estimating the Operating Empty Mass (OEM) in Class 1 Sizing Methods without defining seating configurations was proposed in the thesis of Alessandro Borgia [9]. Building on the $\mathrm{c_1}$, $\mathrm{c_2}$, and $\mathrm{c_3}$ values defined by Torenbeek for single-and double-aisle aircraft [83], Borgia introduced a payload-based classification, adding a new category for small commuter aircraft (CS-23) with payloads under 2 tonnes. The corresponding coefficients for each category are presented in the Table 4.8.

Table 4.8: Parameters for estimating the OEM, based on the payload mass of the aircraft [83][9]

Aircraft Class	**Payload (PL)**	$\mathrm{c_1}$	$\mathrm{c_2}$	$\mathrm{c_3}$	**Source**
Small Commuter (CS-23)	$\mathrm{PL} < 2$ t	1.15	0.19	250	Borgia [9]
Single Aisle	3 t $< \mathrm{PL} < 25.5$ t	1.25	0.20	500	Torenbeek [83]
Double Aisle	$\mathrm{PL} \geq 25.5$ t	1.50	0.20	600	Torenbeek [83]

The unity equation by Torenbeek [83] expresses the relation between the OEM, MPLM (Maximum Payload Mass), EM (Energy Mass), and the MTOM (Maximum Takeoff Mass) for an aircraft operating in its harmonic range (as defined by its TLARs, or Top Level Aircraft Requirements) and can be expressed by:

$$\frac{\mathrm{OEM}}{\mathrm{MTOM}} + \frac{\mathrm{MPLM}}{\mathrm{MTOM}} + \frac{\mathrm{EM}}{\mathrm{MTOM}} = 1 \tag{4.143}$$

Combining Equations 4.143 and 4.142, Wolleswinkel et. al. presented equations for estimating the OEM and the OEM/MTOM fraction for Class 1 Weight Estimation as defined by two primary TLARs: first, the MPLM defined by payload requirements, and second, the energy fraction (EM/MTOM) that is defined by the range requirements of the aircraft:

$$\mathrm{OEM_{estimate}} = \mathrm{c_1} + \frac{\mathrm{c_2}(1+\mathrm{c_1})}{1-\frac{\mathrm{EM}}{\mathrm{MTOM}}-\mathrm{c_2}} \cdot \mathrm{MPLM} + \frac{\mathrm{c_2 c_3}}{1-\frac{\mathrm{EM}}{\mathrm{MTOM}}} + \mathrm{c_3} \tag{4.144}$$

$$\frac{\mathrm{OEM}}{\mathrm{MTOM}} = \frac{(\mathrm{c_1}+\mathrm{c_2})\cdot \mathrm{MPLM} - \mathrm{c_1}\cdot \mathrm{MPLM}\cdot \frac{\mathrm{EM}}{\mathrm{MTOM}} + \mathrm{c_3}\left(1+\frac{\mathrm{EM}}{\mathrm{MTOM}}\right)}{(1+\mathrm{c_1})\cdot \mathrm{MPLM} + \mathrm{c_3}} \tag{4.145}$$

Equation 4.144 presents a fundamental modification to Torenbeek's method (given by Equation 4.142) for approximating the OEM of hybrid-electric/hydrogen-powered aircraft designs. It takes into account the reduced energy mass fraction when hydrogen is utilized as the primary energy carrier instead of kerosene-based jet fuel, thereby helping to avoid an overestimation of the aircraft OEM through conventional Class 1 weight estimation methods that do not integrally account for an energy mass fraction (EM/MTOM).

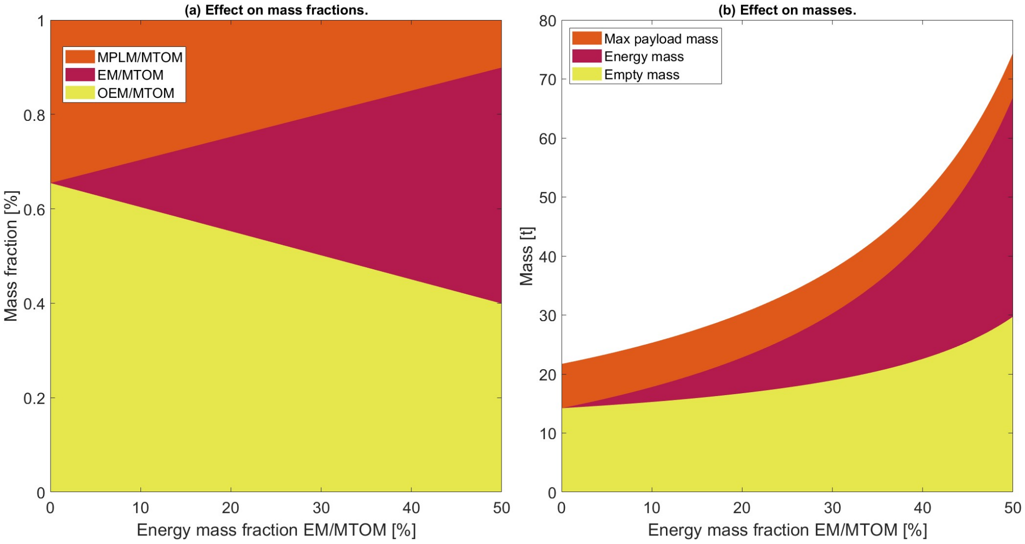
(a) Effect on mass fractions.

(b) Effect on masses.

Figure 4.13: Effect of $\mathrm{EM/MTOM}$ fraction on the mass breakdown of a single-aisle aircraft with MPLM = 7500 kg

Once the OEM is estimated using the energy mass fraction $\mathrm{EM/MTOM}$, it is first corrected by subtracting the mass of a reference gas turbine engine (estimated using the installed gas turbine thrust at sizing conditions) and the reference wing before adding the weights of the components of the SOFC-GT powertrain (SOFC stacks, heat exchangers, LH_2 management system including the integral LH_2 tank and pumps, supply lines for fuel and air, electrical components, gearbox, and the fuselage extensions to house both the LH_2 tanks and the SOFC stacks) and the actual wing weight. The corrected OEM of the SOFC-GT aircraft is estimated using Equation, as shown below:

$$\begin{aligned}\mathrm{OEM_{actual}} = \mathrm{OEM'} &+ \mathrm{M_{GT}} + \mathrm{M_{SOFC}} + \mathrm{M_{HX}} + \mathrm{M_{LH_2\ System}} \\ &+ \mathrm{M_{LH_2\ Tank}} + \mathrm{M_{Pneumatic\ System}} + \mathrm{M_{Fuselage\ Extensions}} \\ &+ \mathrm{M_{Electrical\ System}} + \mathrm{M_{Wing}}\end{aligned} \tag{4.146}$$

where,$\mathrm{OEM'}$ is the estimated OEM of the aircraft minus the mass of the reference wing and the powertrain, given by:

$$\mathrm{OEM'} = \mathrm{OEM_{estimate}} - \mathrm{M_{GT,ref}} - \mathrm{M_{Wing,ref}} \tag{4.147}$$

The mass of the reference gas turbine powertrain ($\mathrm{M_{GT,ref}}$) used in Equation 4.147 is estimated by considering an equivalent conventional gas turbine powertrain that provides the required amount of propulsive power for the aircraft in sizing conditions. The mass of one such conventional gas turbine engine is calculated as a function of the installed power, and then multiplied by the number of engines (N) (which is a top level aircraft requirement) before subtracting the total reference powertrain mass $(\mathrm{M}_{\mathrm{GT,ref}})$ from the estimated value of the OEM:

$$\mathrm{M}_{\mathrm{GT,ref}} = \mathrm{N} \times f\left(\frac{\mathrm{P}_{\mathrm{s1,sizing}}}{\mathrm{N}} \cdot \frac{1}{\eta_{\mathrm{gb}}}\right) \tag{4.148}$$

where η_{gb} represents the efficiency of the gearbox used in the powertrain.

The actual gas turbine mass is now estimated similarly as in Equation 4.149, but using the sizing power of the gas turbine instead of the primary shaft:

$$\mathrm{M}_{\mathrm{GT,actual}} = \mathrm{N} \times f\left(\frac{\mathrm{P}_{\mathrm{GT,sizing}}}{\mathrm{N}}\right) \tag{4.149}$$

The following simplified approximation is used by Torenbeek [84] to predict the wing mass for Class 1 Weight estimation methods. It is worth noting here that although the original approximation by Torenbeek is not directly applicable to engine-mounted wing configurations due to the absence of a correcting factor to account for the load alleviation due to the wing-mounted engine weight, a correction factor K_n has been applied in the approximation shown below to avoid an over-prediction of the wing weight.

$$\begin{aligned} M_{w,\mathrm{ref}} = \mathrm{K}_{\mathrm{comp}}\left(1+\mathrm{K}_s+\mathrm{K}_n+\mathrm{K}_{\mathrm{lg}}+\mathrm{K}_f\right) \cdot \Bigg[\mathrm{ZFM} \cdot 6.67 \times 10^{-3} \cdot b_{s,\mathrm{ref}}^{0.75} \\ \cdot \left(1+\sqrt{\frac{1.905}{b_{s,\mathrm{ref}}}}\right) \cdot n_{\mathrm{ult}}^{0.55} \cdot \left(\frac{b_{s,\mathrm{ref}}/t_{r,\mathrm{ref}}}{\mathrm{ZFM}/\mathrm{S}_{w,\mathrm{ref}}}\right)^{0.3}\Bigg] \end{aligned}$$

where the variable definitions used in this equation are as presented below:

- $\mathrm{K}_{\mathrm{comp}}$ — Correction factor accounting for composite materials used in the wing
- K_s — Correction factor for spoilers
- K_n — Correction factor for wing-mounted engines
- K_{lg} — Landing gear correction factor
- K_f — Correction for Fowler-type flaps
- ZFM — Zero fuel mass $[\mathrm{kg}]$
- $b_{s,\mathrm{ref}}$ — Corrected reference wing span, accounting for wing sweep $[\mathrm{m}]$
- $t_{r,\mathrm{ref}}$ — Reference root chord thickness $[\mathrm{m}]$
- $\mathrm{S}_{w,\mathrm{ref}}$ — Wing reference area $[\mathrm{m}^2]$
- n_{ult} — Ultimate load factor

The reference wing span $(b_{s,\mathrm{ref}})$ and the reference wing root thickness thickness $(t_{r,\mathrm{ref}})$ are estimated as shown in Table 4.9:

The actual wing mass can now be calculated through the Torenbeek's method, by simply substituting the actual wing span $(b_{s,\mathrm{actual}})$, wing area $(\mathrm{S}_{\mathrm{w,actual}})$, and the wing root thickness $(t_{r,\mathrm{actual}})$ as defined by the value of wing loading of the actual aircraft sized for minimum wing area:

$$\begin{aligned} \mathrm{M}_{\mathrm{wing}} = \mathrm{K}_{\mathrm{comp}}\left(1+\mathrm{K}_s+\mathrm{K}_n+\mathrm{K}_{\mathrm{lg}}+\mathrm{K}_f\right) \cdot \Bigg[\mathrm{ZFM} \cdot 6.67 \times 10^{-3} \cdot b_{s,\mathrm{actual}}^{0.75} \\ \cdot \left(1+\sqrt{\frac{1.905}{b_{s,\mathrm{actual}}}}\right) \cdot n_{\mathrm{ult}}^{0.55} \cdot \left(\frac{b_{s,\mathrm{actual}}/t_{r,\mathrm{actual}}}{\mathrm{ZFM}/\mathrm{S}_{w,\mathrm{actual}}}\right)^{0.3}\Bigg] \end{aligned}$$

Table 4.9: Estimation of reference wing parameters for use in Torenbeek's wing mass estimation method

Expression	**Description**	**Units**
$q_{\text{landing}} = \frac{1}{2}\,\rho_{\text{landing}}\,\mathrm{V}_{\text{stall}}^2$	Dynamic pressure	Pa
$(\mathrm{W/S})_{\text{ref}} = \dfrac{\mathrm{C}_{L,\max} \cdot q_{\text{landing}}}{\mathrm{M}_{\text{landing}}/\mathrm{MTOM}}$	Wing loading	$\mathrm{N/m^2}$
$\mathrm{S}_{w,\text{ref}} = \dfrac{\mathrm{MTOM} \cdot g}{(\mathrm{W/S})_{\text{ref}}}$	Wing reference area	$\mathrm{m^2}$
$b_{\text{ref}} = \sqrt{\mathrm{S}_{w,\text{ref}} \cdot \mathrm{AR}_{\text{wing}}}$	Wing span	m
$t_{r,\text{ref}} = \left(\dfrac{t}{c}\right) \cdot \dfrac{2 \cdot \sqrt{\mathrm{S}_{w,\text{ref}}/\mathrm{AR}_{\text{wing}}}}{1+\lambda}$	Root chord thickness	m
$b_{s,\text{ref}} = \dfrac{b_{\text{ref}}}{\cos\Lambda}$	Corrected wing span (for wing sweep)	m

As shown by equation 4.10, the mass of additional components need to be added to the value of OEM' in order to get the actual value of the aircraft operating empty weight. The Class 1 weight estimation methods for these components are presented below in subsequent sections.

4.10.1. SOFC Mass

The total mass of the SOFC stacks is calculated quite straightforwardly by multiplying the total number of stacks by the mass of a single SOFC stack, as shown below in Equation 4.150:

$$\mathrm{M}_{\mathrm{FC}} = n_{stacks} \times \mathrm{M}_{fc,stack} \tag{4.150}$$

where the mass of the SOFC system at the stack level can be expressed as the sum of the mass of the cells within a single stack, plus the masses of the cathode and anode current collectors:

$$\mathrm{M}_{\text{fc,stack}} = (n_{cells} \times \mathrm{M}_{\mathrm{SOFC}}) + 2\mathrm{M}_{\text{current collector}} \tag{4.151}$$

The mass of a single cell is estimated by taking into account the tubular geometry of the baseline SOFC used in this study. As previously discussed in Section 4.3.1, this baseline SOFC is a high power density (HPD) derivative of the Siemens Westinghouse cathode-supported tubular geometry, featuring concentric layers of the cathode substrate, electrolyte, and anode, along with the cell interconnect. The tubular geometry of this baseline SOFC allows for a rather straightforward estimation of the masses of its individual components, given the densities of the materials used in these layers are known. While the electrode and electrolyte layers are considered to be hollow cylinders, the geometry of the interconnect is approximated as a rectangular prism with a width of approximately $1/8^{th}$ of the outer cell diameter. The length of all layers is taken to be equal to the total length of the cell, and an overview of the volume estimation of individual layers is presented below:

$$V_{\text{anode}} = \pi \cdot \left(\mathrm{r}_{\text{cell,outer}}^2 - \mathrm{r}_{\text{anode}}^2\right) \cdot l_{\text{cell}} \tag{4.152}$$

$$V_{\text{electrolyte}} = \pi \cdot \left(\mathrm{r}_{\text{anode}}^2 - \mathrm{r}_{\text{electrolyte}}^2\right) \cdot l_{\text{cell}} \tag{4.153}$$

$$V_{\text{cathode}} = \pi \cdot \left(\mathrm{r}_{\text{electrolyte}}^2 - \mathrm{r}_{\text{cathode}}^2\right) \cdot l_{\text{cell}} \tag{4.154}$$

$$V_{\text{interconnect}} = \left(\frac{\pi \cdot l_{\text{cell}} \cdot \mathrm{d}_{\text{cell,outer}}}{8}\right) \cdot \mathrm{t}_{\text{interconnect}} \tag{4.155}$$

where the radii of the concentric electrode and electrolyte layers are calculated using known values of layer thicknesses and cell dimensions.

Once the volume of individual components are estimated, the masses can be estimated using the densities of the materials corresponding to the electrodes, electrolyte, and the interconnect layers. The masses of individual components are summed up to get the total mass of an individual SOFC:

$$\mathrm{M}_{\mathrm{SOFC}} = \sum_{i=1}^{n} \rho_i \, V_i \tag{4.156}$$

where i represents each component of the cell (electrodes, electrolyte, or interconnect) and ρ represents their individual densities. The thicknesses of each layer, the materials used, and their respective densities are summarized below in Table 4.10:

Table 4.10: Porosity-Adjusted Densities of SOFC Materials

Component	**Thickness** (μm)	**Material Used**	**Theoretical Density** (g/cm^3)	**Porosity** (%)	**Material Density** (g/cm^3)	**References**
Cathode	570	Ca/Ce-doped $LaMnO_3$	6.30	20	5.00	[4, 69]
Electrolyte	11	8YSZ or ScSZ	5.90	5	5.60	[58, 17, 57]
Anode	67	Ni–YSZ cermet	5.56	20	4.44	[95, 13]
Interconnect	110	Ca/Al-doped $LaCrO_3$	6.46	≤6	6.00	[46, 39]
Anode Current Collector	1000	Ni Foam	8.90	55	4.00	[3, 37]
Cathode Current Collector	1000	Porous LSM	6.50	37	4.10	[5, 73]

At the stack level, the additional mass of the current collectors plates for the anode and the cathode is estimated by considering a thickness of 1 mm for both current collector plates. The volume of the current collector plates is calculated using this thickness and the dimensions of the SOFC stack geometry chosen for this study (Refer to Section 4.3.1). The materials used as the current collectors, and their corresponding densities, are also presented in Table 4.10.

4.10.2. LH_2 Tank and Fuel Management System

In Class 1 weight estimation methods, the tank gravimetric density (GI) is an important design parameter that can be used to estimate the empty weight of the LH_2 tank. According to Mukhopadhya et. al., this can be defined as the ratio of the LH_2 fuel mass contained in the tank, to the combined mass of the LH_2 fuel and the tank [65]:

$$\mathrm{GI}_{\mathrm{LH_2,\,tank}} = \frac{m_{\mathrm{LH_2}}}{m_{\mathrm{LH_2}} + m_{\mathrm{tank}}} \tag{4.157}$$

Using this definition of the tank gravimetric density (as presented in Equation 4.157), the empty mass of the LH_2 tank can now be estimated as shown below in Equation 4.158; where a conservative value of the LH_2 tank gravimetric density (0.42) is chosen from the range of values proposed by Montellano in his thesis [64]:

$$\mathrm{M}_{\mathrm{LH_2,\,tank}} = \frac{1 - \mathrm{GI}_{\mathrm{LH_2,\,tank}}}{\mathrm{GI}_{\mathrm{LH_2,\,tank}}} \tag{4.158}$$

The mass of the LH_2 management system can be estimated by considering the masses of the LH_2 pumps, valves, tank refuel system, tank venting (safety) system, and the length of the fuel supply lines used in the powertrain architecture. For the chosen SOFC-GT architecture in this study, three LH_2 boost pumps (for the main LH_2 line) and two LH_2 high-pressure pumps for the SOFC LH_2 line (one per engine, to pressurize the LH_2 to stack operating pressure) are considered, along with 156 m of main LH_2 supply lines from the LH_2 tank [31], and an additional line length of 0.5 m/stack to account for the increased fuel line length in an SOFC-GT system. The masses of the LH_2 pumps have been estimated according to the work of Brewer [10], who used a sizing characteristic based on fuel mass flow rates. For SOFC-GT systems, the additional valve mass is assumed to be 25% more than Brewer's predictions of valve mass for LH_2-based propulsion systems (6.7 kg/engine), while the mass of the tank venting and refuel systems is considered to be constant with tank size, as per the assumptions of Garcia [31].

An overview of the sizing characteristics used for the LH_2 management system is presented in Table 4.11:

Table 4.11: Sizing characteristics of LH_2 fuel system components for Class 1 Mass Estimation

Component	Number	Sizing Characteristic	Source
LH_2 Boost Pump	3	$3 \times 524.4\,\mathrm{kg\,(kg/s)^{-1}\,LH_2}$	[10] [31]
LH_2 High Pressure Pump	2	$2 \times 542.2\,\mathrm{kg\,(kg/s)^{-1}\,LH_2}$	[10] [31]
LH_2 Supply Lines	Conventional LH_2 Powertrain: 156 m SOFC-GT Powertrain: $156 + 0.5 \times n_{\mathrm{stacks}}$	$1.5\,\mathrm{kg/m}$	[31]
Fuel Supply Valves	NA	Conventional LH_2 Powertrain: $6.7\,\mathrm{kg/engine}$ SOFC-GT Powertrain: $1.25 \times 6.7\,\mathrm{kg/engine}$	[10] [31]
Tank Refuel System	1	$82\,\mathrm{kg}$ (constant with tank size)	[31]
Tank Venting and Safety System	1	$66\,\mathrm{kg}$ (constant with tank size)	[31]

4.10.3. Heat Exchangers, Air Supply, and Exhaust Management Systems

The mass of the air supply and exhaust gas lines connecting the gas turbine engine to the preheat heat exchangers (for both air and fuel heating before the SOFC stacks) is estimated analogously to that of the LH_2 supply lines. For the SOFC-GT powertrain, the total line length needed for high-pressure air supply to the stacks and exhaust gas supply to the preheaters scales with the number of stacks (assumed based on the author's own elaboration at 1.5 m/stack and 0.75 m/stack for the high pressure lines and exhaust gas lines respectively), and a rather conservative value for the mass/unit length is considered at 1 kg/m for both air supply/exhaust gas lines. This is in alignment with industry-grade values for high-pressure pneumatic supply lines, where the values for lightweight polymeric hoses used for aerospace applications (e.g., polyurethane or PTFE-lined) typically range from 0.15 to 1.5 kg/m [68].

The mass estimation for the heat exchangers which pre-heat the air and fuel for the SOFC stacks scales with the total area of heat transfer $\mathrm{A_{HX}}$ (calculated using the effectiveness-NTU method, discussed in Section 4.7), using a gravimetric index ($\mathrm{kg/m^2}$). Therefore, the mass of the heat exchangers used in the SOFC-GT powertrain can be expressed as shown below in Equation 4.159:

$$\mathrm{M_{HX}} = \mathrm{A_{HX}} \times \mathrm{GI_{HX}} \tag{4.159}$$

The temperature range of heat exchanger operation influences the type of material that can be used for the preheaters. Considering a plate thickness of 0.4 mm for the preheaters and the operational temperature range, the gravimetric index also changes according to the type of material used, as shown in Table 4.12. In this study, three types of materials are primarily considered for preheater design based on the inlet temperature of the hot side ($\mathrm{T_{h,in}}$) namely, Inconel 625 for $\mathrm{T_{h,in}} > 1400\mathrm{K}$, Silicon Carbide for $700\mathrm{K} < \mathrm{T_{h,in}} < 1400\mathrm{K}$, and Brazed Aluminum for $\mathrm{T_{h,in}} < 700\mathrm{K}$. Although Ni-based alloys such as Inconel 625 offer significant limitations, such as a reduced gravimetric index and low thermal conductivities, they are preferred due to their high resistance to oxidation, thermal fatigue, and creep for temperatures greater than 1400 K [71]. On the other hand, high-temperature ceramics such as SiC mitigate the disadvantages of Ni-based alloys by offering high thermal conductivities and reasonable gravimetric density along with high-temperature strength, excellent oxidation resistance, minimal high-temperature creep, and thermal shock resistance, making them ideal candidates for the design of compact plate and fin heat exchangers (PFHEs) up to a temperature of 1400 K [79]. The thermal conductivities of the different materials listed below in Table 4.12 are used to calculate the overall heat transfer coefficient U through the fin efficiencies, as explained earlier in Section 4.7.

Table 4.12: Heat exchanger material selection based on inlet temperature range

Material	Temperature Range ($\mathrm{T_{hin}}$) [K]	$\mathrm{GI_{HX}}$ [kg/m^2]	Density [kg/m^3]	Thermal Conductivity [W/mK]	Source
Inconel 625	$\mathrm{T_{hin}} > 1400\,\mathrm{K}$	3.376	8440	20	[35]
Silicon Carbide	$700 < \mathrm{T_{hin}} \leq 1400\,\mathrm{K}$	1.284	3210	100	[50] [33]
Brazed Aluminum	$\mathrm{T_{hin}} \leq 700\,\mathrm{K}$	1.080	2160	237	[59] [76]

4.10.4. Fuselage Extensions for $\mathrm{LH_2}$ Tanks and SOFC Stacks

Following from the estimation of LH_2 tank mass, it is also necessary to correct the value of the operating empty weight minus the reference wing and powertrain (OEM', described by Equation 4.147) for the additional mass of the fuselage extension which would be required to house the integral LH_2 fuel tank considered in this study. This is shown by Equation 4.160, where η_{tank} is a parameter that accounts for the gap between the tank wall and the fuselage skin, while $\mathrm{V}_{\mathrm{venting}}$ accounts for the additional volume of the tank for LH_2 boil-off and safe venting volume. Overall, a 10% additional fuselage volume is considered, taking into account both venting requirements and tank integration within the fuselage.

$$\mathrm{V}_{\mathrm{Fuselage,H_2}} = \frac{M_{\mathrm{H_2,\,total}}}{\rho_{\mathrm{LH_2}}} \cdot \mathrm{V}_{\mathrm{venting}} \cdot \frac{1}{\eta_{\mathrm{tank}}} \tag{4.160}$$

Assuming the geometry of the fuselage extension to be perfectly cylindrical, the length of the fuselage can now be derived using Equation 4.161:

$$l_{\mathrm{fuselage,H_2\ tank}} = \frac{\mathrm{V}_{\mathrm{H_2}}}{\pi \left(\frac{D_{\mathrm{fuselage}}}{2}\right)^2} \tag{4.161}$$

where, the diameter of the fuselage (D_{fuselage}) and the mass per unit length of the fuselage ($\mathrm{M}_{\mathrm{fuselage}}/\mathrm{m}$) can be estimated in Class 1 Sizing Methods as a function of the payload mass, according to Borgia [9] as shown in Table 4.13:

Table 4.13: Fuselage diameter and structural weight per meter as a function of payload

Payload Mass (PLM) [t]	Fuselage Diameter [m]	$\mathrm{M}_{\mathrm{fuselage}}/\mathrm{m}$ [kg/m]
$\mathrm{PLM} \leq 9.5$	2.8	350
$9.5 < \mathrm{PLM} \leq 25$	4.0	450
$\mathrm{PLM} > 25$	6.0	600

The mass of the fuselage extension due to the integral LH_2 tank can now be estimated as:

$$\mathrm{M}_{\mathrm{Fuselage,H_2}} = l_{\mathrm{fuselage,H_2\ tank}} \times \mathrm{M}_{\mathrm{fuselage}}/\mathrm{m} \tag{4.162}$$

Similarly, the volume of the SOFC stacks in the SOFC-GT powertrain can also be accommodated within a cylindrical fuselage extension. The total volume occupied by the SOFC stacks is first calculated using the sized number of stacks and the volume occupied by a single SOFC stack, as shown below in Equation 4.163:

$$\mathrm{V}_{\mathrm{SOFC,total}} = \mathrm{V}_{\mathrm{SOFC,stack}} \times n_{\mathrm{stacks}} \tag{4.163}$$

where, the volume of a single SOFC stack ($\mathrm{V}_{\mathrm{SOFC,stack}}$) is calculated using the dimensions of the SOFC stack considered in this study (Refer to Section 4.3.1, as shown below:

$$l_{\mathrm{SOFC,stack}} = l_{\mathrm{SOFC}} \tag{4.164}$$

$$t_{\mathrm{SOFC,stack}} = 12 \times d_{\mathrm{cell,outer}} \tag{4.165}$$

$$b_{\mathrm{SOFC,stack}} = 8 \times d_{\mathrm{cell,outer}} \tag{4.166}$$

$$V_{\mathrm{SOFC,stack}} = l_{\mathrm{SOFC,stack}} \times t_{\mathrm{SOFC,stack}} \times b_{\mathrm{SOFC,stack}} \tag{4.167}$$

and the additional length of the cylindrical fuselage required to accommodate the total volume of the SOFC stacks is given by:

$$l_{\text{fuselage,SOFC}} = \frac{V_{\text{SOFC,total}} \times 1.05}{\pi \left(\frac{D_{\text{fuselage}}}{2}\right)^2} \tag{4.168}$$

where a factor of 1.05 for an additional 5% of SOFC volume is considered to account for packing efficiency and the volume of electrical cabling, and the required amount of tubing (fuel and pneumatic).

Finally, the mass of the fuselage extension to accommodate the SOFC stacks can be calculated by:

$$\mathrm{M}_{\text{Fuselage,SOFC}} = l_{\text{fuselage,SOFC}} \times \mathrm{M}_{\text{fuselage}}/\mathrm{m} \tag{4.169}$$

4.10.5. Electrical System Mass

The mass of the electrical system is estimated by accounting for both the mass of the electric motor that converts the electrical power output from the SOFC stacks into mechanical power via a gearbox, as well as the mass of the power management and distribution system (PMAD). As mentioned previously in Section 2.2, the PMAD consists of power converters, transformers, and smaller electrical elements that are not modeled in the Series-Parallel Partial Hybrid (SPPH) architecture [19] in the Double-Hybrid Powertrain Model [9]. As such, in this study, the mass breakdown of the PMAD is rather simplified by only accounting for the masses of the inverters and the DC-DC converters that regulate the electrical power output from the SOFC stacks. The sizing approximation for inverters and DC-DC converters suggested by Brewer [10] is used for this, which uses gravimetric power indices (in $\mathrm{kW/kg}$) of 2.5 kW/kg and 9.8 kW/kg for the DC-DC converters and the inverters, respectively. By knowing the maximum power output (sizing condition) from the SOFC stacks and the gravimetric densities of PMAD components, the mass of the PMAD can now be estimated as shown below in Equation 4.170:

$$\begin{aligned} \mathrm{M}_{\text{PMAD}} &= \mathrm{M}_{\text{DC converter}} + \mathrm{M}_{\text{inverter}} \\ &= \frac{\mathrm{P}_{\text{FC,sizing}}}{\mathrm{GI}_{\text{DC converter}}} + \frac{\mathrm{P}_{\text{FC,sizing}}}{\mathrm{GI}_{\text{inverter}}} \\ &= \mathrm{P}_{\text{FC,sizing}} \left(\frac{1}{\mathrm{GI}_{\text{DC converter}}} + \frac{1}{\mathrm{GI}_{\text{inverter}}} \right) \end{aligned} \tag{4.170}$$

The mass of the electric motor that couples the SOFC stacks to the primary powertrain via a gearbox is estimated as a function of the sizing power of the primary electrical machine (P_{EM1}). The mass of one electrical motor is calculated and then multiplied by the number of engines (N), to get the total mass of the electrical motors:

$$\mathrm{M}_{\text{EM1}} = \mathrm{N} \times f\left(\frac{\mathrm{P}_{\text{EM1,sizing}}}{\mathrm{N}}\right) \tag{4.171}$$

Finally, the total mass of the electrical system is calculated by adding the masses of the PMAD and the primary electrical motors, as shown below:

$$\mathrm{M}_{\text{Electrical System}} = \mathrm{M}_{\text{EM1}} + \mathrm{M}_{\text{PMAD}} \tag{4.172}$$

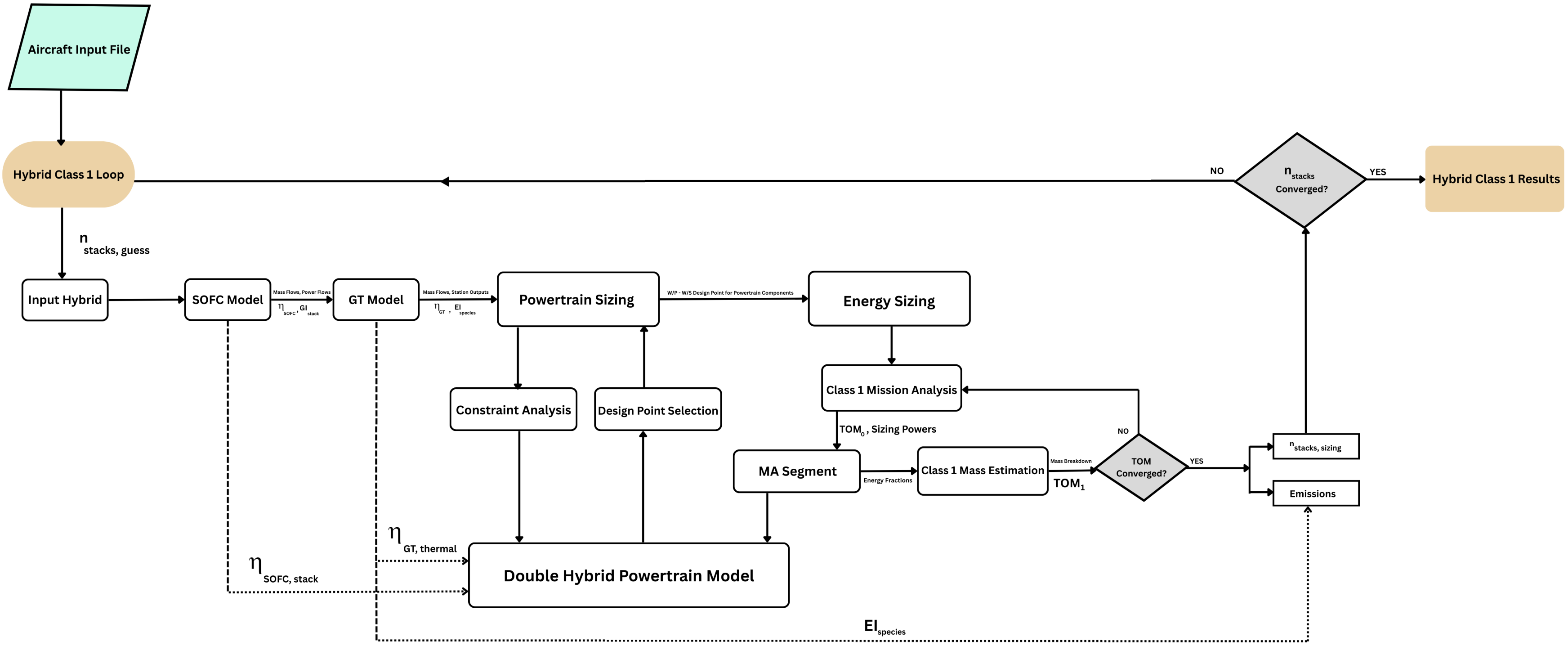

Figure 4.14: A schematic of the Hybrid Class 1 Sizing Loop of the Aircraft Design Initiator for SOFC-GT Powertrains

4.11. Emissions Estimation Methodology

4.11.1. Emissions through Kerosene Combustion

The combustion of kerosene in the presence of air leads to the formation of various chemical species, which can be broadly classified into two categories: those whose emissions are proportional to the amount of fuel consumed, and those that are non-proportional to it.

The proportional emissions include:

- Carbon dioxide (CO_2)
- Water vapor (H_2O)
- Sulphur oxides (SO_x)

These species arise directly from the stoichiometric combustion of fuel and therefore scale linearly with fuel flow across all phases of flight.

On the other hand, the non-proportional emissions, including nitric oxides (NO_x), carbon monoxide (CO), and unburnt hydrocarbons (HC), are not directly tied to fuel flow:

- NO_x emissions originate from the thermal fixation of atmospheric nitrogen (N_2) in the high temperature environment of the combustion chamber. Their formation is highly sensitive to the local temperature and pressure, particularly within the primary combustion zone.
- CO and HC emissions, on the other hand, primarily result from incomplete combustion and their levels are inversely proportional to the combustion efficiency. Since combustion efficiency generally increases with engine thrust (especially under sea-level static conditions), the emission indices (EI) for CO and HC typically decrease with increasing fuel flow.

The **Emission Index (EI)** is defined as the mass of a given pollutant emitted per unit mass of fuel burned, and is commonly expressed in grams per kilogram of fuel ($\mathrm{g/kg}$). For simplicity, the total emissions for the entire duration of flight are estimated based on the emission indices of proportional and non-proportional species during cruise flight only.

Table 4.14 presents the averaged EI values for the proportional species under standard conditions, assuming complete stoichiometric combustion of jet fuel. However, for the purpose of this study, a slightly lower averaged value for $\mathrm{EI_{CO_2}}$ is assumed. This accounts for the fact that combustion during cruise is not always perfectly stoichiometric ($\phi \neq 1$), and some fraction of the carbon in the jet fuel is converted to CO rather than fully oxidized to CO_2. The emissions data for the PW127F engine used on the ATR 72-600 (refer to Table 4.17) show some amount of CO (one of the non-proportional species) being produced in cruise conditions, thereby supporting the previous assumption of non-stoichiometric combustion of kerosene-based jet fuel during cruise.

Table 4.14: Emission Indices for proportional chemical emissions [55][23] [45]

Species	EI CO_2 (g/kg)	EI H_2O (g/kg)	EI SO_x (g/kg)
Value	3160	1240	0.06

Table 4.15 outlines the ICAO standard Landing and Take-Off (LTO) cycle modes, each associated with a representative thrust setting and mode duration. These values apply to uninstalled turbofan and turbojet engines.

Table 4.15: ICAO LTO Cycle operating modes [45]

Mode	Thrust Setting (%)	Duration (min)
Take-Off	100	0.7
Climb-Out	85	2.2
Approach	30	4.0
Idle	7	22.0

4.11.2. Hydrogen Emissions

The emissions resulting from hydrogen combustion differ significantly from those produced by kerosene combustion, particularly due to hydrogen's higher flame temperature and lower heating value (LHV). According to Funke et.al. [26], hydrogen combustion involves no carbon species, thereby eliminating emissions of CO_2, CO, unburnt hydrocarbons (HC), and soot. Additionally, due to the absence of aromatic compounds in hydrogen, the formation of SO_x is also prevented.

The representative combustion reaction for hydrogen in air can be written as:

$$\mathrm{H_2} + \frac{a}{2}(\mathrm{O_2} + z\mathrm{N_2}) \rightarrow \mathrm{H_2O} + \frac{(a-1)}{2}\mathrm{O_2} + \frac{az}{2}\mathrm{N_2} \tag{4.173}$$

As a result, hydrogen combustion leads to increased emissions of both water vapour (H_2O) and nitric oxides (NO_x) per kilogram of fuel burned, when compared to conventional kerosene-based fuels.

Fuel Cell Emissions

For hydrogen fuel cells, the estimation of emissions is more straightforward. In the electrochemical reaction between H_2 and O_2, water is the only product of a stoichiometric reaction. Therefore, no emissions of NO_x or any other pollutant species occur under ideal stoichiometric conditions.

The emission indices (EI) for H_2O resulting from hydrogen combustion and hydrogen utilization in SOFCs at stoichiometric conditions are similar at 9000 $\mathrm{g/kg}$, as the number of moles of the reacting H_2 and produced H_2O are the same, from a balanced chemical reaction.

NO_x Emissions from Hydrogen Combustion

To estimate NO_x emissions from hydrogen combustion, Funke et.al. [26] suggests applying a correction factor of approximately +30% relative to the NO_x emissions from kerosene combustion. Therefore, a preliminary estimation of NO_x emissions for hydrogen combustion can be expressed as:

$$\mathrm{EI}_{\mathrm{NO_x}}^{(\mathrm{H_2})} = 1.3 \cdot \mathrm{EI}_{\mathrm{NO_x}}^{(\mathrm{kerosene,BFFM2})} \tag{4.174}$$

Here, $\mathrm{EI}_{\mathrm{NO_x}}^{(\mathrm{kerosene,BFFM2})}$ represents the NO_x emission index derived using the Boeing Fuel Flow Method 2 (BFFM2) for kerosene.

4.11.3. Boeing Fuel Flow Method 2

This section explains the **Boeing Fuel Flow Method 2 (BFFM2)** [21], a semi-empirical method used to estimate emission indices (EI) under cruise and climb conditions based on values measured at sea level during the ICAO Landing and Take-Off (LTO) cycle (refer to Table 4.15). The method accounts for variations in engine fuel flow, ambient pressure and temperature, and flight Mach number.

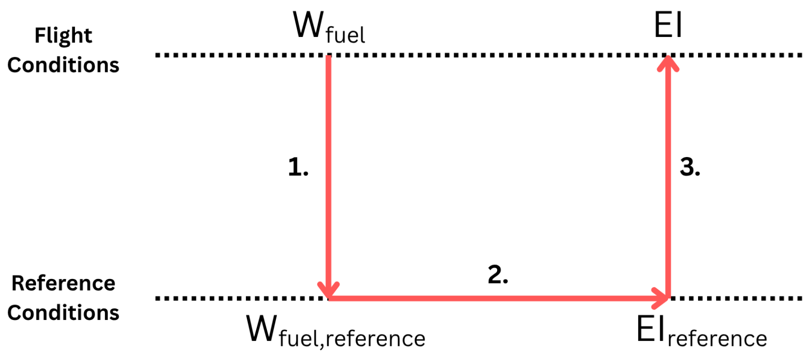

Figure 4.15: A schematic of the Boeing Fuel Flow Method 2 [21]

The method involves three main steps:

1. **Adjustment of fuel flow to reference conditions:**
   The actual engine fuel flow (known/computed value) during a flight phase (e.g. cruise), W_f, is corrected to a reference condition fuel flow factor, W_{ff}, as follows:

$$W_{ff} = \frac{W_f \cdot \theta^{3.8} \cdot e^{0.2M^2}}{\delta} \tag{4.175}$$

   where:

   - $\theta = T/T_{\text{SL}}$ is the ambient-to-sea-level temperature ratio,
   - $\delta = P/P_{\text{SL}}$ is the ambient-to-sea-level pressure ratio,
   - M is the Mach number.

2. **Application of engine installation correction factor:**
   Boeing recommends using a correction factor r to adjust the reference emission indices from the ICAO database to account for installation effects such as bleed air extraction. These correction factors are thrust-mode dependent and are shown in Table 4.16.

Table 4.16: Correction factors applied to thrust settings (as per BFFM2)

Operating Mode	Take-Off	Climb-Out	Approach	Idle
Correction Factor r	1.010	1.013	1.020	1.100

3. **Conversion of reference emission indices to in-flight values:**
   Once the corrected reference values are available, the emission indices for in-flight conditions are estimated using the following relations:

$$\text{EI}_{\text{CO}} = \text{EI}_{\text{CO,ref}} \cdot \frac{\theta^{3.3}}{\delta^{1.02}} \tag{4.176}$$

$$\text{EI}_{\text{HC}} = \text{EI}_{\text{HC,ref}} \cdot \frac{\theta^{3.3}}{\delta^{1.02}} \tag{4.177}$$

$$\text{EI}_{\text{NO}_x} = \frac{\text{EI}_{\text{NO}_x\text{,ref}}}{r} \cdot \frac{1}{\delta^{1.02} \cdot \theta^{3.3}} \cdot e^H \tag{4.178}$$

   The term H is a correction factor for humidity and is computed as:

$$\begin{aligned} \beta &= 7.90298(1-\tau) + 3.00571 + 5.02808\log_{10}(\tau) \\ &\quad + (1.3816 \times 10^{-7})\left[1 - 10^{11.344(1-1/\tau)}\right] \\ &\quad + (8.1328 \times 10^{-3})\left[10^{3.49149(1-\tau)} - 1\right] && (4.179) \\ P_v &= 0.014504 \cdot 10^{\beta} && (4.180) \\ \omega &= \frac{0.62197058 \cdot \phi \cdot P_v}{P_{\text{amb}} - \phi \cdot P_v} && (4.181) \\ H &= -19(\omega - 0.00634) && (4.182) \end{aligned}$$

   where:

   - $\tau = T_{\text{amb}}/T_{\text{std}}$ is the temperature ratio,
   - P_v is the vapour pressure (valid for $0.6 < P_v < 0.75$),
   - ϕ is the relative humidity,
   - P_{amb} is the ambient pressure,
   - ω is the humidity ratio (kg water/kg dry air).

These relations enable the estimation of non-proportional emissions (CO, HC, and NO_x) for cruise and climb conditions, using only LTO data, corrected fuel flow, and environmental parameters.

4.12. Emission Indices of Non-Proportional Species

Table 4.17 presents the emission indices for non-proportional species (NO_x, CO, and unburnt hydrocarbons) which are emitted during the combustion of kerosene-based jet fuel in the PW127F engine during different phases of flight. The fuel flows corresponding to the emission indices of these species during various engine operating conditions (Take-off, Climb-Out, Approach, and Idle) is used to estimate the emission indices for the fuel flow in cruise (for kerosene, H_2 combustion, and the SOFC-GT) by using the Boeing Fuel Flow Method 2 (BFFM2) described previously in Section 4.15.

Table 4.17: PW127F engine gaseous emissions [7]

Mode	Power Setting (%)	SHP	Fuel Flow (kg/min)	EI CO (g/kg)	EI UHC (g/kg)	EI NO_x (g/kg)
Min. flight idle	3	27	1.58	26.3	3.8	4.5
Min. ground idle	45	1.32	36.6	16.5	4.1	
Nominal idle	7	192	3.06	9.2	0	6.9
Approach	30	825	5.15	3.7	0	9.8
Max cruise	78	2132	8.28	2.2	0	15.6
Max climb	80	2192	8.38	2.0	0	16.2
Max continuous	90	2475	9.22	2.0	0	16.5
Take-off	100	2750	9.90	2.0	0	17.7

It is worth noting that for the architecture of the SOFC-GT powertrain chosen for this study, Equation 4.174 does not hold true for the estimation of NO_x emissions through the Boeing Fuel Flow Method (BFFM2), due to the presence of steam (a product of the electrochemical reaction between H_2 and O_2 in the SOFC stacks) in the combustion chamber (refer to Section 4.6). For conditions close to stoichiometry and high water loading (approximately 10% by mass), the presence of steam in the combustion chamber can lead to a reduction of approximately 50% in NO_x emissions [15]. It was therefore deemed necessary to include a simple combustion model to account for the reduction in the emission index of NO_x due to the presence of steam in the combustion chamber.

The emission indices for water and NO_x for hydrogen combustion, including the steam that exits the SOFC stacks, are estimated by knowing the mass fractions of steam and (NO_x in the combustion product ($\mathrm{Y_{H_2O,\,exhaust}}$ and $\mathrm{Y_{NOx}}$), along with the fuel mass flows into the SOFC stacks and the combustion chamber. The mass fraction of the species within the combustion product is a function of the combustor operating conditions, namely, the adiabatic flame temperature ($\mathrm{T_{adiabatic}}$), the combustor operating pressure ($\mathrm{P_{comb}}$), the equivalence ratio (Φ), and the ratio of the steam exiting the SOFC stacks to the total mass flow of the air and fuel within the combustion chamber. These mass fractions are determined using the GRI-30 combustion mechanism in CANTERA, and are also used in the computation of exhaust gas properties ($\mathrm{c_p}$ and γ_g) for the gas turbine thermodynamic cycle analysis calculations, which were discussed previously in Section 4.6.3.

The emission indices of water and NO_x in the exhaust gases exiting the combustion chamber (in $\mathrm{g/kg}$) can therefore be estimated as shown below:

$$\mathrm{EI_{H_2O}} = \frac{\dot{m}_{\mathrm{H_2O,\,exhaust}} \times 10^3}{\dot{m}_{\mathrm{fb}} + \dot{m}_{\mathrm{H_2,fc}}} \tag{4.183}$$

$$\mathrm{EI_{NOx}} = \frac{\dot{m}_{\mathrm{NOx}} \times 10^3}{\dot{m}_{\mathrm{fb}} + \dot{m}_{\mathrm{fu}}} \tag{4.184}$$

where,

$$\dot{m}_{\mathrm{H_2O,\,exhaust}} = \mathrm{Y_{H_2O,\,exhaust}} \times \dot{m}_7 \tag{4.185}$$

$$\dot{m}_{\mathrm{NOx}} = \mathrm{Y_{NOx}} \times \dot{m}_7 \tag{4.186}$$

5

Verification and Validation

This chapter presents the results of the Class 1 Sizing Loop of the Aircraft Design Initiator for three different powertrains: a. the conventional ATR 72-600 aircraft with a kerosene-based powertrain, b. a modified aircraft with the top-level aircraft requirements (TLAR) of the ATR 72-600 and a LH_2 powertrain, and finally, c. a modified aircraft with the top-level aircraft requirements (TLAR) of the ATR 72-600 and a SOFC-GT powertrain. It begins by first validating the results of the 0-D SOFC electrochemical model and the SOFC-GT powertrain model against experimental data available from literature, and proposes modifications at the SOFC level for better agreement with experimental data at different operating conditions. A comparison of the Class 1 sizing results for the ATR 72-600 aircraft with the conventional kerosene-based powertrain follows, after which, the Class 1 sizing results for a modified aircraft (with similar TLAR as the ATR 72-600) but with different LH_2-based powertrains are presented and compared against the baseline aircraft for changes in aircraft weights, thermal efficiencies and environmental impact.

5.1. Fuel Cell Model

5.1.1. Verification of the 0-D electrochemical model

In this section, the results of the 0-D SOFC electrochemical model that is implemented in the Class 1 hybrid sizing loop of the Aircraft Design Initiator (refer to Section 4.2) are presented. These results are first compared to those of two SOFC models in literature that operate under similar conditions. Going ahead, the trends of different SOFC operating parameters(operating voltage, stack power, and net stack power) across a range of current densities are compared to the trends (experimental and theoretical) observed in literature.

Table 5.1: Reference SOFC Operating Conditions

Operating Condition	Unit	Value
SOFC Temperature	°C	900
Cathode Inlet Pressure	atm	4.5
Fuel Utilization	%	75
Air Stoichiometric Ratio (anode excess air)	–	4.0
Anode H_2 Composition	%	97

The SOFC operating conditions chosen for comparison against the outputs of the SOFC model by Freeh et.al. [25] and Wilson et.al. [91] (operated under the same conditions) are presented below in Table 5.1; where the reference SOFC chosen for comparison is the Siemens Westinghouse Tubular SOFC, more about which is explained in Section 4.3.1. The SOFC model adopted by Freeh et.al. was developed within the NPSS (Numerical Propulsion Systems Simulation) environment of NASA, and is a steady-state zero-dimensional thermodynamic analysis code that uses JANNAF/CEA thermodynamic databases, while the model adopted by Wilson et.al. [91] is developed in ProMax. The comparison of the SOFC model outputs from the Class 1 hybrid sizing loop of the Aircraft Design Initiator with the model outputs of Freeh et.al. [25] and Wilson et.al. [91] is presented in Table 5.3.

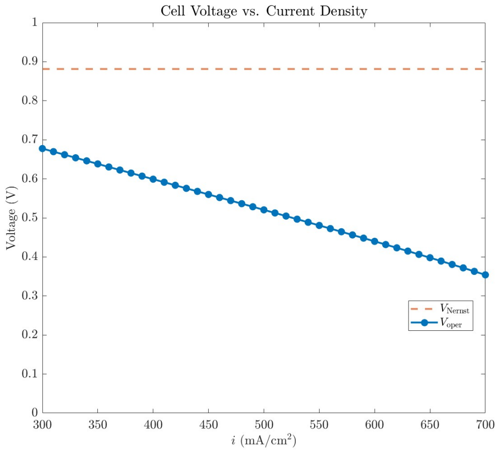

(a) Voltage v/s Current Density Curve

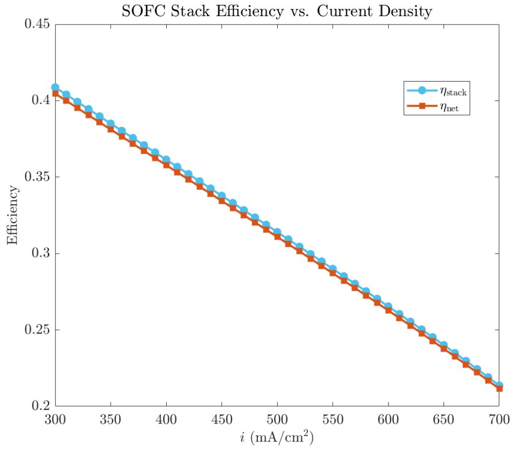

(b) Variation of Stack-level Thermal Efficiency ($\eta_{\text{fc,thermal}}$) with Current Density i

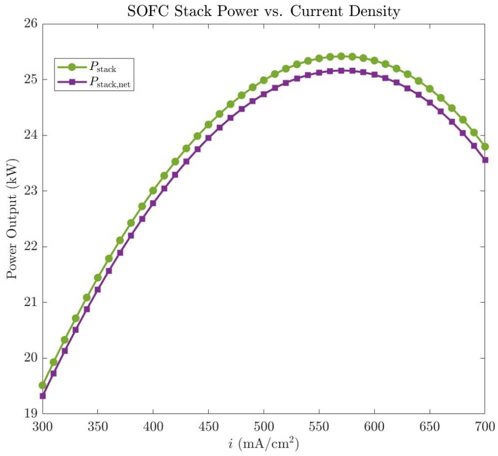

(c) SOFC Power Output ($\mathrm{P_{fc}}$) v/s Current Density Curve

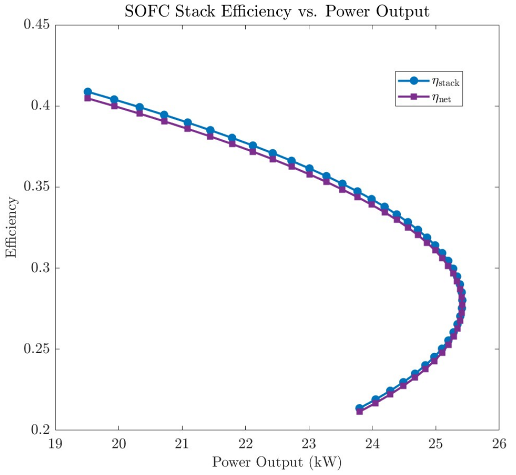

(d) Variation of Stack-level Thermal Efficiency ($\eta_{\text{fc,thermal}}$) with SOFC Power Output ($\mathrm{P_{fc}}$)

The electrochemical parameters of the reference SOFC under these operating conditions are presented in Table 5.2:

Table 5.2: Electrochemical Parameters of the Siemens Westinghouse Tubular SOFC at the operating conditions presented in Table 5.1

Parameter	Symbol	Unit	Value	Source
Exchange Current Density	i_0	mA/cm^2	300	[25]
Internal Current Density	i_n	mA/cm^2	2	[25]
Charge Transfer Coefficient	α	–	1.38	[25]
Limiting Current Density	i_L	mA/cm^2	900	[25]
Bulk Internal ASR	r	Ω/cm^2	0.605	Derived from [27]

Table 5.3: Comparison of SOFC Model Output with Literature Values

Parameter	Symbol	Unit	Model Output	Freeh et al.	% Diff.	Wilson et al.	% Diff.
Nernst Voltage	V_{Nernst}	V	0.886	0.878	0.91	0.876	1.14
Operating Voltage	$V_{\mathrm{operating}}$	V	0.525	0.571	-8.05	0.568	-7.57
Power Density	P_{fc}	mW/cm^2	263	285	-7.71	284	-7.39
Electrochemical Efficiency	$\eta_{\mathrm{electrochemical}}$	–	59.27	64.9	-8.67	64.9	-8.67

5.1.2. Validation against experimental data for varying operating conditions

This section presents the outputs of the 0-D SOFC electrochemical model implemented within the Class 1 hybrid sizing loop of the Initiator, evaluated under varying SOFC operating conditions, namely, the system pressure, temperature, and anode fuel composition. The model predictions are compared against experimental SOFC data from literature across similar operating conditions. To improve the agreement of the model results with experimental data, electrochemical parameters of the SOFC model (i_o,i_L, and α) are tuned based on their sensitivity to varying SOFC operating conditions. These calibrated parameters improve the fidelity of the 0-D SOFC model and help to better predict SOFC thermal efficiency values within the Class 1 hybrid sizing loop, for different design/operating conditions of the SOFC-GT powertrain. While experimental data from the Siemens Westinghouse tubular SOFC stacks [87] is used for studying the effects of pressure variation on the model, data from the PNNL (Department of Energy Pacific Northwest National Laboratory) button cell SOFC [92] is used for validating the model for temperature sensitivities and anode fuel composition.

5.1.3. Pressure Variation

The effect of varying system pressures, ranging from 1 to 15 atm was studied by comparing the results of the 0-D SOFC electrochemical model to the Siemens Westinghouse stack pressure data in [87]. In order to remain consistent with the compared experimental data, an SOFC operating temperature of 1000°C, anode fuel composition of 89%, fuel utilization factor of 85%, air stoichiometric ratio of 4, and an exchange current density (i_0) of 350.89 $\mathrm{mA/cm^2}$ was chosen for the model; while α, i_n, and i_l were assumed to stay unchanged. The results of the pressure sweep are presented in Figure 5.2a, where a noticeable deviation is observed between the experimental voltage values and those predicted by the model, particularly at higher system pressures, where the discrepancy becomes more pronounced.

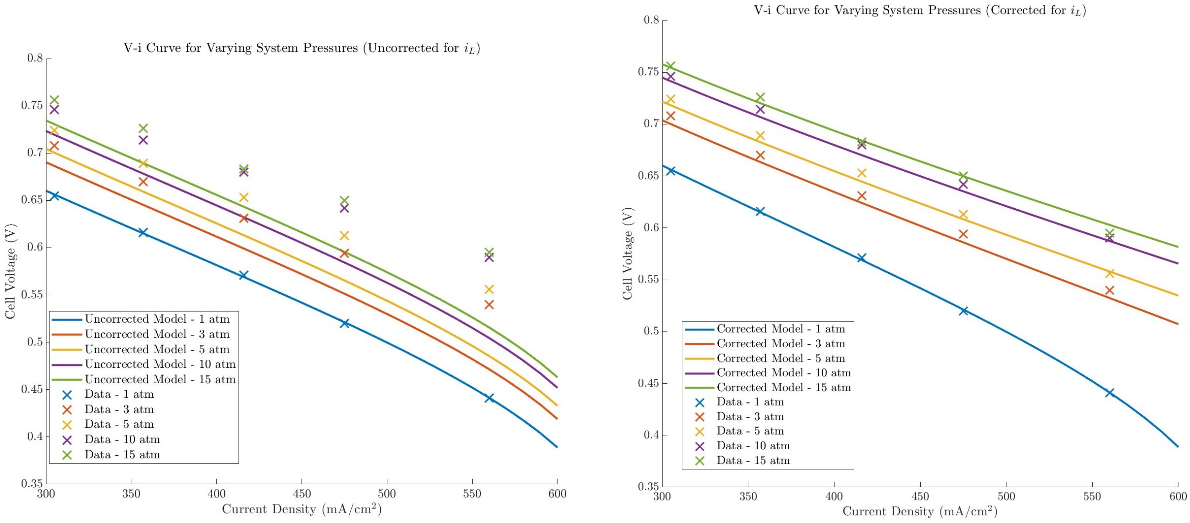

(a) Uncorrected for i_L

(b) Corrected for i_L

Figure 5.2: Comparison of V–i curves for varying system pressures, with and without correction for limiting current density (i_L).

In order to correct for this discrepancy between model and experimental data, Freeh et.al. proposed a correction for the limiting current density (i_L) of the model, in order to account for the impact of increasing system pressure on the mass diffusion of reacting species [87] which results in a reduction of the concentration losses at higher current densities (refer to Section 4.2.4). Therefore, i_L was modified to account for the sensitivity of concentration polarization to SOFC system pressure, as shown below:

$$i_L = i'_L \times \left(\frac{p}{p'}\right)^a \tag{5.1}$$

where a is an experimentally determined constant, p is the system pressure, and p' is the atmospheric pressure at standard conditions (1 atm).

By implementing this correction for the SOFC electrochemical model, the experimental data were found to be in good agreement with system pressure variations of the model (shown in Figure 5.2). As suggested by Freeh et.al., a value of 0.35 was used for the correction of i_L in Equation 5.1, with its magnitude ranging from 650 $\mathrm{mA/cm^2}$ to 1677 $\mathrm{mA/cm^2}$ for pressures of 1 and 15 atm, respectively. With the model already showing good agreement with experimentally obtained data, the variation of the charge transfer coefficient (α, which affects the activation losses of the SOFC; as explained in Section 4.2.2) with variations in system pressure is assumed to be negligible. This is a reasonable modeling simplification, as the activation losses for IT/HT SOFCs are usually small, due to the magnitude of the exchange current densities being on the scale of the operating current densities (refer to the Butler Volmer Equation in Section 4.2.2).

Table 5.4: Comparison of Experimental and Model-Predicted SOFC Voltages (Corrected vs Uncorrected) at 416 $\mathrm{mA/cm^2}$ for Varying System Pressures

Pressure (atm)	Experimental Voltage (V)	Uncorrected Model	Error (%)	Corrected Model	Error (%)
1	0.571	0.569	-0.35	0.569	-0.35
3	0.631	0.599	-5.07	0.624	-1.10
5	0.653	0.613	-6.12	0.648	-0.76
10	0.680	0.632	-7.05	0.670	-1.47
15	0.683	0.643	-5.85	0.684	0.14

5.1.4. Temperature Variation

As mentioned in Section 5.1.2, the validation of the 0-D SOFC electrochemical model for varying SOFC operating temperatures is done by comparing the model outputs to the data of a PNNL SOFC [92]. As the conditions of the reference SOFC for which the experimental data was sampled was not readily available from literature, a reference temperature was selected ($700°\mathrm{C}$) and the SOFC model parameters (i_0, r, α, i_L, and p_{system}) were tuned to best fit with experimental data at $700°\mathrm{C}$. The fitted parameters for the PNNL SOFC at $700°\mathrm{C}$ are presented in Table 5.5.

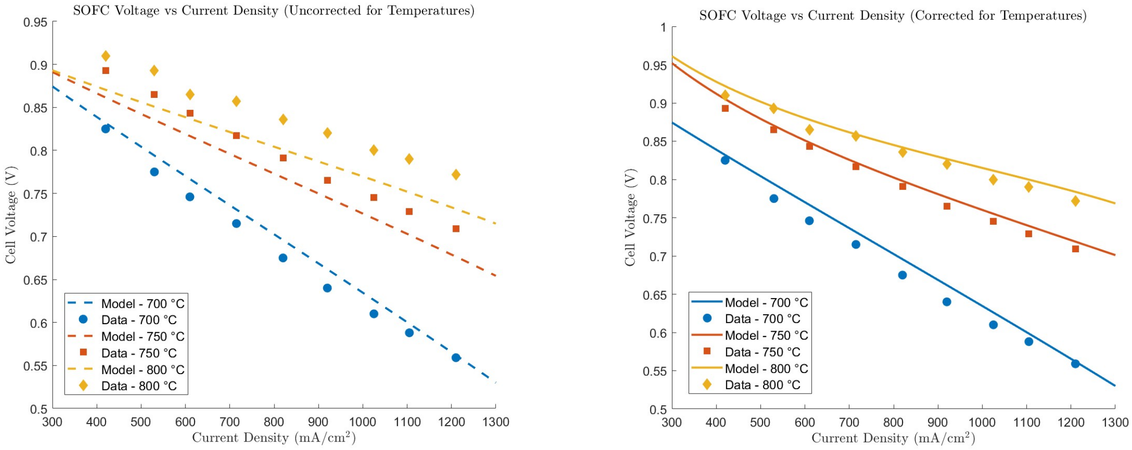

(a) Uncorrected for Temperature

(b) Corrected for Temperature

Figure 5.3: SOFC Voltage vs Current Density: Comparison of Temperature-Corrected and Uncorrected Results

Table 5.5: Fitted electrochemical parameters of the PNNL SOFC at $700°\mathrm{C}$, 23 atm, and anode fuel composition of 89%

Parameter	Symbol	Unit	Value
Exchange Current Density	i_0	mA/cm^2	377
Charge Transfer Coefficient	α	–	0.5
Limiting Current Density	i_L	mA/cm^2	1948
Bulk Internal ASR	r	Ω/cm^2	0.11

As the bulk internal area specific resistance (ASR) term r is the only temperature-sensitive electrochemical parameter in the 0-D SOFC electrochemical model, it tends to under-predict the voltage values for SOFC operating temperatures above the reference value of $700°\mathrm{C}$, as shown in Figure 5.3a. These differences between model and experimental data at higher temperatures can be attributed to the modeling discrepancies in the internal ASR term using only bulk values ($\mathrm{A} = 6.38 \times 10^{-7}$ and $\mathrm{E} = 10,000$ in Equation 4.13, from Section 4.2.3) and the absence of a temperature dependency on other electrochemical parameters of the SOFC. As such, the temperature dependency of electrochemical parameters such as α, i_L, and r can be further improved by calibrating the model to temperature data at $750°\mathrm{C}$ and $800°\mathrm{C}$ by adopting a polynomial fit of the form $\Delta x(\mathrm{T}) = a + b(\Delta\mathrm{T}) + c(\Delta\mathrm{T})^2$ as proposed by Datta for PEMFCs [18] [31], where x stands for the SOFC modeling parameter and $\Delta\mathrm{T}$ represents the difference between the operating and reference temperatures. Implementing these temperature-dependent corrections for the reference PNNL SOFC electrochemical parameters produces good agreement with experimental data, as shown in Figure 5.3b. It is also worth noting here that, as the sensitivity of the activation losses to the SOFC operating temperature was found to be more reliant on the charge transfer coefficient α than the exchange current density i_0, the change in i_0 with respect to SOFC operating temperature is assumed to be negligible and is not modeled in this study. However, this modeling assumption can vary according to the type of SOFC used, and an accurate temperature sensitivity for i_0 can only be modeled with the help of corresponding experimental data.

Table 5.6: Comparison of Experimental and Model-Predicted SOFC Voltages (Corrected vs Uncorrected) at 610 $\mathrm{mA/cm^2}$ for Varying SOFC Operating Temperatures

Temperature ($°\mathrm{C}$)	Experimental Voltage (V)	Uncorrected Model	Error (%)	Corrected Model	Error (%)
700	0.746	0.763	2.27	0.763	2.27
750	0.843	0.813	-3.55	0.844	0.11
800	0.865	0.833	-3.69	0.874	1.04

5.1.5. Anode Fuel Composition

Table 5.7: Electrochemical parameters of the PNNL SOFC at $725°\mathrm{C}$, 23 atm, and anode fuel composition of 97%

Parameter	Symbol	Unit	Value
Exchange Current Density	i_0	mA/cm^2	377
Charge Transfer Coefficient	α	–	1.16
Limiting Current Density	i_L	mA/cm^2	820
Bulk Internal ASR	r	Ω/cm^2	0.22

The validation of the 0-D SOFC electrochemical model for varying H_2 concentrations at the anode is also done using reference experimental data from the PNNL SOFC [92]. As the temperature at which this data was sampled is not known, the model is calibrated with experimental data at 97% anode fuel composition and a system pressure of 23 atm (similar to the reference conditions for temperature data) using a least squares regression method to find the reference temperature. As such, the data was found to be sampled at $725°\mathrm{C}$, and the electrochemical parameters of the model (r, α, i_L) are adjusted to the reference operating temperature. The temperature-corrected electrochemical parameters for the SOFC model are presented in Table 5.7, and the variation of cell operating voltages with current densities at different values of anode fuel composition (24% - 97% H_2) is shown in Figure 5.4a.

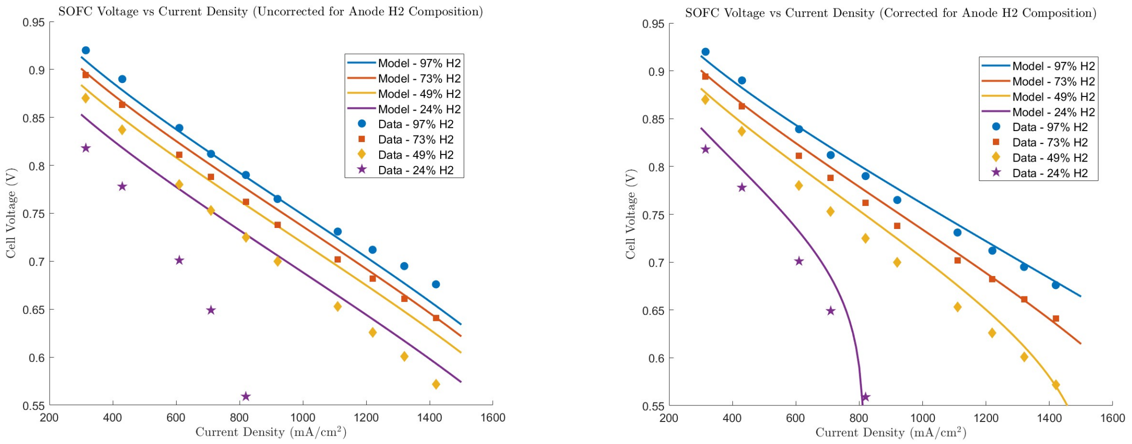

(a) Uncorrected for Anode H_2 Composition

(b) Corrected for Anode H_2 Composition

Figure 5.4: Effect of Anode H_2 Composition on SOFC Voltage vs Current Density

From Figure 5.4b, it can be observed that the discrepancies between experimental data and model output voltages become quite significant at lower values of anode fuel composition and higher current densities. This is as expected, as it is widely known from literature that the anode concentration losses dominate at higher current densities due to a lack in the supply of fuel at the Triple Phase Boundary (TPB), where the cell reaction kinetics are dominant [67] [25]. This phenomenon becomes increasingly dominant at lower values of anode fuel composition and higher operating current densities, requiring a correction in the electrochemical parameters of the model. As the mass transport losses are the dominating polarization phenomenon, the model is adjusted for varying values of limiting current density (i_L) to best fit the experimental data. As shown in Figure 5.4b, this correction for i_L already leads to good agreement with experimental data (< 5%), so the sensitivities of other cell parameters can safely be assumed negligible while modeling the effects of anode fuel composition on operating cell voltage. The difference between the experimental and model-predicted values of cell operating voltage with varying anode fuel concentration, for both the corrected and uncorrected models, is tabulated in Table 5.9, and the implemented i_L corrections for varying anode fuel compositions are presented in Table 5.8.

Table 5.8: Implemented Limiting Current Density (i_L) Corrections for Varying Anode Fuel Compositions

Anode H_2 Composition (%)	**Corrected i_L (mA/cm^2)**
97	3000
73	1900
49	1550
24	820

Table 5.9: Comparison of Experimental and Model-Predicted SOFC Voltages (Corrected vs Uncorrected) at 610 $\mathrm{mA/cm^2}$ for Varying Anode H_2 Compositions

Anode H_2 Composition (%)	**Experimental Voltage (V)**	**Uncorrected Model**	**Error (%)**	**Corrected Model**	**Error (%)**
97	0.839	0.835	-0.48	0.841	0.23
73	0.811	0.823	1.48	0.822	1.36
49	0.780	0.805	3.21	0.800	2.56
24	0.701	0.775	10.55	0.731	4.27

5.2. Class 1 Sizing Verification

Table 5.10: Top Level Aircraft Requirements (TLAR) for the baseline ATR 72-600 aircraft

Parameter	Value	Units
Number of passengers	72	–
Payload Mass	7500	kg
Aspect Ratio	12	–
Design range (758 NM)	1403	km
Landing field length	1200	m
Take-off field length	1333	m
Cruise Mach Number	0.44	-
Cruise altitude	5200	m
Diversion range	160	km
Loiter Time	30	min

The results of the hybrid class 1 sizing loop for conventional kerosene-based, conventional LH_2-based, and SOFC-GT aircraft are presented in the subsequent sections. The top-level aircraft requirements (TLAR) are based on those of the baseline ATR 72-600 aircraft (refer to Section 4.8), and are presented below in Table 5.10. The results of the hybrid class 1 sizing loop are then verified and validated against OEM data for the conventional kerosene-based aircraft and with a similar model from literature for the conventional LH_2 aircraft.

5.2.1. Conventional Kerosene-based Aircraft

Table 5.11: Comparison of the class 1 sizing results of the Double-Hybrid Model [9] against ATR 72-600 data [6]

Parameter	Units	Double-Hybrid Powertrain Model	ATR 72-600	Error (%)
OEM	tonnes	14.72	13.45	9.4
MTOM	tonnes	25.04	23.00	8.8
Wing Span	m	26.95	27.05	-0.36
Wing Area	m^2	60.56	61.00	-0.72
GT Mass	kg	578.15	480	20.44
Fuel Mass	tonnes	2.82 (Baseline full range mission)	NA	-
		0.88 (300 NM mission)	0.87	1.1
Total Propulsive Power	SHP	2081.60	2192.00	-5.04

Table 5.13 presents the results of the hybrid class 1 sizing loop for the conventional kerosene-based aircraft with top-level aircraft requirements of the ATR 72-600, and compares them to manufacturer data that is available from ATR [6], Pratt and Whitney (for the PW127M engine), and literature. As seen in Table 5.13, most of the top-level results lie within 10% of manufacturer data, with the wing dimensions showing the best agreement (-0.36% and -0.72% for the wingspan and area, respectively). The gas turbine mass, however, exhibits the maximum discrepancy at around 20%, which is attributable to inaccuracies in the statistical database that correlates the gas turbine's installed power (at reference, sea-level conditions) with its mass. However, the total propulsive power at sizing conditions (which is at top of climb with all engines operative, as shown in Figure 5.5d) and the fuel mass show better agreement with manufacturer data at around -5% and +1.1% respectively, keeping the error in OEM and MTOM predictions below 10%. The sizing diagrams showing the feasible design space and design points for individual powertrain components of the conventional kerosene-based aircraft are presented in Figure 5.5. The feasible design space is bounded by the powered stall speed constraint, which determines the limiting value of wing loading, while the design point is selected based on the minimum wing surface area within the feasible design space and corresponds to the lowest power loading value for all constraints. Figure 5.6 presents the mass breakdown of the Class 1 results, where fuel (11.3%) and the wing (9.6%) make up the largest components following the aircraft payload.

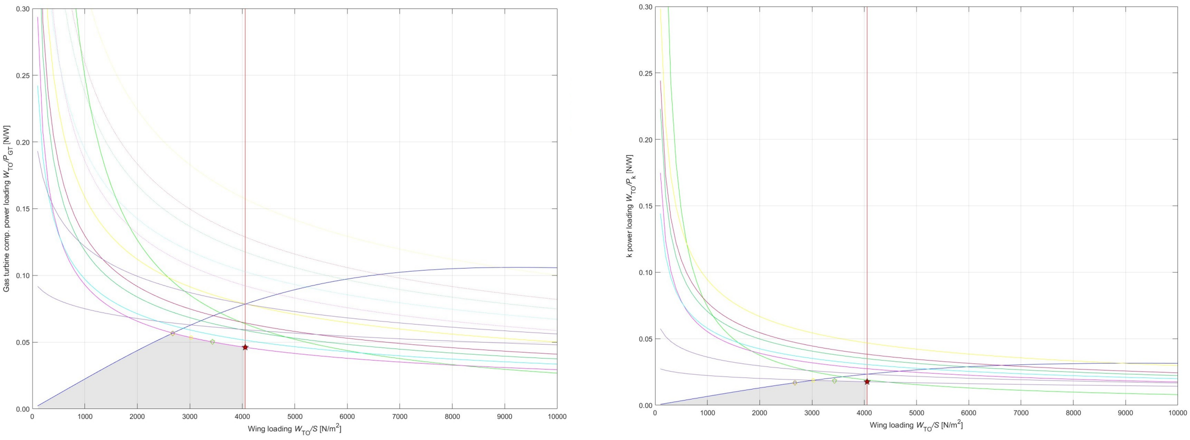

(a) Gas turbine component power

(b) Kerosene-based fuel power

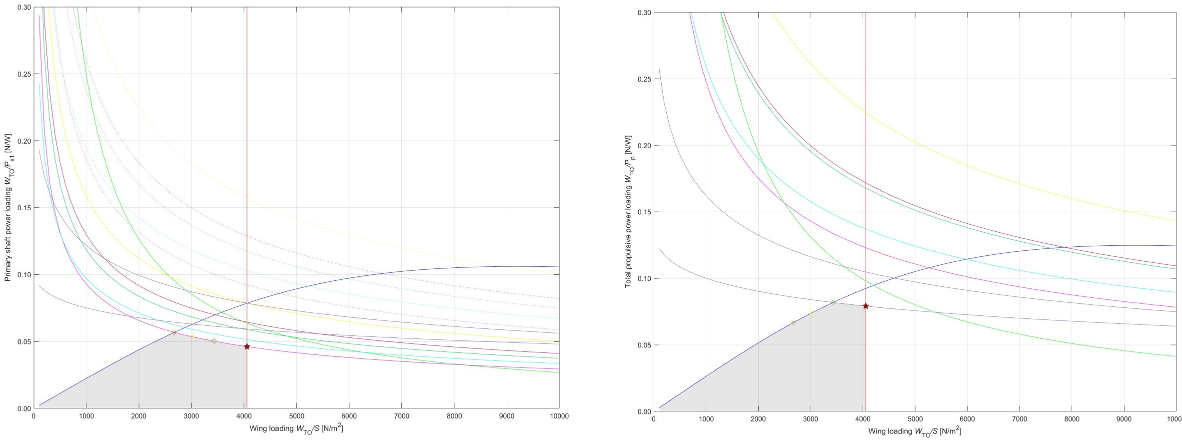

(c) Primary shaft power

(d) Total propulsive power

Figure 5.5: Constraint sizing diagrams $(\mathrm{WP}/\mathrm{WS})$ for various components of the conventional kerosene-based powertrain, showing the chosen design point, and the feasible design space

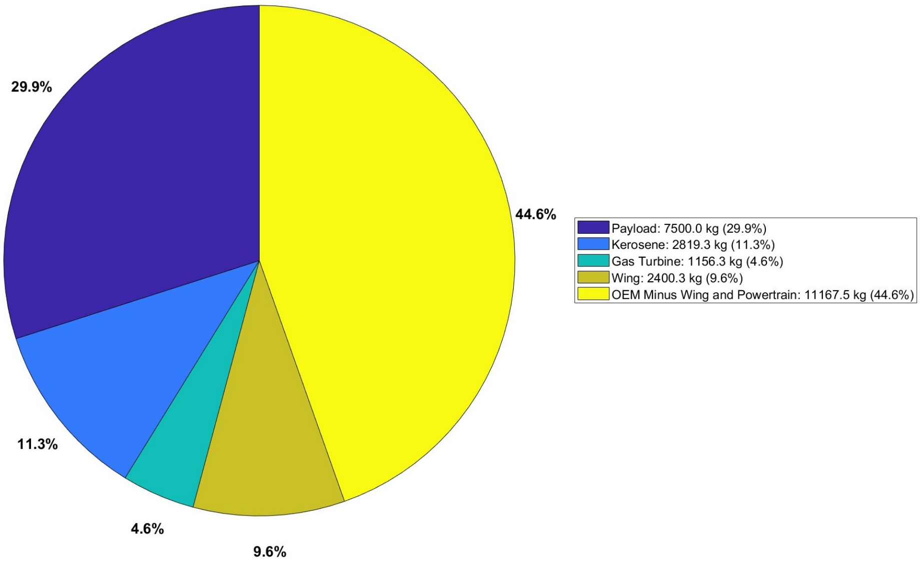

Figure 5.6: Class-1 Weight Breakdown of Components - Conventional Kerosene-Based Powertrain

5.2.2. Conventional LH_2 Aircraft

For the Class 1 sizing results of the conventional LH_2-based aircraft, verification was conducted against the Class 2 sizing results of an LH_2 turboprop aircraft by Mukhopadhaya et al. [65], whose top-level aircraft requirements are similar to the ATR 72-600 (although the cruise altitude and the wing aspect ratio are higher), and presented below in Table 5.12. It is important to note here that while the top-level requirements shown in Table 5.12 are used for validation of the sizing methodology, the LH_2 aircraft that is used for comparison against the conventional kerosene-based and SOFC-GT aircraft in the subsequent sections is sized according to the top-level requirements of the ATR 72-600 (given in Table 5.10). The Class 1 mass breakdown of this LH_2 turboprop aircraft is presented below in Figure 5.7.

Table 5.12: Top Level Aircraft Requirements for the Modified LH_2 turboprop aircraft (based on the ATR 72-600), as used by Mukhopadhaya et al. [65]

Parameter	Value	Units
Range	1420	km
Passenger	70	–
Payload Mass	6500	kg
Mach Number	0.45	–
Aspect Ratio	15	–
Take-off Distance	1400	m
Tank Gravimetric Index (GI)	0.35	–
Cruise Altitude	6100	m
Diversion range	185	km
Loiter Time	45	min

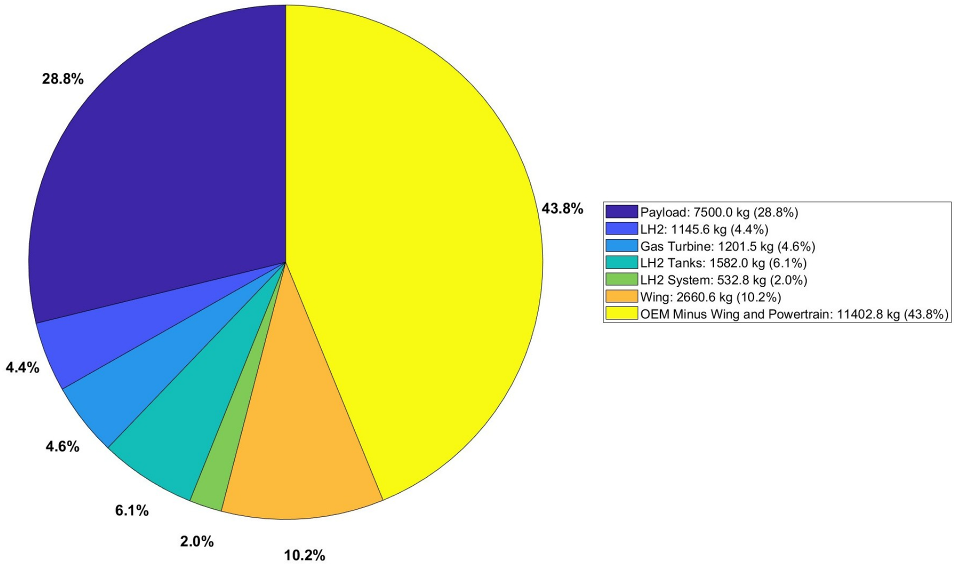

Figure 5.7: Class-1 Weight Breakdown of Components - Conventional LH_2 Powertrain

Table 5.13 presents the comparison of Class 1 sizing results of the conventional LH_2-based turboprop aircraft against the Class 2 sizing results presented by Mukhopadhaya et al. [65]. As expected for Class 1 sizing methods, all top-level results lie within 10% of Class 2 sizing results, with the wing span (-8.4%) and MTOM (-5.21%) showing the maximum and least discrepancies, respectively. Although the OEM decreases significantly by -7.86%, the 5.2% MTOM decrease is linked to the increased fuel mass for the design range of the aircraft, and is likely attributable to the conservative value of gas turbine thermal efficiency assumed in the double-hybrid powertrain model.

Table 5.13: Comparison of the Class 1 sizing results of the Double-Hybrid Model [9] against Class 2 sizing results of an LH_2 turboprop based on the TLAR of the ATR 72-600 by Mukhopadhaya et.al. [65]

Parameter	Units	Double-Hybrid Powertrain Model	Modified LH_2 Turboprop by Mukhopadhaya	Error (%)
OEM	tonnes	16.40	17.80	-7.86
MTOM	tonnes	24.17	25.50	-5.21
Wing Span	m	29.77	32.5	-8.40
Fuel Mass	tonnes	1.27	1.19	6.72

The constraint sizing diagrams for the powertrain components of the LH_2 turboprop aircraft are presented below from Figures 5.8a to 5.8d. While the gas turbine and the primary shaft are sized according to the One-Engine-Inoperative (OEI) balked landing requirements, the fuel and total propulsive power are sized for the OEI second segment climb segment.

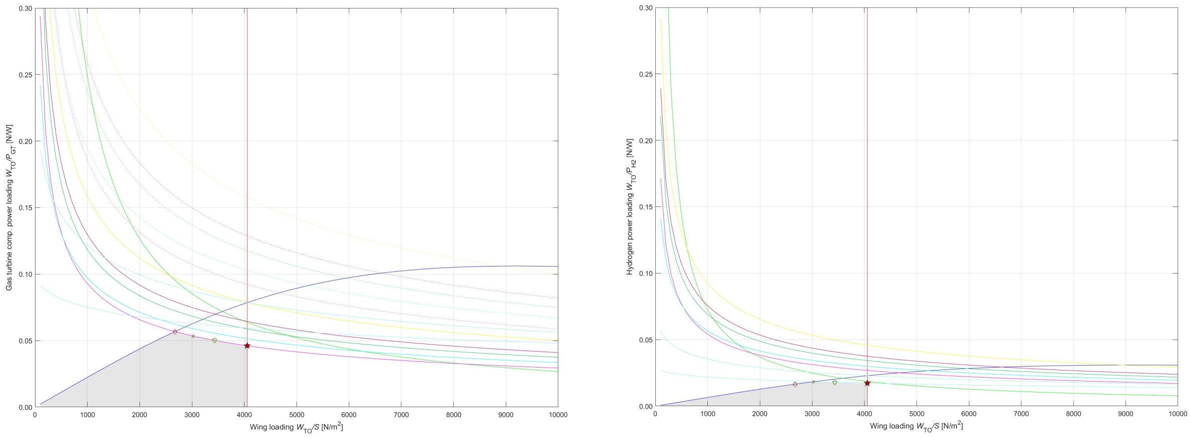

(a) Gas turbine component power

(b) LH_2 fuel power

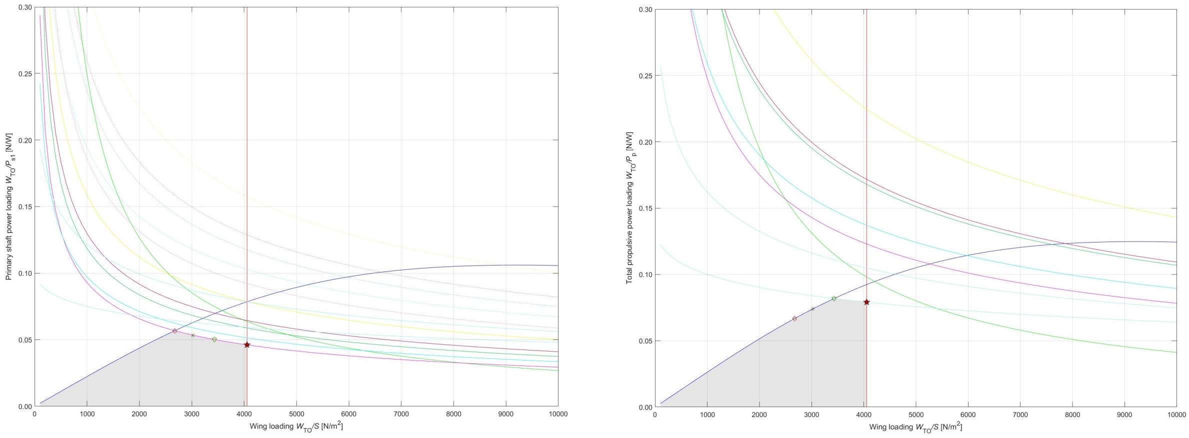

(c) Primary shaft power

(d) Total propulsive power

Figure 5.8: Constraint sizing diagrams $(\mathrm{WP/WS})$ for various components of the conventional LH_2-based powertrain, showing the chosen design point, and the feasible design space

5.2.3. SOFC-GT Aircraft

The following sections present the Class 1 sizing results for an SOFC-GT LH_2 aircraft, and compare them to conventional kerosene-based and LH_2 -based aircraft, respectively. The SOFC-GT aircraft is observed to be considerably heavier than its counterparts, with the SOFC stacks along with the Balance of Plant (BoP) now constituting a significant share of the aircraft's OEM. This results in a larger wing for the same design $\mathrm{W/S}$ and thereby, a higher energy requirement for the nominal mission. A Class

1 mass breakdown of the components of the SOFC-GT aircraft is presented in Figure 5.10, and the sizing diagrams for the SOFC-GT powertrain components are shown from Figures 5.9a to 5.9f. For this study, a non-zero value for $\mathrm{H}_{2_{\mathrm{split}}}$ is used in cruise conditions only; hence, the SOFC stacks and $\mathrm{EM1}$ are sized according to the cruise speed constraint, as seen in Figures 5.9c and 5.9d.

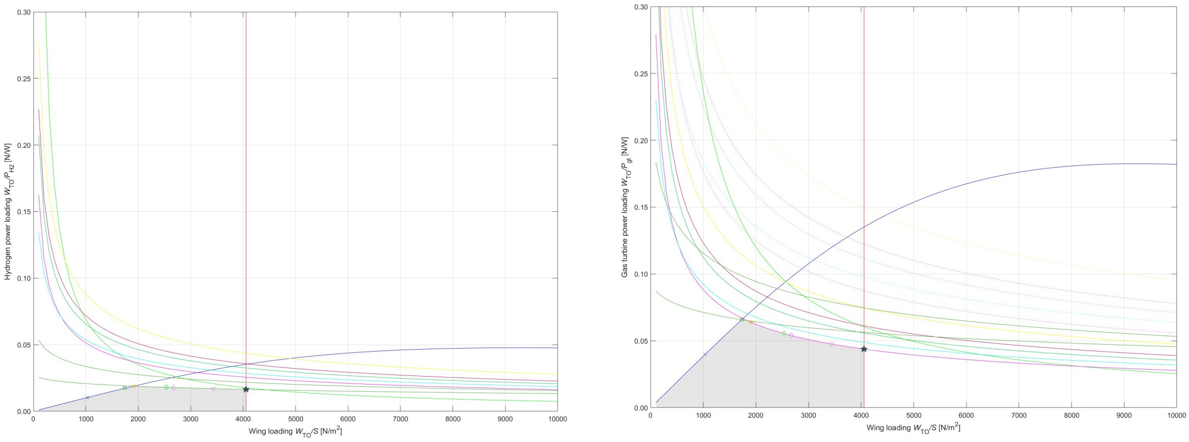

(a) LH_2 fuel power

(b) Gas turbine component power

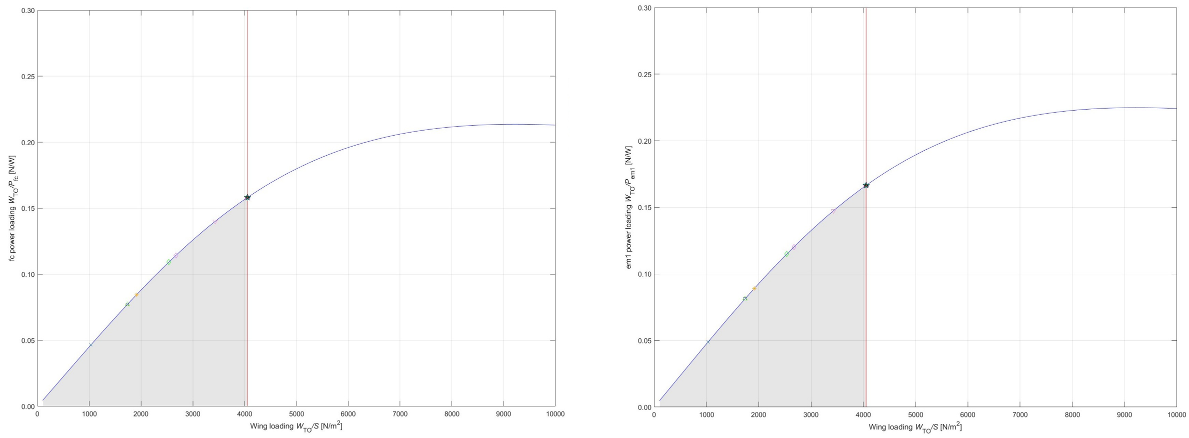

(c) Fuel cell power

(d) Primary electrical machine $(\mathrm{EM1})$ power

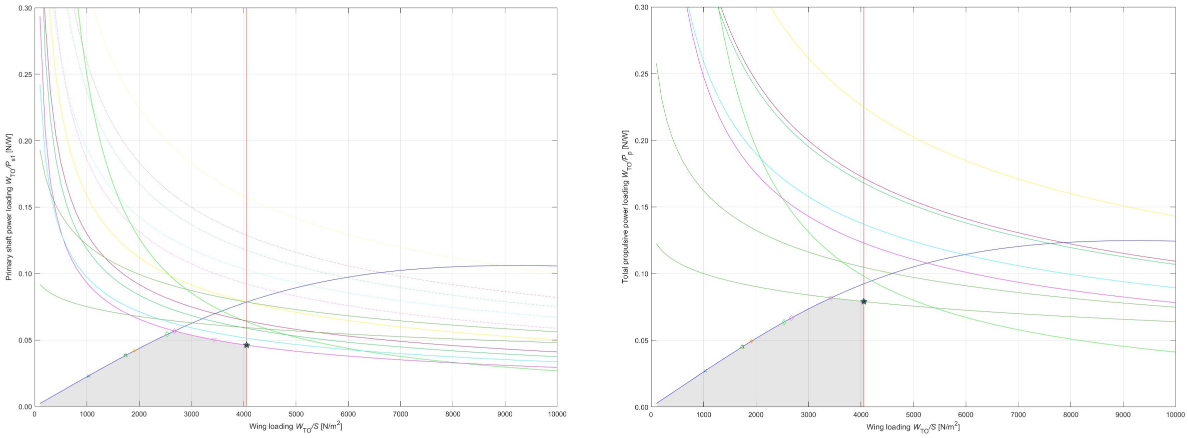

(e) Primary shaft power

(f) Total propulsive power

Figure 5.9: Constraint sizing diagrams $(\mathrm{WP}/\mathrm{WS})$ for various components of the SOFC-GT powertrain, showing the chosen design point, and the feasible design space

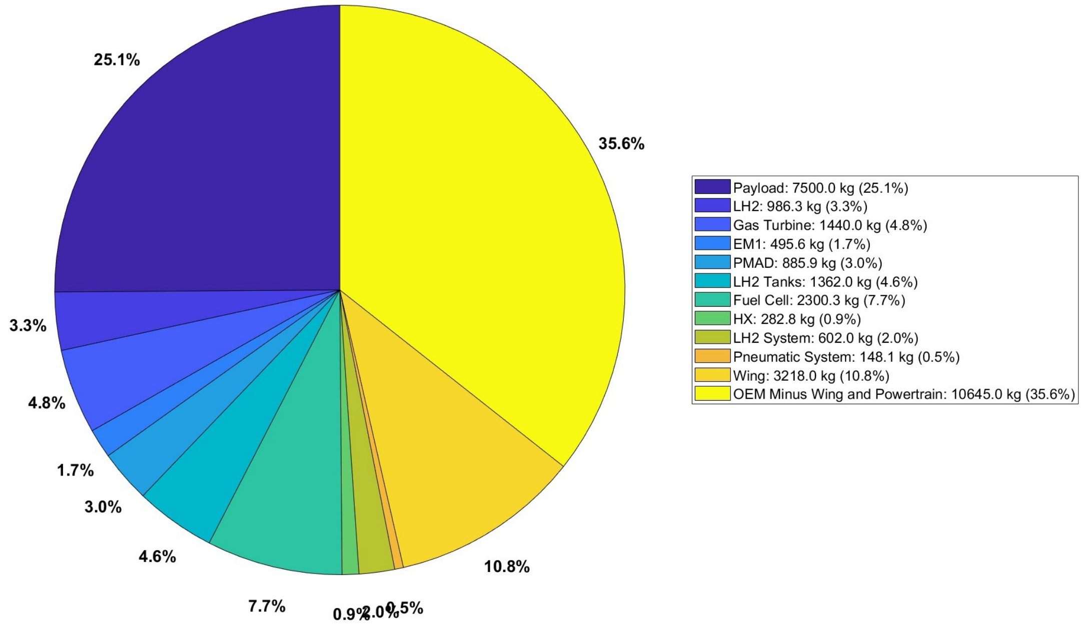

Figure 5.10: Class-1 Weight Breakdown of Components for SOFC-GT Powertrain

5.2.4. Comparison with LH_2-Based Conventional and SOFC-GT Aircraft

Table 5.14: Comparison between Class 1 Sizing Results

Parameter	**Conventional (kerosene-based)**	**Conventional (LH_2-based)**	**SOFC–GT (at 400 mA/cm^2)**	**% diff. (kerosene-based)**	**% diff. (LH_2-based)**
MTOM [t]	25.04	26.03	29.86	+19.24%	+14.71%
OEM [t]	14.72	17.38	21.38	+45.24%	+23.01%
Energy Mass [t]	2.82	1.14	0.986	-65.03%	-13.50%
$\eta_{\mathrm{overall,thermal}}$ [%]	29.77	30.66	44.17	+48.37%	+44.06%
Wingspan [m]	26.95	27.48	29.44	+9.23%	+7.13%

Table 5.14 presents a comparison of the Class 1 sizing results of the SOFC-GT aircraft (sized for 50% cruise hydrogen split and design current density of 400 $\mathrm{mA/cm^2}$) against conventional kerosene-based and LH_2 aircraft, respectively. As mentioned previously, the OEM increases significantly for the SOFC-GT aircraft due to the mass of the stacks (at a stack-level gravimetric density of 0.75 $\mathrm{kW/kg}$, this adds around 2.31 tonnes of empty mass to the aircraft alone) and the supporting Balance of Plant (BoP) components, including the mass of LH_2 tanks, fuel conditioning and management systems, preheaters, and the electrical system. As a result, a larger wing area is required to provide sufficient lift in landing conditions, leading to a higher wing span and a heavier wing for a similar wing aspect ratio. Although this significant increase in the aircraft's empty mass naturally leads to a higher energy requirement in all flight conditions, the massive increase in overall thermal efficiency of the SOFC-GT powertrain (48.37% and +44.06% improvement when compared to the conventional kerosene and LH_2 powertrains, respectively) reduces the fuel mass required for the nominal mission. As a result, the MTOM of the SOFC-GT aircraft doesn't increase as much as the OEM, with a +19.24% and +14.71% increase in comparison to the MTOM of conventional kerosene and LH_2 aircraft, respectively.

Environmental Emissions

The overall emissions of the SOFC-GT aircraft in comparison to those of the conventional kerosene and LH_2 based aircraft are presented in Table 5.15. The significant improvement in the overall thermal efficiency of the SOFC-GT aircraft, along with the reduced energy requirement for the nominal mission, translates into lower emissions of both proportional and non-proportional species in comparison to the conventional LH_2 aircraft (-15.3% for H_2O and -50.26% for NOx respectively).

Table 5.15: Emission indices and total emissions (in kg) for conventional, LH_2 combustion, and SOFC–GT powertrains

	Conventional (Kerosene)	**Conventional (LH_2-based)**	**SOFC–GT (400 mA/cm^2, 900°C)**
		Emission Indices of Proportional Species (g/kg)	
$\mathrm{EI_{H_2O}}$	1240	9000	8763.60 (Cruise Conditions) 9000 (other flight conditions)
$\mathrm{EI_{CO_2}}$	3160	–	–
$\mathrm{EI_{SO_x}}$	0.06	–	–
		Emissions (kg)	
$\mathrm{H_2O}$	3721.56	10310.05	8718.60
$\mathrm{CO_2}$	9483.99	–	–
$\mathrm{SO_x}$	0.18	–	–
CO	8.29	–	–
$\mathrm{NO_x}$	97.68	18.62	9.26

As explained previously in Section 4.11, the emission indices of the non-proportional species emitted through LH_2 combustion are estimated using the Boeing Fuel Flow Method (BFFM2) for all flight conditions except cruise. For cruise segments (including diversion) where the SOFC-GT powertrain is employed, the emission indices of H_2O and NOx are estimated using species mass fractions data from CANTERA results, as explained in Section 4.12 and B.2. Table 5.16 presents the emission indices of non-proportional species for all three powertrains and flight conditions, along with the fuel mass flows and energy requirement for each flight segment. It is important to note here that due to the assumptions of fixed energy fractions for short flight segments (taxi, takeoff, and landing) in Class 1 energy sizing methods, the fuel mass flow rates could not be reliably estimated for use within the Boeing Fuel Flow Method. As such, the emission indices of non-proportional species for short flight segments are assumed to be equal to those for climb (for takeoff) and descent (for landing), respectively.

Table 5.16: Emission Indices of Non-Proportional Species, per Flight Condition

Flight Condition	$\mathrm{EI_{CO}}$	$\mathrm{EI_{NOx}}$	$\dot{m}_{\mathbf{fuel}}$	$M_{\mathbf{fuel}}$
		Conventional-Kerosene		
Climb	1.99	65.57	0.34	333.34
Cruise	1.98	28.40	0.30	2061.80
Descent	34.99	4.47	0.01	14.19
Diversion Climb	2.18	57.23	0.48	66.67
Diversion Cruise	2.17	25.31	0.24	219.44
Diversion Descent	32.94	4.86	0.02	5.95
Loiter	5.30	9.93	0.08	139.30
		Conventional-LH_2		
Climb	—	25.19	0.19	127.10
Cruise	—	15.41	0.11	790.56
Descent	—	5.33	0.01	5.35
Diversion Climb	—	25.40	0.17	27.33
Diversion Cruise	—	13.96	0.09	73.87
Diversion Descent	—	5.66	0.01	2.25
Loiter	—	7.57	0.03	57.78
		SOFC-GT (400 mA/cm^2, 900°C)		
Climb	—	29.01	0.23	153.60
Cruise	—	5.45	0.06	609.47
Descent	—	5.38	0.01	6.48
Diversion Climb	—	28.76	0.21	33.48
Diversion Cruise	—	5.65	0.05	56.93
Diversion Descent	—	5.73	0.01	2.72
Loiter	—	8.18	0.04	70.83

6

Results and Discussion

6.1. Pressure Sweep

In this study, the system pressure of the SOFC-GT powertrain is varied from 8.27 bars up to 21.3 bars to observe the sensitivities of different Class 1 sizing outputs across varying design current densities. At the cathode side, this is done by varying the pressure ratio of the HPC from 3.873 (similar to the PW127) to 10 (for the same RPM of the HP spool, this results in an increasing number of HPC stages), while for the fuel delivered to the anode, the effect of increasing system pressure is modeled by increasing the mass of the LH_2 pumps by 2.5%, 5%, 7.5%, and 10% for every step of system pressure increase (8.27,10.67,14.94,19.21, and 21.3 bars respectively). The effect of increasing system pressure on SOFC performance at the cell level is modeled through the limiting current density i_L, which increases proportionately with the system pressure as per the relation given by Freeh et.al. [25], expressed in Equation 5.1.

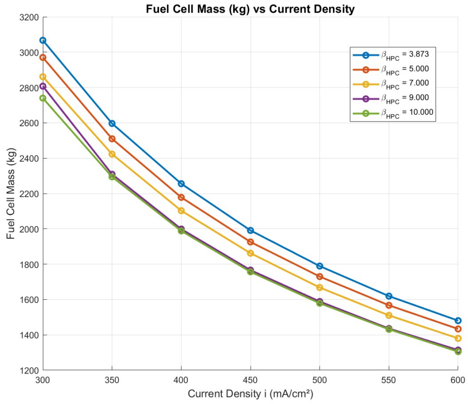

Figure 6.1: Fuel Cell Mass vs Current Density for different β_{HPC} values

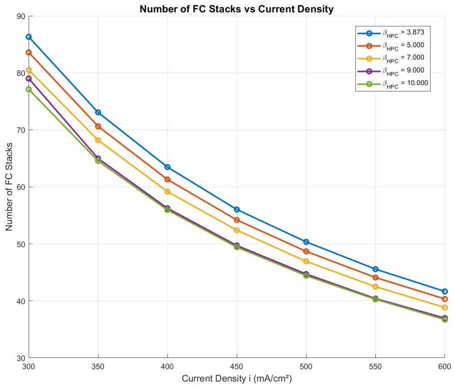

Figure 6.2: Number of Stacks vs Current Density for different β_{HPC} values

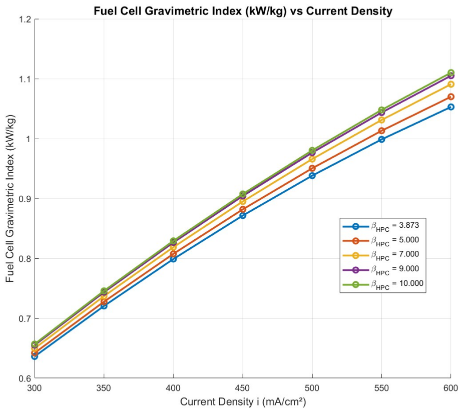

Figure 6.3: $\mathrm{GI}_{\mathrm{FC}}$ vs Current Density for different β_{HPC} values

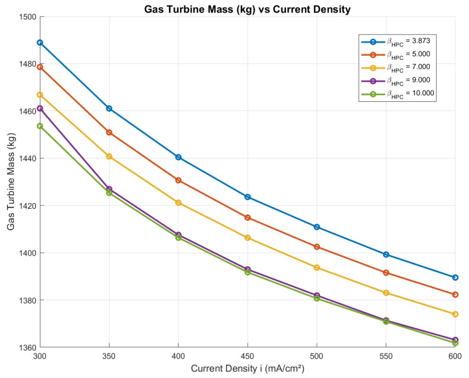

Figure 6.4: Gas Turbine Mass vs Current Density for different β_{HPC} values

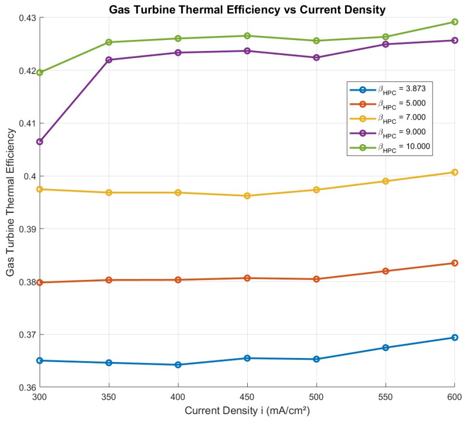

Figure 6.5: η_{GT} vs Current Density for different β_{HPC} values

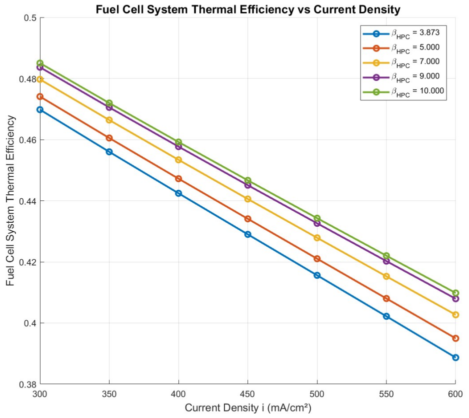

Figure 6.6: η_{FC} vs Current Density for different β_{HPC} values

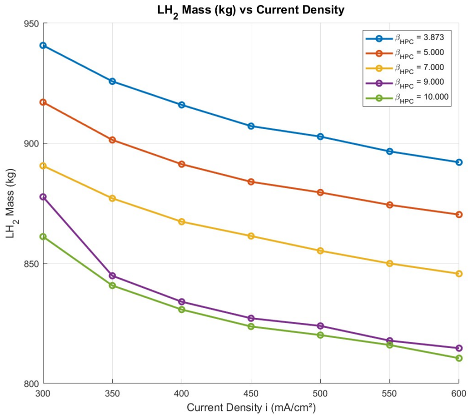

Figure 6.7: LH2 Mass vs Current Density for different β_{HPC} values

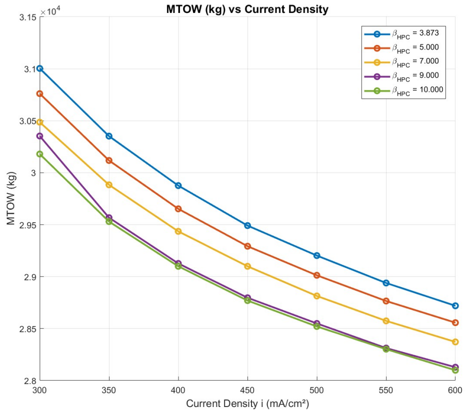

Figure 6.8: MTOM vs Current Density for different β_{HPC} values

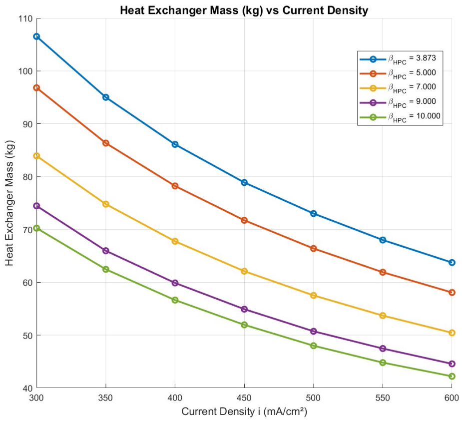

Figure 6.9: HX Mass vs Current Density for different β_{HPC} values

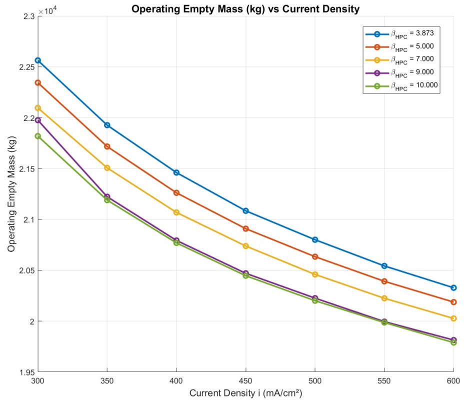

Figure 6.10: OEM vs Current Density for different β_{HPC} values

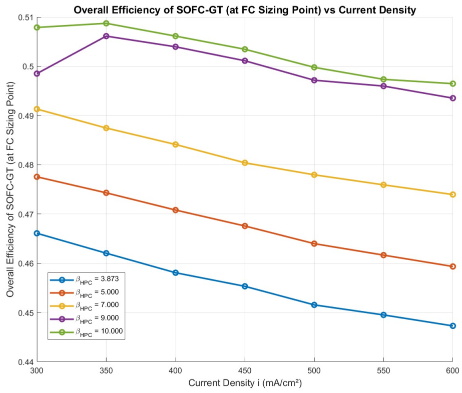

Figure 6.11: Overall Thermal Efficiency vs Current Density for different β_{HPC} values

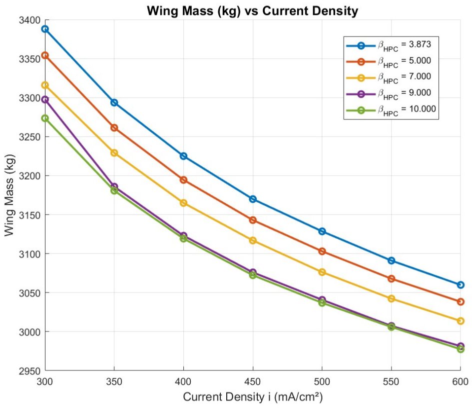

Figure 6.12: Wing Mass vs Current Density for different β_{HPC} values

As expected, both the efficiencies of the fuel cell and the gas turbine increase with increasing system pressure, leading to a corresponding increase in the overall thermal efficiency of the system as shown in Figure 6.11. This also results in a decrease in the fuel cell mass (owing to a decrease in the number of SOFC stacks, as shown in Figure 6.2). Although increasing the pressure ratio of the HPC leads to an increasing number of stages, the gas turbine mass is also observed to be decreasing due to it being scaled with the total required propulsive power, which is a function of the system mass. The energy required for the same range decreases as well (as can be seen in Figure 6.7, the OEM decreases due to a lighter wing, SOFC-GT powertrain, and fuselage extensions, which ultimately reflects in a 2.6% and 2% decrease in the MTOW for design current densities of 300 and 600 $\mathrm{mA/cm^2}$ respectively. However, it is also worth noting that the benefits of increasing the system pressure show an asymptotic behavior, with the changes in MTOM and overall thermal efficiency observed to show only a -0.1% and +0.6% change from 19 to 21 bars respectively, at a design current density of 600 $\mathrm{mA/cm^2}$.

6.2. Temperature Sweep

The sensitivity of the Class 1 sizing results to the SOFC operating temperature is studied in this section, where the temperature of the stacks is varied from 800 $^\circ\mathrm{C}$ to 1000 $^\circ\mathrm{C}$ in increments of 50 $^\circ\mathrm{C}$. To reasonably model the system-level effects of increasing the SOFC operating temperature, two main assumptions are considered in this study; 1) the exchange current density i_0 of the SOFC increases by 10% with every incremental step in operating temperature above 800 $^\circ\mathrm{C}$, and 2) the gravimetric power density of the SOFC at stack level (in $\mathrm{kW/kg}$) decreases by 3% with every 50 $^{\circ}\mathrm{C}$ increment from 900$^{\circ}\mathrm{C}$. While the former assumption is based on experimentally observed trends for HT-SOFCs, where a slight increase in the exchange current density i_0 is observed with increasing operating temperature [20] (this counteracts the increase in the $\mathrm{RT/n\alpha F}$ term with operating temperature), the latter builds upon the consideration that higher SOFC operating temperatures necessitate the use of heavier materials (such as ceramics and high temperature alloys) which are both thermally and chemically stable to be used at the cell level, directly leading to lower values of gravimetric power densities at the stack level [36] [94].

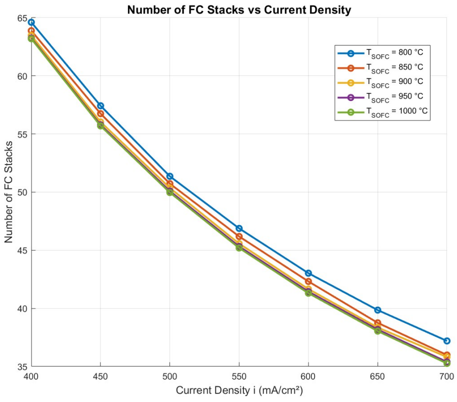

Figure 6.13: Number of Stacks vs Current Density for different T_{SOFC} values

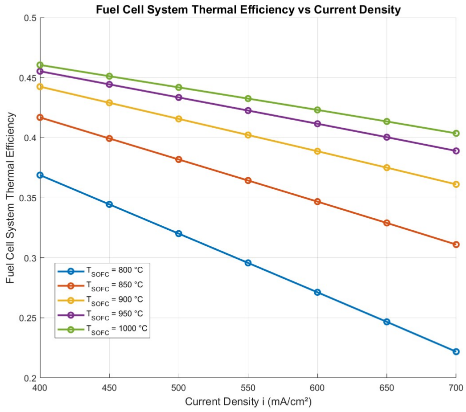

Figure 6.14: η_{FC} vs Current Density for different T_{SOFC} values

The number of stacks is observed to decrease with both increasing current density and SOFC operating temperature, due to the increasing power density at the cell level in both cases. The dominant ohmic losses decrease with increasing SOFC operating temperature, and this leads to better fuel cell performance at higher cell temperatures, which can be observed from Figure 6.14 as well. However, it is also important to note that the benefits of increasing the SOFC operating temperature for better cell performance shows limited improvement after 950 $^{\circ}\mathrm{C}$; primarily owing to the increasing effect of other temperature-dependent loss mechanisms (especially mass transport losses) over the dominant ohmic loss mechanism, which decreases with increasing cell operating temperature as mentioned earlier. Conversely, the gravimetric power density and fuel cell mass trends (shown by Figures 6.15 and 6.16 reverses after 950 $^{\circ}\mathrm{C}$, an after-effect of the modeling assumptions of this study, which considers an increase in stack weight (attributable to the use of denser, thermally-stable cell materials) at higher cell operating temperatures.

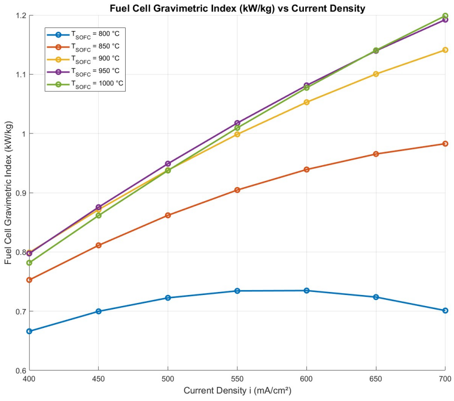

Figure 6.15: $\mathrm{GI_{FC}}$ vs Current Density for different T_{SOFC} values

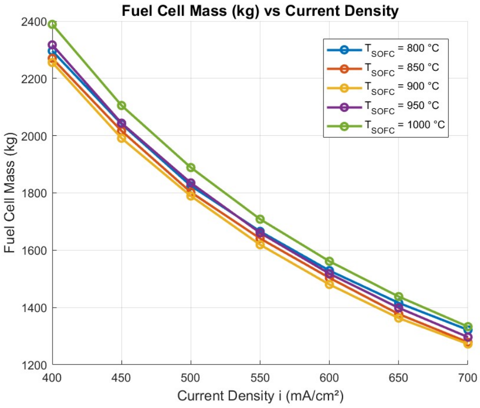

Figure 6.16: Fuel Cell Mass vs Current Density for different T_{SOFC} values

Figures 6.15 and 6.16 show the effect of changing SOFC operating temperature on the gas turbine, where the gas turbine thermal efficiency drops with increasing operating temperature. This can quite straightforwardly be attributed to better cell performance at elevated temperatures, leading to less heat being passed to the underutilized air for combustion, and consequently lowering the total flow enthalpy that is available for combustion and expansion within the turbines. As a result of the reduced thermal efficiency, the gas turbine also gets heavier for the same design current density, as shown in Figure 6.16. The increase in the gas turbine mass can also be explained as a direct consequence of the increasing aircraft mass, as well, which increases the required amount of propulsive power to be provided by the powertrain proportionately.

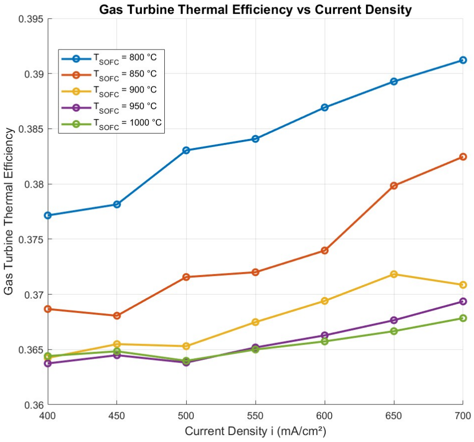

Figure 6.17: η_{GT} vs Current Density for different T_{SOFC} values

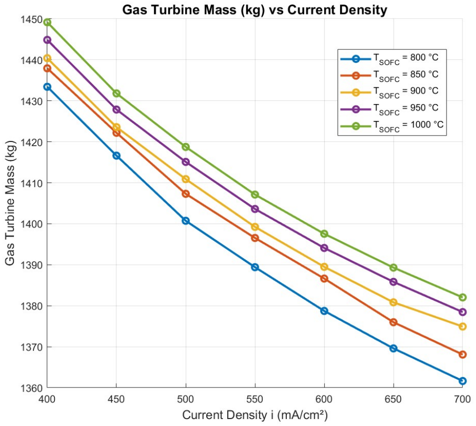

Figure 6.18: Gas Turbine Mass vs Current Density for different T_{SOFC} values

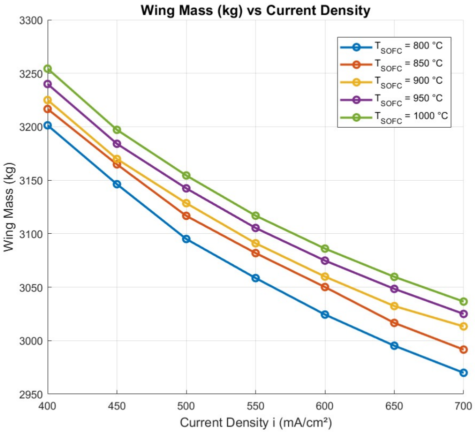

Figure 6.19: Wing Mass vs Current Density for different T_{SOFC} values

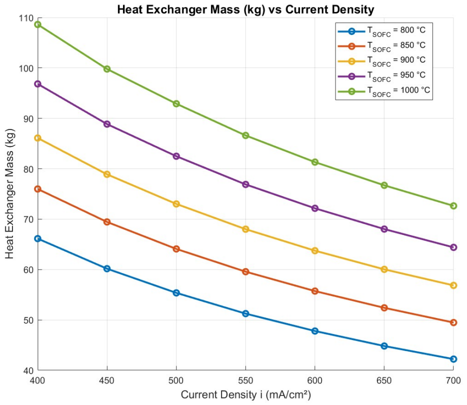

Figure 6.20: HX Mass vs Current Density for different T_{SOFC} values

The changes in the wing mass, HX mass, MTOM, OEM, and the fuel mass are presented in Figures 6.19 to 6.24 respectively. The total mass of the heat exchangers is observed to increase with SOFC operating temperatures, which is expected, as a higher operating cell temperature would require a larger area for the heat transfer (especially in the air and H_2 preheaters, which bring the air and fuel to operating temperature), for given mass flow rates of the cold side (pressurized air from the HPC, or LH_2 fuel from the tanks) and the hot side (exhaust gas) fluids. The operating empty mass (OEM) and the maximum take-off mass (MTOM) show trends that are quite similar to those of the gas turbine, wing, and fuel cell masses, strongly suggesting that the MTOM is more sensitive to these parameters than the fuel mass.

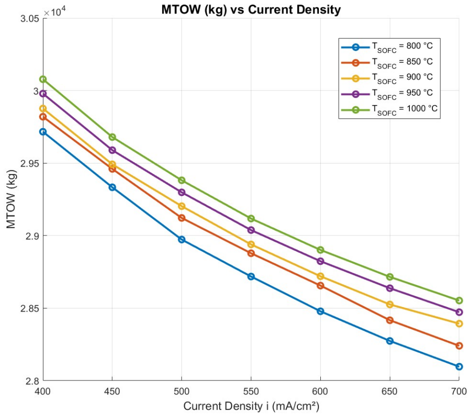

Figure 6.21: MTOM vs Current Density for different T_{SOFC} values

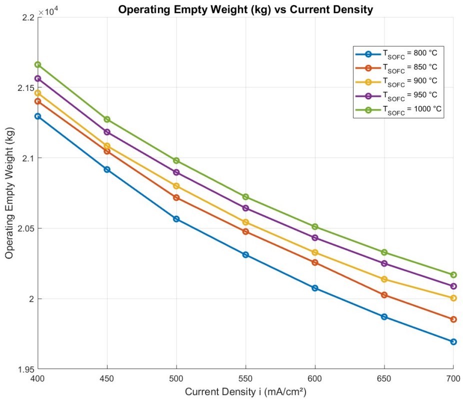

Figure 6.22: OEM vs Current Density for different T_{SOFC} values

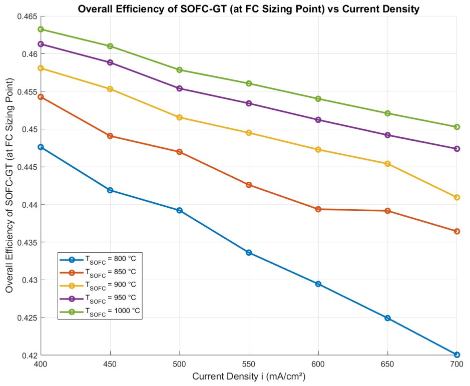

Figure 6.23: Overall Thermal Efficiency vs Current Density for different T_{SOFC} values

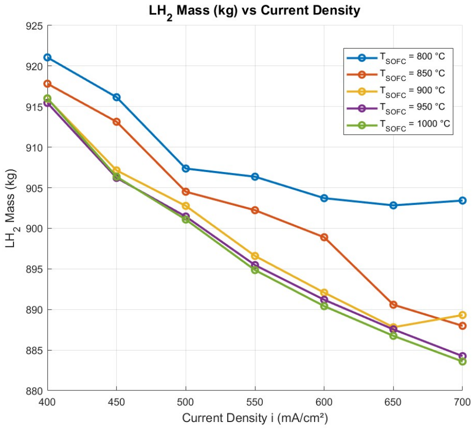

Figure 6.24: LH2 Mass vs Current Density for different T_{SOFC} values

Figures 6.23 and 6.24 show the variation in overall thermal efficiency of the SOFC-GT powertrain and the required LH_2 mass, for varying design current densities and cell operating temperatures. As seen in Figure 6.23, the overall efficiency of the system decreases steadily with the design current density (similar in trend to the fuel cell thermal efficiency in Figure 6.14, suggesting a strong dependence), and increases with the cell operating temperature. The LH_2 mass, on the other hand, shows an initial steady dip before increasing at higher current densities, a phenomenon which is more prominent at lower cell operating temperatures. This parabolic trend of fuel mass can be attributed to the decreasing overall efficiency now playing a more dominant role over the effect of the system mass in determining the total energy required for the mission, especially at higher design current densities. As we move to higher cell operating temperatures, however, the lower FC gravimetric power densities make the system heavier, leading to any system mass saved through a lower number of stacks at higher design current densities being more dominant with respect to the decreasing overall thermal efficiency (which now exhibits a more gradual gradient compared to lower cell operating temperatures). This leads to the gradient switch being delayed at higher current densities at higher cell operating temperatures, a trend that is visible from Figure 6.24.

6.3. Fuel Utilization

In this section, the sensitivities of Class 1 sizing results to fuel utilization factors across a range of design current densities is studied. The fuel utilization at the stack level is varied from 20% to 90%, with the SOFC cell model accounting for the increased H_2 requirement at lower values of fuel utilization. The increased fuel requirement at the anode for lower values of fuel utilization also results in a corresponding improvement to the diffusion kinetics at the anode, which is modeled through a proportionate increase in the limiting current density to account for better power densities at the stack level. As such i_L values of 900, 1000, 1300, 2000, and 3000 $\mathrm{mA/cm^2}$ is assumed for fuel utilization factors of 90%, 85%, 60%, 40%, and 20%, respectively.

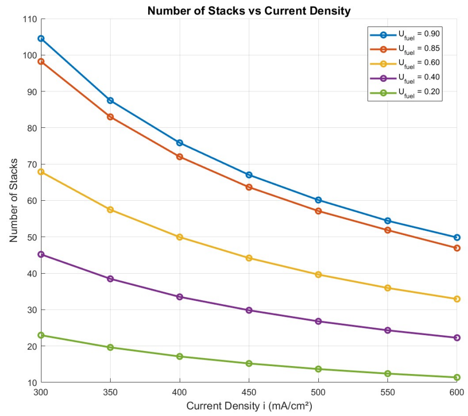

Figure 6.25: Number of Stacks vs Current Density for different $\mathrm{U_{fuel}}$ values

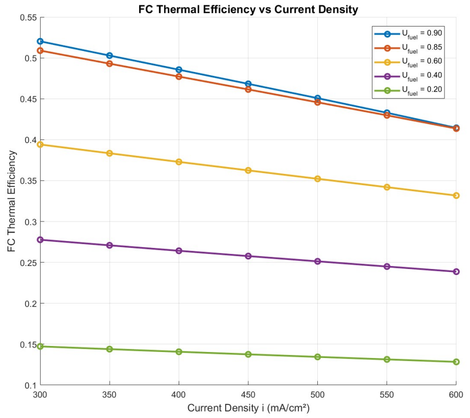

Figure 6.26: η_{FC} vs Current Density for different $\mathrm{U_{fuel}}$ values

From Figures 6.25 and 6.26, it can be observed that both the number of stacks and the fuel cell thermal efficiency show decreasing trends with respect to the fuel utilization factor. While this may seem quite counterintuitive, this behavior can be explained through the increasing demand of H_2 fuel with decreasing fuel utilization at the stack level, reducing the fuel cell thermal efficiency at the stack level. The reduced number of stacks at lower fuel utilization values can be explained through the increasing gravimetric power density at the stack level, which is suggestive of lesser losses (specifically mass transport losses) at lower values of fuel utilization. The combination of a higher fuel requirement (to maintain the same design current density) and a greater gravimetric power density at both cell and stack levels explains this trend. The fuel cell mass, which scales with the total number of stacks, shows a similar trend as the number of stacks, as shown in Figure 6.28.

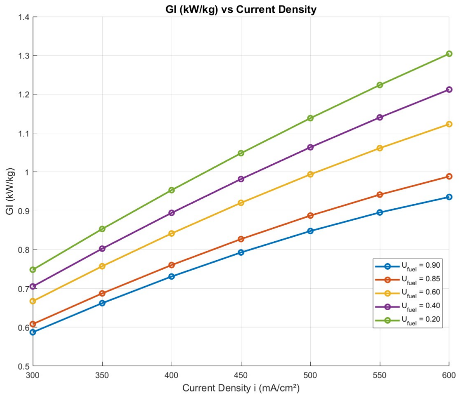

Figure 6.27: $\mathrm{GI_{FC}}$ vs Current Density for different $\mathrm{U_{fuel}}$ values

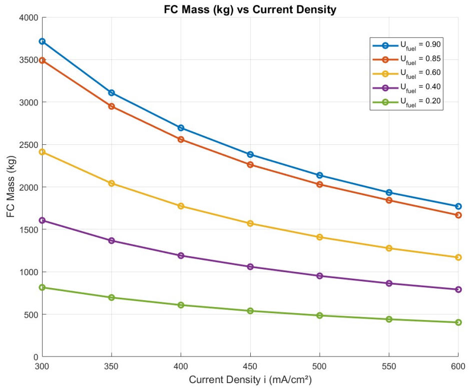

Figure 6.28: Fuel Cell Mass vs Current Density for different $\mathrm{U_{fuel}}$ values

On the other hand, the gas turbine thermal efficiency in cruise (shown in Figure 6.29) generally shows an increasing trend with decreasing fuel utilization. This is a direct consequence of the lesser sizing number of stacks at lower values of fuel utilization, leading to a lower requirement of preheated air and a lower total temperature drop of exhaust gases passing through the air preheater. Therefore, the total flow enthalpy available for propulsion through the power turbine also increases, leading to a proportionate increase in the value of η_{GT}. This trend however, shows a reversal after $\mathrm{U}_{\mathrm{fuel}} = 0.85$, with 95% fuel utilization showing a slightly higher value of η_{GT}. This can be explained through the effect of the released waste heat $\dot{\mathrm{Q}}_{\mathrm{SOFC}}$, which adds to the total enthalpy of the species exiting the SOFC (excess air, fuel, and steam), being dominant at higher values of fuel utilization, where η_{FC} is also less. Consequently, the gas turbine and the heat exchanger mass, shown in Figures 6.30 and 6.32, also show a decreasing trend with reducing fuel utilization. While the gas turbine mass is a function of the required total propulsive power at sizing conditions, the area for heat transfer scales with the total heat load, which in this case, decreases with lower fuel utilization as the air mass flow requirement to the preheaters also decreases.

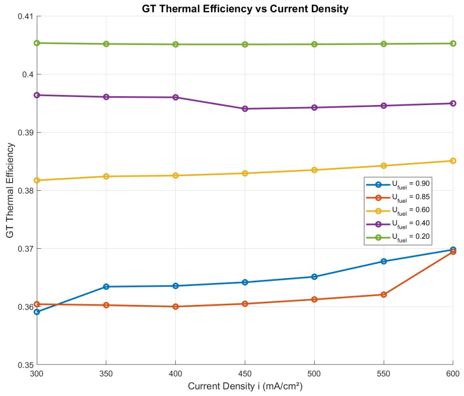

Figure 6.29: η_{GT} vs Current Density for different $\mathrm{U}_{\mathrm{fuel}}$ values

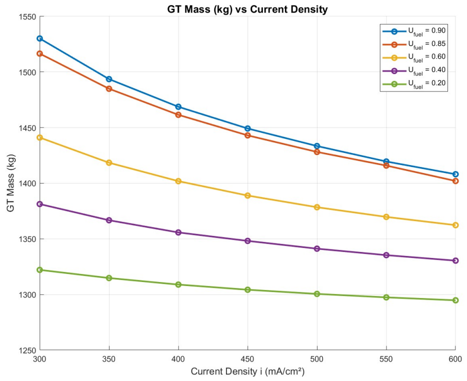

Figure 6.30: GT Mass vs Current Density for different $\mathrm{U}_{\mathrm{fuel}}$ values

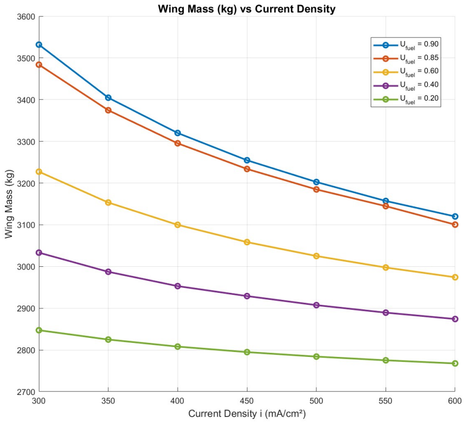

Figure 6.31: Wing Mass vs Current Density for different $\mathrm{U}_{\mathrm{fuel}}$ values

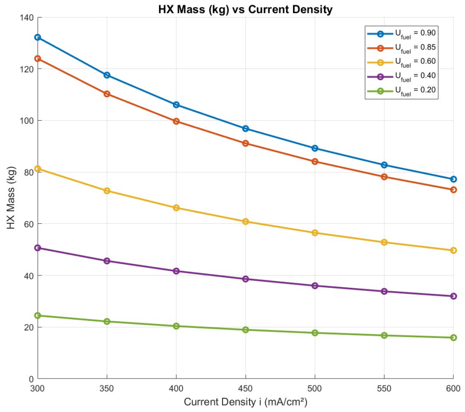

Figure 6.32: HX Mass vs Current Density for different $\mathrm{U}_{\mathrm{fuel}}$ values

As expected, the trends of the MTOM and OEM are quite similar, which suggests that the influence of the powertrain and the wing is quite dominant over fuel mass (or the energy requirements for the sizing mission). The overall SOFC-GT thermal efficiency and the $\mathrm{LH_2}$ mass also generally show a decreasing trend with lower values of fuel utilization; however, the fuel requirement at 85% and 90% utilization shows an interesting crossover at a design current density of 350 $\mathrm{mA/cm^2}$. This can be explained on similar lines as the increase in gas turbine efficiency at higher fuel utilization values, where the dominance of the heat produced by the large number of stacks reduces the energy requirement from the LH_2 fuel. Additionally, Figure 6.36 also shows a crossover between the trends at 20% and 40% fuel utilization at 500 $\mathrm{mA/cm^2}$, where the decrease in the overall thermal efficiency (-5.1%) is larger than the decrease in OEM (-4.5%), thereby leading to a slightly higher energy requirement despite the savings in the operating empty mass of the system.

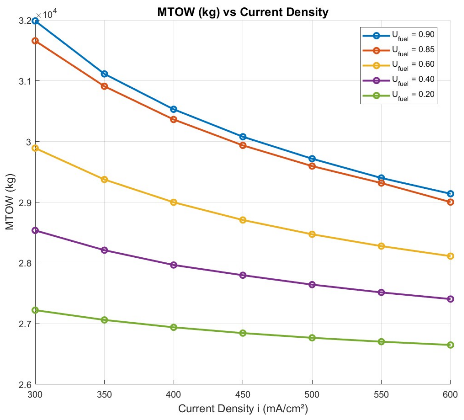

Figure 6.33: MTOM vs Current Density for different $\mathrm{U_{fuel}}$ values

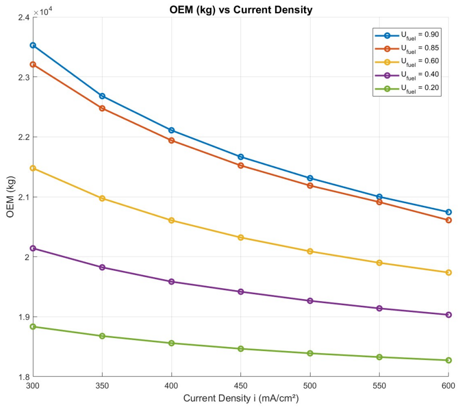

Figure 6.34: OEM vs Current Density for different $\mathrm{U_{fuel}}$ values

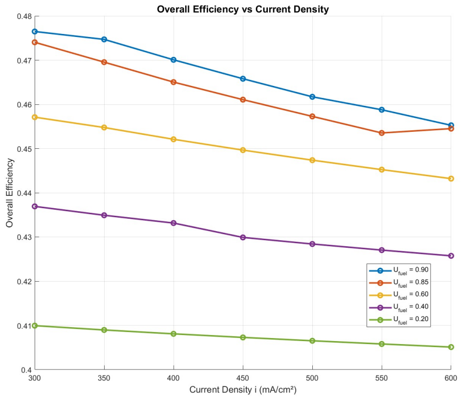

Figure 6.35: Overall Thermal Efficiency vs Current Density for different $\mathrm{U_{fuel}}$ values

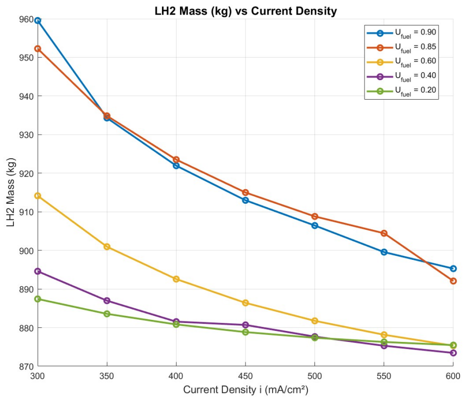

Figure 6.36: LH2 Mass vs Current Density for different $\mathrm{U_{fuel}}$ values

6.4. Air Stoichiometric Ratios

The effects of increasing the air supplied to the cathodes of the SOFC stacks on the Class 1 sizing results is studied in this section; where the excess air ratio λ_{air} is varied from stoichiometric values (i.e. $\lambda_{\mathrm{air}} = 1$) to 8 times the stoichiometric requirement. As mentioned previously in Section 4.6.1, an excess of air is always supplied to the SOFC stacks in order to help maintain the SOFC operating temperature and to ensure minimal mass transport losses during fuel cell operation. As such, the reduction in mass transport losses with higher excess air supply to the SOFC cathodes can be modeled by using the limiting current density i_L (similar to the effect of decreasing fuel utilization); where values of 650, 750, 2000, and 3000 $\mathrm{mA/cm^2}$ are assumed for λ values of 1,3,6 and 8 respectively. The value of the limiting current density at $\lambda_{\mathrm{air}} = 4$ is estimated for the system pressure of 4.5 atm at 1114 $\mathrm{mA/cm^2}$, using the pressure correction for the limiting current density as proposed by Freeh et.al. in Equation 5.1.

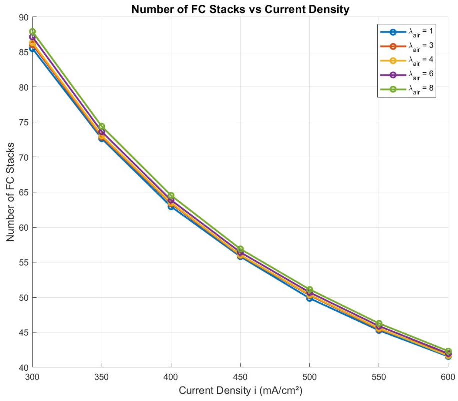

Figure 6.37: Stack Count vs Current Density for different air stoichiometric ratios

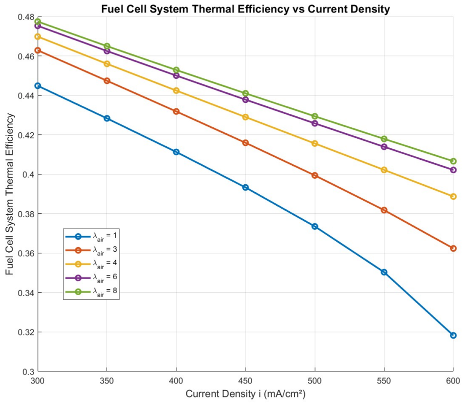

Figure 6.38: η_{FC} vs Current Density for different air stoichiometric ratios

Figures 6.37 and 6.38 show the variation in the number of stacks and the fuel cell thermal efficiency, for varying design current densities and air stoichiometric ratios. From Figure 6.38, the fuel cell thermal efficiency at the stack level increases with increasing values of λ, which can be attributed to lower mass transport losses at the cell and stack levels. Consequently, the number of stacks show a reverse trend, with a slight increase in the number of stacks at higher λ values. Although the fuel cell is more efficient with increasing excess air at the cathode, the corresponding design power loading of the fuel cell system at sizing conditions ($(\mathrm{W/P})_{\mathrm{FC,design}}$) is also proportionately lower (suggesting a higher sizing power). The increase in the sizing power of the fuel cell system (10.3%) between $\lambda = 1$ and $\lambda = 8$ at 300 $\mathrm{mA/cm}^2$ is higher than the stack power density improvement (7.3%), which translates to a slightly higher number of stacks at $\lambda = 8$ despite an increase in the SOFC thermal efficiency at the stack level. The increase in the gravimetric power density at the stack level (shown in Figure 6.39) follows from the increase in the fuel cell thermal efficiency, while the trend of the fuel cell mass (shown in Figure 6.40) follows directly from the trend for the number of stacks.

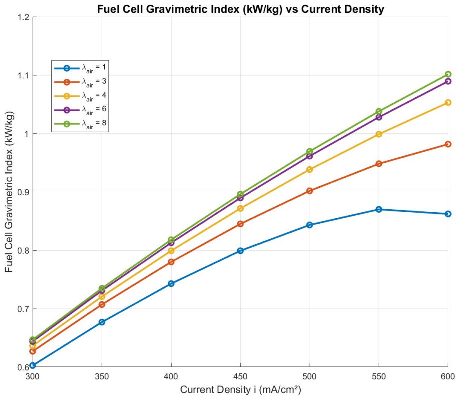

Figure 6.39: $\mathrm{GI}_{\mathrm{FC}}$ vs Current Density for different air stoichiometric ratios

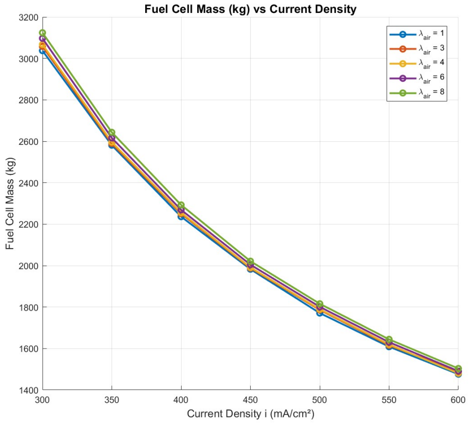

Figure 6.40: Fuel Cell Mass vs Current Density for different air stoichiometric ratios

The gas turbine efficiencies show an opposite trend, increasing with λ values close to stoichiometric conditions, with the change being higher with increasing current densities. The incremental change between $\lambda = 1$ and $\lambda = 8$ at 600 $\mathrm{mA/cm}^2$ is +9.2% compared to +6.4% at 300 $\mathrm{mA/cm}^2$, which is expected, as the SOFC rapidly loses efficiency at higher current densities owing to mass transport losses. The gas turbine mass also scales accordingly, showing an increase of +1.1% and +1.6% between λ values of 1 and 8 at design current densities of 300 and 600 $\mathrm{mA/cm}^2$ respectively. As mentioned previously, this is also a direct consequence of the increasing system mass- with increasing λ, the mass of the wing, stacks, gas turbine, and the heat exchangers all show an increase, resulting in a similar trend with the OEM as well (Figure 6.46). The increase in the heat exchanger area with λ values can be attributed to the increasing mass flow of air at the cold side of the air preheater, increasing the heat minimum heat capacity ($\mathrm{C_{min}}$, which is mostly for the cold side in this case) of the air preheater, leading to an corresponding increase in heat transfer area as well.

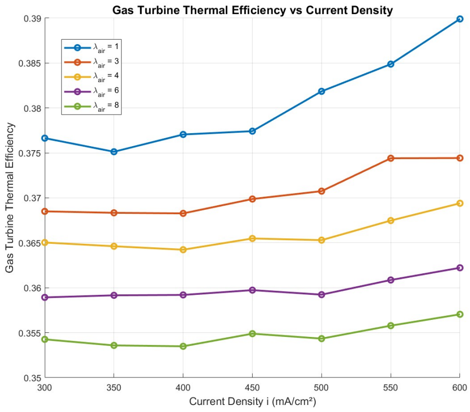

Figure 6.41: η_{GT} vs Current Density for different air stoichiometric ratios

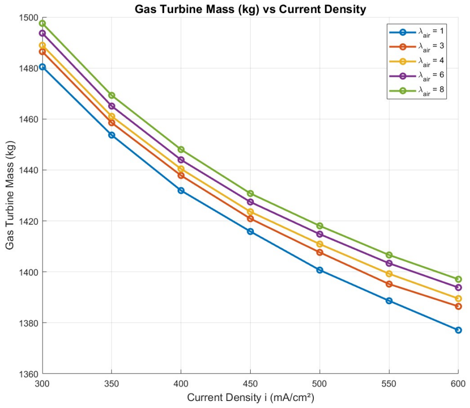

Figure 6.42: GT Mass vs Current Density for different air stoichiometric ratios

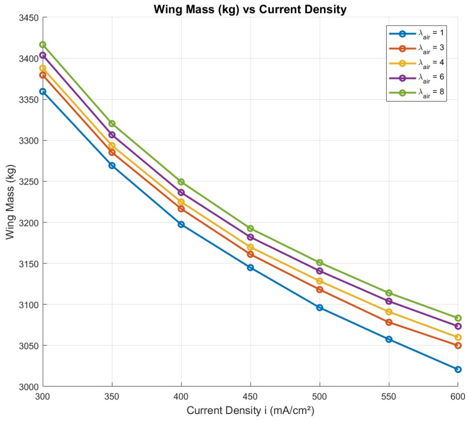

Figure 6.43: Wing Mass vs Current Density for different air stoichiometric ratios

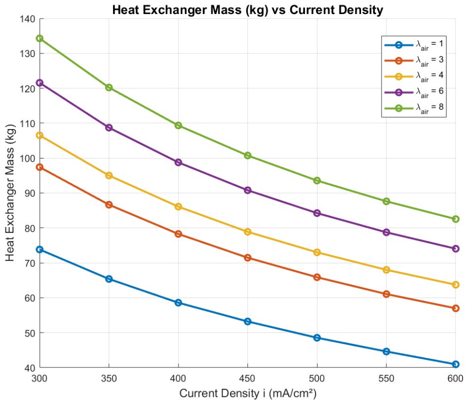

Figure 6.44: HX Mass vs Current Density for different air stoichiometric ratios

The overall thermal efficiency of the SOFC-GT powertrain is observed to decrease with increasing excess air being supplied to the stacks, and this can be explained by the dominating effect of the gas turbine efficiency over the fuel cell thermal efficiency at higher values of λ. At a design current density of 300 $\mathrm{mA/cm^2}$, although the drop in gas turbine thermal efficiency (-5.8%) between $\lambda = 1$ and $\lambda = 8$ is lower than the gain in fuel cell thermal efficiency (7.3%) within the same range of λ, the air and fuel mass flows being diverted to the gas turbine for combustion is larger than the mass flows (both fuel and air) being utilized within the stacks, leading to a dominating contribution of the gas turbine to the output shaft power of the SOFC-GT powertrain. This phenomenon becomes more significant at lower values of $\mathrm{H_{2,split}}$, $\mathrm{U_{fuel}}$, and higher values of λ, wherein the fuel cell has to be extremely efficient with respect to the gas turbine to have a dominating effect on the output shaft power that is used for propulsion.

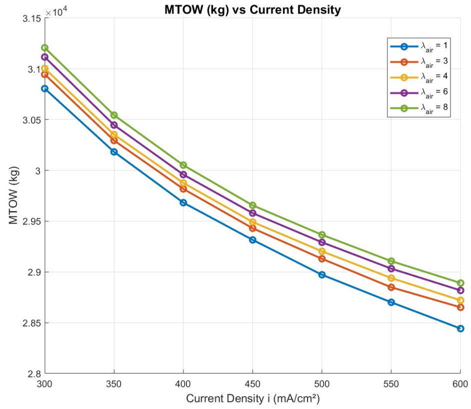

Figure 6.45: MTOM vs Current Density for different air stoichiometric ratios

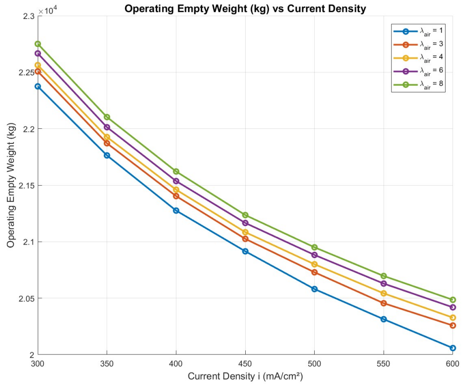

Figure 6.46: OEM vs Current Density for different air stoichiometric ratios

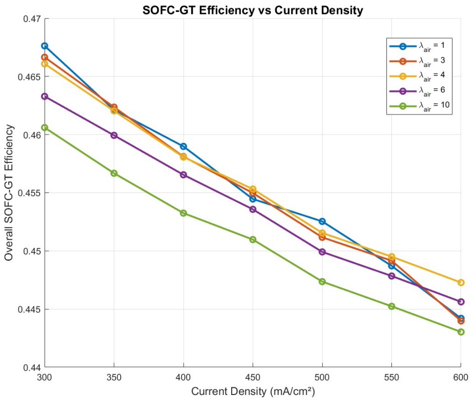

Figure 6.47: Overall Thermal Efficiency vs Current Density for different air stoichiometric ratios

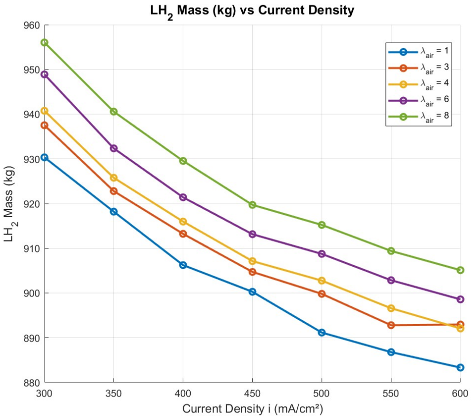

Figure 6.48: LH2 Mass vs Current Density for different air stoichiometric ratios

Additionally, it can also be observed from Figure 6.47 that the overall thermal efficiency values for $\lambda = 6$ and $\lambda = 8$ show a sharp dip at higher design current densities ($> 500\mathrm{mA/cm^2}$), where the drop in fuel cell thermal efficiency and the gravimetric power density at the stack level also show a sharp dip due to lower values of i_L, or significant mass transport losses. The LH_2 mass in Figure 6.48 also shows an abrupt jump for $\lambda = 3$ after $550\mathrm{mA/cm^2}$, which can be correlated to the slight drop in gas turbine thermal efficiency for the same conditions (refer to Figure 6.42). The fuel mass trend, shown in Figure 6.48, generally increases with λ, and this is expected, as the OEM also increases with increasing excess air ratios. This leads to the trend of the MTOM replicating the trend of the OEM, as can be seen in Figure 6.45.

6.5. Hydrogen Power Split in Cruise

As mentioned in the previous section, the hydrogen split to the fuel stacks in cruise is a design parameter which, if increased, could possibly lead to a greater contribution of the fuel cell stacks to the output shaft power. While earlier sweeps of fuel utilization and air stoichiometric ratios increased the fuel and air mass flows to the gas turbine at an $\mathrm{H_{2,split}}$ of 0.5, necessitating the fuel cell stacks to be highly thermally efficient in comparison to the gas turbine, this section studies the influence of increasing the fuel mass flow supplied to the SOFC stacks by varying the cruise hydrogen power split from 0.5 to 0.9. A higher hydrogen split is expected to make the best possible use of the higher fuel cell efficiency, and the effects of this on system masses and overall efficiencies is shown from Figures 6.49 to 6.72.

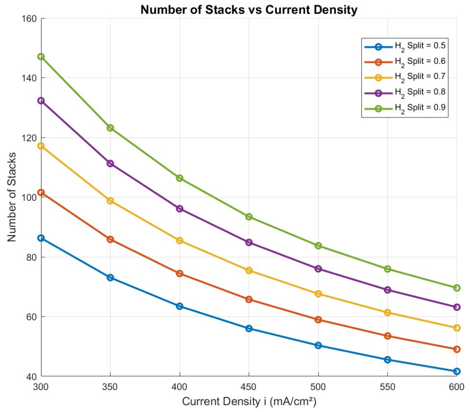

Figure 6.49: Stack Count vs Current Density for different cruise hydrogen splits

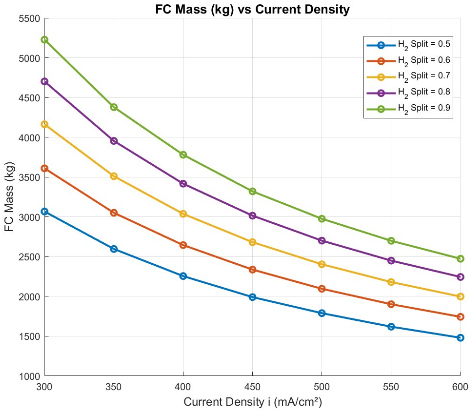

Figure 6.50: Fuel Cell Mass vs Current Density for different cruise hydrogen splits

The number of FC stacks increases quite significantly with an increase in the cruise hydrogen power split, and this results directly from a greater sizing power for the fuel cell system at higher $\mathrm{H}_{2,\mathrm{split}}$ values. From Figure 6.49, it can be observed that while the increase in the number of stacks between $\mathrm{H}_{2,\mathrm{split}}$ values of 0.5 and 0.9 at 300 $\mathrm{mA/cm^2}$ is around 70%, this value decreases slightly to around 66% at 600 $\mathrm{mA/cm^2}$- a trend that can be attributed to the greater gravimetric power density at higher design current densities. As expected, both gravimetric power densities and fuel cell thermal efficiencies at the stack level do not change with respect to $\mathrm{H}_{2,\mathrm{split}}$ values and only show sensitivities to changing design current densities. The fuel cell mass scales with the number of stacks just as with the previous sweeps, and is shown in Figure 6.50.

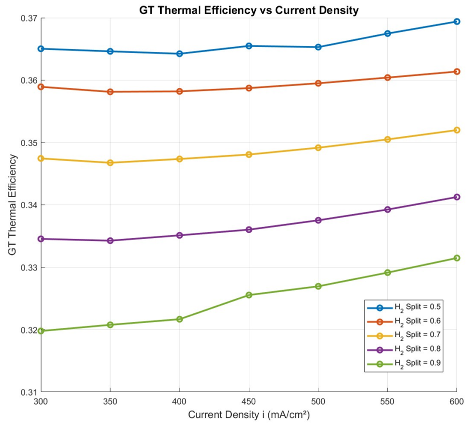

Figure 6.51: η_{GT} vs Current Density for different cruise hydrogen splits

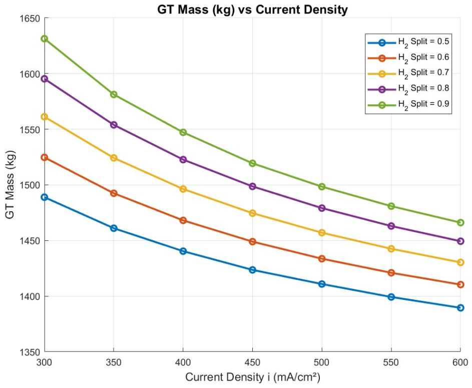

Figure 6.52: Gas Turbine Mass vs Current Density for different cruise hydrogen splits

From Figure 6.51 it can be seen that the trend for gas turbine thermal efficiencies decreases with increasing $\mathrm{H}_{2,\mathrm{split}}$ in cruise, while increasing for higher design current densities. At higher values of $\mathrm{H}_{2,\mathrm{split}}$, the fuel mass flow to the gas turbine combustor decreases for a fixed value for fuel utilization (in this case, 75%), thereby reducing the total flow enthalpy of the exhaust gases in comparison to cases where the value of $\mathrm{H}_{2,\mathrm{split}}$ is lower. For a given pressure ratio of the compressors, SOFC operating temperature, air stoichiometric ratio, and fuel utilization factor, this would mean that the total enthalpy available for the power turbine (and therefore for propulsion) decreases. The total temperature drop of the hot exhaust gases in the heat exchangers is also higher in this case due to the need to preheat more air for the larger number of stacks, further exacerbating this effect. However, it is worth noting that the gain in the gas turbine thermal efficiencies with respect to design current densities is higher at

$\mathrm{H_{2,split}} = 0.9$ (3.6%) than at $\mathrm{H_{2,split}} = 0.5$ (1.2%), which can again be explained by the larger number of stacks at $\mathrm{H_{2,split}} = 0.9$, that now release more heat with decreasing fuel cell thermal efficiency at higher SOFC power densities.

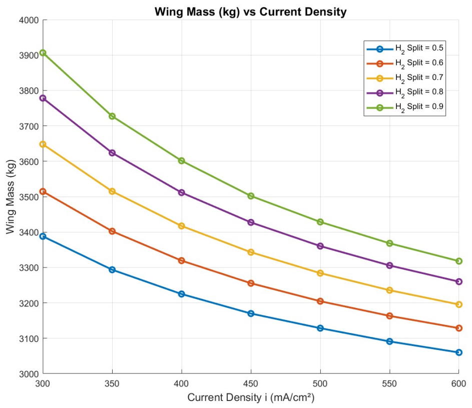

Figure 6.53: Wing Mass vs Current Density for different cruise hydrogen splits

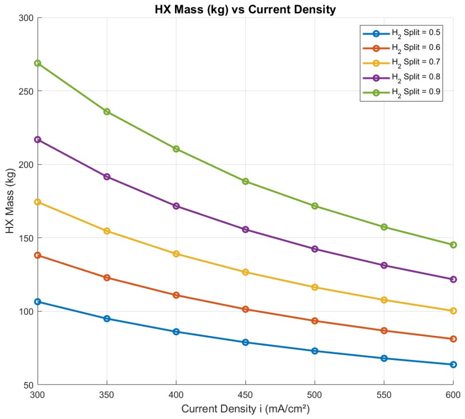

Figure 6.54: HX Mass vs Current Density for different cruise hydrogen splits

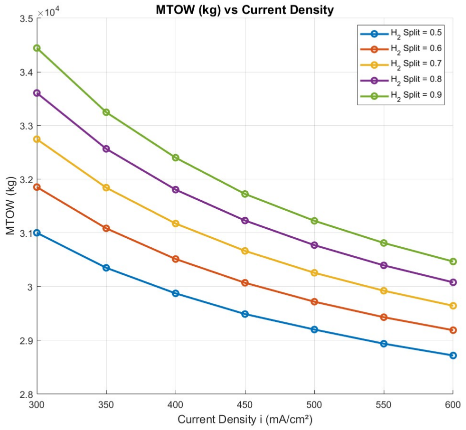

Figure 6.55: MTOM vs Current Density for different cruise hydrogen splits

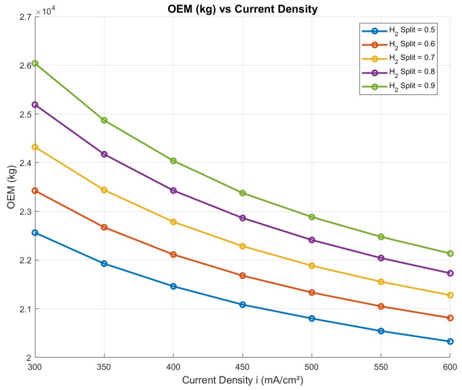

Figure 6.56: OEM vs Current Density for different cruise hydrogen splits

As expected, the operating empty mass shows an increasing trend with $\mathrm{H_{2,split}}$; as the wing, powertrain (GT and SOFC), and the heat exchangers all show an increase. The fuel cell mass increases quite significantly, especially at lower design current densities, and has a dominant contribution to the OEM. The gas turbine mass on the other hand, scales as a function of the total propulsive power requirement at sizing conditions (this increases with higher $\mathrm{H_{2,split}}$ values as the aircraft gets heavier) and the gas turbine thermal efficiency (which decreases at higher $\mathrm{H_{2,split}}$ as shown in Figure 6.51). The heat exchanger mass, which scales with the total area required for heat transfer, is also higher due to the larger number of stacks (this increases both the air and fuel mass flow requirements to the SOFC stacks, subsequently increasing the value of the minimum heat capacity, $\mathrm{C_{min}}$, for heat transfer). Consequently, the OEM shows quite a significant increase at $\mathrm{H_{2,split}} = 0.9$ in comparison to $\mathrm{H_{2,split}} = 0.8$, with a 15% increase observed at 300 $\mathrm{mA/cm^2}$ and an 8.8% increase at 600 $\mathrm{mA/cm^2}$ respectively.

Figures 6.57 and 6.56 show the trends of the overall thermal efficiency and the LH_2 mass requirement, for varying design current densities and hydrogen power split ratios. As expected, an $\mathrm{H_{2,split}}$ of 0.9 gives the highest values of overall thermal efficiencies, ranging from 55% to 51% for the range of design current densities considered. The significantly higher values of overall thermal efficiency at 90% $\mathrm{H_{2,split}}$

partially negate the effects of increasing system mass with regards to the energy requirements for the design mission range, as seen in Figure 6.56. The required LH$_2$ mass is still lesser for 90% $\mathrm{H}_{2,\mathrm{split}}$ than at 50%, even though the OEM is significantly larger in this case. The difference between the energy requirements at 50% and 90% $\mathrm{H}_{2,\mathrm{split}}$ becomes larger at higher design current densities as the aircraft gets even lighter, leading to the high overall thermal efficiencies playing a more significant role in reducing the LH$_2$ mass - at 600 $\mathrm{mA/cm^2}$, the decrease in the OEM is 8.1% in comparison to the increase in the overall thermal efficiency at 14.2%.

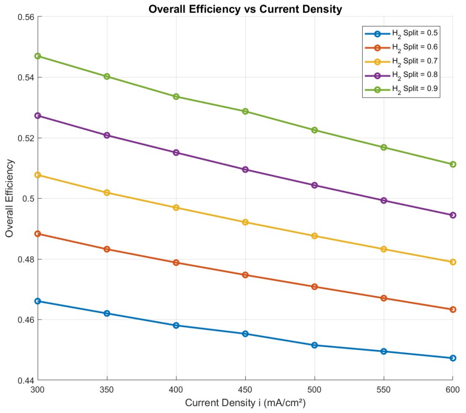

Figure 6.57: Overall Thermal Efficiency vs Current Density for different cruise hydrogen splits

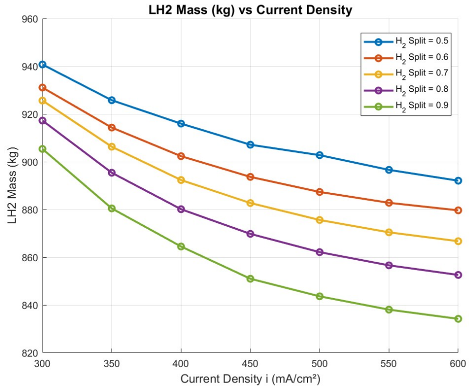

Figure 6.58: $\mathrm{M}_{\mathrm{LH}_2}$ vs Current Density for different cruise hydrogen splits

6.6. SOFC Technology Scenarios

In this section, the effect of varying SOFC technological scenarios on the Class 1 sizing results is studied. To exclusively isolate the effects of technological improvement in SOFCs, the technology scenarios considered in this study assume no significant improvements to other components of the aircraft (for example- the gravimetric indices of the hydrogen tank, heat exchangers, LH$_2$ management system, electric machines, PMAD and fuselage extensions; along with the efficiencies of other powertrain components are taken to be constant). As seen in previous sections, the mass of the SOFC stacks is a prominent driver in the significant increase of the operating empty mass and the energy requirement for the design range of the aircraft. As such, the technology scenarios for SOFCs considered in this study focus on improving the SOFC gravimetric power density at the stack level, by assuming improvements in the cell effective area and the stack mass; along with cell electrochemical parameters such as the limiting current density and the area specific resistance (ASR) which determine the most dominant losses (mass transport and ohmic) in the operation of HT-SOFCs. For the same number of cells in a single stack, the effective area per cell is varied from 1000 to 3000 $\mathrm{cm^2}$ in increments of 500 $\mathrm{cm^2}$, while the stack mass is considered to decrease by 20% with every incremental increase in effective cell area. Cell electrochemical parameters such as i_l and r are also considered to improve with technological scenarios, with i_L showing a 10% improvement and the parameters of the bulk area specific resistance term r in Equation 4.13, showing a 20% decrease with every technological scenario.

As expected, the number of stacks (Figure 6.60) decreases significantly with the increase in gravimetric power densities at the stack level (Figure 6.61). As seen in Figure 6.60, the fuel cell thermal efficiency shows a massive jump between the first two technological scenarios, with the difference being the highest at 600 $\mathrm{mA/cm^2}$ (24%); owing to the significant reduction in ohmic losses. For better technological scenarios however (or higher effective cell areas), the reduction in ohmic losses becomes less significant in further improving the fuel cell thermal efficiency, with the higher value of i_L being more dominant, especially at higher current densities. This is also the reason why the value of the fuel cell thermal efficiency is seen to be reaching a maximum value with better technology scenarios, but this should be considered only as a limitation of the modeling assumptions taken in this study.

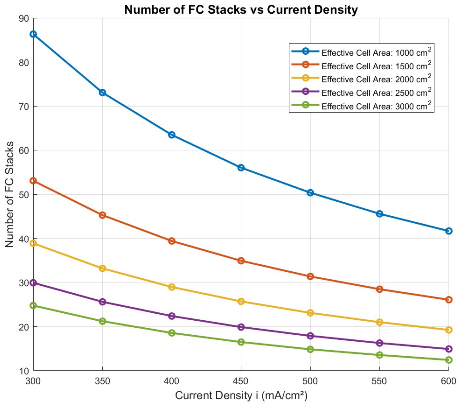

Figure 6.59: Number of Stacks vs Current Density for different SOFC technology scenarios

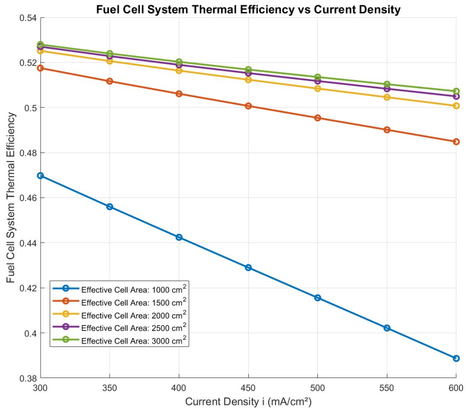

Figure 6.60: η_{FC} vs Current Density for different SOFC technology scenarios

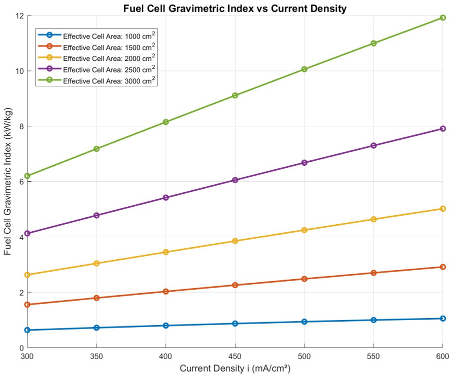

Figure 6.61: $\mathrm{GI}_{\mathrm{FC}}$ vs Current Density for different SOFC technology scenarios

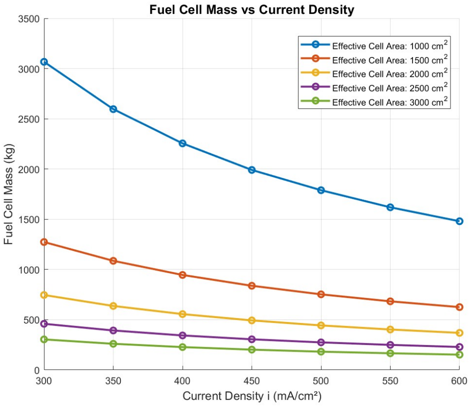

Figure 6.62: Fuel Cell Mass vs Current Density for different SOFC technology scenarios

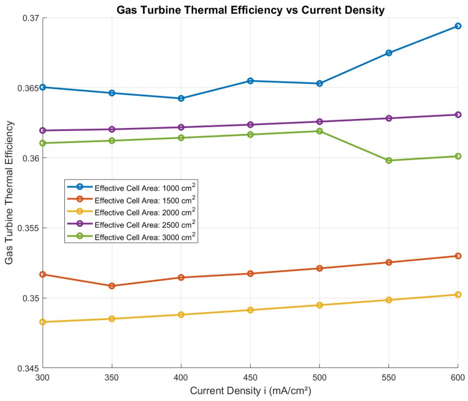

Figure 6.63: η_{GT} vs Current Density for different SOFC technology scenarios

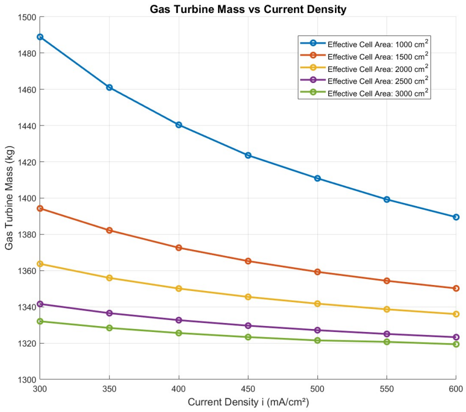

Figure 6.64: GT Mass vs Current Density for different SOFC technology scenarios

The fuel cell mass decreases proportionately with the number of stacks, showing a significant 83% decrease at a design current density of 300 $\mathrm{mA/cm^2}$ due to the massive jump in the stack level gravimetric power density from 0.65 to 6.1 $\mathrm{kW/kg}$ between the first and the most optimistic technological scenarios considered. It is also worth noting from Figure 6.62 that the gradient of the fuel cell mass trend with design current densities is not as steep for the most optimistic technology scenario in comparison to the first technological scenario. This can be explained by the fact that although both the stack-level gravimetric power density and the number of stacks decrease with increasing design current density, the fuel cell sizing power also proportionately reduces (owing to the significantly lighter system) for the most optimistic technological scenario, leading the fuel cell mass to be nearly constant across design current densities.

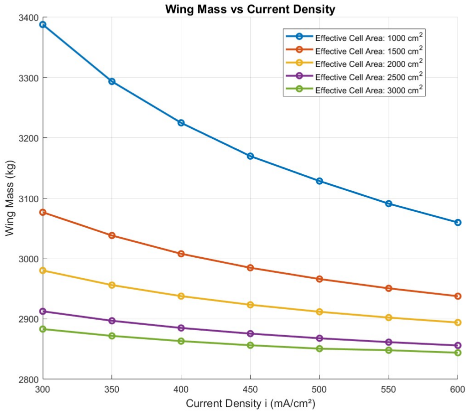

Figure 6.65: Wing Mass vs Current Density for different SOFC technology scenarios

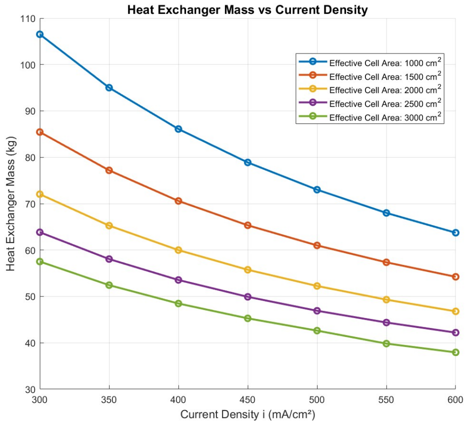

Figure 6.66: HX Mass vs Current Density for different SOFC technology scenarios

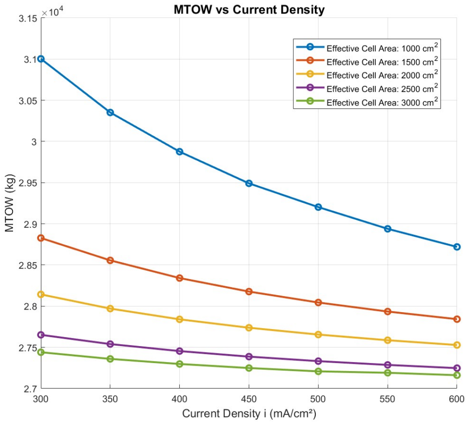

Figure 6.67: MTOM vs Current Density for different SOFC technology scenarios

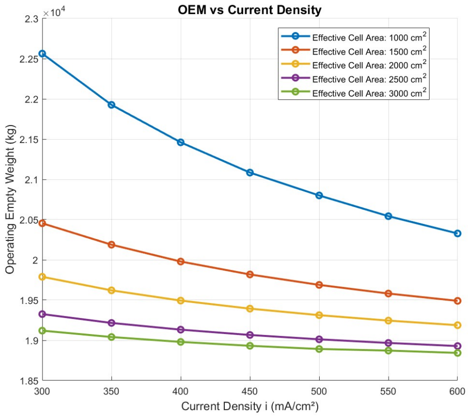

Figure 6.68: OEM vs Current Density for different SOFC technology scenarios

An interesting trend can be observed from Figure 6.63, where the gas turbine efficiencies show a decreasing trend (due to better fuel cell thermal efficiencies) until the fourth technological scenario ($\mathrm{A_{cell}} = 2500\ \mathrm{cm}^2$), where the gas turbine efficiency values how a sudden jump, before decreasing slightly again for the most optimistic technology scenario ($\mathrm{A_{cell}} = 3000\ \mathrm{cm}^2$). While this seems counter-intuitive, as the fuel cell thermal efficiency only keeps getting better with technological scenarios, the increase in the effective cell area now becomes a driving factor in determining the total heat released from each stack, thus leading to the jump in gas turbine thermal efficiency. This trend again reverses in the final technological scenario, where the increase in the fuel cell efficiency and the reduced number of sizing stacks both reduce the total heat being released from the SOFC stacks, despite an increase in the effective cell area. Additionally, the most optimistic technological scenario also shows a drop in gas turbine thermal efficiency values beyond 500 $\mathrm{mA/cm^2}$, which can be attributed to the lesser number of stacks at very high stack gravimetric power densities.

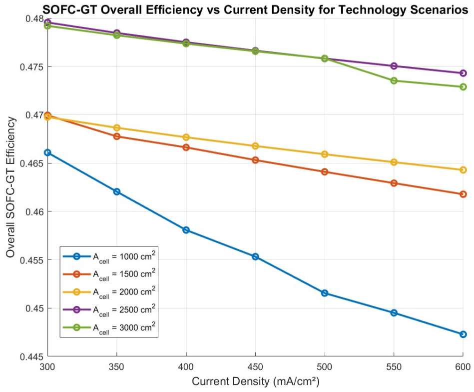

Figure 6.69: Overall Thermal Efficiency vs Current Density for different SOFC technology scenarios

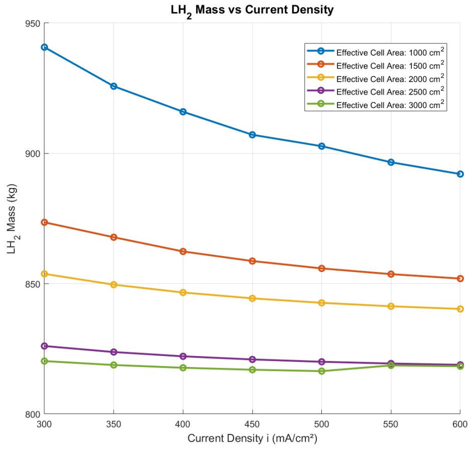

Figure 6.70: LH2 Mass vs Current Density for different SOFC technology scenarios

As a direct consequence of the reduced SOFC stack mass, the GT mass and the wing mass also reduce as the aircraft now gets significantly lighter. The HX mass also reduces with better technology scenarios as the air and $\mathrm{LH_2}$ requirement for the reduced number of stacks is also lesser, directly resulting in a reduced area for heat transfer. Overall, this leads to a significant decrease in both the energy requirement for the design mission and the MTOM. At the 50% hydrogen power split considered in this study, the overall efficiencies for all technological scenarios is also influenced by the gas turbine efficiency trend, where the last two technological scenarios show a significant increase in overall thermal efficiency values, owing to both better fuel cell thermal efficiency as well as a reversal in the gas turbine efficiency trend (as mentioned previously, this increases significantly for $\mathrm{A_{cell}}$ values greater than 2500 $\mathrm{cm^2}$). The dip in the η_{overall} values and the increase in the $\mathrm{LH_2}$ mass for the most optimistic technological scenario beyond design current densities of 500 $\mathrm{mA/cm^2}$ strikingly corresponds to the gas turbine efficiency trend shown in Figure 6.63, suggesting a strong influence.

6.7. Wing Aspect Ratios

In this section, the wing aspect ratio is varied from 12 to 15 to study its sensitivity to Class 1 sizing results of the SOFC-GT aircraft. The results for various parameters, evaluated for the range of wing aspect ratios and the design current densities considered in this study, are presented from Figures 6.72 to 6.85. The design wing loading also shows a sensitivity to the chosen wing aspect ratio values, decreasing by 2.25% between wing aspect ratios of 10 and 15, resulting in a corresponding increase in the wing area along with the wing span, as shown in Figures 6.80 and 6.81.

As seen in Figure 6.72, the number of stacks decreases with increasing wing aspect ratios, as the sizing power for the FC stacks in cruise now decreases due to the reduced induced drag coefficient associated with high aspect ratio wings. Although the wing area does increase slightly at higher aspect ratios in this study (due to the decrease in the design wing loading as shown in Figure 6.71), the reduction in the cruise drag coefficient is more significant, resulting in the reduction of the total drag and the SOFC sizing power requirement in cruise conditions.

The fuel cell mass also decreases correspondingly, scaling with the number of stacks and decreasing with increasing design current densities (due to the increase in the stack gravimetric power density). As expected, the fuel cell thermal efficiency and the gravimetric power density at the stack level only show sensitivities to the design current densities, as can be seen in Figures 6.73 and 6.74.

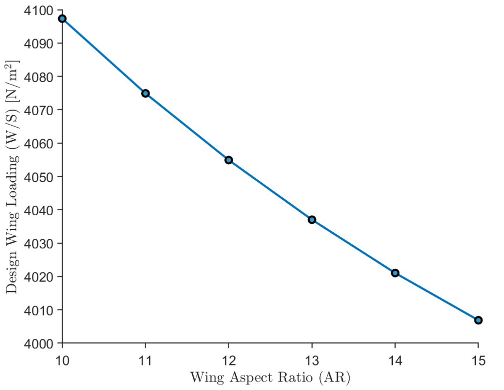

Figure 6.71: Variation of design wing loading with respect to increasing wing aspect ratios

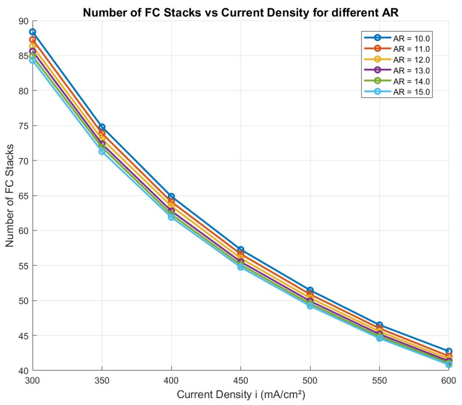

Figure 6.72: Stack Count vs Current Density for different wing aspect ratios

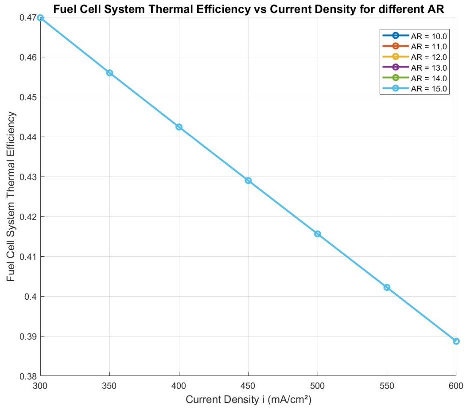

Figure 6.73: η_{FC} vs Current Density for different wing aspect ratios

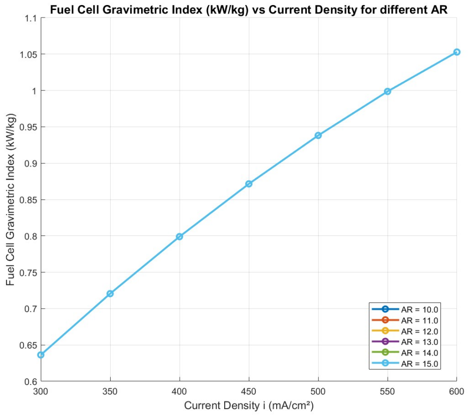

Figure 6.74: $\mathrm{GI}_{\mathrm{FC}}$ vs Current Density for different wing aspect ratios

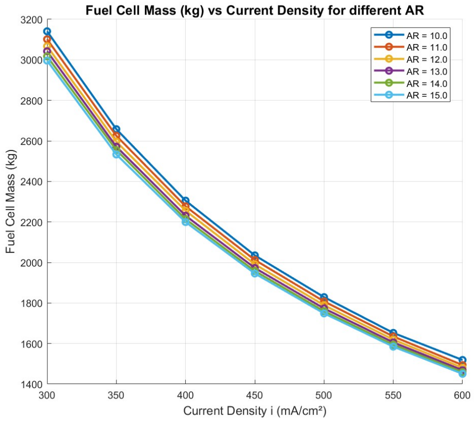

Figure 6.75: Fuel Cell Mass vs Current Density for different wing aspect ratios

The gas turbine efficiency trend shows a decrease with increasing wing aspect ratios, primarily due to the reduced number of stacks and the reduced amount of hydrogen fuel available for combustion (from both the LH_2 tanks and the underutilized fuel from the SOFC stacks). As mentioned previously, the reduced amount of fuel available for combustion decreases the total flow enthalpy of the exhaust gases available for expansion through the power turbine, directly leading to a reduction in the gas turbine efficiency. As usual, the gas turbine efficiency values also show a positive gradient with increasing design current densities, which is, as expected, due to the reduced fuel cell thermal efficiency and the increase in the waste heat rejected by the SOFC stacks.

All components except for the wing show a reduction in mass with increasing wing aspect ratios, which can be observed from the trends of the OEM and the MTOM as well (Figures 6.83 and 6.82). The heat exchanger mass (shown in Figure 6.79) also reduces due to the reduced number of stacks and the corresponding decrease in the mass flow requirements of air and LH_2 to the SOFCs via the heat exchangers, resulting in a reduction of the heat transfer area. Consequently, the LH_2 mass also decreases at higher wing aspect ratios due to the reduction in the operating empty weight of the aircraft, while the overall thermal efficiency in cruise shows an opposite trend with increasing wing aspect ratios. This can be explained by the 50% hydrogen power split considered in this study, where the gas turbine efficiency trend influences the trend of the overall thermal efficiency, primarily due to two reasons: 1) the higher mass flow available for combustion in the gas turbine in comparison to higher values of $\mathrm{H}_{2,\mathrm{split}}$, and 2) the insensitivity of the fuel cell thermal efficiency values to the wing aspect ratios. However, as mentioned previously in Section 6.5, this trend can show a reversal at higher values of $\mathrm{H}_{2,\mathrm{split}}$, albeit at the cost of the increased energy requirement for the same design range.

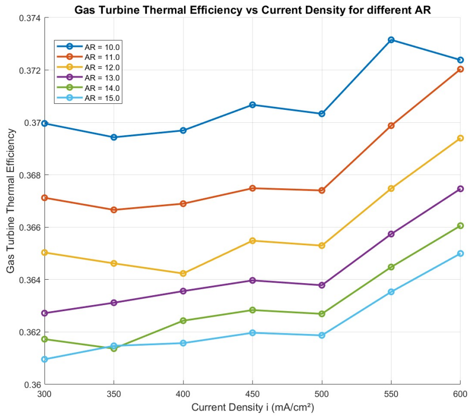

Figure 6.76: η_{GT} vs Current Density for different wing aspect ratios

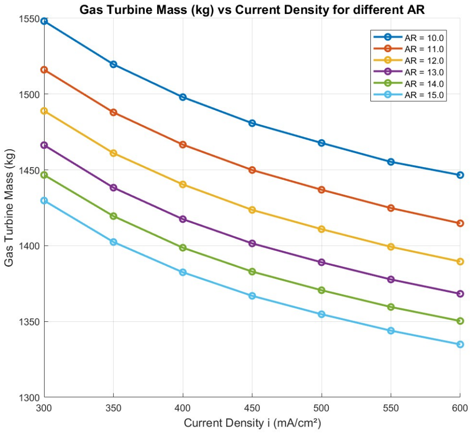

Figure 6.77: GT Mass vs Current Density for different wing aspect ratios

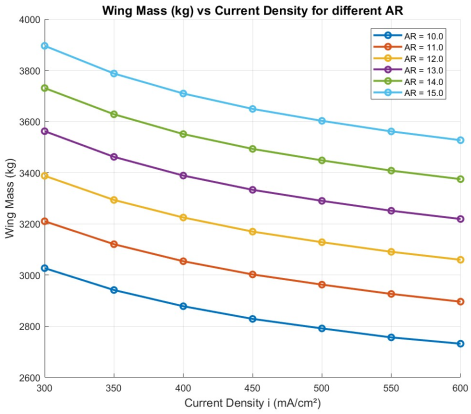

Figure 6.78: Wing Mass vs Current Density for different wing aspect ratios

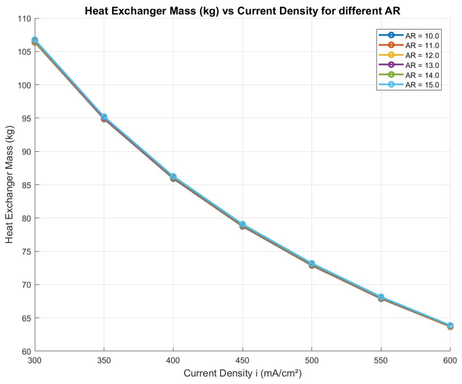

Figure 6.79: HX Mass vs Current Density for different wing aspect ratios

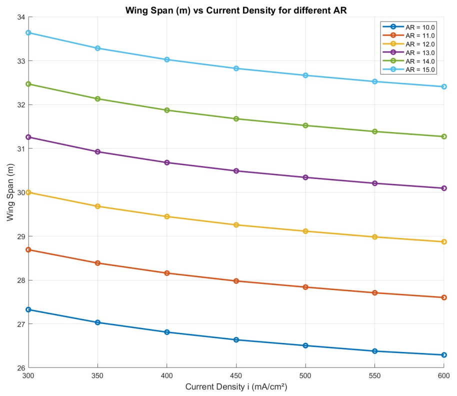

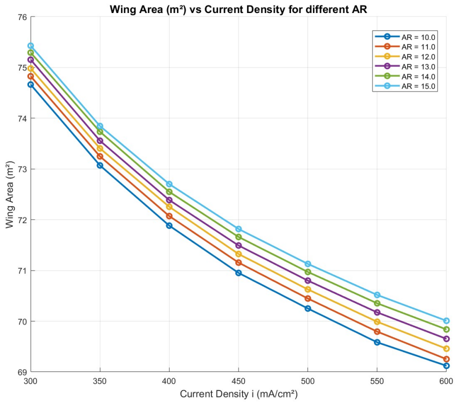

Figure 6.80: Wing Span vs Current Density for different wing aspect ratios

Figure 6.81: Wing Area vs Current Density for different wing aspect ratios

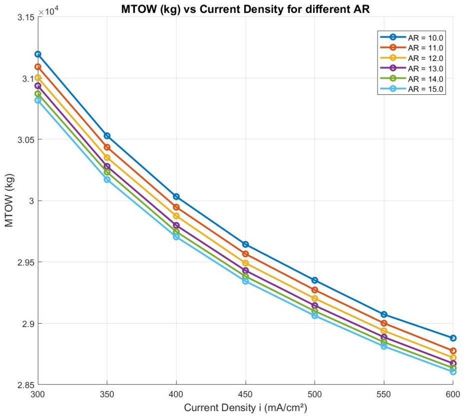

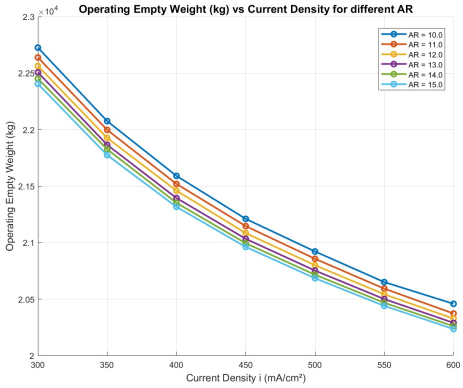

Figure 6.82: MTOM vs Current Density for different wing aspect ratios

Figure 6.83: OEM vs Current Density for different wing aspect ratios

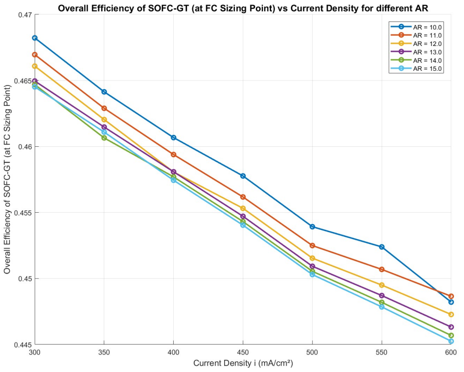

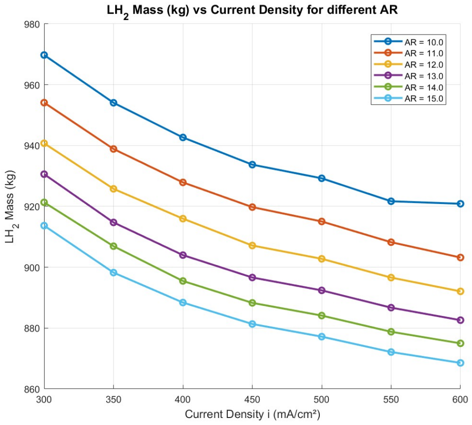

Figure 6.84: Overall Thermal Efficiency vs Current Density for different wing aspect ratios

Figure 6.85: $\mathrm{M_{LH_2}}$ vs Current Density for different wing aspect ratios

7

Conclusions and Recommendations

In the previous chapters, the influence of key design parameters on the performance, sizing, and feasibility of the SOFC–GT powertrain was systematically investigated and studied at the aircraft level. The following observations now summarize the major trends identified from the parametric analyses of SOFC-GT design parameters, highlighting the trade-offs between thermal efficiency, mass, geometry constraints, and mission energy requirements.

- Although SOFC-GT aircraft are generally observed to be **considerably heavier** than conventional kerosene andLH_2-based counterparts (MTOM increases by +19.24% and +14.71% respectively) for similar top-level requirements, they are also significantly **more efficient** (48.37% and +44.06% improvement compared to conventional kerosene and LH_2 powertrains, respectively) overall, leading to reduced energy mass and lower overall emissions over the design range of the aircraft. Although heavier, the increased thermal efficiency makes SOFC-GT powertrains attractive for future regional turboprop aircraft.
- The **hydrogen split ratio in cruise**, $\mathrm{H}_{2,\mathrm{split}}$, is observed to be the **most influential design parameter** in utilizing the potential of the SOFC-GT powertrain. As the SOFC thermal efficiency is not bound by a theoretical limit, such as the ideal Carnot efficiency for gas turbine engines, the best possible way to utilize the maximum potential of the HT-SOFC is to have a greater share of the output shaft power coming from the fuel cells (i.e.more fuel being supplied to the SOFC stacks) in comparison to power output of the gas turbine.
- It is also observed that while a greater value of cruise $\mathrm{H}_{2,\mathrm{split}}$ is beneficial in maximizing the potential of the SOFC-GT powertrain, a low fuel utilization factor would proportionately increase the amount of fuel available for combustion, decreasing the overall thermal efficiency of the system in two ways: 1) by increasing the contribution of the lesser efficient gas turbine to the shaft output power, and 2) by reducing the fuel cell thermal efficiency at the stack level, as a low fuel utilization would need a proportionate amount of fuel to be supplied to the stacks in order to maintain a desired stack power density.
- While a higher value of fuel utilization ($> 75\%$) increases the overall thermal efficiency of the system through better fuel cell thermal efficiencies at the stack level, it can come at the cost of a decline in the stack-level gravimetric power densities due to the increased mass transport losses associated with a lower value of the limiting current density i_L. In order to reduce the mass transport losses at the cell level, higher amounts of excess air $\lambda > 4$ can be supplied to the SOFC stacks. It is also worth noting here that although higher values of λ are extremely beneficial in improving SOFC performance at the cell level, the maximum value of λ is heavily dependent on the number of stacks (this determines the air requirement for the stacks, and is limited by the air mass flow into the gas turbine inlet). Consequently, the maximum possible value of λ for the fixed value of inlet air mass flow considered in this study ($8.49\,\mathrm{kg/s}$), ranges from 8 to 5 for $\mathrm{H}_{2,\mathrm{split}}$ values of 0.5 to 0.95, respectively.
- Although a higher value of $\mathrm{H}_{2,\mathrm{split}}$ in cruise increases the overall cruise thermal efficiency of the

SOFC-GT powertrain, this comes at the cost of increased aircraft mass. For a 90% $\mathrm{H_{2,split}}$ and design current density of 300 $\mathrm{mA/cm^2}$, the operating empty mass (OEM) of the aircraft shows a significant 16% increase in comparison to the 50% $\mathrm{H_{2,split}}$ case, and was expected to increase the energy mass of the aircraft for the same design mission range. However, the relatively higher values of overall cruise thermal efficiency at higher $\mathrm{H_{2,split}}$ values (55% for 300 $\mathrm{mA/cm^2}$ and 90% $\mathrm{H_{2,split}}$) were observed to nullify this increase in the OEM, with the aircraft also requiring a lower energy mass (-3.8%) for the same design mission range across the entire range of design current densities considered.

- The SOFC system pressure and operating temperature are important design parameters that can improve the performance of the SOFC-GT powertrain. However, it is observed that the overall thermal efficiency in cruise shows an **asymptotic behavior at high temperatures and system pressures**, reaching a peak beyond which further improvement in stack level gravimetric power density comes at the penalty of increasing system mass for high operating temperatures and reduced gas turbine and SOFC thermal efficiencies (due to the increased BoP power demands) for higher system pressures.
- The mass of the SOFC stacks, which is a function of the stack level gravimetric power density, is observed to be a prominent driver in increasing the operating empty mass of the aircraft. As such, improving the stack level gravimetric power density of SOFCs through advancements in SOFC technology at the cell level (reduced mass transport and ohmic losses, higher effective cell area, and reduced cell mass) can prove to be a deciding factor in the practical feasibility of SOFC-GT powertrains in short-medium range aircraft.
- For design values of $\mathrm{H_{2,split}} > 0.9$ in the baseline aircraft, improvements in SOFC technology should focus on achieving stack-level gravimetric power densities of atleast 1.8 $\mathrm{kW/kg}$ or above to stay within 10% of the reference wingspan, and within 20% of the reference MTOM. Although the maximum wing span of the sized SOFC-GT aircraft at a wing aspect ratio of 12 (which is 31.75 m at $\mathrm{H_{2,split}} = 0.95$, $\mathrm{GI_{FC,stack}} = 646\mathrm{W/kg}$ and $i =$ 300 $\mathrm{mA/cm^2}$) never exceeds the maximum span limit of 36 m for ICAO Class C aircraft (per ICAO Annex 14 Volume 1 [44]) across the range of current densities considered in this study, the 10% and 20% constraints on the wing span and MTOM are considered for the best compliance with existing airport infrastructure operating the ATR 72-600 aircraft.
- The effect of increasing the wing aspect ratio of the baseline aircraft design to reduce the cruise drag and, correspondingly, the SOFC sizing power requirement in cruise comes with several considerations. At a design $\mathrm{H_{2,split}}$ of 0.95, current density of 300 $\mathrm{mA/cm^2}$, and technology scenario corresponding to a stack level gravimetric power density of 646 $\mathrm{W/kg}$, a variation in the wing aspect ratio was observed to result in a negligible reduction in overall thermal efficiency values (-0.13% between aspect ratios 12 and 15). However, a more significant change in the energy mass was observed, with the $\mathrm{LH_2}$ mass decreasing by 2.9% for the same range of aspect ratio values. Although a higher wing aspect ratio increases the wing mass due to a larger wing span and area, the OEM still reduces by around 1% due to the reduction in SOFC, GT, HX, and $\mathrm{LH_2}$ tank masses. However, it should be noted that this decrease in the OEM driving the savings in total energy mass is heavily dependent on the reduction in the number of stacks and the value of the stack-level gravimetric density. As such, for improved SOFC technological scenarios, the savings in OEM and $\mathrm{LH_2}$ mass are expected to decrease further, and the reduction in overall system efficiency is anticipated to have a greater impact on the aircraft's energy mass.
- As such, increasing the wing aspect ratio with a slight penalty in the overall system efficiency can only be of practical significance for current SOFC technology scenarios with lower values of stack-level gravimetric density (0.6 - 1.5 $\mathrm{W/kg}$) and design $\mathrm{H_{2,split}} > 0.5$ with its benefits of reducing the system mass, energy requirement, and overall emissions of the aircraft for the nominal design mission. The maximum possible value of wing aspect ratio (calculated at a design current density of 300 $\mathrm{mA/cm^2}$) is sensitive to the value of the design $\mathrm{H_{2,split}}$ considered and is limited by the 36 m span limitation for ICAO Class C aircraft (a design $\mathrm{H_{2,split}} = 0.95$ touches this limit for a wing aspect ratio of 14.5).

7.1. Limitations and Recommendations for Future Work

To further improve the accuracy, applicability, and robustness of the sizing methodologies for SOFC–GT aircraft which were developed throughout this study, several areas of future work have been identified. These recommendations aim to address gaps in modeling fidelity and the integration of additional operating conditions of the SOFC-GT powertrain, along with several others, and are outlined below.

- Performing Class 2 sizing of the SOFC-GT aircraft to evaluate its longitudinal, lateral, and directional stability characteristics, control surface sizing, and trim conditions across the operational envelope. As observed throughout this study, the mass of SOFC stacks for current technology scenarios would be a significant addition to the aircraft's empty mass. As such, the placement of these stacks (including BoP) within the aircraft would affect its stability and require appropriately sized control surfaces to trim the aircraft, adding to the drag and fuel consumption, which can only be studied in sufficient detail through a Class 2 and 2.5 sizing of the SOFC-GT aircraft.
- Develop detailed geometric models of BoP components of the SOFC-GT powertrain, such as LH_2 management and pneumatic systems,LH_2 tanks, exhaust gas lines, gas turbines, and heat exchangers for specific top-level requirements. For example, the sizing of LH_2, air, and exhaust gas supply lines in this study linearly scales with the number of stacks, and is only an approximation based on the author's elaboration.
- Improvement in the fidelity of the gas turbine combustion model to better predict the mechanism of hydrogen combustion under a wider range of operating conditions, especially for higher equivalence ratios (fuel-rich conditions), system pressures, and operating temperatures. Although the GRI-Mech 3.0 mechanism (which is used in this study to model exhaust gas properties) fairly predicts the kinetics of H_2 combustion under pre-mixed, lean conditions, it is not optimized for pure hydrogen flames and pressures exceeding 10 atm.
- The current work exclusively focuses on sizing the SOFC-GT aircraft for cruise conditions, and only analyzes the energy requirement of such aircraft for nominal missions which utilize the SOFC-GT powertrain in cruise conditions (including diversion) and the gas turbine engine for the rest. As such, this presents the scope for analyzing missions where the SOFC-GT powertrain is also utilized in conditions other than cruise, and the possibility of incorporating this into an optimization framework that minimizes total energy requirement and emissions over the design range of the aircraft.
- As mentioned earlier in the conclusions of this study, an improvement of SOFC stack-level gravimetric power densities (> 1.5 $\mathrm{kW/kg}$) would be crucial in practically achieving higher levels of cruise $\mathrm{H_{2,split}}$, without significant penalties on aircraft mass and energy requirements for the design mission. However, achieving these levels of gravimetric power densities necessitates optimization of SOFC geometry at both cell and stack levels, which presents an opportunity for future work.
- Integration of 1-D SOFC electrochemical models within the SOFC-GT sizing loop, which takes into account spatial variations in SOFC operating temperature, species concentration, and cell current densities across the length of the cells and stacks, for a better prediction of SOFC performance (stack efficiencies and power densities) without significantly increasing computational costs.
- Perform failure mode analysis for SOFC-GT powertrains, including possible inclusion of batteries for redundancy, emergency power requirements, and better transient response to varying load conditions across the flight envelope. Studying the transient behavior of SOFC-GT powertrains, therefore, presents a scope for future work, including the detailed modeling of the secondary powertrain to improve the dynamic response of the system.
- As mentioned in Section 6.6, the technology scenarios in this study assume no major improvements to other SOFC-GT aircraft components, in order to isolate the effects of SOFC advancements at the aircraft level. This is not fully representative, as future advancements in materials, gas turbine engines, and electrical systems could significantly affect SOFC-GT powertrain design and their practical application in regional turboprop aircraft. Hence, analyzing improvements across all possible technology scenarios in future work would be beneficial to fully understand their full impact on SOFC-GT aircraft sizing.

References

[1] RK Ahluwalia et al. "Performance and cost of fuel cells for urban air mobility". In: *International Journal of Hydrogen Energy* 46.74 (2021), pp. 36917–36929.

[2] Khaled Alsamri et al. "Dynamic modeling of Hydrogen SOFC/GT powered Aircraft with integration analysis". In: *AIAA SCITECH 2024 Forum*. 2024, p. 1532.

[3] John W Arblaster. *Selected values of the crystallographic properties of elements*. ASM International, 2018.

[4] Eglantine Arendt et al. "Structuration of LaMnO3 perovskite catalysts on ceramic and metallic monoliths: Physico-chemical characterisation and catalytic activity in methane combustion". In: *Applied Catalysis A: General* 339.1 (2008), pp. 1–14.

[5] Tad J Armstrong and Anil V Virkar. "Performance of solid oxide fuel cells with LSGM-LSM composite cathodes". In: *Journal of the Electrochemical Society* 149.12 (2002), A1565.

[6] ATR Aircraft. *ATR 72-600 Brochure*. `https://www.atr-aircraft.com/wp-content/uploads/2020/07/Factsheets_-_ATR_72-600.pdf`. Accessed: 2025-07-12. 2023.

[7] Avions de Transport Régional (ATR). *ATR: The Optimum Choice for a Friendly Environment*. Brochure. CO/EM 467/00. 1 allée Pierre Nadot, 31712 Blagnac Cedex, France, June 2001. url: `https://www.atraircraft.com`.

[8] Ahmad Baroutaji et al. "Comprehensive investigation on hydrogen and fuel cell technology in the aviation and aerospace sectors". In: *Renewable and sustainable energy reviews* 106 (2019), pp. 31–40.

[9] Alessandro Borgia. *Double-Hybrid Powertrain Modelling and Integration in a Conceptual Design Method of Hydrogen Powered Aircraft*. 2025.

[10] G Daniel Brewer. *Hydrogen aircraft technology*. Routledge, 2017.

[11] A. Burcat and B. Ruscic. *Third Millennium Ideal Gas and Condensed Phase Thermochemical Database for Combustion*. Tech. rep. ANL-05/20. Argonne National Laboratory, 2005. url: `https://chemweb.bgu.ac.il/thermodynamics/`.

[12] Q Cai et al. "A sizing-design methodology for hybrid fuel cell power systems and its application to an unmanned underwater vehicle". In: *Journal of Power Sources* 195.19 (2010), pp. 6559–6569.

[13] Michele Casarin and Vincenzo M Sglavo. "Influence of processing conditions on the microstructure of NiO-YSZ supporting anode for solid oxide fuel cells". In: *Ceramics International* 41.2 (2015), pp. 2543–2557.

[14] Jeffryes W Chapman. "Utilizing electrical power extraction for stability bleed reduction within gas turbine engines". In: *AIAA Propulsion and Energy 2021 Forum*. 2021, p. 3477.

[15] Riccardo Concetti et al. "On the Chemical Effect of Steam Addition to Premixed Hydrogen Flames with Respect to NO x Emissions and Flame Speed". In: *Flow, Turbulence and Combustion* 113.2 (2024), pp. 519–534.

[16] David L Cook. "Development of the PW100 turboprop engines". In: *SAE transactions* (1985), pp. 740–746.

[17] V Danchuk et al. *Nanocrystalline cubic phase scandium-stabilized zirconia thin films. Nanomaterials. 2024; 14: 708*.

[18] Anubhav Datta. "PEM fuel cell model for conceptual design of hydrogen eVTOL aircraft". In: (2021).

[19] [Reynard] De Vries. “Hybrid-Electric Aircraft with Over-the-Wing Distributed Propulsion: Aerodynamic Performance and Conceptual Design”. In: *Journal Name* (2024). doi: `10.4233/uuid:ef87dc11-e7b2-4726-a41f-28588d64c58d`. url: `https://doi.org/10.4233/uuid:ef87dc11-e7b2-4726-a41f-28588d64c58d`.

[20] Andrew L Dicks and David AJ Rand. *Fuel cell systems explained*. John Wiley & Sons, 2018.

[21] Doug DuBois and Gerald C Paynter. “” Fuel Flow Method2” for Estimating Aircraft Emissions”. In: *Sae Transactions* (2006), pp. 1–14.

[22] Reno Elmendorp, Roelof Vos, and Gianfranco La Rocca. “A conceptual design and analysis method for conventional and unconventional airplanes”. In: *29th Congress of the International Council of the Aeronautical Sciences*. Vol. 1. International Council of Aeronautical Sciences. 2014.

[23] EMEP/EEA. *EMEP/EEA Air Pollutant Emission Inventory Guidebook 2022*. `https://www.eea.europa.eu/publications/emep-eea-guidebook-2022`. European Environment Agency, Copenhagen, Denmark. 2022.

[24] Ahmed Fathy et al. “Minimum hydrogen consumption based control strategy of fuel cell/PV/battery/supercapacitor hybrid system using recent approach based parasitism-predation algorithm”. In: *Energy* 225 (2021), p. 120316.

[25] Joshua E. Freeh, Joseph W. Pratt, and Jacob Brouwer. *Development of a Solid-Oxide Fuel Cell/Gas Turbine Hybrid System Model for Aerospace Applications*. Accessed: [Insert access date]. 2004. url: `http://www.sti.nasa.gov`.

[26] HH-W Funke, Nils Beckmann, and Sylvester Abanteriba. “An overview on dry low NOx micromix combustor development for hydrogen-rich gas turbine applications”. In: *International Journal of Hydrogen Energy* 44.13 (2019), pp. 6978–6990.

[27] Randall S Gemmen et al. “Development of dynamic modeling tools for solid oxide and molten carbonate hybrid fuel cell gas turbine systems”. In: *Turbo Expo: Power for Land, Sea, and Air*. Vol. 78552. American Society of Mechanical Engineers. 2000, V002T02A068.

[28] R. George and N. F. Bessette. “Seal-less planar solid oxide fuel cell design”. In: *Journal of Power Sources* 71.1-2 (1998), pp. 131–137.

[29] R. A. George. “An overview of tubular solid oxide fuel cell (SOFC) technology”. In: *Journal of Power Sources* 86 (2000), pp. 134–139.

[30] Raymond A George. “Status of tubular SOFC field unit demonstrations”. In: *Journal of Power Sources* 86.1-2 (2000), pp. 134–139.

[31] Pedro Garcia Gonzalez. “Preliminary Sizing Methodologies for Regional Aircraft with Liquid Hydrogen Fuel and SOFC-GT-Battery Hybrid-Electric Powertrains”. Supervisors: C.M. Servi, C. Mourao (EMBRAER). Master’s thesis. Delft University of Technology, 2022. url: `https://resolver.tudelft.nl/uuid:65cbbdf3-3627-4829-bd69-208fffc8eba9`.

[32] Eduardo López González et al. “Experimental evaluation of a passive fuel cell/battery hybrid power system for an unmanned ground vehicle”. In: *international journal of hydrogen energy* 44.25 (2019), pp. 12772–12782.

[33] Jürgen Haunstetter, Volker Dreißigacker, and Stefan Zunft. “Ceramic high temperature plate fin heat exchanger: Experimental investigation under high temperatures and pressures”. In: *Applied Thermal Engineering* 151 (2019), pp. 364–372.

[34] Martin Hepperle. “Electric flight-potential and limitations”. In: (2012).

[35] High Temp Metals, Inc. *Inconel 625 Technical Data Sheet*. Accessed: 6 September 2025. 2025. url: `https://www.hightempmetals.com/techdata/hitempInconel625data.php`.

[36] *High-temperature solid oxide fuel cells: fundamentals, design and applications*. Elsevier, 2003.

[37] Chihiro Hiraiwa et al. “Application of ni porous metal to solid oxide fuel cells”. In: *Sci. Technical Review* 83 (2016), pp. 59–65.

[38] Jan-Philipp Hofmann et al. “A comprehensive approach to the assessment of a hybrid electric powertrain for commuter aircraft”. In: *AIAA Aviation 2019 Forum*. 2019, p. 3678.

[39] Teruhisa Horita. “LaCrO3-Based perovskite for SOFC interconnects”. In: *Perovskite Oxide for Solid Oxide Fuel Cells*. Springer, 2009, pp. 285–296.

[40] K. S. Howe, G. J. Thompson, and K. Kendall. “Silver as a contact material in SOFCs: Performance and degradation studies”. In: *Journal of Power Sources* 196 (2011), pp. 1677–1686.

[41] Kevin Huang and John B Goodenough. “Solid oxide fuel cell technology: principles, performance and operations”. In: (2009).

[42] Kevin Huang and Subhash C Singhal. “Cathode-supported tubular solid oxide fuel cell technology: A critical review”. In: *Journal of power sources* 237 (2013), pp. 84–97.

[43] D Hyde et al. “Target True Zero-Unlocking Sustainable Battery and Hydrogen-Powered Flight; Insight Report”. In: *World Economic Forum: Geneva, Switzerland*. 2022.

[44] International Civil Aviation Organization (ICAO). *Annex 14 to the Convention on International Civil Aviation, Volume I: Aerodrome Design and Operations*. 8th. Montreal, Canada: ICAO, 2018.

[45] International Civil Aviation Organization (ICAO). *ICAO Aircraft Engine Emissions Databank*. `https://www.easa.europa.eu/en/domains/environment/icao-aircraft-engine-emissions-databank`. Available at `https://www.easa.europa.eu/en/domains/environment/icao-aircraft-engine-emissions-databank`. 2023.

[46] Akihiro Ishii et al. “Rapid Laser Processing of Thin Sr-Doped LaCrO3–δ Interconnects for Solid Oxide Fuel Cells”. In: *Energy Technology* 8.10 (2020), p. 2000364.

[47] RASHEED MICHAEL ISHOLA. “Thermodynamic analysis of a turboprop engine with regeneration and intercooling”. In: (2019).

[48] Askin T Isikveren et al. “Pre-design strategies and sizing techniques for dual-energy aircraft”. In: *Aircraft Engineering and Aerospace Technology: An International Journal* 86.6 (2014), pp. 525–542.

[49] Zhixing Ji et al. “Performance characteristics of a solid oxide fuel cell hybrid jet engine under different operating modes”. In: *Aerospace Science and Technology* 105 (2020), p. 106027.

[50] Song Jialiang et al. “A novel silicon carbide plate-fin heat exchanger and its thermal and hydraulic performance for SOFC cathode air preheater application”. In: *Case Studies in Thermal Engineering* 64 (2024), p. 105570.

[51] Wei Jiang and Babak Fahimi. “Active current sharing and source management in fuel cell–battery hybrid power system”. In: *IEEE Transactions on Industrial Electronics* 57.2 (2009), pp. 752–761.

[52] J Larminie and A Dicks. “Fuel Cell Systems Explained, Jhon Wiley”. In: *New York* (2000).

[53] L. Lawlor et al. “A study of tubular solid oxide fuel cells: configurations and performance analysis”. In: *Journal of Power Sources* 193.2 (2009), pp. 387–399.

[54] David S Lee et al. “The contribution of global aviation to anthropogenic climate forcing for 2000 to 2018”. In: *Atmospheric environment* 244 (2021), p. 117834.

[55] David S. Lee et al. “Aviation and global climate change in the 21st century”. In: *Atmospheric Environment* 43.22-23 (2010), pp. 3520–3537. doi: `10.1016/j.atmosenv.2009.04.024`. url: `https://doi.org/10.1016/j.atmosenv.2009.04.024`.

[56] Charles Lents and Larry Hardin. “Fuel burn and energy consumption reductions of a single-aisle class parallel hybrid propulsion system”. In: *2019 AIAA/IEEE Electric Aircraft Technologies Symposium (EATS)*. IEEE. 2019, pp. 1–8.

[57] Y Li, H Sun, J Song, et al. *Effect of two-step sintering on the mechanical and electrical properties of 5YSZ and 8YSZ ceramics. Materials 16 (5), 2019 (2023)*.

[58] Lidia Licu et al. “Exploring the Potential of Robocasting for High-Density Electrolytes in Solid Oxide Fuel Cells”. In: *Inorganics* 12.12 (2024), p. 300.

[59] Kevin M Lunsford. “Advantages of brazed aluminum heat exchangers”. In: *Hydrocarbon Processing* 75.7 (1996).

[60] Maria Chiara Massaro et al. “Optimal design of a hydrogen-powered fuel cell system for aircraft applications”. In: *Energy Conversion and Management* 306 (2024), p. 118266.

[61] Maria Chiara Massaro et al. “Potential and technical challenges of on-board hydrogen storage technologies coupled with fuel cell systems for aircraft electrification”. In: *Journal of Power Sources* 555 (2023), p. 232397.

[62] Nguyen Quang Minh and Takehiko Takahashi. *Science and technology of ceramic fuel cells*. Elsevier, 1995.

[63] Fred Mitlitsky et al. “Reversible (unitised) PEM fuel cell devices”. In: *Fuel Cells Bulletin* 2.11 (1999), pp. 6–11.

[64] T. Oom Ortiz de Montellano. “Structural Analysis of a New Integral Tank Concept for Hydrogen Storage On-board Commercial Aircraft”. Supervisors: M.F.M. Hoogreef, A. Heidebrecht, J.M.J.F. van Campen, C. Varriale. Master’s thesis. Delft University of Technology, 2024. url: `https://resolver.tudelft.nl/uuid:8ab68eb3-77dc-4acf-9768-6b379b8ef24d`.

[65] Jayant Mukhopadhaya and Dan Rutherford. “Performance analysis of evolutionary hydrogen-powered aircraft”. In: *International Council on Clean Transportation* (2022).

[66] National Academies of Sciences, Engineering, and Medicine. *Commercial Aircraft Propulsion and Energy Systems Research: Reducing Global Carbon Emissions*. National Academies Press, Sept. 2016, pp. 1–122. isbn: 9780309440961. doi: `10.17226/23490`.

[67] Ryan O’hayre et al. *Fuel cell fundamentals*. John Wiley & Sons, 2016.

[68] Polyhose Aerospace. *Aerospace PTFE Hose Catalog (AS1946, MIL□DTL□25579)*. Weights range 0.089–1.5kg/m depending on diameter and pressure rating. 2023.

[69] Materials Project. *LaMnO3 (orthorhombic, Pnma)*. `https://materialsproject.org/materials/mp-17554/`.

[70] Zonghua Pu et al. “Regenerative fuel cells: Recent progress, challenges, perspectives and their applications for space energy system”. In: *Applied Energy* 283 (2021), p. 116376.

[71] JM Rakowski and CP Stinner. “Nickel-base alloys for heat exchangers”. In: *CORROSION 2006*. Association for Materials Protection and Performance. 2006, pp. 1–14.

[72] Hegazy Rezk et al. “Fuel cell as an effective energy storage in reverse osmosis desalination plant powered by photovoltaic system”. In: *Energy* 175 (2019), pp. 423–433.

[73] AK Sahu, A Ghosh, and AK Suri. “Characterization of porous lanthanum strontium manganite (LSM) and development of yttria stabilized zirconia (YSZ) coating”. In: *Ceramics International* 35.6 (2009), pp. 2493–2497.

[74] P. Sarkar et al. “Development of ceramic technologies for solid oxide fuel cells”. In: *International Journal of Applied Ceramic Technology* 4.2 (2007), pp. 103–108.

[75] Bulent Sarlioglu and Casey T Morris. “More electric aircraft: Review, challenges, and opportunities for commercial transport aircraft”. In: *IEEE transactions on Transportation Electrification* 1.1 (2015), pp. 54–64.

[76] Marc Schmelcher and Jannik Häßy. “Hydrogen fuel cells for aviation? A potential analysis comparing different thrust categories”. In: (2022).

[77] Clean Sky et al. “Hydrogen-powered aviation: a fact-based study of hydrogen technology, economics, and climate impact by 2050”. In: (2020).

[78] Mehdi Soleymani et al. “Hydrogen propulsion systems for aircraft: A review on recent advances and ongoing challenges”. In: *International Journal of Hydrogen Energy* 91 (Nov. 2024), pp. 137–171. issn: 0360-3199. doi: `10.1016/j.ijhydene.2024.10.131`.

[79] Andrew Sommers et al. “Ceramics and ceramic matrix composites for heat exchangers in advanced thermal systems—A review”. In: *Applied Thermal Engineering* 30.11-12 (2010), pp. 1277–1291.

[80] Fredrik Svensson, Anders Hasselrot, and Jana Moldanova. “Reduced environmental impact by lowered cruise altitude for liquid hydrogen-fuelled aircraft”. In: *Aerospace Science and Technology* 8.4 (2004), pp. 307–320.

[81] David E Tew et al. “Perspective—the role of solid oxide fuel cells in our carbon-neutral future”. In: *Journal of The Electrochemical Society* 169.2 (2022), p. 024508.

[82] Saurav Tiwari, Michael J Pekris, and John J Doherty. “A review of liquid hydrogen aircraft and propulsion technologies”. In: *International Journal of Hydrogen Energy* 57 (2024), pp. 1174–1196.

[83] Egbert Torenbeek. *Advanced aircraft design: conceptual design, analysis, and optimization of subsonic civil airplanes*. 2013.

[84] Egbert Torenbeek. *Synthesis of subsonic airplane design: an introduction to the preliminary design of subsonic general aviation and transport aircraft, with emphasis on layout, aerodynamic design, propulsion and performance*. Springer Science & Business Media, 2013.

[85] ES Van der Sman et al. “Destination 2050”. In: (2020).

[86] Dries Verstraete. “The Potential of Liquid Hydrogen for long range aircraft propulsion”. In: (2009).

[87] Anil V Virkar, Kuan-Zong Fung, and Subhash C Singhal. *The effect of pressure on solid oxide fuel cell performance*. Tech. rep. Utah Univ., Dept.. of Materials Science and Engineering, Salt Lake City, UT …, 1997.

[88] Philip P. Walsh and Paul Fletcher. “Appendix A: Engine Station Numbering and Nomenclature”. In: *Gas Turbine Performance*. Accessed: 2025-07-14. Blackwell Science Ltd, 2004, pp. 617–624. doi: `10.1002/9780470774533.app1`. url: `https://onlinelibrary.wiley.com/doi/10.1002/9780470774533.app1`.

[89] H Webber and S Job. “Realising Zero-Carbon Emission Flight. Primary Energy Source Comparison and Selection”. In: (2021).

[90] Andre Weber et al. “Oxidation of H2, CO and methane in SOFCs with Ni/YSZ-cermet anodes”. In: *Solid State Ionics* 152 (2002), pp. 543–550.

[91] Joshua A Wilson et al. “Hybrid solid oxide fuel cell/gas turbine model development for electric aviation”. In: *Energies* 15.8 (2022), p. 2885.

[92] Charles F Windisch et al. *Experimentally-Calibrated, Spreadsheet-Based SOFC Unit-Cell Performance Model*. Tech. rep. Pacific Northwest National Lab.(PNNL), Richland, WA (United States), 2002.

[93] Liangcai Xu et al. “A comprehensive review on fuel cell UAV key technologies: propulsion system, management strategy, and design procedure”. In: *IEEE Transactions on Transportation Electrification* 8.4 (2022), pp. 4118–4139.

[94] Z Gary Yang et al. *Materials properties database for selection of high-temperature alloys and concepts of alloy design for SOFC applications*. Tech. rep. Pacific Northwest National Lab.(PNNL), Richland, WA (United States), 2002.

[95] W Yoshito et al. “Reduction kinetics of NiO–YSZ composite for application in solid oxide fuel cell”. In: *Journal of thermal analysis and calorimetry* 97.1 (2009), pp. 303–308.

[96] Xin Zhao et al. “Off-design performance analysis of hybridised aircraft gas turbine”. In: *The Aeronautical Journal* 123.1270 (2019), pp. 1999–2018.

A

Hydrogen based HEPS Configurations

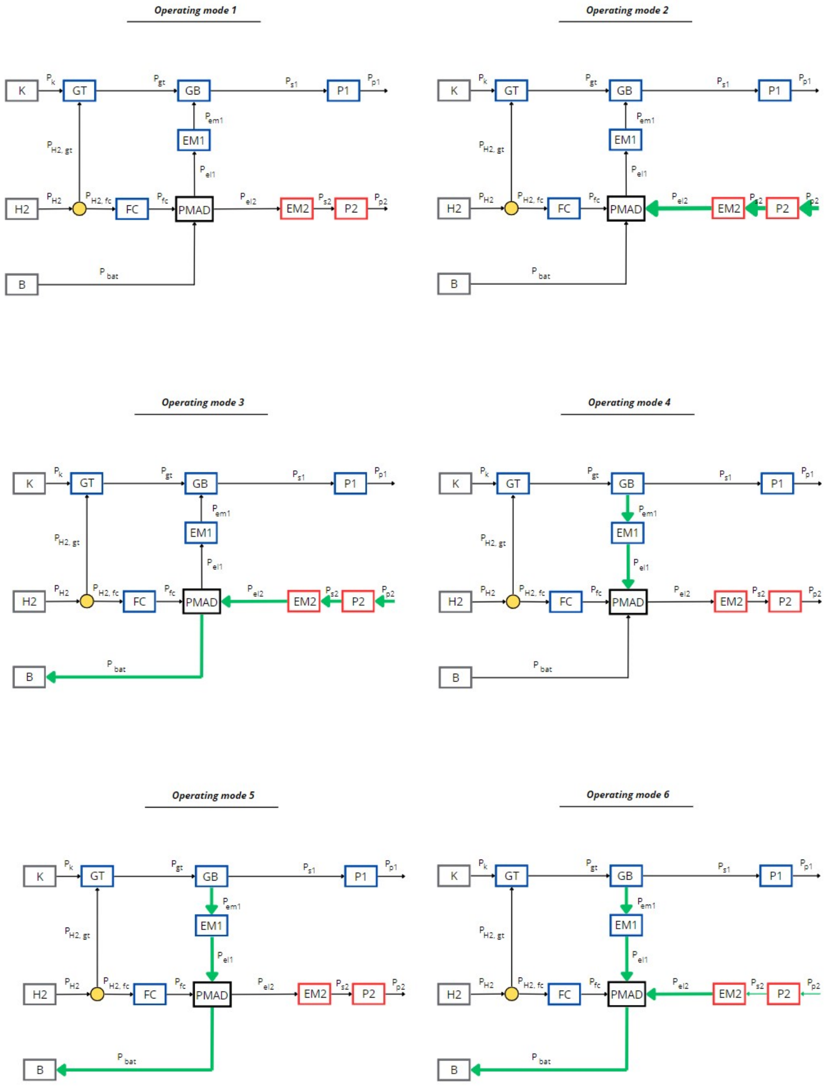

Figure A.1: Operating Modes 1-6, H_2-based Hybrid Electric Powertrains [9]

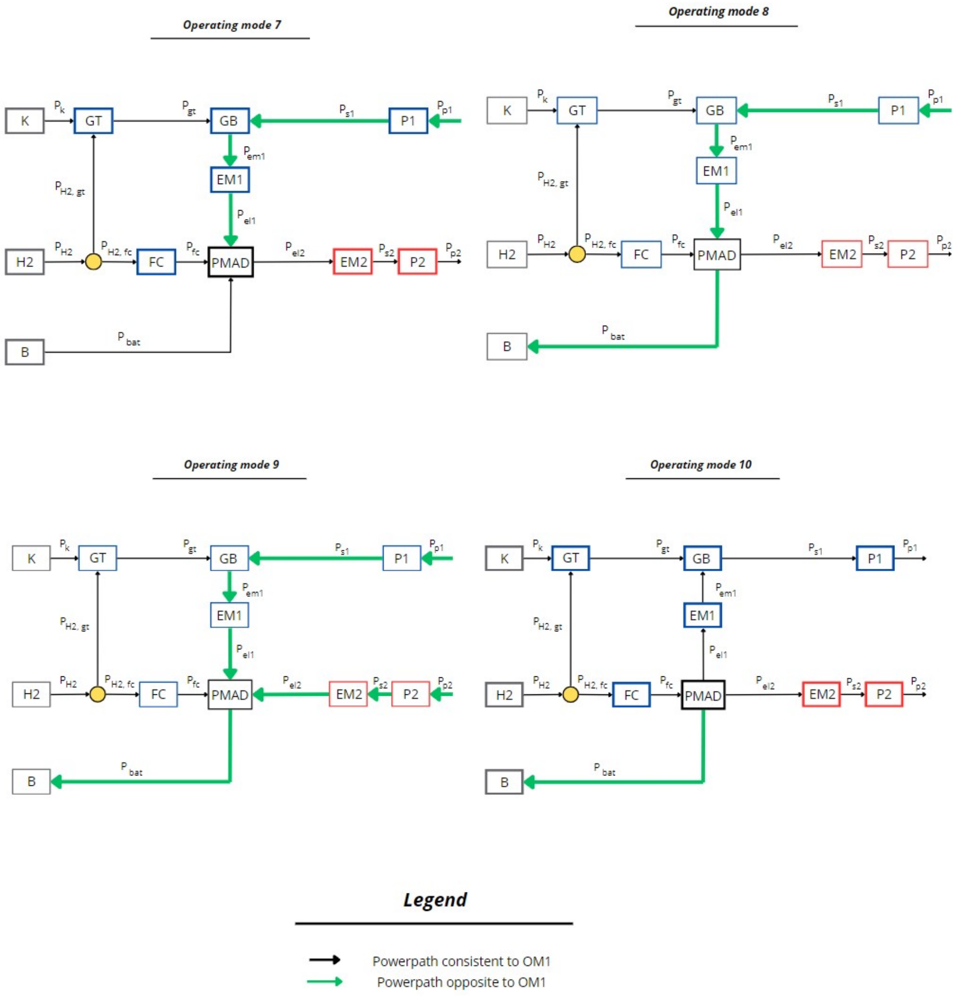

Figure A.2: Operating Modes 7-10, H_2-based Hybrid Electric Powertrains [9]

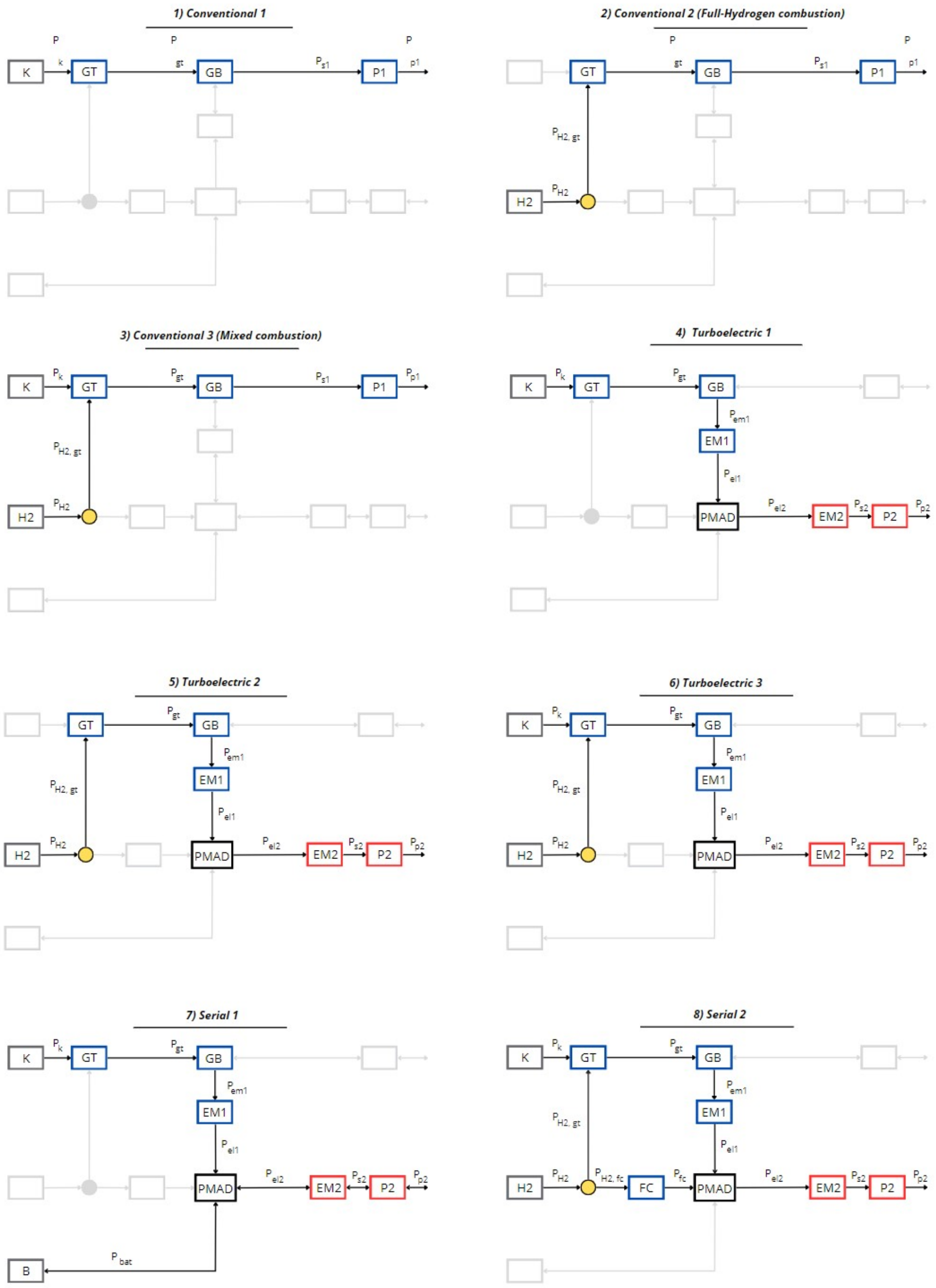

1) Conventional 1

2) Conventional 2 (Full-Hydrogen combustion)

3) Conventional 3 (Mixed combustion)

4) Turboelectric 1

5) Turboelectric 2

6) Turboelectric 3

7) Serial 1

8) Serial 2

Figure A.3: Configurations 1-8, H_2-based Hybrid Electric Powertrains [9]

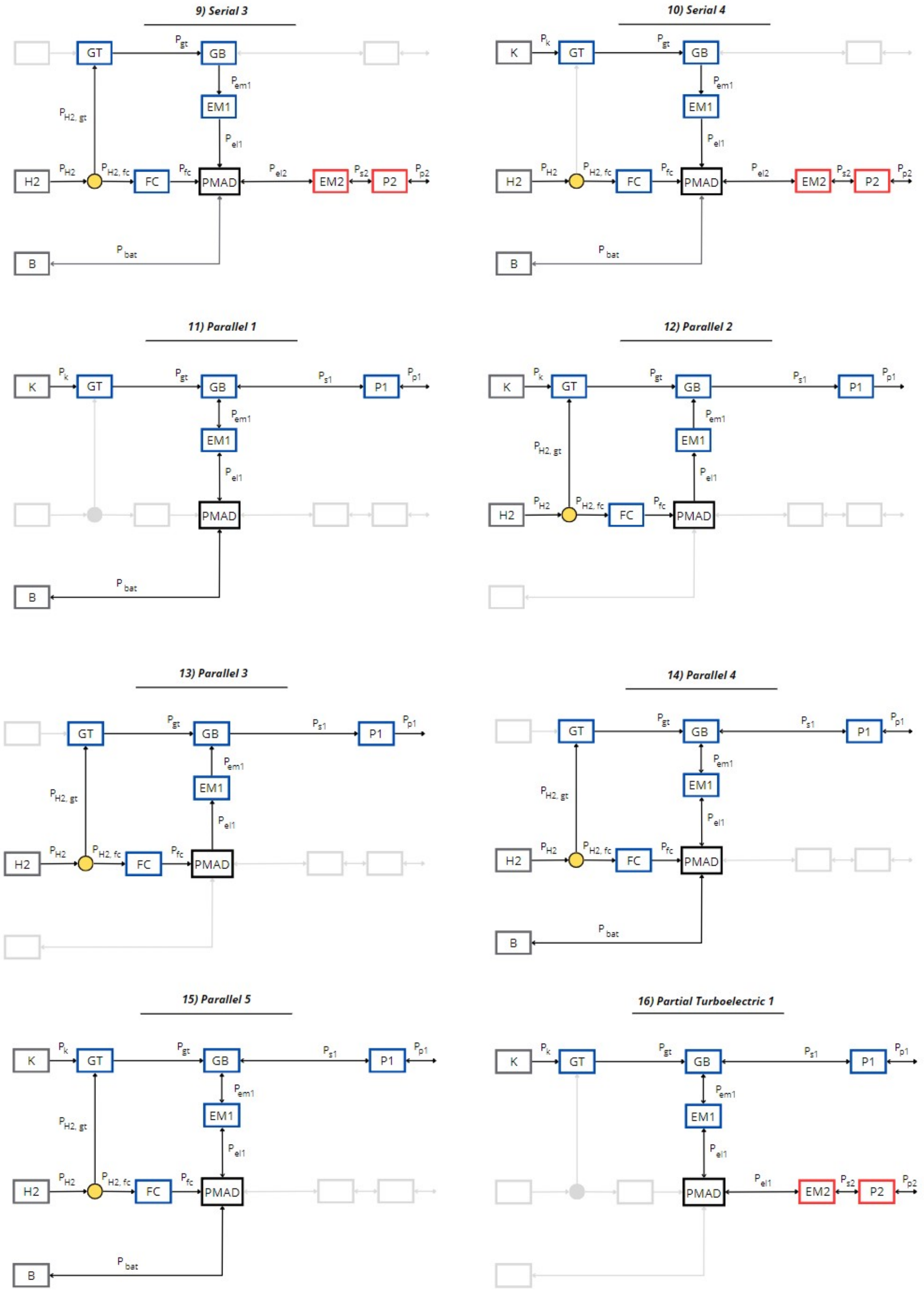

9) Serial 3

10) Serial 4

11) Parallel 1

12) Parallel 2

13) Parallel 3

14) Parallel 4

15) Parallel 5

16) Partial Turboelectric 1

Figure A.4: Configurations 9-16, H_2-based Hybrid Electric Powertrains [9]

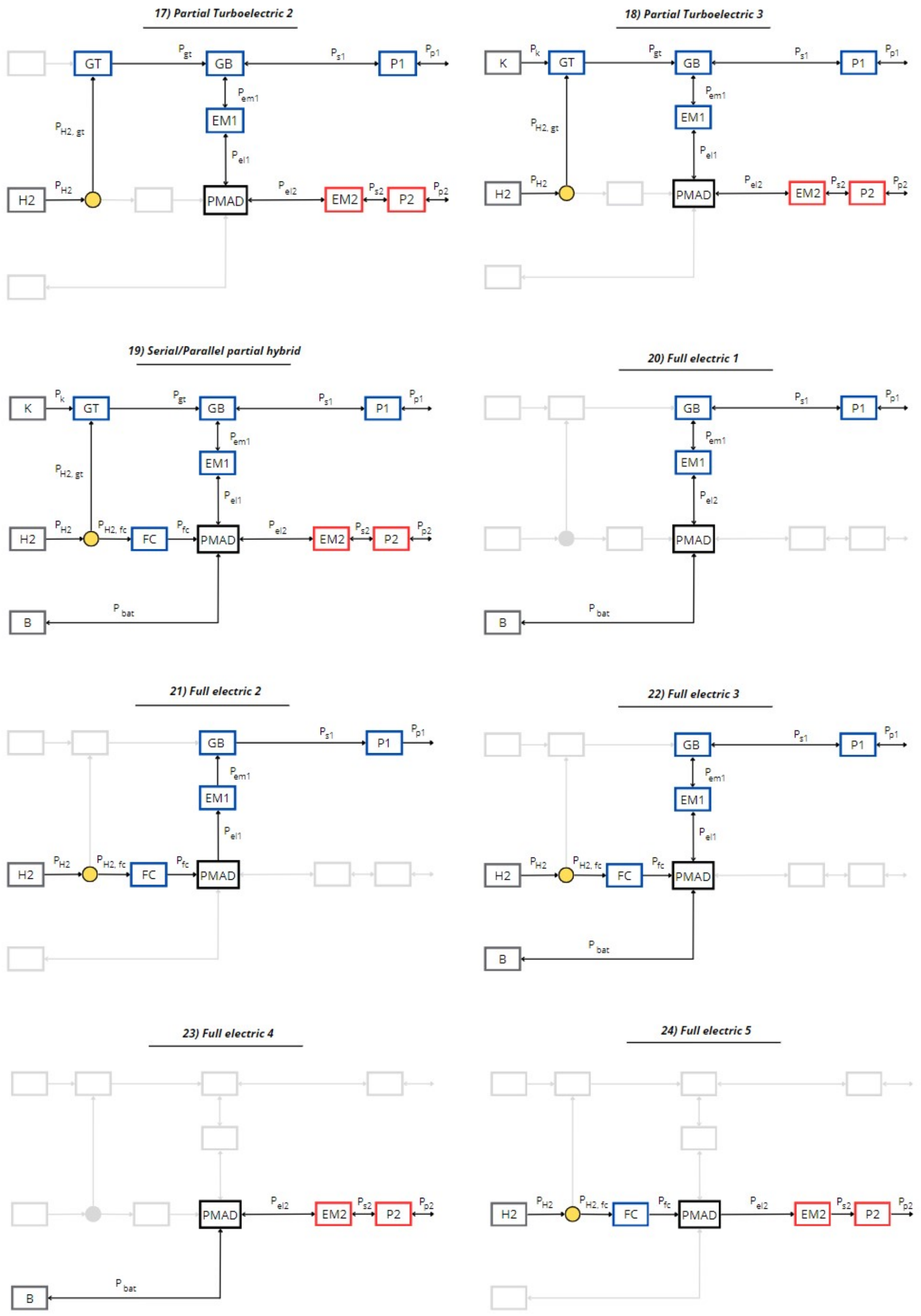
17) Partial Turboelectric 2

18) Partial Turboelectric 3

19) Serial/Parallel partial hybrid

20) Full electric 1

21) Full electric 2

22) Full electric 3

23) Full electric 4

24) Full electric 5

Figure A.5: Configurations 17-24, H_2-based Hybrid Electric Powertrains [9]

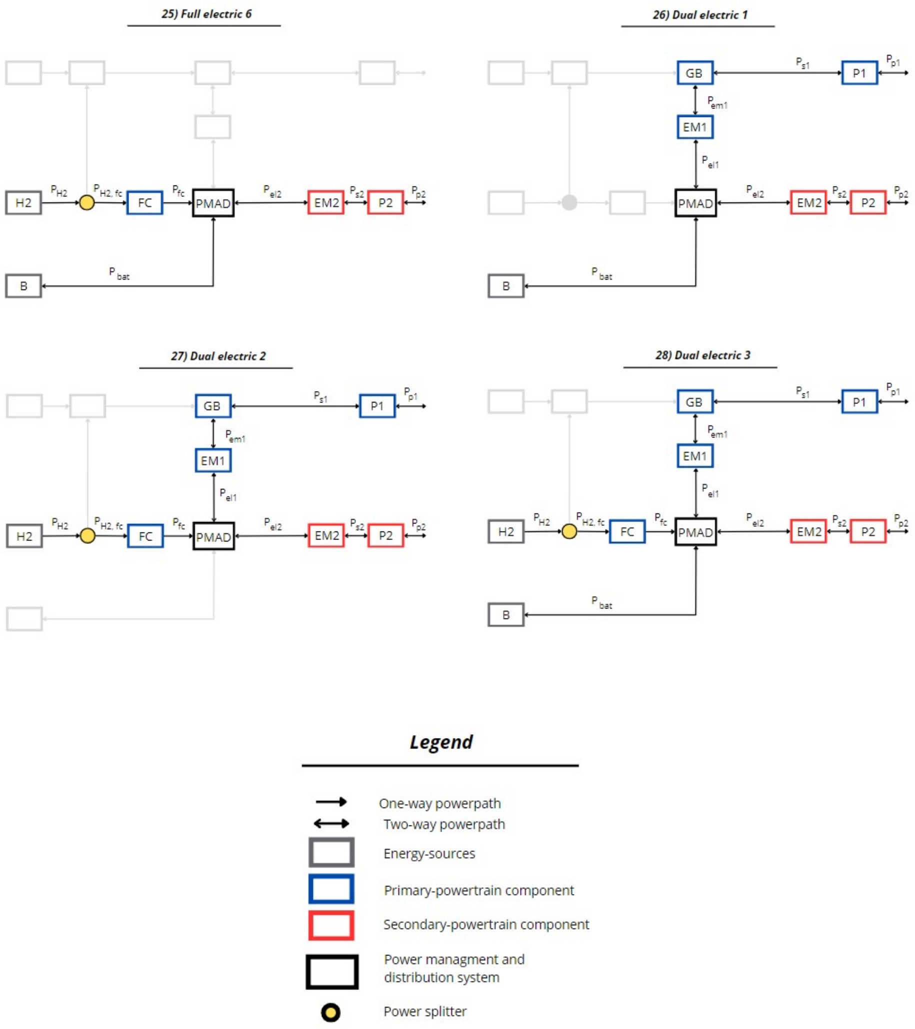

Figure A.6: Configurations 25-28, H_2-based Hybrid Electric Powertrains [9]

B

Supplementary Material

B.1. Legend Chart - Sizing Diagrams

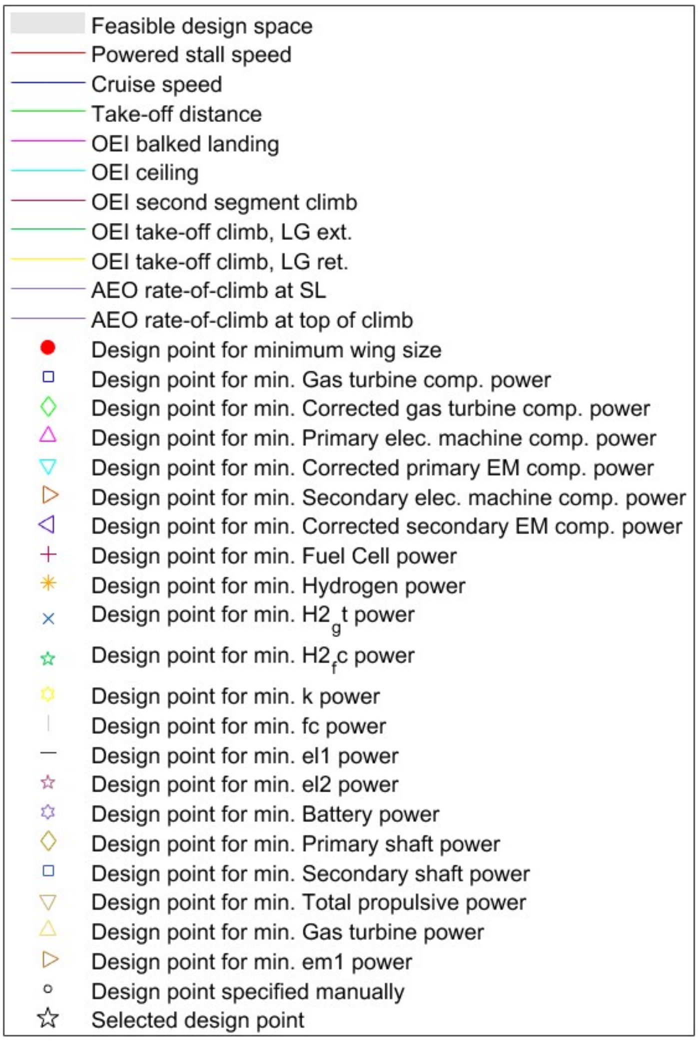

Figure B.1: Legend for the constraint curves and design points used WP/WS sizing diagrams

B.2. Computation of Exhaust Gas Properties for Steam-Injected Hydrogen Combustion

To compute the thermodynamic properties of the exhaust gas resulting from hydrogen combustion with steam injection, a method was implemented to estimate the mass-weighted specific heat at constant pressure (c_p) and the ratio of specific heats ($\gamma = c_p/c_v$) for the chemically equilibrated exhaust mixture. The procedure takes as input the temperature (T) of the exhaust gas after combustion, the equivalence ratio (ϕ) of the fuel–air mixture prior to combustion, the total pressure (P) of the exhaust gas, and the steam injection ratio, defined as the mass of added H_2O divided by the mass of the dry fuel–air mixture. Equilibrium species mass fractions are interpolated from precomputed Cantera simulation data, and species-specific heat contributions are computed using NASA polynomial fits over a blend of low- and high-temperature ranges.

The function uses precomputed equilibrium species mass fractions obtained from Cantera simulations as a function of temperature, equivalence ratio, pressure, and steam injection. For a given input condition, the species mass fractions are interpolated from two separate datasets: one for low temperatures (100–1000 K) and another for high temperatures (1000–3000 K). A smooth sine-based blending is performed in the transition region (centered at 1000 K) to ensure continuity.

The specific heat of the gas mixture is computed as:

$$c_p = \sum_i Y_i \cdot c_{p,i}(T)$$

$$\gamma = \frac{c_p}{c_p - \frac{R_{\text{mix}}}{1000}}$$

where Y_i is the mass fraction and $c_{p,i}$ is the specific heat of species i calculated using NASA 7-coefficient polynomial fits of the form:

$$c_{p,i}(T) = \left(a_1 + a_2 T + a_3 T^2 + a_4 T^3 + a_5 T^4\right) \cdot \frac{R_i}{1000}$$

The constants R_i (specific gas constants) and NASA polynomial coefficients a_1 to a_5 used in the model are summarized in Tables B.1 and B.2, respectively.

Table B.1: Specific Gas Constants for Major Species

Species	**Symbol**	**R**$_i$ [J/kg·K]
Water vapor	H_2O	461.5
Hydrogen	H_2	4124
Oxygen	O_2	259.8
Nitrogen	N_2	296.8
Hydroxyl	OH	296.8
Nitric oxide	NO	296.8

Table B.2: NASA Polynomial Coefficients (a_1 to a_5) for High and Low Temperature Ranges [11]

Species	**Range**	a_1	a_2	a_3	a_4	a_5
H_2O	Low	4.198640	-2.0364×10^{-3}	6.5204×10^{-6}	-5.4880×10^{-9}	1.7720×10^{-12}
	High	3.033992	2.1769×10^{-3}	-1.6407×10^{-7}	-9.7042×10^{-11}	1.6820×10^{-14}
H_2	Low	2.344331	7.9805×10^{-3}	-1.9478×10^{-5}	2.0157×10^{-8}	-7.3761×10^{-12}
	High	3.337279	-4.9405×10^{-5}	4.9946×10^{-7}	-1.7957×10^{-10}	2.0026×10^{-14}
O_2	Low	3.782456	-2.9967×10^{-3}	9.8473×10^{-6}	-9.6813×10^{-9}	3.2437×10^{-12}
	High	same as low				
OH	Low	3.992015	-2.4013×10^{-3}	4.6179×10^{-6}	-3.8811×10^{-9}	1.3641×10^{-12}
	High	3.092888	5.4843×10^{-4}	1.2651×10^{-7}	-8.7946×10^{-11}	1.1741×10^{-14}
N_2	Low	3.531005	-1.2366×10^{-4}	-5.0300×10^{-7}	2.4353×10^{-9}	-1.4088×10^{-12}
	High	same as low				
NO	Low	same as N_2				
	High	same as N_2				

The NASA polynomial coefficients are based on the Burcat thermodynamic database [11] and JANAF tables.

B.3. Alternative HX Placements

In this section, a second SOFC-GT powertrain architecture is studied, where the heat exchangers are placed between the High Pressure Turbine (HPT) and the Power Turbine (PT). This is in contrast to the configuration chosen in this study (refer to Figure 4.8), where the heat exchangers were placed right after the combustion chamber. This alternative architecture was explored for its improved overall thermal efficiency, due to the lower total pressure losses when the exhaust gases are passed through the heat exchangers after expansion through the HPT. However, such a configuration has significant design and operational limitations on the SOFC operating temperature, which must remain below the HPT outlet temperature to avoid a non-physical value (i.e., $\epsilon < 1$) for heat exchanger effectiveness. It is for this reason that an architecture where the heat exchangers are placed after the PT is not explored altogether, as the temperature of the exhaust gases exiting the power turbine is not sufficient enough to preheat the air or fuel to the range of SOFC operating temperatures considered in this study.

As such, the consecutive arrangement of both air and fuel preheaters as seen in Figure 4.8 cannot be used directly in the case where the exhaust gases are drawn from the HPT exit. This is due to two reasons, namely, 1) the significant temperature drop of the exhaust gases after passing through the air preheater, and 2) the large temperature difference between the fuel inlet and SOFC operating temperatures in the H_2 preheater. This leads to the temperature of the exhaust gases exiting the air preheater not being sufficient enough to preheat the fuel passing through the H_2 preheater. As a result, both the preheaters need to be arranged in parallel to each other, with the exhaust gases exiting the HPT being split into two streams for the hot sides of both air and H_2 preheaters.

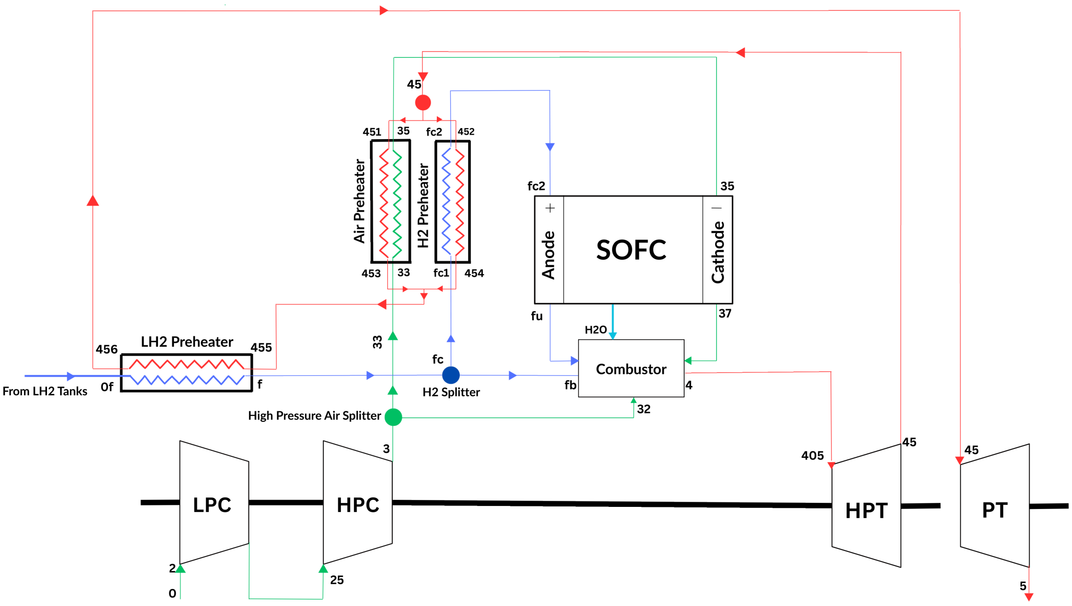

Figure B.2: A schematic of the SOFC-GT powertrain architecture, with the preheaters placed after the HPT

The splitting ratio of the exhaust gas to the air preheater, which is denoted by σ, represents the ratio of the exhaust gas mass flow to the air preheater with respect to the total exhaust gas mass flow ($\dot{m}_{45} = \dot{m}_4$):

$$\sigma = \frac{\dot{m}_{451}}{\dot{m}_{451} + \dot{m}_{452}} = \frac{\dot{m}_{451}}{\dot{m}_{45}} \tag{B.1}$$

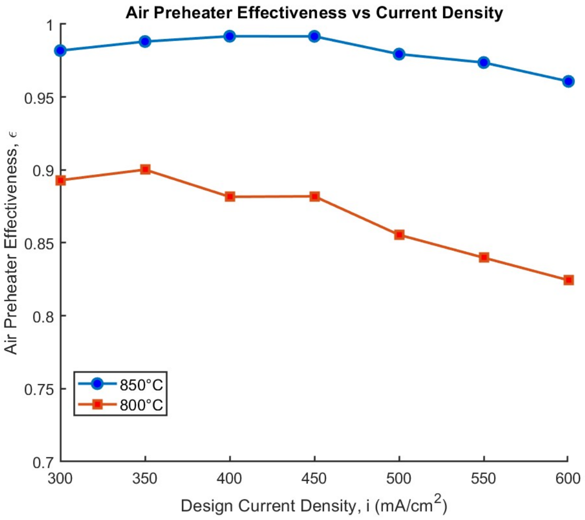

Figure B.3: Variation of air preheater effectiveness ϵ with design current densities and SOFC operating temperatures, at $\mathrm{H_{2,split}} = 50\%$ and $\sigma = 0.9$

As mentioned previously, the SOFC operating temperature is significantly limited by the exit temperature of the exhaust gases from the HPT. With the constraining value of preheater effectiveness to be maintained below 1, the HPT exit temperature limits the SOFC operating temperature to be strictly below 850 $^\circ\mathrm{C}$ for all design current densities and cruise H_2 split ratios. This can be observed from Figure B.3, where the effectiveness values touch their maximum physical limit for $\mathrm{T_{SOFC}} = 850^\circ\mathrm{C}$ at 50% cruise H_2 split and $\sigma = 0.9$.

B.3.1. Effect of varying σ

The exhaust gas splitting ratio σ, between the air and fuel preheaters, is varied for two cases- the first with an equal split ($\sigma = 0.5$) between the two preheaters and second, with 90% and 10% splits ($\sigma = 0.9$) between the air and fuel preheaters, respectively. For the first case, the limiting value of the cruise $\mathrm{H_{2,split}}$ was found to be 0.7, beyond which the increasing air mass flow requirement (due to the higher number of stacks) caused a significant temperature drop in hot exhaust gases across the air preheater, resulting in the effectiveness exceeding 1 ($\Delta\mathrm{T_{hot}} > \Delta\mathrm{T_{HX,max}}$). This is also because at $\sigma = 0.5$ and $\mathrm{H_{2,split}} > 0.7$, the heat capacity of the hot stream ($\mathrm{C_{hot}}$) becomes considerably smaller than that of the cold stream ($\mathrm{C_{cold}}$ due to increasing air mass flow requirement to the stacks), thereby resulting in the effectiveness of the air preheater $\mathrm{H_{2,split}}$ being determined by the temperature drop in the hot side.

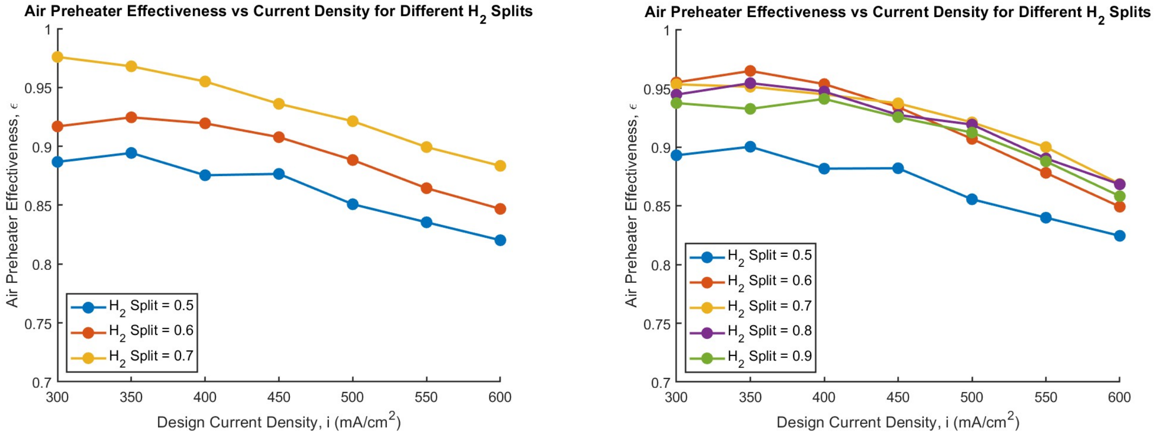

(a) $\sigma = 0.5$ **(b)** $\sigma = 0.9$

Figure B.4: Variation of air preheater effectiveness ϵ with design current densities and $\mathrm{H_{2,split}}$, for $\mathrm{T_{SOFC}} = 800^\circ\mathrm{C}$.

For the second case (shown in Figure B.4b) however, the value of the cruise $\mathrm{H}_{2,\mathrm{split}}$ does not become limiting, as the value of the hot side heat capacity $\mathrm{C}_{\mathrm{hot}}$ always remains higher than the cold side for all values of i and cruise $\mathrm{H}_{2,\mathrm{split}}$ values. In this case, the effectiveness of the air preheater becomes solely dependent on the SOFC operating temperature and the HPT exit temperature alone, with the latter always remaining higher than $800°\mathrm{C}$ for all values of i and cruise $\mathrm{H}_{2,\mathrm{split}}$. Additionally, it can be observed from Figures B.4b and B.5 that for a given i, the variation of air preheater effectiveness with cruise $\mathrm{H}_{2,\mathrm{split}}$ mirrors that of the HPT exit temperature T_{45}; which, after showing an initial drop, shows a consistent increase post $\mathrm{H}_{2,\mathrm{split}} = 0.6$ as the number of stacks increases (for a fuel utilization of 75%, an increase in the number of stacks also significantly increases the underutilized fuel available for combustion, raising both T_4 and T_{45}).

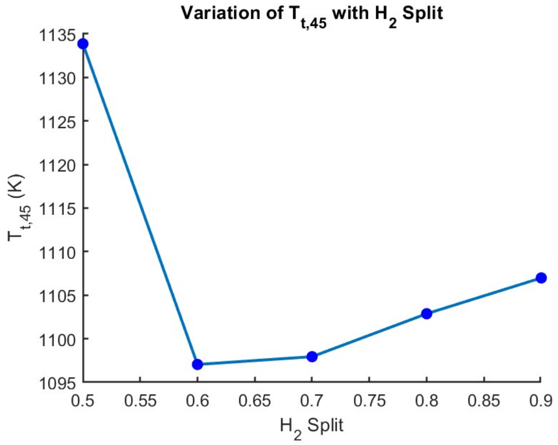

Figure B.5: Variation of HPT Exit Temperature $\mathrm{T}_{\mathrm{t},45}$, with cruise $\mathrm{H}_{2,\mathrm{split}}$, for $i = 300\ \mathrm{mA/cm}^2$

Figure B.6 shows the feasible design space at $\sigma = 0.9$ for the range of the most influential parameters (design current densities, cruise hydrogen split ratios, and the SOFC operating temperatures) which are considered in this study. It is important to note here that the rest of the powertrain design parameters, such as operating pressure, fuel utilization, and the excess air supplied to the cathode, are kept unchanged.

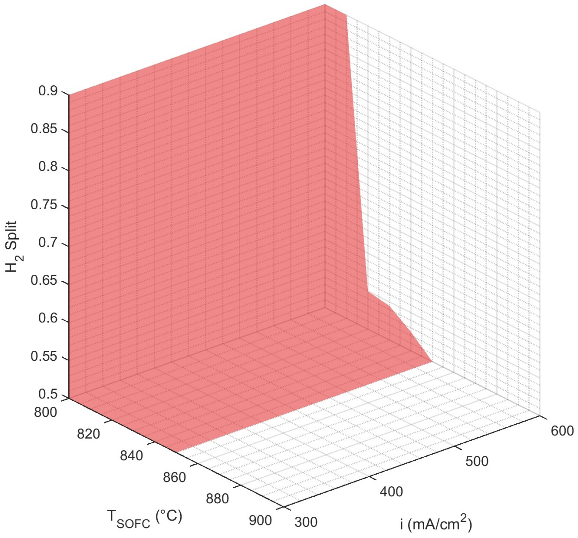

Figure B.6: Feasible Design Space with respect to current densities, cruise $\mathrm{H}_{2,\mathrm{split}}$, and SOFC operating temperatures, when the preheaters are placed between the HPT and PT, $\sigma = 0.9$

C

Contour Plots

C.1. HPC Pressure Ratio

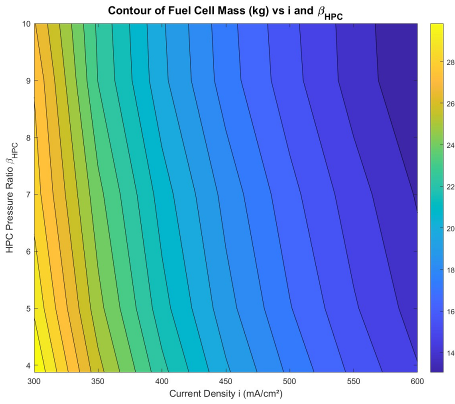

Figure C.1: Contour of Fuel Cell Mass vs i and β_{HPC}

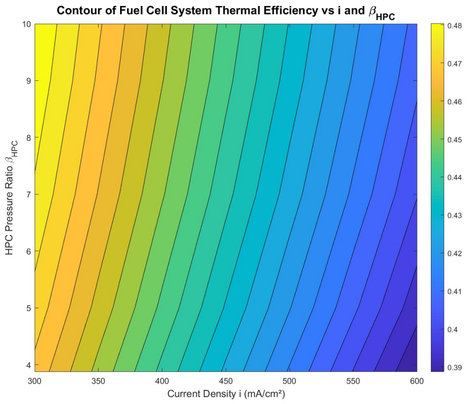

Figure C.2: Contour of η_{FC} vs i and β_{HPC}

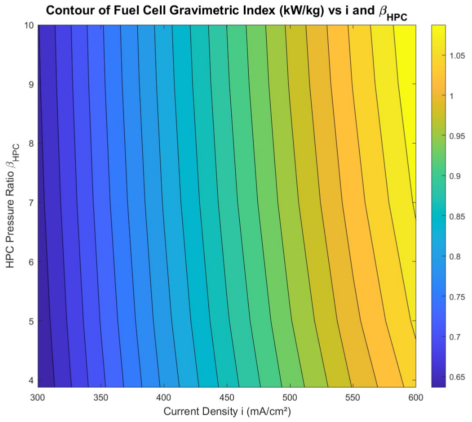

Figure C.3: Contour of $\mathrm{GI}_{\mathrm{FC}}$ vs i and β_{HPC}

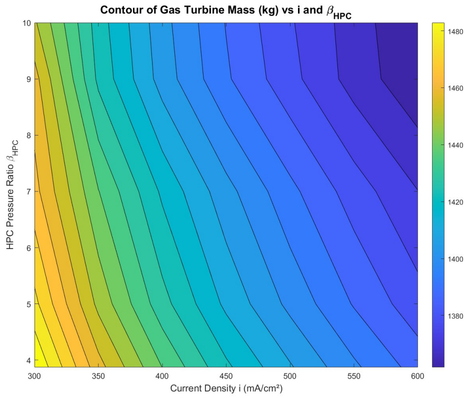

Figure C.4: Contour of GT Mass vs i and β_{HPC}

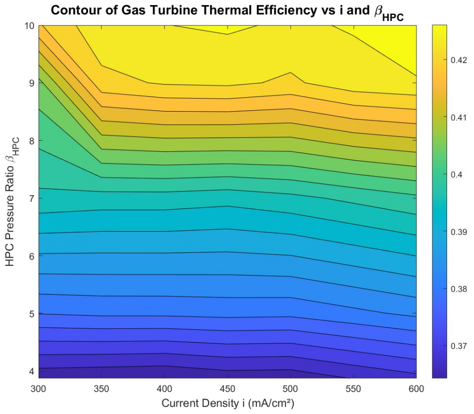

Figure C.5: Contour of η_{GT} vs i and β_{HPC}

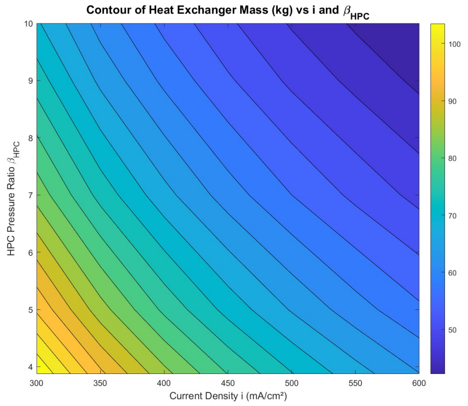

Figure C.6: Contour of HX Mass vs i and β_{HPC}

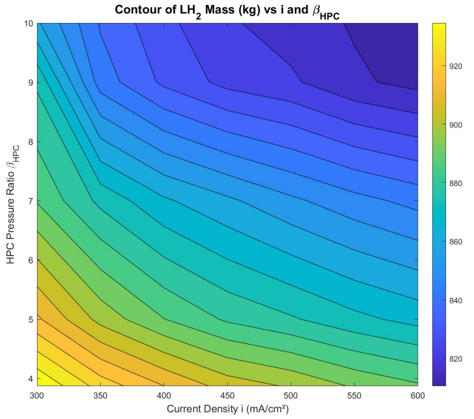

Figure C.7: Contour of LH2 Mass vs i and β_{HPC}

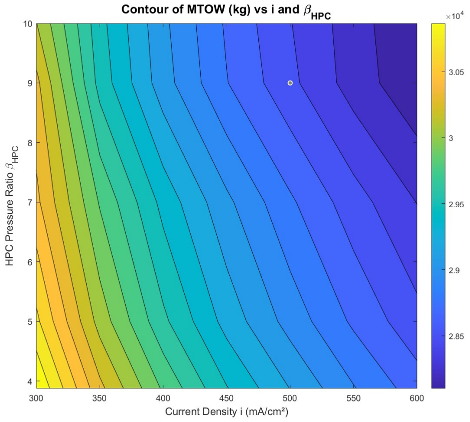

Figure C.8: Contour of MTOM vs i and β_{HPC}

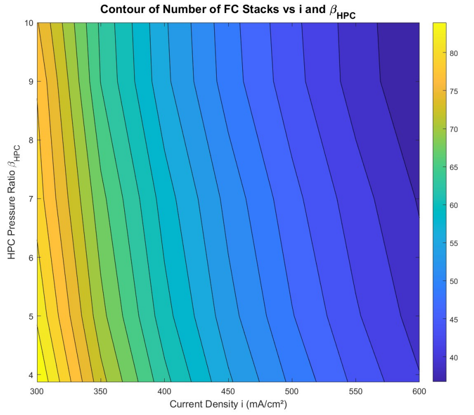

Figure C.9: Contour of Number of Stacks vs i and β_{HPC}

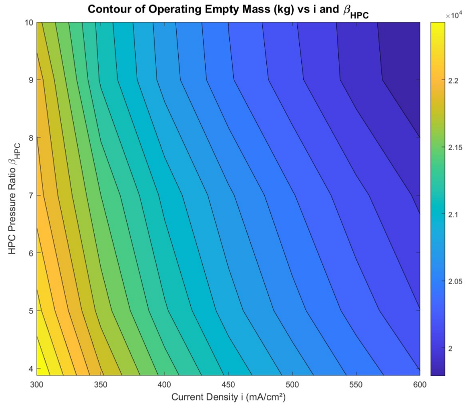

Figure C.10: Contour of OEM vs i and β_{HPC}

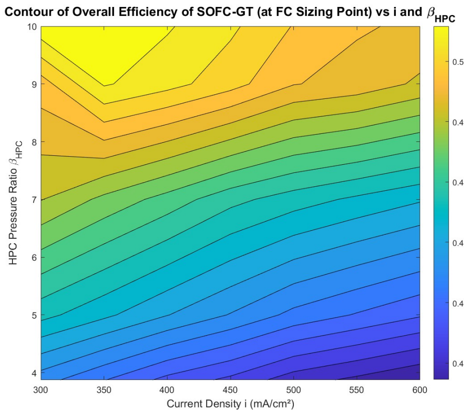

Figure C.11: Contour of Overall Thermal Efficiency vs i and β_{HPC}

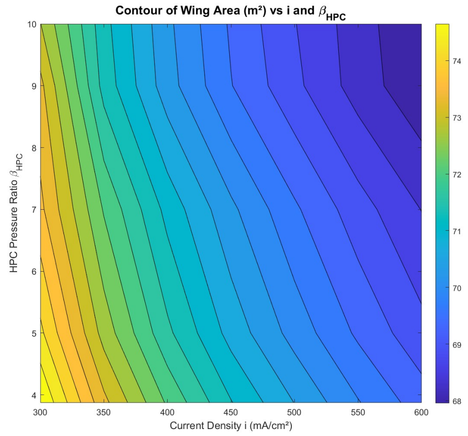

Figure C.12: Contour of Wing Area vs i and β_{HPC}

Figure C.13: Contour of Wing Mass vs i and β_{HPC}

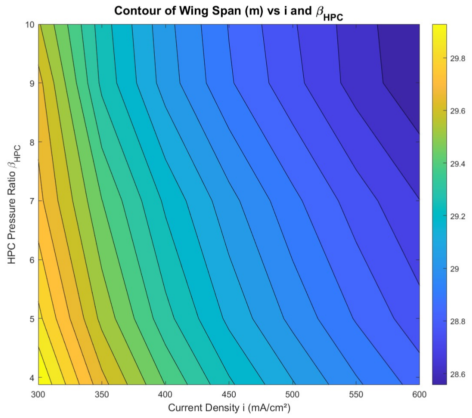

Figure C.14: Contour of Wing Span vs i and β_{HPC}

C.2. SOFC Operating Temperature

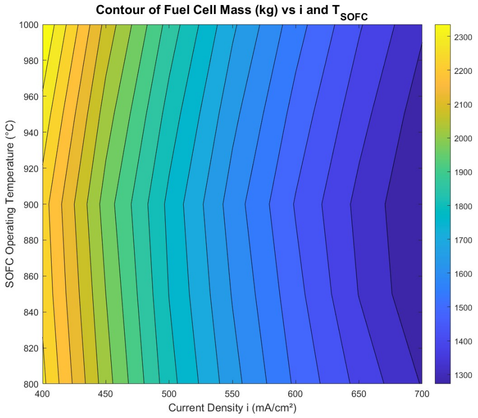

Figure C.15: Contour of Fuel Cell Mass vs i and T_{SOFC}

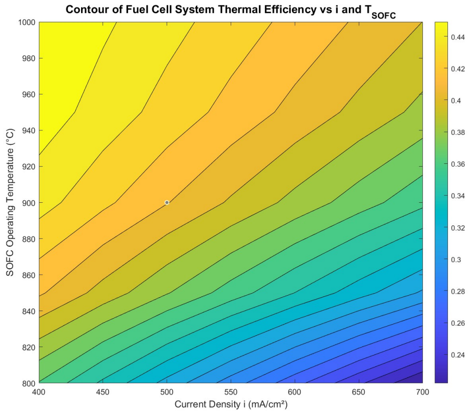

Figure C.16: Contour of η_{FC} vs i and T_{SOFC}

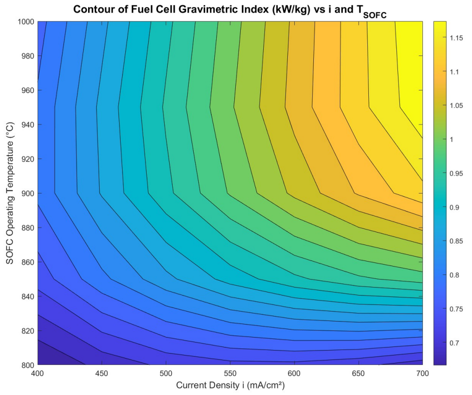

Figure C.17: Contour of $\mathrm{GI_{FC}}$ vs i and T_{SOFC}

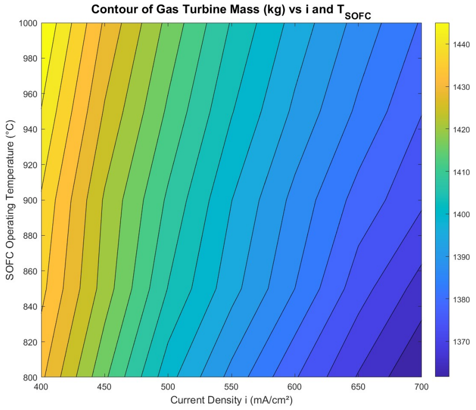

Figure C.18: Contour of Gas Turbine Mass vs i and T_{SOFC}

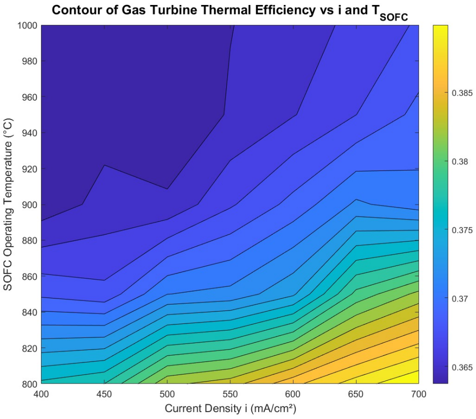

Figure C.19: Contour of η_{GT} vs i and T_{SOFC}

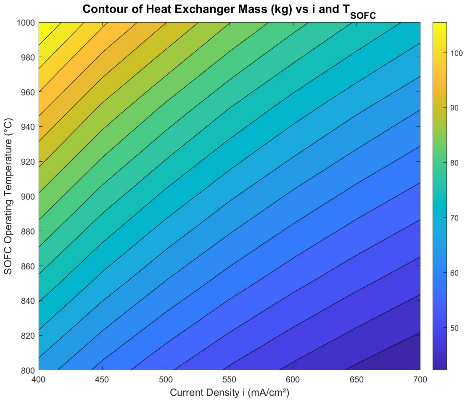

Figure C.20: Contour of $\mathrm{M_{HX}}$ vs i and T_{SOFC}

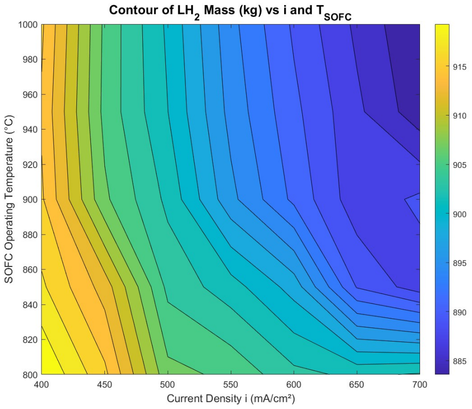

Figure C.21: Contour of $\mathrm{M_{LH2}}$ vs i and T_{SOFC}

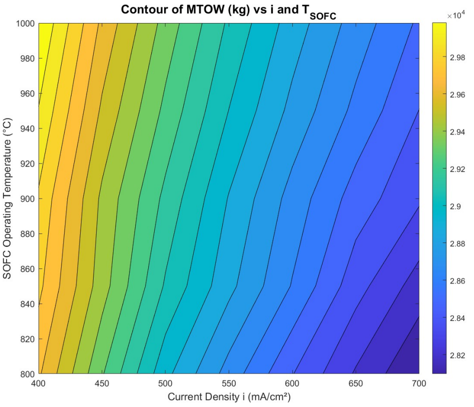

Figure C.22: Contour of MTOM vs i and T_{SOFC}

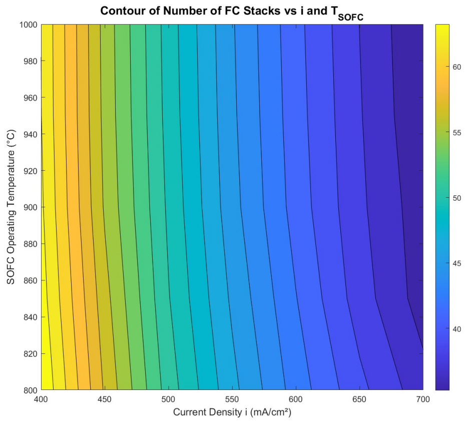

Figure C.23: Contour of Stack Count vs i and T_{SOFC}

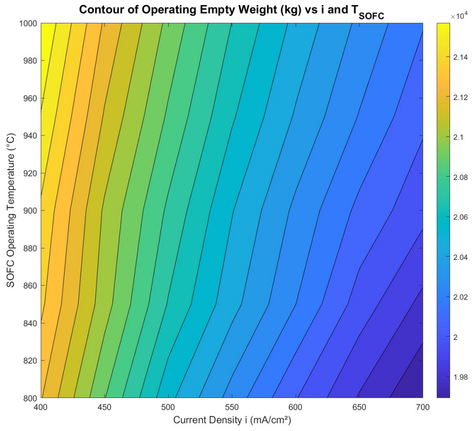

Figure C.24: Contour of OEM vs i and T_{SOFC}

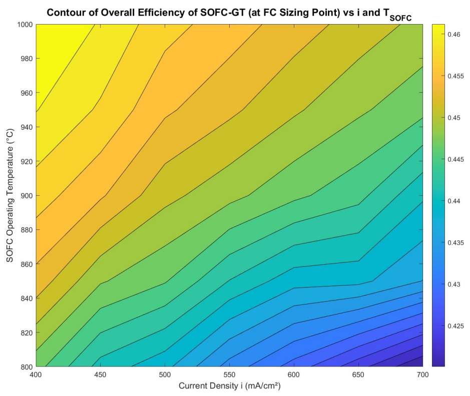

Figure C.25: Contour of $\eta_{\text{thermal,overall}}$ vs i and T_{SOFC}

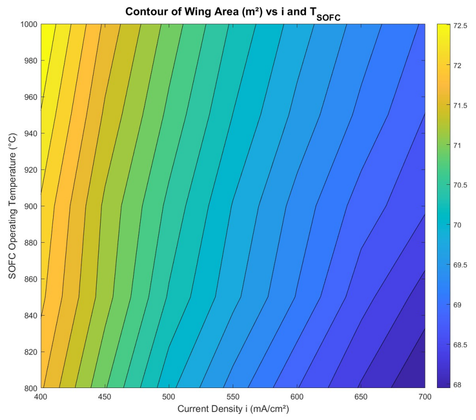

Figure C.26: Contour of Wing Area vs i and T_{SOFC}

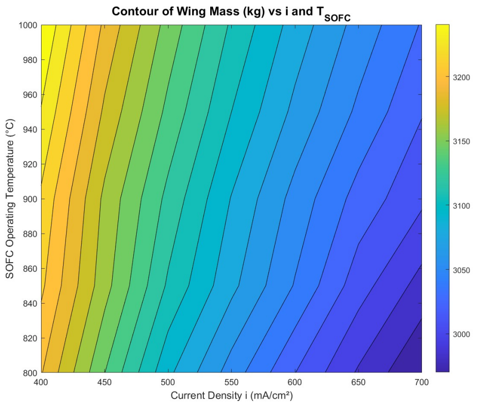

Figure C.27: Contour of Wing Mass vs i and T_{SOFC}

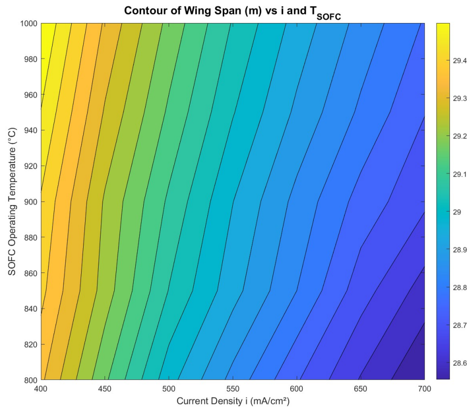

Figure C.28: Contour of Wing Span vs i and T_{SOFC}

C.3. Anode Fuel Composition

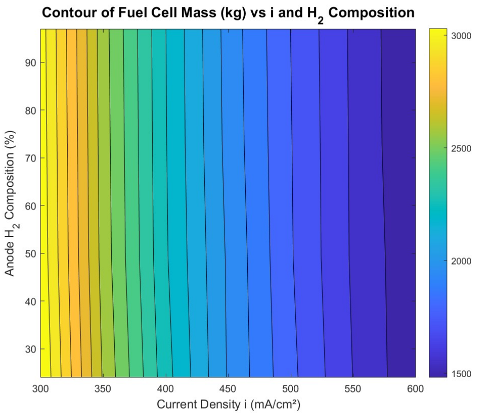

Figure C.29: Contour of Fuel Cell Mass vs i and anode H_2 composition

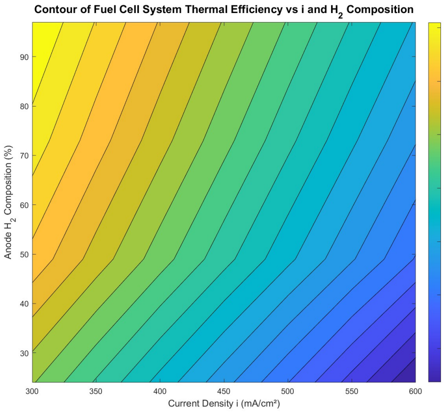

Figure C.30: Contour of η_{FC} vs i and anode H_2 composition

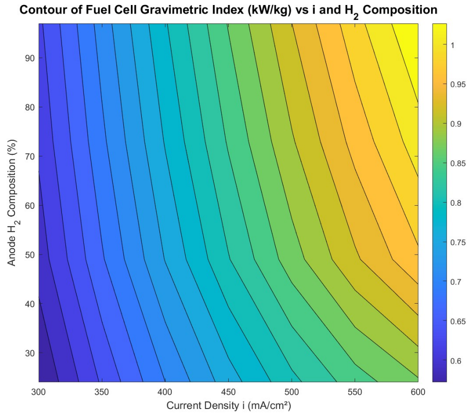

Figure C.31: Contour of $\mathrm{GI}_{\mathrm{FC}}$ vs i and anode H_2 composition

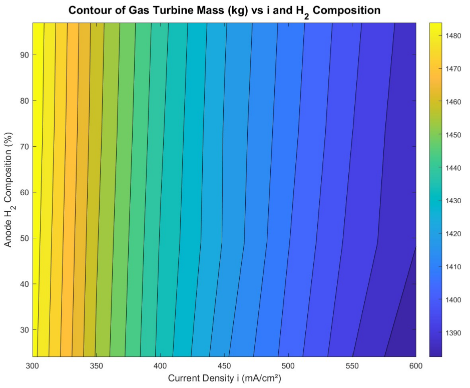

Figure C.32: Contour of GT Mass vs i and anode H_2 composition

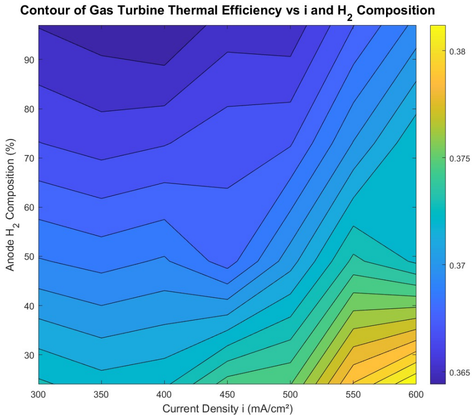

Figure C.33: Contour of η_{GT} vs i and anode H_2 composition

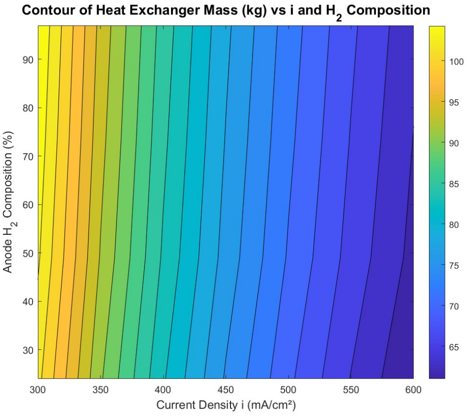

Figure C.34: Contour of HX Mass vs i and anode H_2 composition

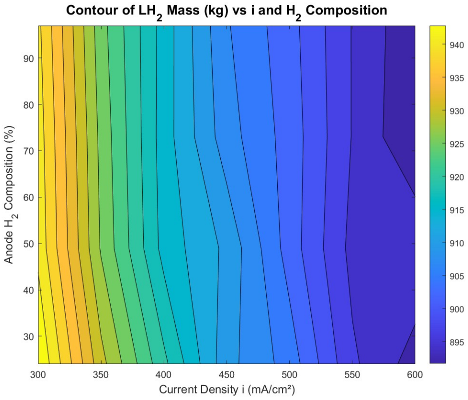

Figure C.35: Contour of $\mathrm{M_{LH2}}$ vs i and anode H_2 composition

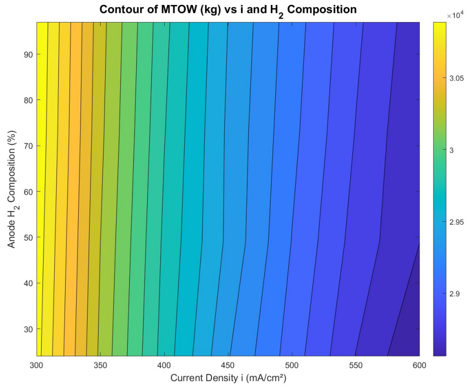

Figure C.36: Contour of MTOM vs i and anode H_2 composition

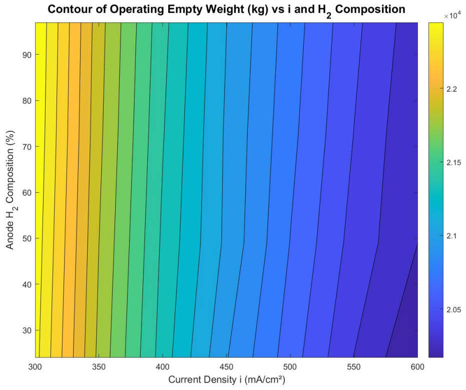

Figure C.37: Contour of OEM vs i and anode H_2 composition

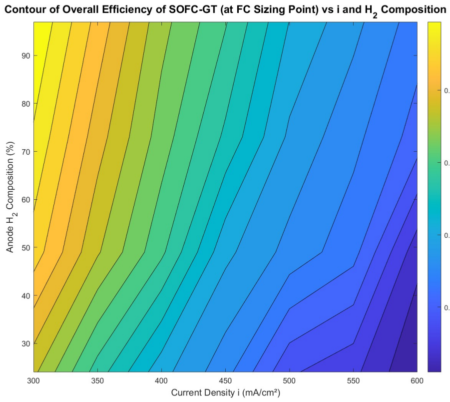

Figure C.38: Contour of η_{overall} vs i and anode H_2 composition

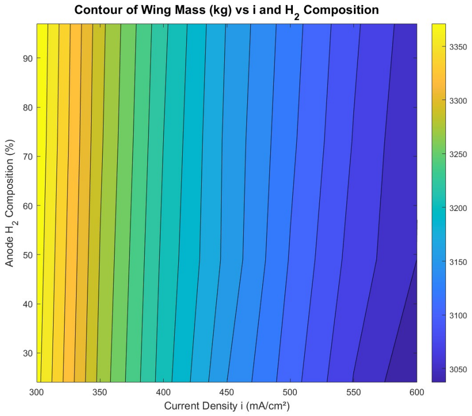

Figure C.39: Contour of Wing Mass vs i and anode H_2 composition

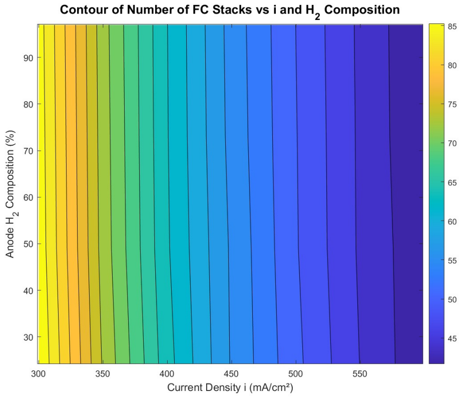

Figure C.40: Contour of Stack Count vs i and anode H_2 composition

C.4. Anode Fuel Utilization

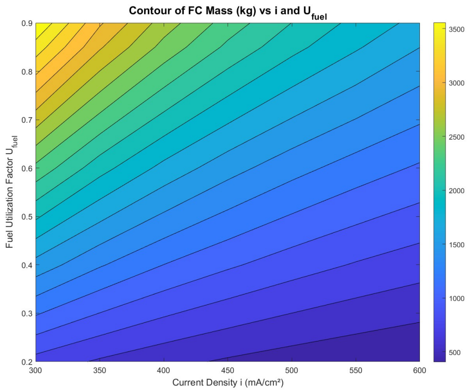

Figure C.41: Contour of Fuel Cell Mass vs i and $\mathrm{U_{fuel}}$

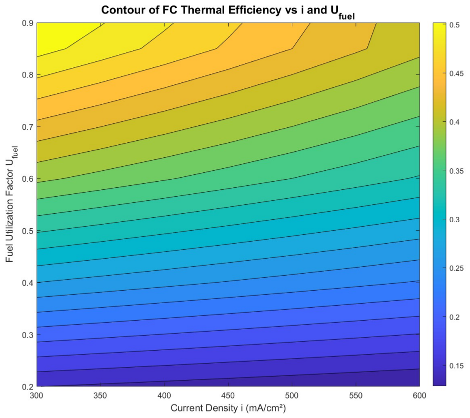

Figure C.42: Contour of η_{FC} vs i and $\mathrm{U_{fuel}}$

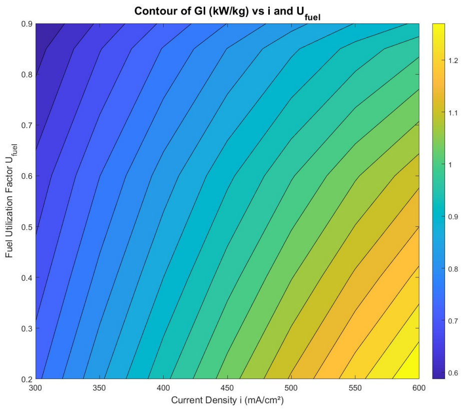

Figure C.43: Contour of $\mathrm{GI_{FC}}$ vs i and $\mathrm{U_{fuel}}$

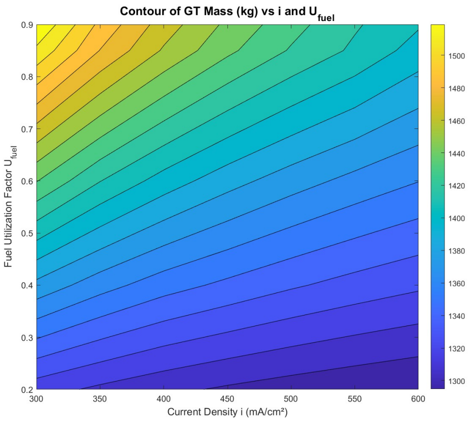

Figure C.44: Contour of GT Mass vs i and $\mathrm{U_{fuel}}$

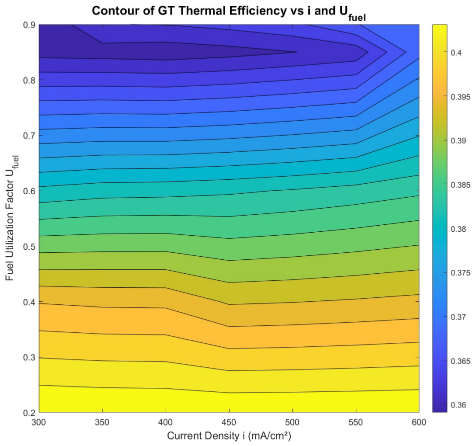

Figure C.45: Contour of η_{GT} vs i and $\mathrm{U_{fuel}}$

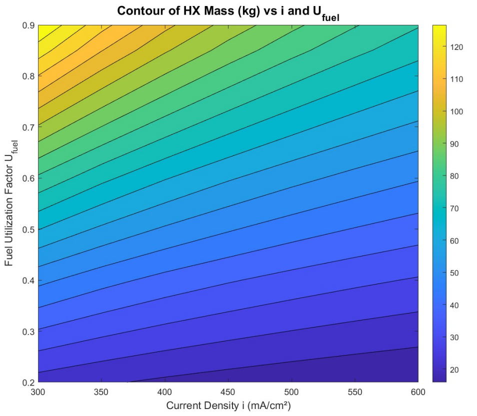

Figure C.46: Contour of HX Mass vs i and $\mathrm{U_{fuel}}$

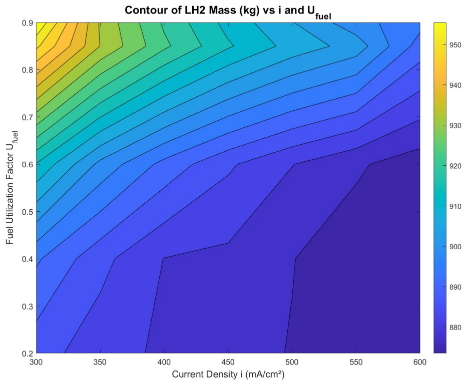

Figure C.47: Contour of $\mathrm{M_{LH2}}$ vs i and $\mathrm{U_{fuel}}$

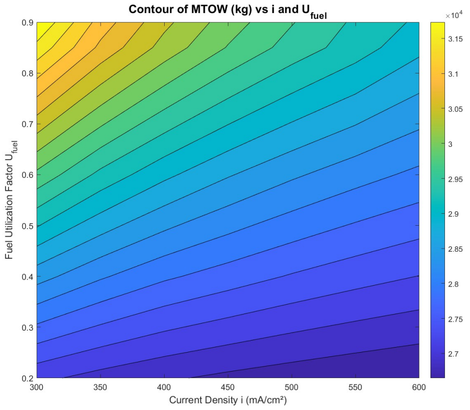

Figure C.48: Contour of MTOM vs i and $\mathrm{U_{fuel}}$

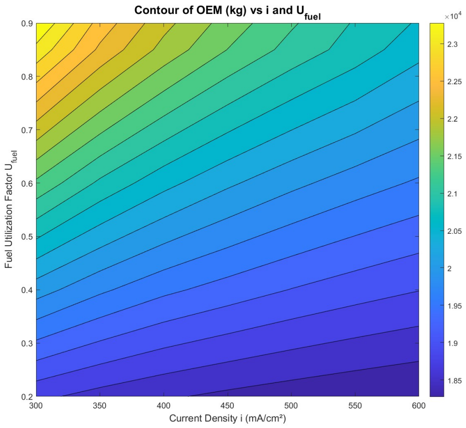

Figure C.49: Contour of OEM vs i and $\mathrm{U_{fuel}}$

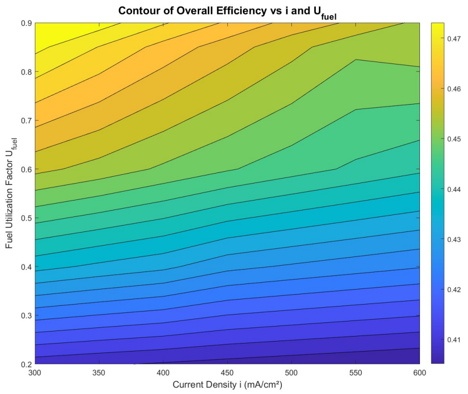

Figure C.50: Contour of η_{overall} vs i and $\mathrm{U_{fuel}}$

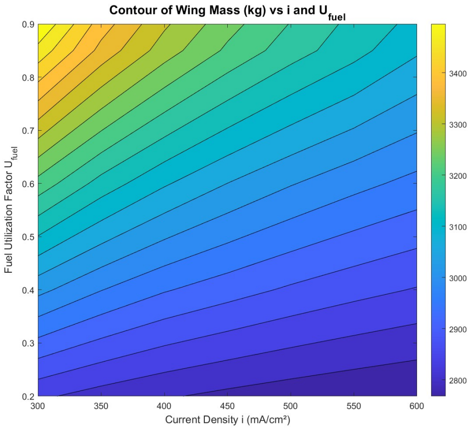

Figure C.51: Contour of Wing Mass vs i and $\mathrm{U_{fuel}}$

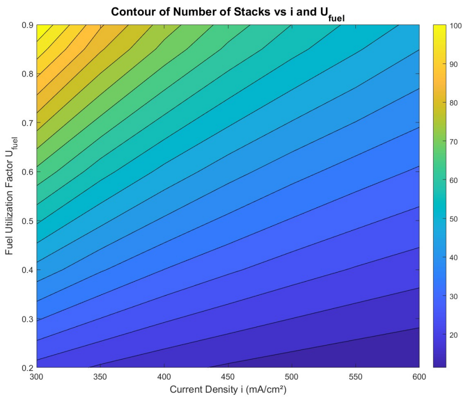

Figure C.52: Contour of Stack Count vs i and $\mathrm{U_{fuel}}$

C.5. Air Stoichiometric Ratio

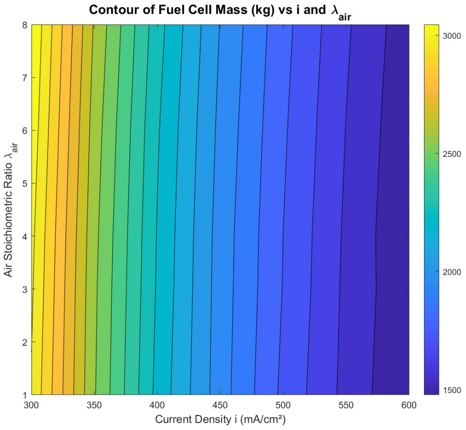

Figure C.53: Contour of Fuel Cell Mass vs i and air stoichiometric ratio

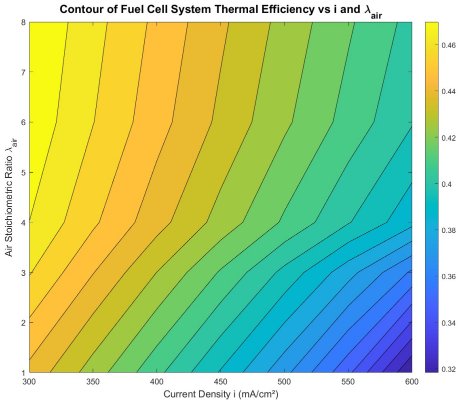

Figure C.54: Contour of η_{FC} vs i and air stoichiometric ratio

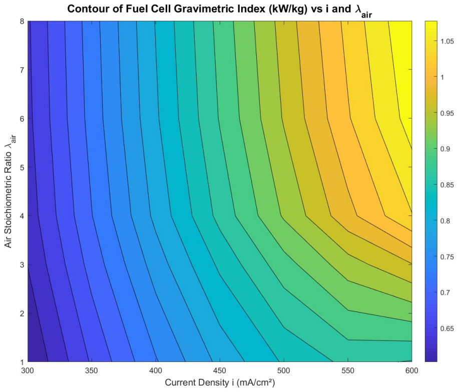

Figure C.55: Contour of $\mathrm{GI}_{\mathrm{FC}}$ vs i and air stoichiometric ratio

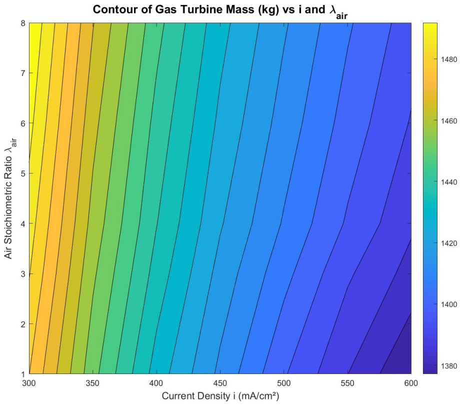

Figure C.56: Contour of GT Mass vs i and air stoichiometric ratio

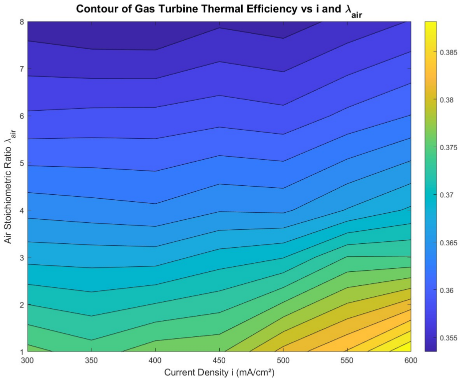

Figure C.57: Contour of η_{GT} vs i and air stoichiometric ratio

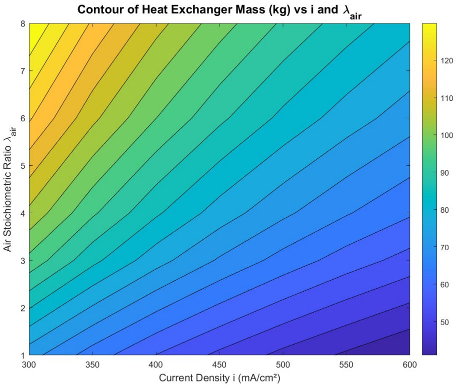

Figure C.58: Contour of HX Mass vs i and air stoichiometric ratio

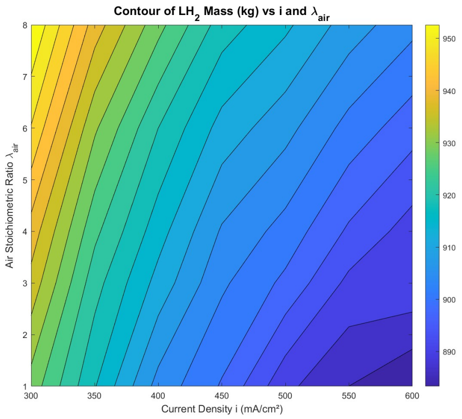

Figure C.59: Contour of $\mathrm{M_{LH2}}$ vs i and air stoichiometric ratio

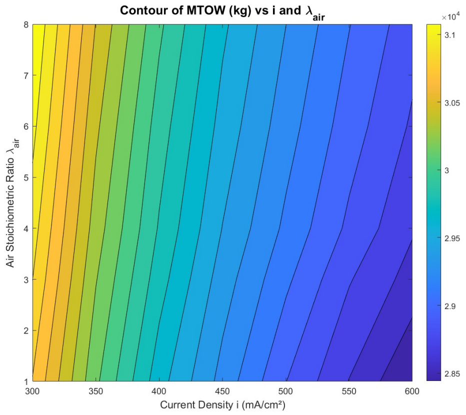

Figure C.60: Contour of MTOM vs i and air stoichiometric ratio

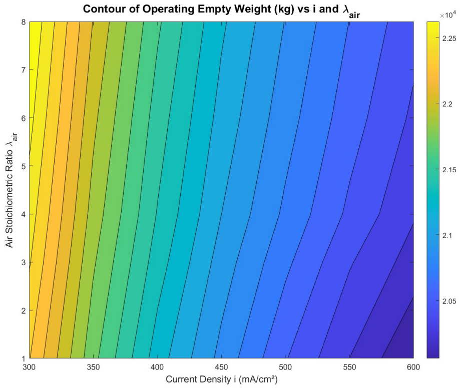

Figure C.61: Contour of OEM vs i and air stoichiometric ratio

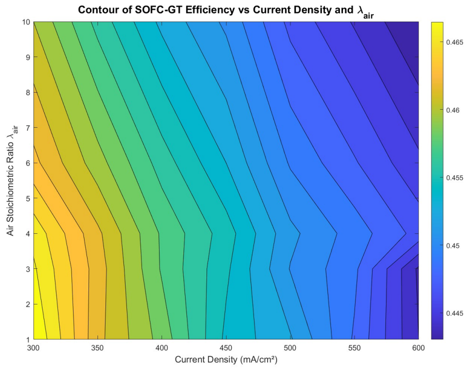

Figure C.62: Contour of η_{overall} vs i and air stoichiometric ratio

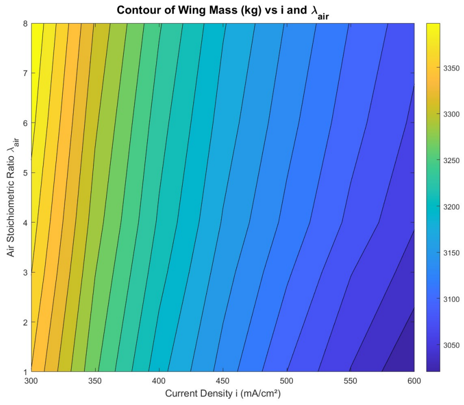

Figure C.63: Contour of Wing Mass vs i and air stoichiometric ratio

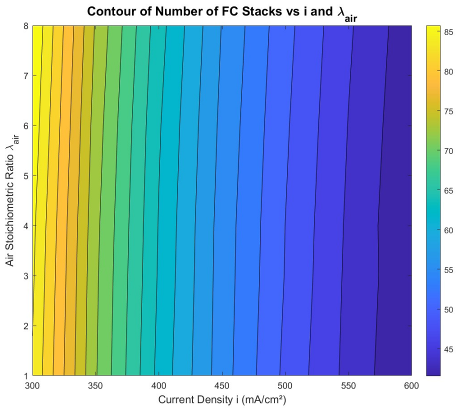

Figure C.64: Contour of Stack Count vs i and air stoichiometric ratio

C.6. Wing Aspect Ratio

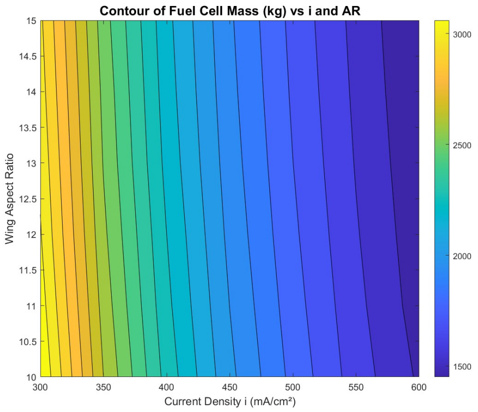

Figure C.65: Contour of Fuel Cell Mass vs i and wing aspect ratio

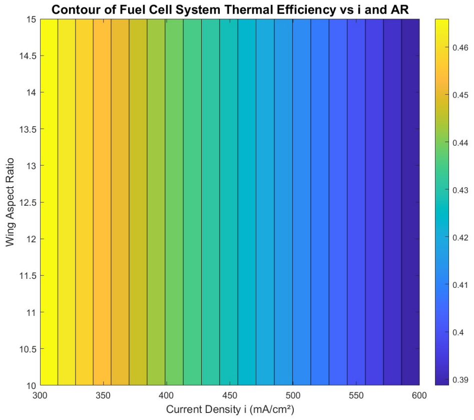

Figure C.66: Contour of η_{FC} vs i and wing aspect ratio

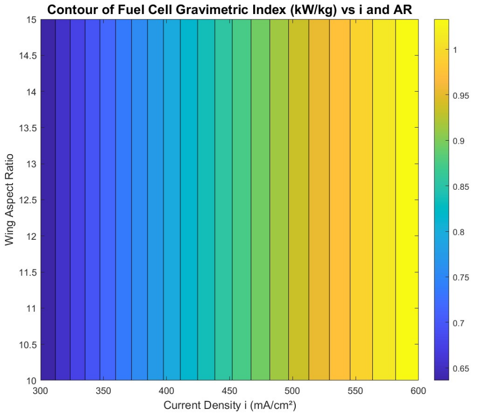

Figure C.67: Contour of $\mathrm{GI}_{\mathrm{FC}}$ vs i and wing aspect ratio

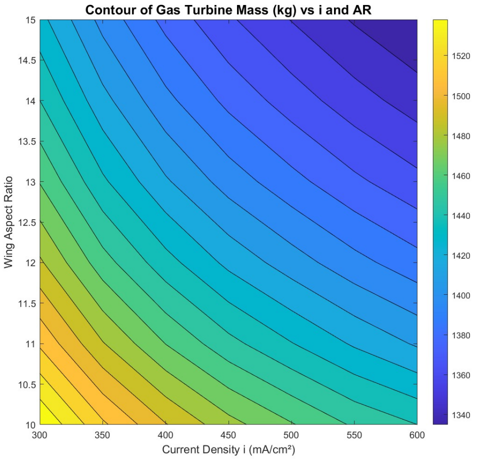

Figure C.68: Contour of GT Mass vs i and wing aspect ratio

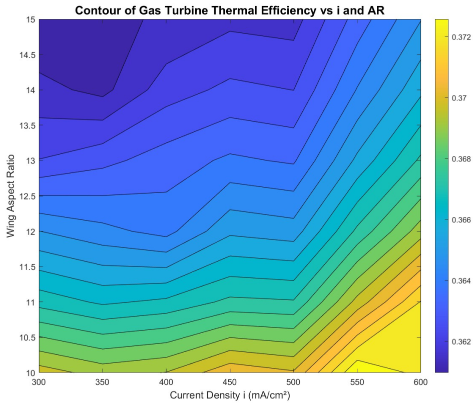

Figure C.69: Contour of η_{GT} vs i and wing aspect ratio

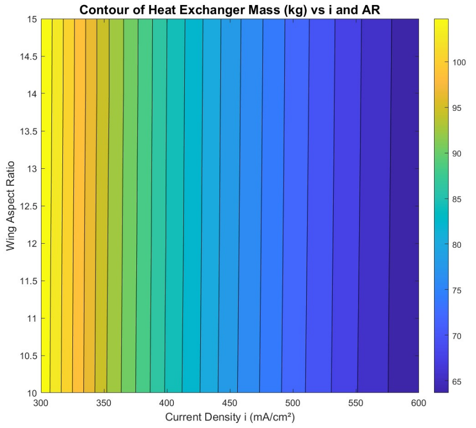

Figure C.70: Contour of HX Mass vs i and wing aspect ratio

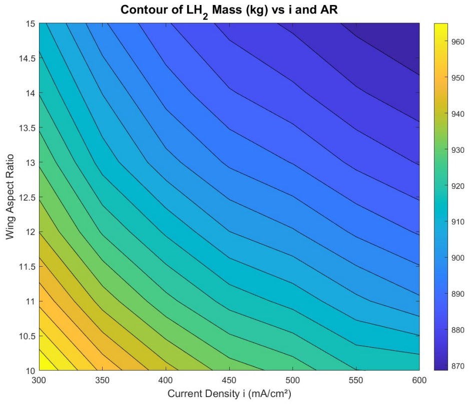

Figure C.71: Contour of $\mathrm{M}_{\mathrm{LH}_2}$ vs i and wing aspect ratio

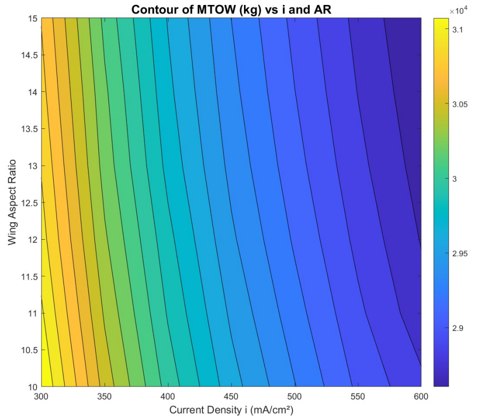

Figure C.72: Contour of MTOM vs i and wing aspect ratio

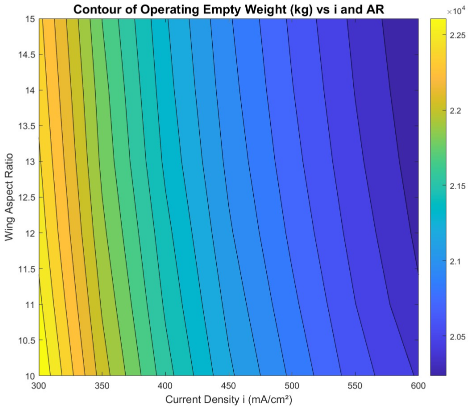

Figure C.73: Contour of OEM vs i and wing aspect ratio

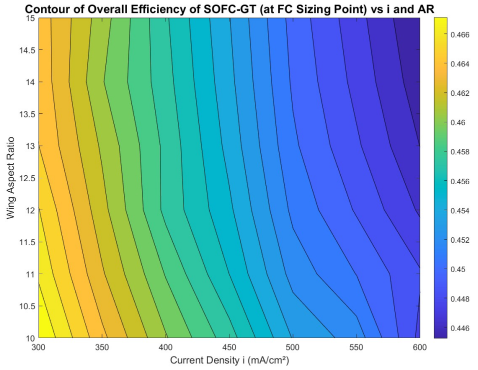

Figure C.74: Contour of η_{overall} vs i and wing aspect ratio

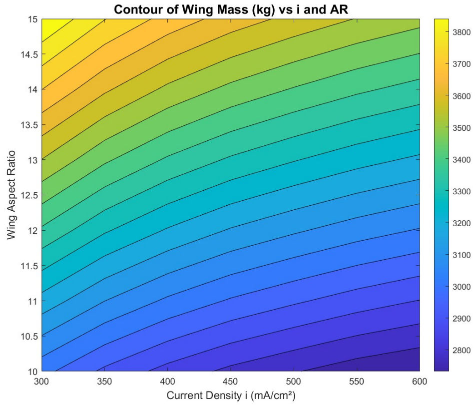

Figure C.75: Contour of Wing Mass vs i and wing aspect ratio

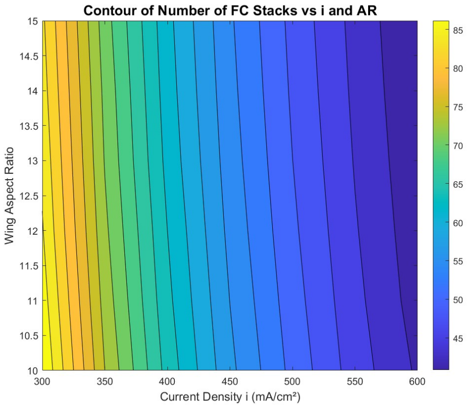

Figure C.76: Contour of Stack Count vs i and wing aspect ratio

C.7. Hydrogen Split in Cruise

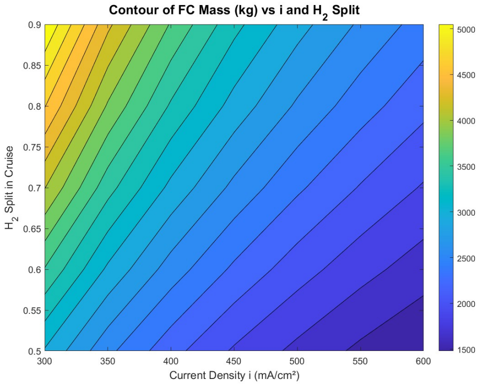

Figure C.77: Contour of Fuel Cell Mass vs i and cruise hydrogen split

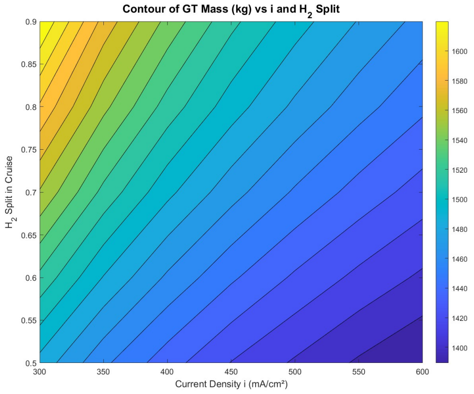

Figure C.78: Contour of GT Mass vs i and cruise hydrogen split

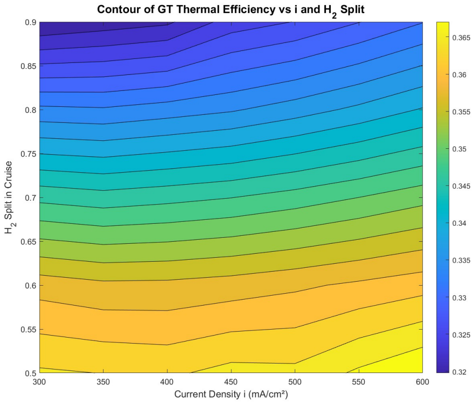

Figure C.79: Contour of η_{GT} vs i and cruise hydrogen split

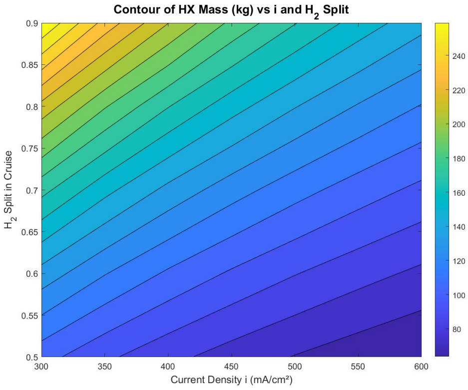

Figure C.80: Contour of HX Mass vs i and cruise hydrogen split

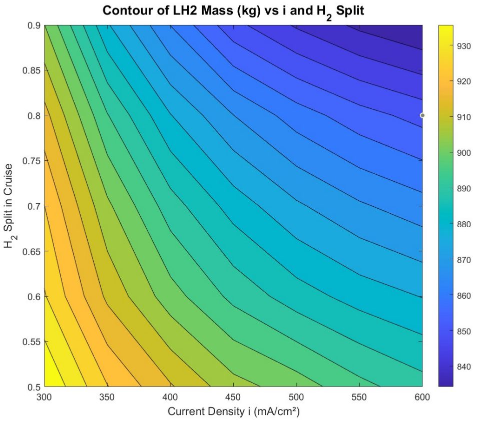

Figure C.81: Contour of $\mathrm{M_{LH_2}}$ vs i and cruise hydrogen split

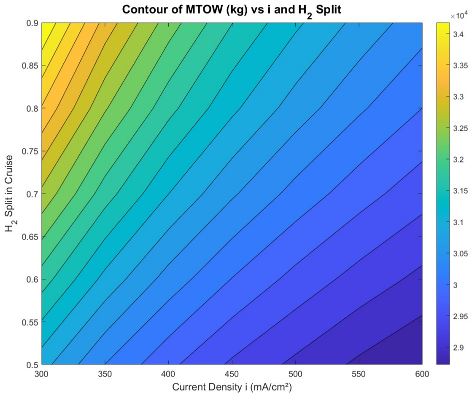

Figure C.82: Contour of MTOM vs i and cruise hydrogen split

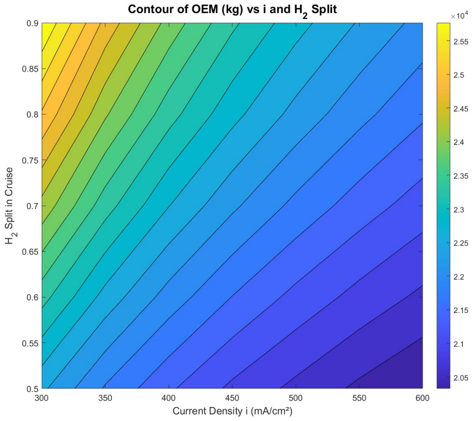

Figure C.83: Contour of OEM vs i and cruise hydrogen split

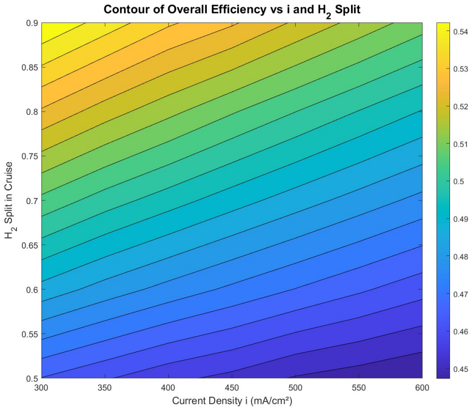

Figure C.84: Contour of η_{overall} vs i and cruise hydrogen split

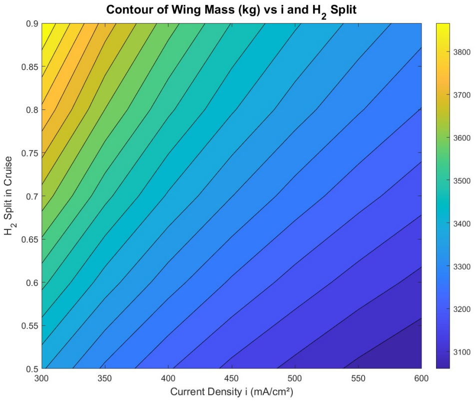

Figure C.85: Contour of Wing Mass vs i and cruise hydrogen split

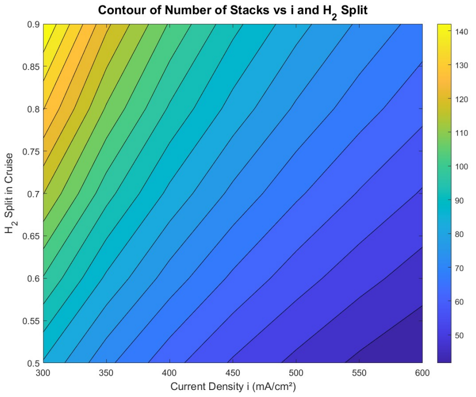

Figure C.86: Contour of Stack Count vs i and cruise hydrogen split

C.8. SOFC Technology Scenarios

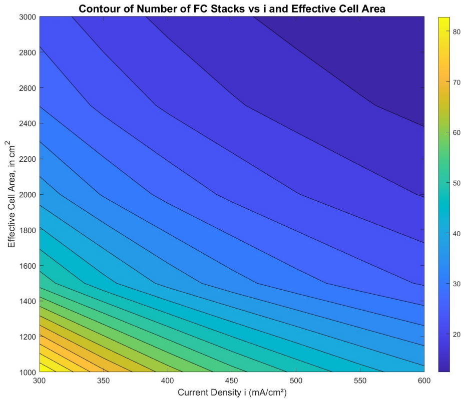

Figure C.87: Contour of Number of Stacks vs i and SOFC technology scenario

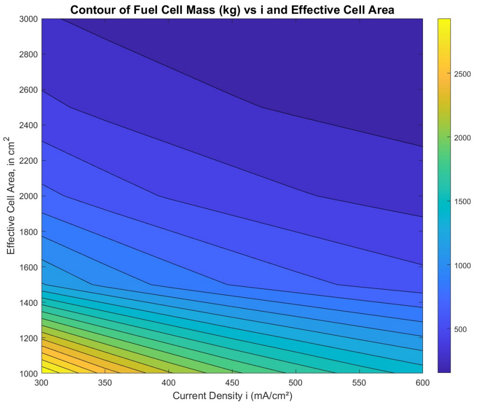

Figure C.88: Contour of FC Mass vs i and SOFC technology scenario

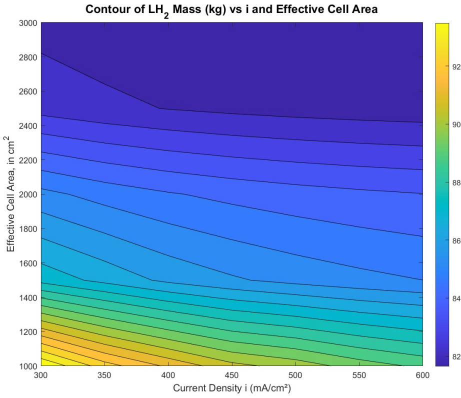

Figure C.89: Contour of $\mathrm{LH_2}$ Mass vs i and SOFC technology scenario

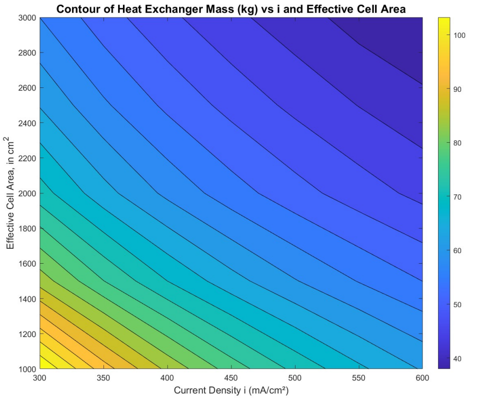

Figure C.90: Contour of HX Mass vs i and SOFC technology scenario

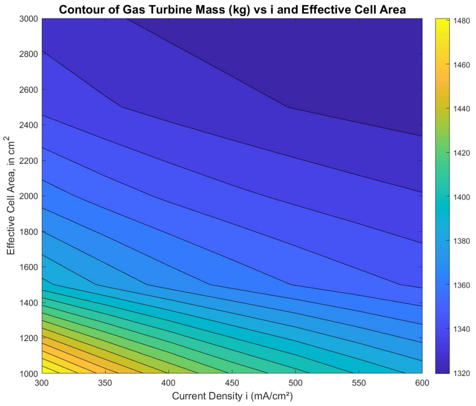

Figure C.91: Contour of GT Mass vs i and SOFC technology scenario

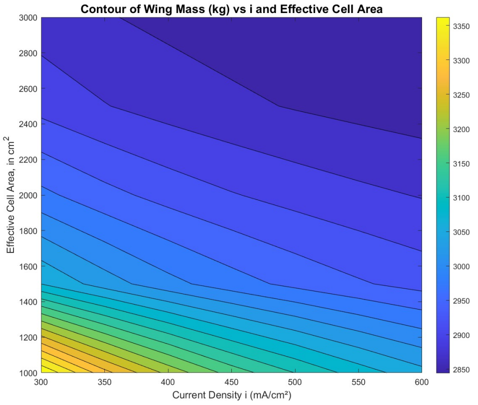

Figure C.92: Contour of Wing Mass vs i and SOFC technology scenario

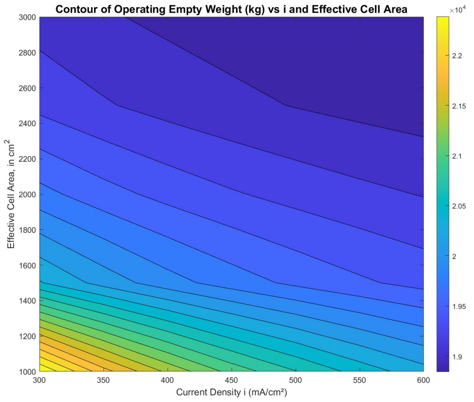

Figure C.93: Contour of OEM vs i and SOFC technology scenario

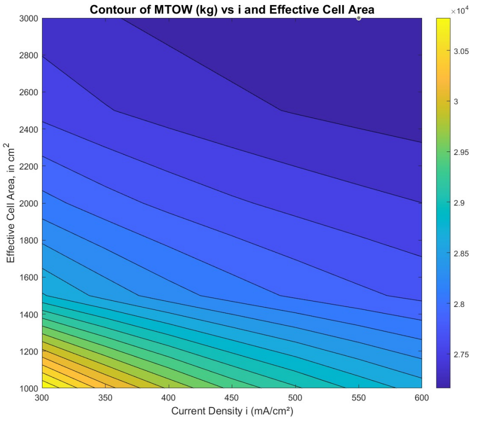

Figure C.94: Contour of MTOW vs i and SOFC technology scenario

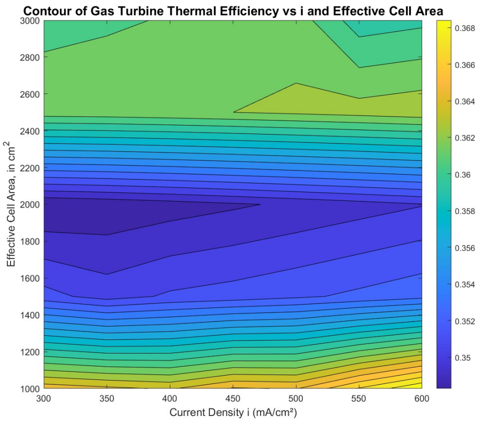

Figure C.95: Contour of η_{GT} vs i and SOFC technology scenario

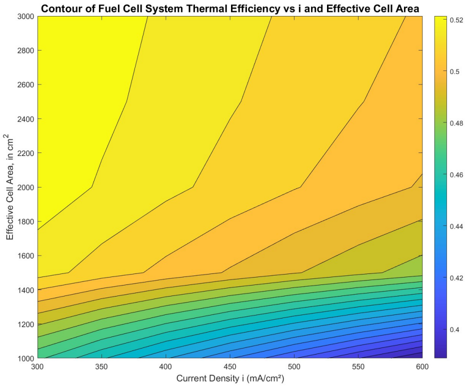

Figure C.96: Contour of η_{FC} vs i and SOFC technology scenario

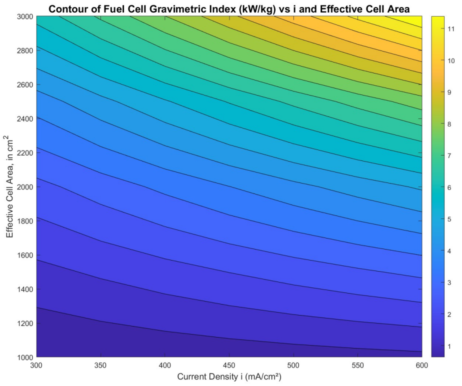

Figure C.97: Contour of $\mathrm{GI}_{\mathrm{FC}}$ vs i and SOFC technology scenario

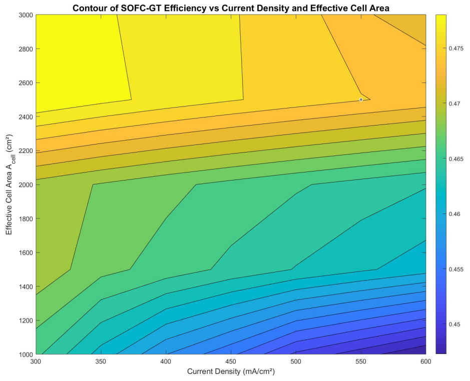

Figure C.98: Contour of η_{overall} vs i and SOFC technology scenario